X-ray Study of Planetary Nebulae

Mio Murashima

Department of Astronomy, School of Science, University of Tokyo,
7-3-1 Hongo, Bunkyo-ku, Tokyo 113-0033, Japan

Reprinted from the Thesis Submitted in
Partial Fulfillment of the Requirements
for the Degree of Doctor of Philosophy (Astrophysics)
the University of Tokyo
December 2005

Abstract

The diffuse X-ray emission from planetary nebulae is thought to originate from shock-heated gas created by fast stellar winds from the central star, and hence to sensitively reflect the nucleosynthesis, especially He-burning, inside intermediate-mass stars. In order to investigate abundances of X-ray emitting materials in planetary nebulae, all the currently available X-ray data were examined. The operating X-ray satellites *Chandra* and *XMM-Newton* provided archival data of 21 planetary nebulae, and X-ray emission was detected in 14 out of them. The X-ray spectra of 8 planetary nebulae (BD +30° 3639, NGC 6543, NGC 7027, NGC 3242, NGC 7009, NGC 2392, NGC 246, and NGC 7293) were studied in detail. In addition to these archival data, an observation of BD +30° 3639 which is the X-ray brightest planetary nebula is performed by the newest X-ray observatory *Suzaku*.

BD +30° 3639 is the most important target in the present thesis. The X-ray spectrum of this planetary nebula was known to show strong emission line at 0.91 keV attributed to helium-like Ne-K line, and a broad feature at 0.3–0.7 keV probably due to a blend of K-lines from C, N, and O. The superior energy resolution of the *Suzaku* X-ray Imaging Spectrometer for the first time revealed a strong emission line at 0.37 keV due to helium-like C K-lines, and clearly resolved helium-like and hydrogen-like O K-lines at 0.56 and 0.65 keV, respectively. This high quality spectrum allowed quantitative studies of the abundances. Since hydrogen and helium lack emission lines in the X-ray band, the study focused on accurate determination of the abundance ratios among heavy ions. Assuming the solar He/H ratio, the C/O, N/O, and Ne/O abundance ratios were then derived as 95(75–110), 3.3(1.0–5.0), and 5.5(4.8–7.3) in the solar unit, respectively, where the range of 90% confidence is in parentheses. These measurements are far more accurate and reliable than any previous X-ray measurements of chemical composition in PNe. Furthermore, these results indicate significantly more extreme abundance patterns than were reported based on infrared-optical-ultraviolet observations.

Analyzing the archival data obtained with *Chandra* and *XMM-Newton*, point-like sources associated with the central stars were detected in NGC 7293, NGC 246, and NGC 6543. The last one also have diffuse X-ray emission. Although NGC 2392 was not resolved by *XMM-Newton*, its X-ray spectrum and derived physical parameters are similar to those of diffuse X-ray emitting planetary nebulae.

A systematic spectral analysis of NGC 7009, NGC 2392, and diffuse component of NGC 6543 yielded abundance patterns similar to that of BD +30° 3639; enhanced C abundances relative to O, and Ne abundances higher than O. This result, together with

that with *Suzaku* on BD $+30^\circ$ 3639, supports the view that the X-ray emission from planetary nebulae directly reflect He-burning products.

The major He-burning products are C and O, and then Ne and Mg follow them. The enhancement of C and Ne observed in X-rays from these planetary nebulae agree qualitatively with the current understanding of He-burning products, while an apparent deficit of oxygen, relative to C and Ne, remains as a puzzle. The case of BD $+30^\circ$ 3639 was examined, and two possible mechanisms which may enhance the Ne/O ratios were an over-ionization in a conductively cooling emission region, and the possible presence of significant amount of metals in dust. Quantitative comparison of the present results with nucleosynthesis calculations, considering these mechanisms, awaits future studies.

In this thesis, the X-ray abundance ratios of a planetary nebula was observationally determined for the first time, and the strongly enhanced C/O ratio was found. The present study thus becomes the first example of X-ray diagnostics of the nucleosynthesis products inside the intermediate-mass stars, and demonstrates that this new method provides valuable information that is inaccessible in other wavelengths.

Contents

Chapter 1

INTRODUCTION

The origin of elements is one of the most fundamental issues in astrophysics. The current consensus is that hydrogen and helium were synthesized in the early universe, while heavier elements inside stars, through quasi-steady nuclear burnings as well as on the occasion of supernova explosions. Supernovae are also regarded as an important process of metal transport out to the interstellar space. However, there is yet another important channel of metal feedback, namely mass loss from low- and intermediate-mass stars. With the initial mass less than $\sim 8\ M_{\odot}$, these stars are plenty, and should contribute significantly to the metal enrichment of the universe. In particular, the mass loss from these stars are considered to play an important role in supplying products of He-burning, which occurs in the later evolutionary stage of these stars. The He-burning products are rich in carbon, nitrogen, oxygen, neon, and magnesium, many of which are utilized by living creature on the earth, including ourselves.

A final stage of a commonplace star is a planetary nebula (PN), which shows beautiful and complicated shapes in the optical band. A PN is regarded as an important messenger as to the nucleosynthesis in the intermediate-mass stars, since it originates from stellar envelopes where the stellar reactor products are stored. As a result, PNe have been observed extensively in radio to ultraviolet frequencies. However, it is not easy to extract pure He-burning products, since the matter in a PN have experienced mixing processes, called "dredge up", in its evolutionary stages.

X-ray emission from PNe has long been predicted by a PN formation model, called "Interacting Stellar Winds model (ISW model)" (Kwok 1982). According to it, fast stellar winds from the central star of a PN produce shock-heated hot plasmas with a temperature of ~ 1 keV, which emit soft X-rays. Since the late 1980s, the predicted soft X-ray emission has been detected with X-ray satellites such as *Einstein*, *EXOSAT*, and *ROSAT*.

Furthermore, recent *Chandra* and *XMM-Newton* observations are revealing that the X-ray emission of some, not all, PNe comes diffusely from the interior of the optical inner shell (Kastner et al. 2000; Kastner et al. 2001; Kastner et al. 2003), in agreement with the ISW model prediction.

In terms of X-ray spectroscopy, an extremely enhanced Ne-K line was detected with *ASCA*, and then with *Chandra*, from BD +30° 3639 which is a prototypical young PN. This PN and several others also exhibited spectral features attributable to emission lines from C, N, and O. These X-ray observations often indicate abundances which are different from the optical nebular abundances (Maness et al. 2003). Based on these results, we have come to believe that the X-ray diagnostics of PNe provide a rare opportunity of probing into the He-burning products, in a more sensitive way than is available in the infrared to ultraviolet wavelengths. However, the energy resolution of *Chandra* and *XMM-Newton* is somewhat too poor to individually resolve characteristic K-emission lines from highly ionized C, N, and O ions.

Now, we have a new X-ray observatory *Suzaku*, successfully launched on 2005 July 10. The *Suzaku* XIS has both a large effective area and a superior energy resolution below 1 keV, and hence is ideal for the spectroscopy of faint diffuse soft X-ray sources such as PNe. In order to determine the X-ray abundances, BD +30° 3639 was observed with *Suzaku* for 34 ks. We have successfully resolved C-K lines at 0.37 keV for the first time, and determined the abundance ratios among C, O, and Ne, with much less uncertainties than were achieved in any previous X-ray observations of PNe. We also searched the public *Chandra* and *XMM-Newton* data for X-ray emitting PNe, and found 14 X-ray emitting PNe out of the 21 observed. Information derived from these sources are utilized to strengthen the *Suzaku* results on BD +30° 3639.

In Chapter 2, we review the stellar nucleosynthesis and X-ray emission from PNe. Chapter 3 describes the instrumentation of *Chandra*, *XMM-Newton*, and *Suzaku*. In Chapter 4, we select sample objects to be studied, and describe their individual properties. Chapter 5 is the main part of the present thesis, where we analyze the spectra of BD +30° 3639. It is followed by Chapter 6, where results on other PNe are presented. Then we discuss our results in Chapter 7, and presented a brief summary in Chapter 8.

Chapter 2

REVIEW

2.1 Chemical Evolution

2.1.1 Chemical evolution of the universe

At the beginning, the universe was very hot and dense. There neutrons and protons were colliding to create deuterons, and then quickly combined into ^{4}He, leaving a much fewer number of ^{3}H and ^{3}He as intermediate products. These ^{3}H and ^{3}He partly combined with ^{4}He to become ^{7}Li and ^{7}Be, respectively. However, there is no stable nuclide with the mass number of 5 or 8; therefore, neither reactions between a proton and ^{4}He, nor those between two ^{4}He nuclei, proceeded. The only remaining way of producing heavier nuclide was nearly simultaneous collisions among three ^{4}He nuclei into ^{12}C, but this did not take place efficiently because of the quickly falling temperature in the expanding universe, and Coulomb barriers. As a result, nuclear reactions ceased when the universe was about 20 minutes old, and no new nuclide were produced any more.

Although the present universe mainly consists of H ($\sim$ 70 %) and He ($\sim$ 28 %) in the mass ratio, it also contains various heavier elements, and actually we know more than 280 natural isotopes. There are stable elements of which the atomic number is up to 82 (Pb), and also even heavier radioactive natural isotopes, such as uranium, with the atomic number of 92. These heavy elements, or "metals", are thought to have been synthesized in the stellar interior (§2.1.2). The very early history of such metal production can be investigated by deriving abundances of high redshift objects such as quasi stellar objects and Lyman break galaxies (Pettini 2004).

Heavy elements are detected not only in stellar materials (and associated planets like Earth), but also in interstellar medium (ISM) of the Milky Way and other galaxies.

Even intergalactic hot plasmas contain a large amount of heavy elements. These imply that the metals synthesized in the stellar furnace are efficiently transported out into the ISM (and even to outside the host galaxy), rather than remaining in the stellar interior. Such "metal transport" is considered to take place via two major processes; supernova explosions (§2.1.3), and stellar mass loss (§2.1.4). The heavy elements transported to the ISM are partially taken into the interior of stars of later generations, thus making them more metal enriched from the birth than their predecessors.

2.1.2 Stellar nucleosynthesis

Heavy elements synthesized inside stars are roughly divided into four groups according to their production process; α nuclides, iron-peak nuclides, s-process products, and those from r-process.

Initial stages of the metal production inside stars proceed as a series of thermonuclear fusion reactions from lighter to heavier elements, namely, "burning" of H, He, C, O, and Si. In the H-burning that is the start point, a ^{4}He nucleus is synthesized from four H nuclei via two kinds of reactions; one is "p-p chain" and the other is "CNO cycle". As the H-burning proceeds, hydrogen becomes exhausted and a He-core starts to grow in the stellar center.

When the He-core becomes hot and dense enough, ^{12}C is produced via three-body collisions of ^{4}He, a process called "triple alpha reaction". In this stage, a star with initial mass of less than $\sim 8M_\odot$ has a degenerated C+O core, and the subsequent thermonuclear reaction in the core dose not occur. As a temperature in the C+O core of a more massive star comes up to be nearly 6×10^8 K, heavier elements are formed by C-burning. When the temperature becomes much higher, O-burning occurs and then Si-burning, depending on the mass. These series of reactions are responsible for the production of such nuclei as ^{4}He, ^{12}C,^{16}O, ^{20}Ne, ^{24}Mg, ^{28}Si, and ^{32}S. These are called α-nuclides because they are formed as multiples of ^{4}He, and their synthesis reactions are called α-process. Simultaneously with the O-burning, α capture by ^{20}Ne starts. When the core temperature reaches $\gtrsim 3\times10^9$ K, ^{4}He is newly formed by photodisintegration of ^{28}Si. Capturing these α particles, and emitting photons, the reaction goes on through ^{28}Si, ^{32}S, ^{36}Ar, ^{40}Ca, ^{44}Ti, ^{48}Cr, ^{52}Fe, and ^{56}Ni.

Under exceedingly hot conditions, other reactions, such as proton or neutron emission by photodisintegration and electron capture, start working. The temperature is so high that nuclei are constantly forming and disintegrating, and consequently the system will become a nuclear statistical equilibrium. This, called e-process, produces iron-peak nuclides around ^{56}Fe, which has the largest binding energy per nucleon. The iron-peak nuclides are those with the atomic number in the range from 40 to 65, which correspond to such elements as Sc, Ti, V, Cr, Mn, Fe, Co, Ni and Cu. Unlike the α-process, the e-process involves weak interactions, so that heavier nuclei become slightly neutron rich; e.g., a ^{56}Fe nucleus is composed of 26 protons and 30 neutrons. When a core composed of Fe is once formed, there is no longer energy production via nuclear fusion. The e-process occurs not only inside stars but also in type Ia supernovae (§2.1.3).

Some reactions (e.g., C-burning, α-captures on ^{13}C and ^{22}Ne) that take place during the nuclear burning release free neutrons. Since a free neutron is not prevented by Coulomb repulsion from approaching a nucleus, it will quickly be absorbed by a nucleus, to form a heavier isotope of the same element; for example, converting ^{56} Fe to ^{57}Fe, both of which are stable. The absorption of free neutrons also produce unstable isotopes which will soon decay mainly via β-process. For example, ^{59}Fe,which is unstable, decays to ^{59}Co, which in turn changes into ^{60}Co by absorbing a free neutron. ^{60}Co is also unstable and β^- decays to ^{60}Ni. In this way, the ^{56}Fe nucleus moves up the periodic table, and elements heavier than iron are synthesized. This neutron capture process is called “s-process”, where “s” represents “slow”. The heaviest isotope that can be produced by the s-process is ^{209}Bi, which is converted to ^{210}Bi by capturing a neutron. ^{210}Bi β^- decays to ^{210}Po, and ^{210}Po α decays to ^{206}Pb which is stable. After three times of neutron capture, ^{206}Pb is converted to ^{209}Pb, but, it is unstable and β^- decays to ^{209}Bi, i.e. back to the start. Enrichment of the s-process elements on the surface of red giants is observed, so that this process is thought to occur inside evolved low- and intermediate-mass stars. However, details still remain a puzzle and a matter of active research.

In order to produce elements heavier than ^{209}Bi, consecutive neutron absorption steps have to proceed more rapidly than β^- decays. Such a process is called “r-process (rapid process)”. Since we know such isotopes are produced through a neutron capture by an isotope with the β^- decay life time of 10^{-6} sec, the r-process is expected to occur where the neutron density is higher than 10^{23} cm^{-3}. The isotopes directly formed by the r-process are unstable against β decay, because of the obvious neutron excess; therefore, they are converted, through a series of β-decays, to stable isotopes which we observe. When the r-process proceeds up to the mass number of $\sim$250 and the atomic number of 94, corresponding to Pu, the produced nuclei start disintegrating into lighter nuclei via nuclear fission, and the r-process will stops. The r-process requires the hot and dense neutron-rich environment. Such condition has been thought to be found in the type II supernova (§2.1.3), and the modeling of nucleosynthesis are going to be improved. Most of nuclides heavier than iron are synthesized by either the s-process or the r-process, or both.

2.1.3 Supernovae

The heavy elements, synthesized in the stellar interior through various reactions (§2.1.2), must be transported out to enrich the ISM. A supernova (SN) is regarded as one of such processes that feed heavy elements back into the interstellar space. At the same time, it is thought to play an important role of production of heavier elements.

Based on optical spectra near the maximum brightness, supernovae (SNe) are empirically classified into two types; "type II" which contains hydrogen lines, and "type I" without them. Type I SNe which show absorption due to Si are called "type Ia", while the other type I SNe are usually called "type Ib". A type Ia SN is thought to result from a thermonuclear explosion of a white dwarf (WD) with a C+O core in a mass-exchanging binary, due to mass accretion from a companion star. In contrast,the other types (Ib and II) of SNe are explained as gravitational collapse of massive stars with the initial mass higher than 8 $M_{\odot}$. Since a SN explosion is a complex phenomenon involving a number of physical processes, its understanding is mainly based on theoretical modelings, with observations providing "calibrations" to modeling details.

A SN Ia is thought to be triggered by central carbon ignition and subsequent disruption of a degenerate WD, when the accreting mass makes the overall WD mass to exceed the Chandrasekhar limit. When a burning wave sweeps through the WD, C and O are converted to iron-group elements. The outer part of the progenitor experiences explosive C and Ne-burning, and further toward the center, explosive O-burning form ^{28}Si and ^{32}S. The higher temperature leads to incomplete Si-burning, and then ^{56}Ni is synthesized together with intermediate nuclei like ^{40}Ca. Products of type Ia SNe are hence expected to rich in the iron-group elements, with the iron abundance typically twice higher, in solar abundance units, than those of Si to Ca. These results resemble the e-process results in the evolved cores of massive stars, but the SN explosion is such a sudden process that the products have not yet reached a β-decay equilibrium. In fact, γ-rays associated with the decay of $^{56}\mathrm{Ni} \rightarrow^{56} \mathrm{Co} \rightarrow^{56}$ Fe are the dominant energy source of early ($\sim 10^2$ day) light curves of type Ia SNe.

Chemical abundances of the products of core-collapse SNe are expected to be significantly different from those of type Ia SNe. According to a theoretical rough-and-ready treatment of core-collapse SNe, mass outside a certain radius of a progenitor is ejected, while that inside falls in to form a compact remnant in the center, i.e. a neutron star or a black hole. This core infall, together with the initial photodissociation of the iron-rich core, makes the ejecta rather devoid of iron-family nuclei. On the other hand, shock waves, created by a core bounce, is expected to sweep up outer regions of the star, and ignite again α-burning processes. Assuming an almost homogeneous distribution of density and temperature behind the shock, the energy released in a supernova, $E_{\rm SN}$, can be equated in a simple form with the radiation energy inside the shock fronts as $E_{\rm SN} = \frac{4}{3}\pi R^3 a T^4$, where R and T are the radius of the shock front and the temperature inside, respectively. As the ejecta expands, the temperature hence falls but the nuclear burning goes on. Until the temperature becomes $\sim 5 \times 10^9$ K, explosive Si-burning occurs, and then incomplete Si-burning follows at $\sim 4 \times 10^9$ K. Subsequently, explosive O-burning and explosive Ne/C-burning take place. As a consequence of these explosive burnings of lighter α-elements (which results from the iron-core disintegration), the products of Type II SNe are rich in intermediate-mass elements, ranging from C to Ca.

2.1.4 Stellar mass loss

In addition to SNe, stellar mass loss is regarded as the other principal process to provide metals, synthesized in the stellar interior, to the ISM. Low- and intermediate-mass stars ($0.8M_\odot < M < 8M_\odot$) stop their thermonuclear reactions when the He burning is completed (§2.1.2), and lose most of their masses due to expansion of outer layers. This occurs in their later evolutionary stages, corresponding to Red Giant Branch (RGB) and Asymptotic Giant Branch (AGB) phases (§2.2.1). Through the stellar mass loss, heavy elements synthesized inside intermediate-mass stars are fed back to the ISM, much more quietly than the transport by SNe. Therefore, mass loss ejecta are expected to contain many pieces of information of nucleosynthesis inside stars.

Through mass loss, intermediate-mass stars provide He burning products (C, O, Ne, and Mg) and s-process elements. Since they are more numerous larger by an order of magnitude than massive stars, overall metal yields of intermediate-mass stars may be significant. Actually, using various nucleosynthesis models and an initial mass function, Henry (2004) computed the total yields, especially of C, N, and He, due to intermediate-mass stars . They conclude that intermediate-mass stars contribute significantly to the supply of C and N compared with massive stars, although the results depend strongly on the model. In addition, a series of X-ray analysis on early galaxies suggest that SNe ejecta mostly escapes away from galaxies, and hence the stellar mass loss principally contributes to metal enrichment of the ISM (Matsushita et al. 2000).

In the present thesis, we attempt to measure directly the abundances of products of intermediate-mass stars. Such stars are thought to evolve into white dwarfs, passing through planetary nebulae (PNe). A PN mainly consists of ionized gas, which is supplied via stellar mass loss and is excited by the central star. Therefore, abundances of PNe are considered to represent the nucleosynthesis inside their progenitors.

In order to assess the relative importance of PNe among intermediate-mass stars, it is necessary to know what fraction of such stars experience the PN phase on the way of their evolution. As a roughly approximation, the number of intermediate-mass stars in our galaxy, their life time, and the dynamical life time of a PN may be assumed to be 10^{10}, 10 Gyr, and 10^4 yr, respectively. Then, the expected number of planetary nebulae to be observed at present is estimated as $\sim 10^4$, assuming that all the intermediate-mass stars experience the PN phase. Based on the local number density of observed PNe, Kwok (2000) estimated the number of PNe in our galaxy as $\sim$ 14000. These number is 5$\sim$10 times larger than the number of cataloged Galactic PNe, about 1700. However, there can be a large number of PNe which remain undetected, due to heavy dust obscuration in the Galactic plane, faintness of old PNe, compactness of young PNe, and so on. If the observed number is corrected for these factors, then the above estimate may be consistent with the observation. At least we can say that a significant fraction of intermediate-mass stars are observed as PNe at the end of their evolution, and that PNe provide a good probe of the nucleosynthesis of intermediate-mass stars.

2.2 Evolution of Intermediate-Mass Stars

2.2.1 Evolutionary track on the H-R diagram

As described briefly in the previous section, an intermediate-mass star lighter than $\sim 8M_\odot$ evolves from a H-burning star into a He-burning red giant with significant stellar mass loss, then experiences a PNe phase, and finally becomes a white dwarf. In this subsection, we overview the evolution of intermediate-mass stars along with the evolutionary track on the Hertzsprung-Russel diagram (H-R diagram), which summarized stars on the plane of luminosity vs. surface temperature. Figure 2.1 gives an examples of H-R diagram together with theoretical evolutionary tracks of stars with particular masses, where intermediate-mass stars are represented by $1M_\odot$ and $5M_\odot$.

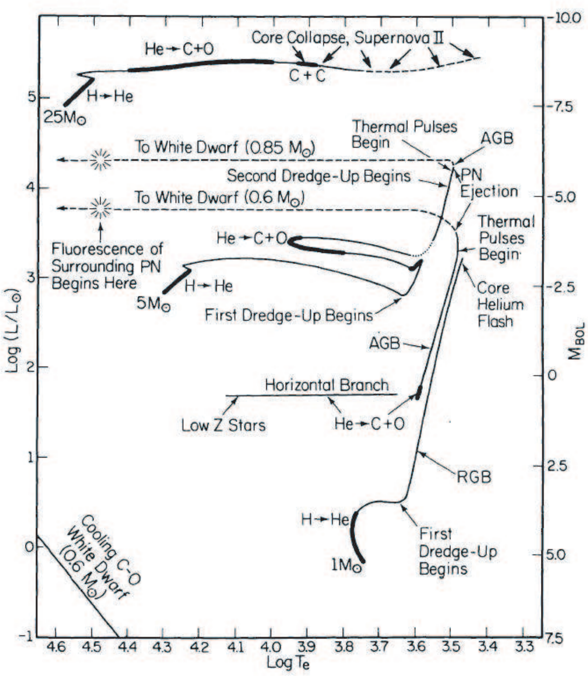

Figure 2.1: The tracks on the H-R diagram of theoretical model stars of low (1 $M_\odot$), intermediate (5 $M_\odot$), and high (25 $M_\odot$) mass (Iben et al. 1991)

Main Sequence

In figure 2.1, the evolutionary track of a star starts from a line called Main Sequence (MS), which is formed by all stars in the H-burning stage. The MS stars thus form a one-parameter family, specified by the mass which increases toward top left of the diagram.

AN intermediate-mass star spends $\sim 80\%$ of its active nuclear-burning lifetime on the MS.

Red Giant Branch

After hydrogen is exhausted at the stellar center, a "helium-core" develops, with the hydrogen burning continuing in a thin shell surrounding the core. The core itself contracts on Kelvin-Helmholtz (thermal) time scale, releasing additional energy. This is a manifestation of "gravothermo catastrophe"; that is, a star is deemed to contract and get hotter unless there is sufficient nuclear energy input. Because of these two energy sources, the star becomes more luminous, and its envelope starts expanding accompanied by a decrease in the effective temperature. As a result, the star gradually moves toward top right on the diagram. Stars in this phase are called red giant stars, and their assembly is called red giant branch (RGB) on the H-R diagram. During the RGB phase, "first dredge-up" occurs. This is a process of convectively transporting fusion products from deep inside the star into the surface. Consequently, the surface abundance changes markedly in the RGB.

He-core burning

As the hydrogen-exhausted core contracts and get heated, the central temperature and density will reach $\sim 10^8$ K and $\sim 10^4$ g cm^{-3}, respectively. Then, helium fusion (the triple α reaction) is ignited at the core, and this terminates, and sometimes reverses, the upward climb of the star along the RGB, because energy release due to the helium burning momentarily suppress the gravothermo catastrophe. Helium burns steadily in the core and is converted into carbon and oxygen (§2.2.3), while H-burning in a thin shell continues. In the case of a lower-mass star ($M < 2M_\odot$) of which the He core is partially degenerated, the He-burning begins unstably. This is called "helium flash". As degeneracy of the core is removed, the core expands and continues steady He-burning. The He-core burning phase lasts typically for $\sim 25\%$ of H-core burning, and the star approximately stays on a position of the H-R diagram.

Asymptotic Giant Branch

Once the star runs out of He in its core, a C+O core starts growing. The star begins to move upward on the H-R diagram again, now along so called asymptotic giant branch (AGB). The helium-exhausted core contracts and heats, while helium continues to burn in a thin shell. Thus C+O and He play essentially the same role as played by H and He, respectively, in the RGB phase. One important difference, however, is that there is still a H-rich envelope on top of the He-rich "inter shell", where the hydrogen shell burning continues. The stellar luminosity is sustained by the two (He and H) shell burnings, as well as by gravitational contraction of the C+O core. At this stage, the star is made up of a C+O core, a He burning shell, a He inter shell, a H burning shell, and a H-rich envelope. A massive ($> 4M_{\odot}$) AGB star has a convectively unstable envelope, where fresh elements, such as C and O, are transported up to the surface. This process, "second dredge-up", is important because it allows a certain fraction of C and O to mix into the outer envelope, and eventually escape via stellar mass loss, instead of being totally taken into the white dwarf.

As a star approaches top of the AGB, the rate of mass loss increases and oscillations develop within the star. In the AGB phase, the two shell burnings occur simultaneously ("double-shell burning"), divided by a thin He-rich layer synthesized by the H-burning. The oscillation is thought to result from a coupling between these double-shell burnings: thermal pulses of the He shell burning induce a flash-driven convection zone, which extends from the He shell to the H shell. As the helium flash dies away, the deposited energy causes expansion and cooling of the envelope, and the bottom of outer convection regions reaches the C-rich region, bringing C and He to the star surface ("third dredge-up" eipsodes).

During the thermal pulses, elements heavier than iron are thought to be synthesized by the s-process (§2.1.2), which proceeds via "slow" neutron captures. In stars heavier than $5M_{\odot}$, another important phenomenon, "hot bottom burning", is thought to occur. In this process, the achieved high temperature ($\sim 10^8$ K) activates the CN cycle within the envelope, converting ^{12}C into ^{13}C and ^{14}N.

post-AGB

A He-exhausted core of an intermediate-mass star consists mainly of carbon and oxygen, and degenerates. The C+O core is not thought to reach a certain critical point, where explosive C+O burning (like the "helium flash" of lower-mass stars) occurs. Consequently, the nuclear-burning lifetime of intermediate-mass stars is likely to end when the He burning is over.

Soon after reaching top of the AGB, the star sheds almost all of the remaining H envelopes. The star becomes blue, marching rapidly leftwards on the H-R diagram. Intense radiation from the star ionizes the ejected H envelope, and make it fluoresce brightly as a planetary nebula where the history of nucleosynthesis is recorded. The He burning gradually ceases and the star reduces its luminosity, moving down on the H-R diagram to become a white dwarf.

2.2.2 Details of hydrogen burning

Hydrogen burning is the main energy source of a star all through its life time, because the energy (per nucleon) released in this fusion process is much larger than those available in any other nuclear reactions in stars. In this burning, a single ^{4}He is synthesized from four protons. It is realized in the stellar interior via two different types of reaction paths; one is "p-p chain" and the other is "CNO cycle". Unlike the α-process which is basically composed of strong interactions, the hydrogen burning inevitably involves weak interactions (or β^+-processes), through which protons are converted to neutrons.

p-p chain

As schematically shown in figure 2.2 (Takahara 1999), the p-p chain consists of three branches. In a lower temperature ($0.8 < T_7 < 1.4$, where T_7 means 10^7 K), the reaction mainly occurs via pp-I branch, as

$$
\begin{aligned}
{}^1\mathrm{H} + {}^1\mathrm{H} &\longrightarrow {}^2\mathrm{H} + \mathrm{e}^+ + \nu_\mathrm{e} && (2.1)\\
{}^2\mathrm{H} + {}^1\mathrm{H} &\longrightarrow {}^3\mathrm{He} + \gamma && (2.2)\\
{}^3\mathrm{He} + {}^3\mathrm{He} &\longrightarrow {}^4\mathrm{He} + 2{}^1\mathrm{H}. && (2.3)
\end{aligned}
$$

The produced positrons annihilate with ambient electrons, and deposit the energy. Excluding the energy carried away by the neutrinos, a net energy of 26.20 MeV is produced per ^{4}He nucleus, or 6.73 MeV per nucleon. The first reaction is a weak interaction, so that it becomes the rate-determining step.

As the ^{4}He concentration increases or the temperature becomes higher ($1.4 < T_7 < 2.3$), pp-II chain becomes a main reaction path. It proceeds as

$$
\begin{aligned}
{}^3\mathrm{He} + {}^4\mathrm{He} &\longrightarrow {}^7\mathrm{Be} + \gamma && (2.4)\\
{}^7\mathrm{Be} + \mathrm{e}^- &\longrightarrow {}^7\mathrm{Li} + \nu_\mathrm{e} && (2.5)\\
{}^7\mathrm{Li} + {}^1\mathrm{H} &\longrightarrow 2{}^4\mathrm{He}. && (2.6)
\end{aligned}
$$

This process provides a net energy of 25.67 MeV (per ^{4}He nucleus).

Under a temperature higher than 2.3×10^7 K, ^{7}Be captures a proton, and pp-III chain begins to play a major role. It goes on as

$$
{}^7\mathrm{Be} + {}^1\mathrm{H} \longrightarrow {}^8\mathrm{B} + \gamma \qquad (2.7)
$$

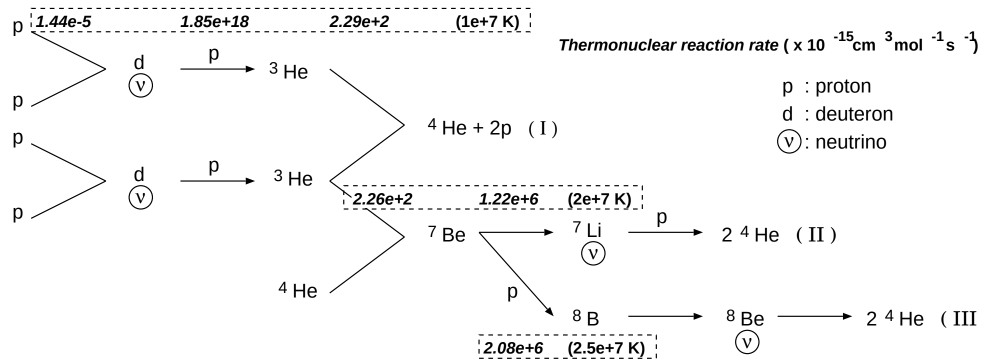

Figure 2.2: A diagram of p-p chain reactions (Takahara 1999).The numbers indicate thermonuclear reaction rates in the unit of 10^{-15} cm^3 mol^{-1} s^{-1} at 1, 2, and 2.5×10^7 K for pp-I, -II, and -III, respectively (Caughlan and Fowler 1988).

$$^{8}\mathrm{B} \longrightarrow {}^{8}\mathrm{Be} + \mathrm{e}^{+} + \nu_{\mathrm{e}} \tag{2.8}$$

$$^{8}\mathrm{Be} \longrightarrow 2{}^{4}\mathrm{He}. \tag{2.9}$$

Since the neutrino produced via ^{8}B β-decay has a rather high energy, 7.27 MeV on average, the net energy available is 19.20 MeV.

The most familiar example of p-p chain is our sun. Its core temperature is estimated as 1.6×10^7 K, so that its main energy source is p-p chain. Among various neutrinos emerging through the p-p chain, those from the ^{8}B β-decay have been detected by the Kamiokande and the Super-Kamiokande experiments, and their deficit has reconfirmed the solar neutrino problem originally pointed out by Davis.

CNO cycle

In a star with a central temperature higher than 1.8×10^7, ^{4}He is produced via so called CNO cycle on condition that the stellar material already contains C, N, and O prior to the current nuclear reaction. The cycle consists of the following reactions;

$$^{12}\mathrm{C} + {}^{1}\mathrm{H} \longrightarrow {}^{13}\mathrm{N} + \gamma \tag{2.10}$$

$$^{13}\mathrm{N} \longrightarrow {}^{13}\mathrm{C} + \mathrm{e}^{+} + \nu_{\mathrm{e}} \tag{2.11}$$

$$^{13}\mathrm{C} + {}^{1}\mathrm{H} \longrightarrow {}^{14}\mathrm{N} + \gamma \tag{2.12}$$

$$^{14}\mathrm{N} + {}^{1}\mathrm{H} \longrightarrow {}^{15}\mathrm{O} + \gamma \tag{2.13}$$

$$^{15}\mathrm{O} \longrightarrow {}^{15}\mathrm{N} + \mathrm{e}^{+} + \nu_{\mathrm{e}} \tag{2.14}$$

$$^{15}\mathrm{N} + {}^{1}\mathrm{H} \longrightarrow {}^{12}\mathrm{C} + {}^{4}\mathrm{He}. \tag{2.15}$$

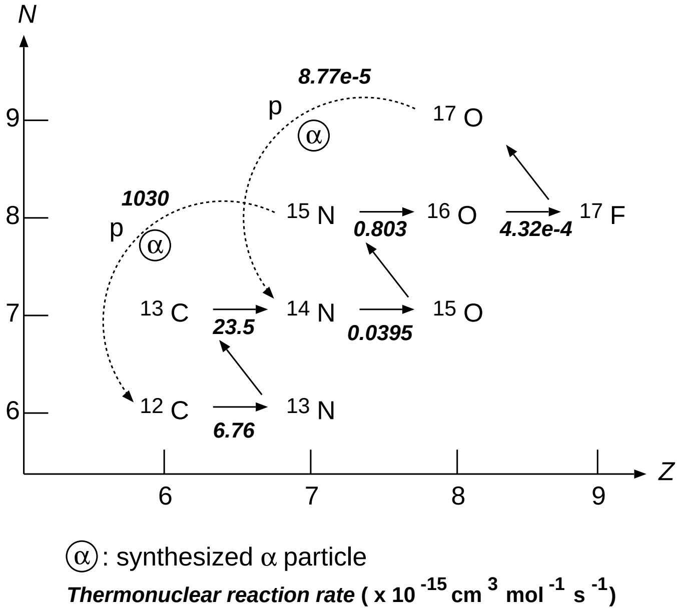

Figure 2.3: Reaction paths of the CNO cycle on the nuclear chart. the numbers indicate thermonuclear proton capture rates in the unit of 10^{-15} cm^3 mol^{-1} s^{-1} at 1.8×10^7 K (Caughlan and Fowler 1988).

This reaction cycle is summarized in figure 2.3. In this process, the rate-determining step is proton capture by ^{14}N, of which the reaction rate is lower by one to two orders of magnitude than those of the other reactions. As the CNO cycle proceeds, ^{14}N becomes much more abundant than C and O. The CNO cycle has a steep temperature dependence; at high temperatures, a reaction branch

$$
\begin{aligned}
{}^{15}\mathrm{N} + {}^{1}\mathrm{H} &\longrightarrow {}^{16}\mathrm{O} + \gamma && (2.16)\\
{}^{16}\mathrm{N} + {}^{1}\mathrm{H} &\longrightarrow {}^{17}\mathrm{F} + \gamma && (2.17)\\
{}^{17}\mathrm{F} &\longrightarrow {}^{17}\mathrm{O} + \mathrm{e}^{+} + \nu_{\mathrm{e}} && (2.18)\\
{}^{17}\mathrm{O} + {}^{1}\mathrm{H} &\longrightarrow {}^{14}\mathrm{O} + {}^{4}\mathrm{He} && (2.19)
\end{aligned}
$$

begins to compete with equation (2.15). Although the ratio of this branch is less than 10^{-3} (figure 2.3), this branch produces ^{14}N and hence increases the efficiency of energy generation.

2.2.3 Details of helium burning

As hydrogen is exhausted, the next fuel to be utilized is helium. Since there are no stable isotopes with the mass number of 5 or 8, a ^{12}C is synthesized from three ^{4}He nuclei

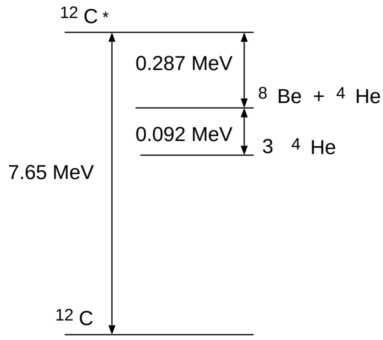

Figure 2.4: Energy levels in the triple α reaction.

through the "triple α reaction", as

$$^{4}\mathrm{He} +^{4}\mathrm{He} + 0.092\ \mathrm{MeV} \longrightarrow {}^{8}\mathrm{Be} \tag{2.20}$$

$$^{8}\mathrm{Be} +^{4}\mathrm{He} + 0.287\ \mathrm{MeV} \longrightarrow {}^{12}\mathrm{C}^{*} \tag{2.21}$$

$$^{12}\mathrm{C}^{*} \longrightarrow {}^{12}\mathrm{C} + \gamma \tag{2.22}$$

where C^{*} means an excited carbon nucleus. As shown in figure 2.4 and equation (2.20), the first step is an endothermic reaction. ^{8}Be is unstable and hence immediately decays into two α particles. In order for the subsequent reaction between ^{8}Be and ^{4}He to occur, a very hot ($\sim 1 \times 10^{8}$) and dense condition is required. This is the reason why ^{8}Be was not synthesized in the early universe (§2.1.1). In a stellar core, however, a tiny abundance of ^{8}Be exists because of high density. An excited state nucleus, $^{12}\mathrm{C}^{*}$, is synthesized via a resonance reaction. This is also an endothermic reaction, and the width of $^{12}\mathrm{C}^{*}$ α decay is larger than that of its decay into the ground state. The abundance of $^{12}\mathrm{C}^{*}$ is tiny like ^{8}Be.

Once ^{12}C is produced, it captures an α particle and synthesizes ^{16}O, as

$$^{12}\mathrm{C} +^{4}\mathrm{He} \longrightarrow {}^{16}\mathrm{O} + \gamma. \tag{2.23}$$

This process is thought to occur simultaneously with the triple α reaction. The cross section of the α capture by ^{12}C , equation (2.23), plays a very important role in the nucleosynthesis of not only intermediate-mass stars but also massive ones, because heavy-element yields in intermediate-mass stars are determined by the reaction rates of He burning, and subsequent hydrostatic burnings in massive stars are also affected by the C/O ratio after the He burning. However, the $^{12}\mathrm{C}(\alpha,\gamma)^{16}\mathrm{O}$ reaction typically takes place around center-of-mass energies of 300 keV in the $\alpha +^{12}\mathrm{C}$ system, where the cross section is too small to measure directly by ground experiments. In addition, the cross section in such low energies is a mixture of ground state and cascade transitions, so that an extrapolation may have large uncertainties.

By means of indirect methods like β-delayed α decay of ^{16}N and elastic scattering, many attempts have been made to estimate the cross section of equation (2.23) (see Buchmann and Barnes 2005, and references therein). Buchmann et al. (1996) analyzed all the available data and yielded reaction rates for a temperature of 1.8×10^8 K between 0.5 and 2.2 $\times 10^{-15}$ cm^3 mol^{-1} s^{-1}. Imbriani et al. (2001) suggested that the central He burning is only marginally affected by a change in the cross section of $^{12}\mathrm{C}(\alpha,\gamma)^{16}\mathrm{O}$. They estimated C and O abundances of each initial-mass star adopting the reaction rates of 0.8 and 1.9 $\times 10^{-15}$ cm^3 mol^{-1} s^{-1} from Caughlan and Fowler (1988) and Caughlan et al. (1985) respectively. The former reaction rate yielded similar abundances between C and O, while the latter gives an O abundance higher by a factor of 2–3 than that of C.

Once a sufficient number of ^{16}O is produced, Ne and Mg are also synthesized by subsequent α captures as,

$$
\begin{aligned}
{}^{16}\mathrm{O} + {}^{4}\mathrm{He} \quad &\longrightarrow \quad {}^{20}\mathrm{Ne} + \gamma && (2.24)\\
{}^{20}\mathrm{O} + {}^{4}\mathrm{He} \quad &\longrightarrow \quad {}^{24}\mathrm{Mg} + \gamma. && (2.25)
\end{aligned}
$$

It has been recently confirmed experimentally that the $^{16}\mathrm{O}(\alpha,\gamma)^{20}\mathrm{Ne}$ reaction has a very small cross section at the He burning temperatures (Kunz et al. 1997; Buchmann and Barnes 2005). Therefore, the He burning in a stellar core is limited essentially to the triple α and $^{12}\mathrm{C}(\alpha,\gamma)^{16}\mathrm{O}$ reactions, and hence carbon and oxygen constitute major products of the He burning.

2.3 Components of Planetary Nebulae

A planetary nebula consists of a central star and surrounding nebula formed by gaseous materials which were once outer portions of the central star. Energetically, it is a simple physical system; all the energy is derived from the central star. Photons emitted from the central star are absorbed and reprocessed by the surrounding nebula. However, a PN contains materials with various densities, temperatures, and morphological structures. We can observe matters in various forms, such as ionized, neutral, and molecular gasses, as well as solid state materials . As a result, a PN emit in a wide wavelength range from radio to ultraviolet (UV). PNe generally exhibit very complex spectral energy distributions with rich features. Figure 2.5 (Kwok 2005) shows a rich spectrum of the PN, BD +30° 3639 which is a young compact PN.

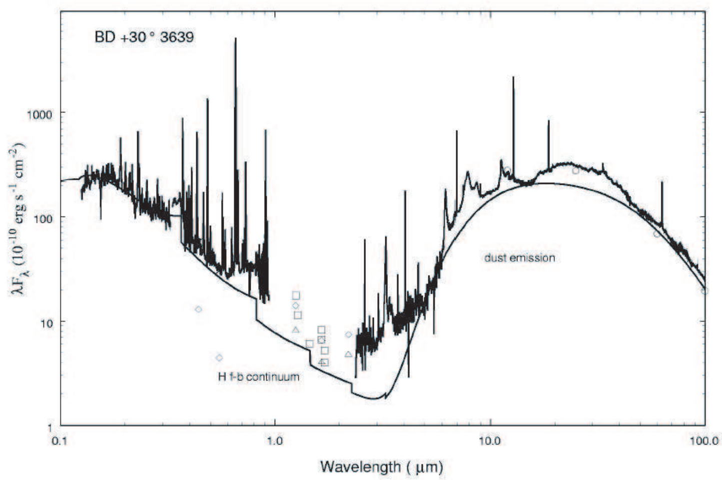

Figure 2.5: The spectral energy distribution of the PN, BD +30° 3639, from ultraviolet to infrared band (Kwok 2005).

2.3.1 Ionized gas

As the central star of a PN evolves to a high temperature of $\sim 10^5$ K, its radiation concentrates in the UV band. UV photons from the central star ionize hydrogen in the surrounding nebula, and ejected electrons cause collisional excitation of heavy elements such as carbon, nitrogen, and oxygen in the nebula. Energy of the free electrons produced by photoionization is determined by the stellar temperature. However, ejected electrons thermalize very quickly due to a large cross section of electron-electron collision. As a result, typical kinetic electron temperatures found in PNe are $\sim 10^4$ K, which is lower than the excitation temperature of $\sim 10^5$ K or 10.2 eV corresponding to the first excited state of hydrogen.

As shown in figure 2.5, emission lines often dominate in the UV and optical spectra of PN. They are produced when atoms or ions in the ionized nebular gas make a transition from one bound electronic state to another bound state at a lower energy, which is referred to as bound-bound transitions. These transitions occur typically in the following two processes. A bound electron may be collisionally excited from a lower state, and then radiatively returns to the lower state by emitting lines which are called "collisionally excited lines". The ionized gas may also produce "recombination lines", which are emitted by cascade transition following recombination between a free electron and an ion.

Continuum emission from the ionized gas is contributed by several processes, including free-bound transition from H and He, free-free emission, and two-photon decay. The free-bound process dominates in the optical band, while the free-free emission becomes stronger in the infrared, and becomes dominant in the radio frequency. Two-photon decay is a transition from a metastable hydrogen ($^2S_{1/2}$) to the ground state. Although the transition from the metastable to the ground state is strictly forbidden, an atom in the metastable state can decay via a virtual intermediate state, and hence emitting two photons. Since the virtual state can occur anywhere between the metastable and the ground state, the emitted two photons will form a continuum extending up to Lyα energy.

2.3.2 Dusts

Although the infrared spectrum was expected to be dominated by forbidden-line emissions from ionized gas, unpredicted strong excess was discovered from many PNe. The infrared emission comes from dusts with a color temperature of ~ 100 K. Observations of circumstellar dust envelopes of AGB stars suggest that the cool dusts in PNe descend from mass-losing AGB stars. A blackbody of 100 K will peak at 30 μm, out of the observable range with ground-based telescopes. After the launch of *InfraRed Astronomical Satellite* in 1983, the wide presence of dust was confirmed. Pottasch et al. (1984) reported that dust temperatures are distributed in a wide range from 40 to 230 K.

Figure 2.5 gives an example of dust emission from a PN, where we can see strong emission features in the infrared range. Features at 3.3, 6.2, 7.7 and 11.3 μm are thought to be due to aromatic hydrocarbons. Aliphatic features are also seen at 3.4 and 6.9 μm in spectra of young planetary nebulae. Some emission features are yet to be identified.

2.3.3 Molecular components

The first detection of CO from a PN, NGC 7027, was reported by Mufson et al. (1975). Since the CO profiles in PNe resemble those observed in AGB stars, the origin of molecular gas in PNe is explained as remnants of the circumstellar envelopes of AGB stars. The first extensive CO survey of PNe was conducted by Huggins and Healy (1989), and the CO emission was detected from 19 PNe out of 100. Estimated CO masses range from 1 $M_{\odot}$ to less than 10^{-3} $M_{\odot}$. Most of CO-detected PNe are younger population located in the Galactic disk, and are thought to have relatively high-mass progenitors. As millimeter interferometry made a progress, CO mappings of PNe have been done extensively, and the CO emitting regions have generally been found to be outside ionized nebula. This result supports the view that the CO emission comes from remnants of AGB envelopes. Davis et al. (1979) detected, for the first time, OH emission from a PN. The double peaked profile are similar to those observed in AGB stars, except the lack of a redshifted component, probably due to absorption by the ionized gas.

The molecular hydrogen, H_2, is excited by collisional excitation in shocked gas or by fluorescent emission. The 2.1 μm line of H_2 is commonly observed from PNe. The location of H_2 emission is illustrated in figure 2.6, together with the CO mapping results (Graham et al. 1993). There are two rings in the H_2 image located in the central CO cavity. The H_2 emission suggests the presence of a photodissociation region, where H_2 is decomposed into H atoms by interaction with UV photons escaping from the H II region. Such a region lies between the ionized region and the molecular envelope. Since CO molecules have a dissociation energy of 11.09 eV, which is higher than that of H_2, CO remain in molecular form even after H_2 is dissociated.

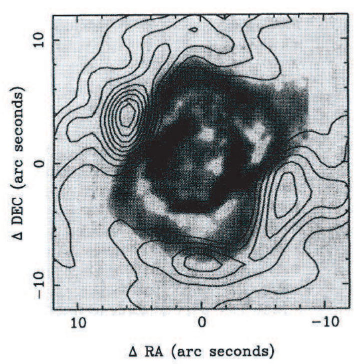

Figure 2.6: The surface brightness contours of CO (1–0) emission from NGC 7027, superposed on the gray scale map of H_2 emission (Graham et al. 1993).

Rotational transitions of more than 50 molecules have been detected in the circumstellar envelopes of AGB stars and PNe, suggesting that these objects play significant role of molecular enrichment of the ISM. Detected molecules include carbon chains as massive as HC_9N, and cyclic molecules such as C_3H_2.

2.3.4 The central star

The central star of a planetary nebula has a high temperature, so that it radiates mainly in the UV band. Due to their faintness and contamination by nebular emissions, however, it is difficult to accurately determine the surface temperature of the central stars. In order to estimate their surface temperature, Zhanstra method is widely utilized. This method derives the temperature by comparing the nebular recombination flux with the stellar continuum magnitude, assuming that the nebula is optically thick in the Lymann continuum. Since PNe change from optically thick to thin in H and He at different times, different temperatures are provided by using H or He. There are also other methods to determine the surface temperature, such as using nebular forbidden- and recombination-line ratios considering energy balance, comparing the observed continuum in UV with a stellar atmosphere model, and resolving the photospheric absorption line profiles by means of very-high-resolution spectroscopy.

Based on the spectra, the central stars are roughly classified into two groups; one group of objects has H deficient atmosphere, while the others are shows H-rich. The ratio of H-rich to H-poor central stars is approximately 1 to 4, which is similar to that observed among white dwarfs. The H-poor central stars primarily have Wolf-Rayet (WR) spectra. Figure 2.7 shows differences between spectra of WR and H-rich central stars (Napiwotzki 1998). Although a central star have a typical mass of $\sim 0.6M_{\odot}$, which is much lower than those of ordinary WR stars, the same classification as that used for massive WR stars applies to the central stars of planetary nebulae with WR spectra; WN or WC, which roughly corresponds to C or N deficient conditions, respectively.

P-Cygni profiles have been observed in the optical and UV spectra of many central stars. This implies the presence of high-speed (typically $\sim$ 1000 km s^{-1}) stellar winds from the central stars. *International Ultraviolet Explorer*, which is the satellite launched in 1978, revealed that $\sim$ 60% of the central stars show such evidence of stellar winds, and the observed terminal velocity is up to $\sim$ 5000 km s^{-1} (Cerruti-Sola and Perinotto 1989). Figure 2.8 shows examples of the observed P-Cygni line profiles in extreme UV band (Zweigle et al. 1997). These fast stellar winds play a major role in X-ray emission

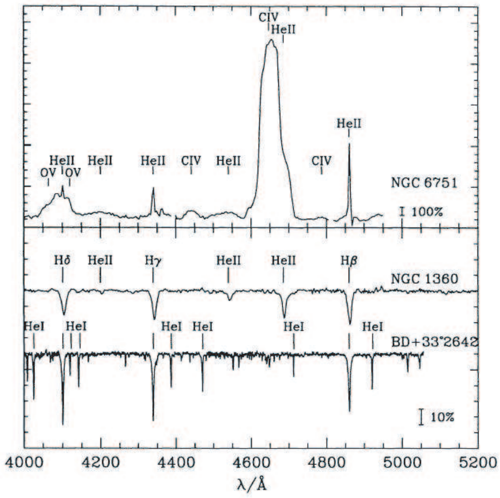

Figure 2.7: Central star spectra (Napiwotzki 1998). NGC 6751 is a WR example, NGC 1360 and BD $+33°$ 2642 are a hot (1.1×10^5 K) and a cool (2.02×10^4 K) central star, respectively.

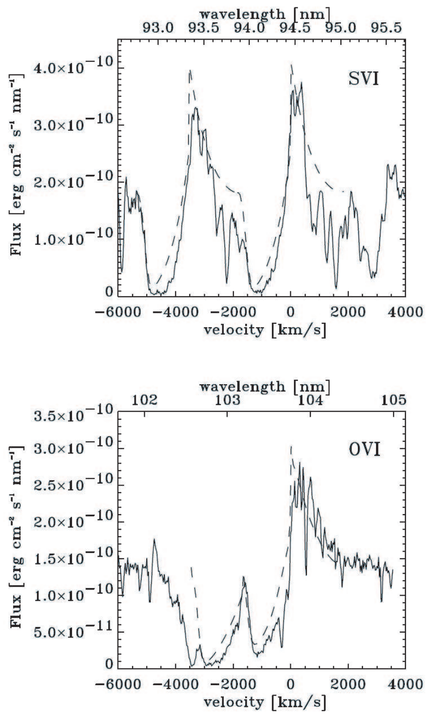

Figure 2.8: P-Cygni line profiles of S VI and O VI lines (Zweigle et al. 1997), observed with ORFEUS-SPAS (Orbiting Retrievable Far and Extreme Ultraviolet Spectrometer on the Shuttle Pallet Satellite). Theoretical line profiles are superposed with dashed lines.

from PNe (§2.4.1).

2.4 X-ray Emission from Planetary Nebulae

2.4.1 Interacting Stellar Winds model

The discovery of extensive mass loss from AGB stars (Gehrz and Woolf 1971; Solomon et al. 1971) inspired astrophysicists to speculate that the envelopes surrounding AGB progenitors could be directly responsible for the formation of planetary nebulae. However, this simple model has several difficulties; the observed expansion velocities of PNe are higher than the velocities with which the AGB mass loss take place; the observed densities of PNe are higher than those of the AGB envelopes; and PNe have sharp inner and outer boundaries while an AGB star has smooth structure. PNe are therefore not formed simply by AGB envelopes diffusing into the ISM. An additional mechanism is needed to accelerate, compress, and shape the AGB envelopes into PNe (Kwok 1982).

The Interacting Stellar Winds (ISW; Kwok et al.1978) model has provided a possible solution to the difficulties described above. Assuming that the AGB mass loss continues until most of the stellar envelope is lost and the core exposed, the central star evolves to become bluer. As the central star becomes hot enough, a new mass loss begins by radiation pressure excited on resonance lines. The terminal velocity of the wind, which is related to the escape velocity of the central star, will be much higher than that of the AGB stellar wind, because of the much reduced radius of the central star than that in the AGB phase. This new fast stellar wind runs into its own ejecta accumulated over the AGB phase, and sweeps them up. The swept-up ejecta are compressed on both sides by dynamical pressure, and form a definite shell structure as observed in PNe.

This model was first formulated for a momentum-conserving case, assuming all the excess energy of the fast wind is radiated away. However, this picture did not seem to explain all PNe, especially those with higher expansion velocities or masses, and motivated a modified picture. Since the speed of the fast stellar wind, typically ~ 1000 km s^{-1}, is much higher than the sound speed in the surrounding media including the AGB-phase ejecta, we expect the formation of strong shocks. The ISW model has thus been extended to the energy-conserving case, invoking the shock formation (Kwok 1982; Kahn 1983; Kwok 1983; Volk and Kwok 1985).

Figure 2.9 schematically illustrates energy-conserving the ISW model. The fast stellar wind with a large Mach number will first sweep up the ejecta and compress them, thus forming a contact discontinuity. When the swept-up materials become thick enough, the fast wind will experience a reverse-shock transition, through which the wind is efficiently thermalized. The post-shock flow will form a hot and subsonic region, and its pressure will accelerate the expansion of the swept-up matter shell. The shell will eventually attain a supersonic speed, and launch another shock (outer shock) propagating ahead of the contact discontinuity into the AGB remnant. The AGB remnant matter compressed through the outer shock will be observed as PNe mainly in the optical band.

As described in §2.3.4, the presence of fast stellar winds, an important ingredient of the ISW model, has been confirmed. Furthermore, the development of optical CCD cameras has revealed faint optical halos surrounding PNe, which are considered as the AGB remnants before swept up by the fast stellar winds. In this way, the ISW model has been confirmed by observations and become one of the most convincing mechanisms of the PNe formation. However, extremely complicated morphology of PNe, recently revealed by the *Hubble Space Telescope*, suggests that the simple scenario of the ISW model needs further refinement.

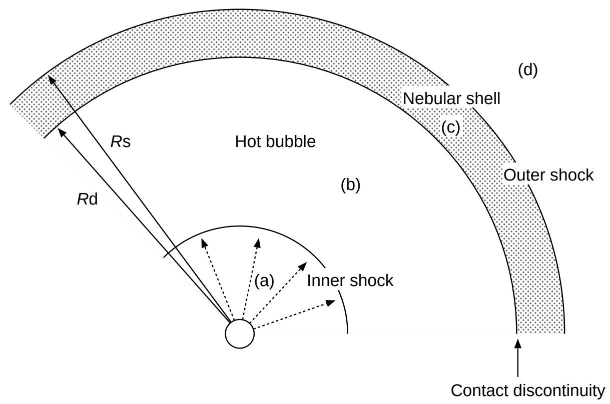

Figure 2.9: A schematic illustration of the ISW model (from Kwok 2000; Volk and Kwok 1985). The regions are (a) the fast stellar wind; (b) the shocked stellar wind; (c) the nebular shell; and (d) the remnant of the AGB.

2.4.2 Shock-heated gas

The ISW model predicts that PNe have hot gas, corresponding to region (b), or "hot bubble", in figure 2.9. In this subsection, let us estimate the temperature of the hot gas. In order to simplify the problem, we assume that the hot bubble and the swept-up gas are separated by a contact discontinuity without either matter or heat passing through it.

Assuming that the nebular shell is thin, we may set its radius as $R \sim R_{\rm d} \sim R_{\rm S}$, where $R_{\rm d}$ and $R_{\rm S}$ are radii of the contact discontinuity and the outer shock front, respectively (figure 2.9). The density ρ_0 of the circumstellar gas in region (c) and the pressure p of the post-shock wind in region (b) are assumed to be uniform. The equations of motion and energy-conservation about the nebular shell are expressed respectively as

$$\frac{d}{dt}\left(\frac{4\pi}{3}R^3\rho_0\dot{R}\right) = 4\pi R^2 p, \tag{2.26}$$

$$\frac{d}{dt}\left(\frac{4\pi}{3}R^3\frac{3}{2}p\right) = L_{\rm W} - p\frac{d}{dt}\left(\frac{4\pi}{3}R^3\right). \tag{2.27}$$

The left-hand side of equation (2.27) means time deviation of internal energy of the post-shock wind, and the second term of its right-hand side means work done per unit time from the wind to the nebular shell. $L_{\rm W} = \frac{1}{2}\dot{M}{V_{\rm W}}^2$ indicates kinetic energy emitted from the central star, where $\dot{M}$ and $V_{\rm W}$ are the mass-loss rate and the speed of the fast stellar wind, respectively. From these two equations, we obtain

$$R = \left(\frac{125}{154\pi}\right)^{1/5}\left(\frac{L_{\rm W}}{\rho_0}\right)^{1/5} t^{3/5} \tag{2.28}$$

$$p = \frac{7}{25}\left(\frac{125}{154\pi}\right)^{2/5}\rho_0\left(\frac{L_{\rm W}}{\rho_0}\right)^{2/5} t^{-4/5}. \tag{2.29}$$

Assuming a uniform density ρ in the hot bubble (figure 2.9), and hence an approximation as $\rho = \frac{\dot{M}t}{4\pi R^3/3}$, and employing the equation of state, we obtain the temperature as

$$T = \frac{\mu m_{\rm H}}{k}\frac{P}{\rho} \sim 1\times 10^7 (V_{1000})^2 \ {\rm K} \sim 0.9(V_{1000})^2 \ {\rm keV}, \tag{2.30}$$

where μ, $m_{\rm H}$, and k are the mean atomic weight ($\sim$ 0.6) per particle, the mass of a proton, and Boltzmann constant, respectively. V_{1000} means the speed of the fast stellar wind in the unit of 10^3 km s^{-1}, which is a typical value observed from the central stars of PNe. Matter of such a high temperature is expected to emit soft X-rays. The ISW model indeed predicted X-ray emission from PNe (Volk and Kwok 1985).

Accordingly to the ISW, we expect the optical nebula and the hot bubble to reflect somewhat different stages of the central star evolution. While the former is composed basically of materials ejected in the AGB phase, the latter consists of those which were located originally deeper inside the star, close to the proto-white-dwarf surface. Therefore, we expect the optical and X-ray spectra of the same PNe to reveal possibly different chemical compositions.

2.4.3 Elementary process of X-ray emission from hot plasma

The ISW model predicts that optically-thin hot plasmas with a temperature of ~ 1 keV are associated with PNe. Such plasmas emit predominantly X-rays, via the following three processes.

- **free-free transition**: thermal bremsstrahlung continuum, produced by free electrons when they receive electric acceleration from ions.
- **bound-bound transition**: discrete emission lines produced by partially ionized ions, when their bound electrons are excited by free electron impact to higher bound levels, and then radiatively return to the ground states.
- **free-bound transition**: recombination continuum produced by a capture of a free electron into a bound state of an ion.

The first two are usually most important processes.

The emissivity of thermal bremsstrahlung is formulated as

$$\frac{\varepsilon_{\rm ff}}{d\nu} = \frac{2^5 \pi e^6}{3 m_{\rm e} c^3} \left(\frac{2\pi}{3 k m_{\rm e}} \right)^{1/2} Z_i^2 n_e n_i \bar{g}_{\rm ff}(T,\nu) T^{-1/2} \exp\left(\frac{-h\nu}{kT} \right), \tag{2.31}$$

where e, $m_{\rm e}$, and n_e are the electron charge, mass, and density; ν the emitted photon frequency, h the Planck constant, and Z_i and n_i are the effective charge and density of the target ion, respectively. $\bar{g}_{\rm ff}(T,\nu)$ is a velocity averaged Gaunt factor, of which the value is of order unity for $h\nu/kT \sim 1$ and is in the range 1 to 5 for $10^{-4} < h\nu/kT < 1$.

The frequency-integrated free-free emissivity is given by

$$\varepsilon_{\rm ff} = \frac{2^5 \pi e^6}{3 c m^2} \left(\frac{2\pi k}{3 h m} \right)^{1/2} T^{1/2} Z_i^2 n_e n_i \bar{g}_B \exp\left(\frac{-h\nu}{kT} \right) \tag{2.32}$$

$$= 1.4 \times 10^{-27} T^{1/2} n_e n_i Z_i^2 \bar{g}_B \ {\rm erg\ s^{-1}\ cm^{-3}}, \tag{2.33}$$

where $\bar{g}_B$ is a frequency average of the velocity averaged Gaunt factor, which is in the range 1.1 to 1.5. The total power per unit volume emitted by thermal bremsstrahlung is thus proportional to $T^{1/2} Z_i^2 n_e n_i$.

Assuming a collisional equilibrium condition, a rate equation describing electronic state distribution of a particular ion is written as

$$0 = N(X_g) n_e S_{gj} - N(X_j) \sum_{h<j} A_{jh}, \tag{2.34}$$

where $N(X_g)$ and $N(X_j)$ are populations (cm^{-3}) of ion X in the electronic ground state and j-th excited state respectively, S_{gj} is the rate coefficient ($\mathrm{cm}^3\ \mathrm{s}^{-1}$) for electron collisional excitation to the level j, and A_{jh} is the probability (s^{-1}) of spontaneous radiative transition from the upper level j to a lower level h. Under the same condition, the volume emissivity (photon $\mathrm{cm}^{-3}\ \mathrm{s}^{-1}$) of a bound-bound transition between two electronic states, i and j, is expressed by

$$\frac{\varepsilon_{\mathrm{bb}}}{d\nu} = P_{ji} = N(X_j)A_{ji} = N(X_g)n_e S_{gj} B\Phi_{ji}(\nu), \tag{2.35}$$

where $B = A_{ij}/\sum_{h<j} A_{jh}$ is the radiative branching ratio, and Φ_{ij} is the line profile which is close to a delta function. The rate coefficient is given as

$$S_{gj} = \left(\frac{2}{\pi^3 m_{\mathrm{e}}^3 k T_{\mathrm{e}}}\right)^{1/2} \frac{h^2\Omega}{4\omega_g} \exp\left(-\frac{\Delta E}{kT_{\mathrm{e}}}\right), \tag{2.36}$$

where ΔE is the excitation energy, ω_g is the statistical weight, and Ω is a dimensionless quantity called "collisional strength". With these equations (2.34)$\sim$(2.36), we obtain the emissivity as

$$\varepsilon_{\mathrm{bb}}(X_j) = \int \frac{\varepsilon_{\mathrm{bb}}(X_j)}{d\nu} d\nu = n_e N(X_j) \left(\frac{2}{\pi^3 m_{\mathrm{e}}^3 kT}\right)^{1/2} \frac{h^3\nu\Omega B}{4\omega_g} \exp\left(-\frac{\Delta E}{kT}\right), \tag{2.37}$$

where $h\nu$ is energy of the transition.

So far, the calculation has considered populations and transitions among different electronic states of a particular ion with a fixed charge. In reality, however, we must also consider how ions of the same element are distributed over different ionization states. Assuming an ionization equilibrium, these distributions can be calculated for individual elements via Saha's equations. Figure 2.10 shows the fractional distributions of various ion species in the case of C, N, O, and Ne, calculated in this way and presented as a function of the plasma temperature in the range of 0.001 to 1 keV. In all cases, the helium-like ion species (with two bound electrons) have large fractional distributions over relatively wide temperature ranges, because of the stable electronic configuration. As the temperature becomes sufficiently higher than the K-shell binding energy, most of the ions become fully ionized.

The two emissivities, $\varepsilon_{\mathrm{ff}}$ and $\varepsilon_{\mathrm{bb}}$, both scale as $\propto n_e n_i$. The total emissivity of these two emission processes, integrated over the frequency, can therefore be written as

$$\varepsilon_{\mathrm{total}} = n_e n_i \Lambda(T, Z), \tag{2.38}$$

where $\Lambda(T, Z)$ is called cooling function, where Z stands for effective charge number of ions. Figure 2.11 shows the temperature dependence of $\Lambda(T, Z)$, together with those of

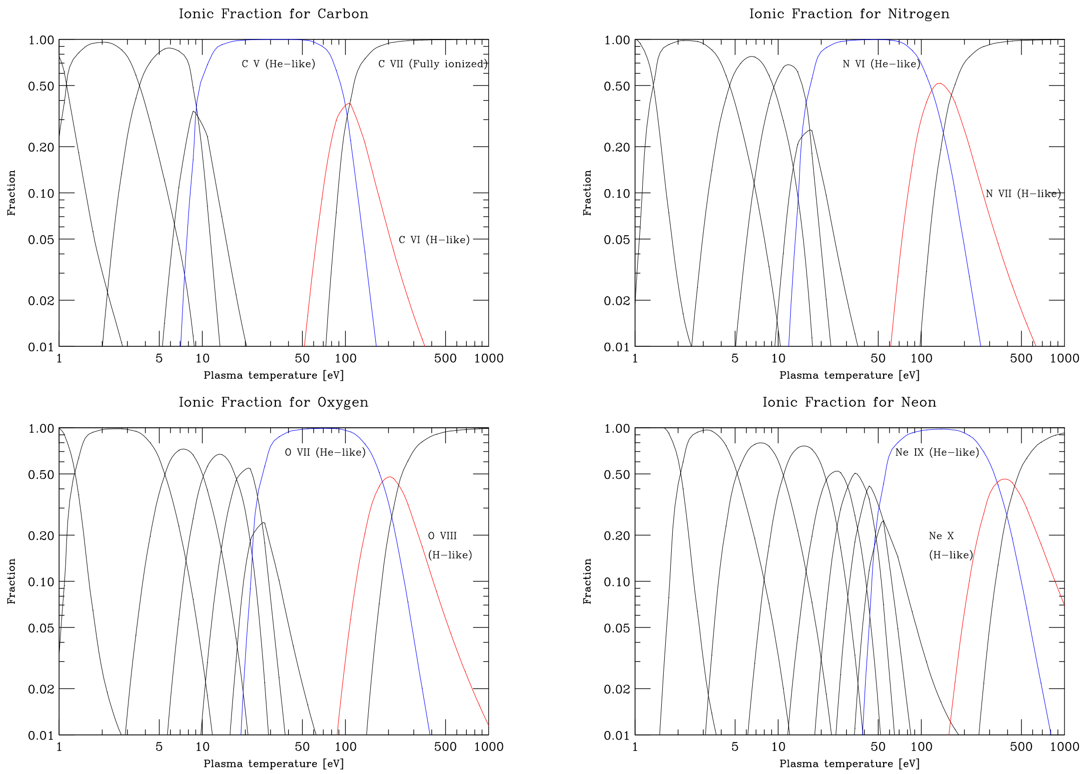

Figure 2.10: Fractional distributions of different ionization states for C (top-left), N (top-right), O (bottom-left), and Ne (bottom-right), shown as a function of the plasma temperature (Mazzotta et al. 1998). In all cases, the plasma is assumed to be in a collisional ionization equilibrium, as well as in thermal equilibrium with identical electron and ion temperatures.

its constituent components (Gehrels and Williams 1993). In the present case of plasmas in PNe with a temperature of $\sim 1 \times 10^7$ K, the line emission by bound-bound transitions dominates the total X-ray emission. A quantity called emission measure denoted EM and defined as

$$EM = \int n_e n_i dV, \tag{2.39}$$

directly determines the X-ray luminosity, or the normalization of the spectra.

X-ray spectra from optically-thin plasmas in collisional ionization equilibria have been calculated by various authors, and have been released as publicly available computational codes. Typical examples include Raymond-Smith model (Raymond and Smith 1977), Masai model (Masai 1984), MEKA and MEKAL model (Mewe et al. 1985; Mewe et al. 1986), and APEC model (Smith et al. 2001). Figure 2.12 gives examples of spectra with the temperature of 1 keV and 0.1 keV, calculated using the APEC model. The solar abundance is assumed, and the normalizations are fixed to unity. The 1 keV spectrum exhibit prominent Fe-L line complex in the range of 0.8–1 keV. In contrast, the 0.1 keV spectrum is dominated by Kα and weaker Kβ lines of C, N, O and Ne ions, in their helium-like and hydrogen-like ionization states.

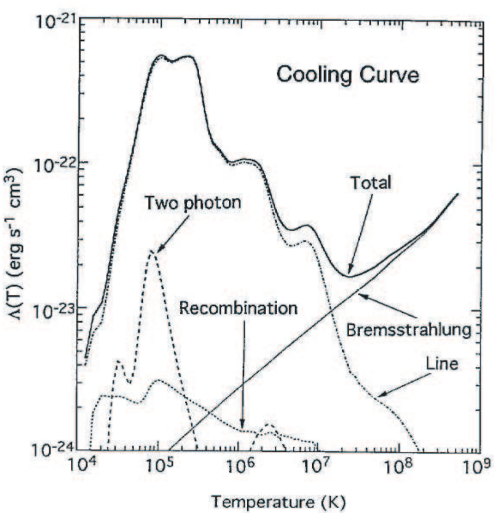

Figure 2.11: The cooling function of optically thin thermal plasmas (Gehrels and Williams 1993).

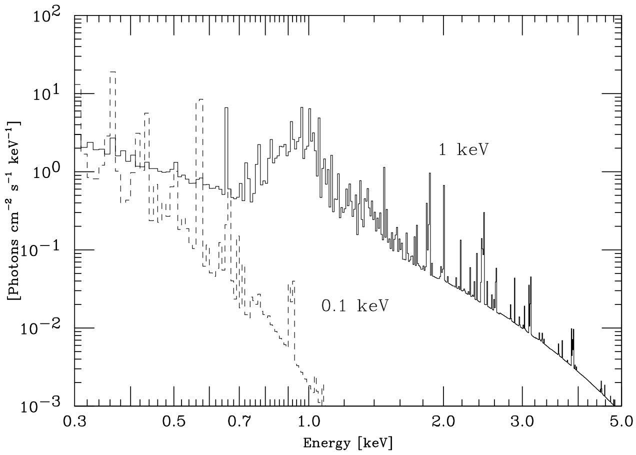

Figure 2.12: X-ray spectra emergent from optically thin thermal plasmas with the temperature of 1 keV (solid line) and 0.1 keV (dashed line), calculated using the APEC model.

2.5 X-ray Observation

2.5.1 Discovery of X-ray emission from planetary nebulae

Before the ISW model (§2.4.1) was proposed, there were already suggestions of planetary nebulae as potential X-ray sources (Hayakawa and Sugimoto 1968; Khromov 1969; Livio and Shaviv 1975). Hayakawa and Sugimoto (1968), which seems to be the first discussion on possible X-ray emission from PNe, suggested that X-rays are emitted from a hot corona surrounding a C+O core. They proposed that a kind of thermal instability, caused by mass accretion onto the C+O core, produces a shock wave and a matter out flow. If this takes place in a dense gas surrounding a star, like a PN, a hot corona may be formed. Although the origin of hot plasma is different from that invoked by the ISW model, the X-ray emission was a common prediction by the ISW model and Hayakawa and Sugimoto (1968). It is very impressive that Hayakawa and Sugimoto (1968) regarded PNe as candidates of Galactic compact X-ray sources, in 1968 when the nature of these sources as accreting collapsed objects was not yet understood.

The predicted X-ray emission from PNe was detected for the first time by *Einstein* and *EXOSAT* (de Korte et al. 1985; Tarafdar and Apparao 1988; Apparao and Tarafdar 1989; Apparao et al. 1992). These authors mainly attempted to explain the X-ray emission as arising from central stars of PNe, based on an analogy to the soft X-ray emission from white dwarfs. Tarafdar and Apparao (1988) reported results on 19 PNe observed by *Einstein*, including four X-ray detections. Apparao and Tarafdar (1989) reported that 12 PNe were observed by *EXOSAT* and 8 of them were found to emit detectable X-rays. They also estimated the effective temperatures to be $\sim 7 - 10 \times 10^4$ K using the observed X-ray flux and the optical magnitude assuming a blackbody spectrum from the surface of the central stars. However, the X-ray fluxes of NGC 1361 observed in four bands of *EXSOSAT* cannot be reproduced by a blackbody emission from the the central star (de Korte et al. 1985).

2.5.2 ROSAT and ASCA results

One of the firmest confirmations of the expected X-ray emission from shock-heated gas, caused by the fast stellar wind (§2.4.2), would be a finite spatial extent of X-rays. Indeed, Kreysing et al. (1992) presented first results from the *ROSAT* All Sky Survey on the X-ray emission of PNe, and claimed that they detected extended X-ray emission from 5 PNe; NGC 6543, NGC 6853, Abell 12, NGC 4361, and LoTr 5. Chu and Ho (1995) reported a detection of diffuse X-rays from Abell 30 by a *ROSAT* observation.

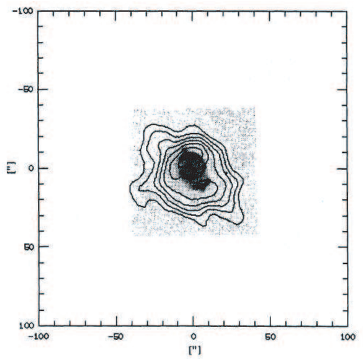

Figure 2.13: A smoothed X-ray image of NGC 6543 obtained with the *ROSAT* PSPC, superposed on a gray scale image of OI emission (Kreysing et al. 1992).

Figure 2.13 gives a smoothed X-ray image of NGC 6543 obtained with *ROSAT*. However, the *ROSAT* Position Sensitive Proportional Counter (PSPC) in the survey mode have an angular resolution of more than $2'$, which is larger than the optical size of NGC 6543 ($\sim 15''$). Chu et al. (1993) carefully analyzed another *ROSAT* PSPC data of NGC 6853, and concluded that its "extended" X-ray emission reported by Kreysing et al. (1992) is a result of an electronic ghost image in the soft energy bands. Similarly the X-ray images of Abell 12 and LoTr 5, obtained by long-exposure observations with the *ROSAT* PSPC, turned out to be consistent with point-like sources coincident in position with the central stars (Chu and Ho 1995). They also suggested that NGC 4361 is also a point-like source because of its similarity to LoTr 5 in the X-ray spectra.

Eventually, extended X-rays were detected by *ROSAT* from 2 PNe; NGC 6543 and Abell 30. The recent analysis of an X-ray image of BD +30° 3639, obtained with the *ROSAT* High Resolution Imager, also confirmed a finite spatial extent of its X-ray emission (Leahy et al. 2000).

An X-ray spectrum reproduced by thin thermal plasma emission would provide another evidence of emission from shock-heated gas. As shown in figure 2.14, the X-ray spectra of NGC 6543, BD +30° 3639, and Abell 30, obtained with the *ROSAT* PSPC, have actually been reproduced successfully by a plasma emission model with temperatures of $\sim 1.6 \times 10^6$, $\sim 2.5 \times 10^6$, and $\sim 4.5 \times 10^5$ K, respectively (Kreysing et al. 1992; Chu and Ho 1995). In contrast, the X-ray spectrum of NGC 6853, which is thought to have a point-like X-ray source, is reproduced by a blackbody with a temperature of $\sim 1.4 \times 10^5$ K (Chu et al. 1993). Although X-ray spectra of NGC 6543 and BD +30° 3639 could be reproduced also by a blackbody, the obtained temperatures are too high ($> 1 \times 10^6$ K) for central stars.

Arnaud et al. (1996) observed BD +30° 3639 with *ASCA*, which has a much better energy resolution than the previous missions. This observation revealed a strongly enhanced emission line at ~ 0.9 keV due to He-like Ne in the spectrum, as described later in detail (§4.3.1). This fine *ASCA* result has provided the first X-ray clue to the metal enhancement in PNe.

2.5.3 Chandra and XMM-Newton results

The *ROSAT* observations thus provided us with morphological and spectroscopic evidence of thermal X-ray emission from shock-heated gas in PNe. However, the angular resolution of *ROSAT* was larger than most of PNe, which have diameters of less than $1'$. Instrumental improvement was required. For these five years, two new X-ray observatories, *Chandra* and *XMM-Newton*, have significantly improved our understandings of X-ray emission from PNe.

Especially, the unprecedented $0.''5$ angular resolution of *Chandra* have revealed in great detail spatial distributions of X-rays from PNe. Kastner et al. (2000) successfully detected diffuse X-ray emission from BD +30° 3639, and Guerrero et al. (2001) resolved spatial X-ray distribution of NGC 6543 in detail. *Chandra* also detected diffuse X-rays from 3 more PNe; Mz 3, NGC 40, and NGC 7027 (Kastner et al. 2003; Kastner et al.

(a) NGC 6543

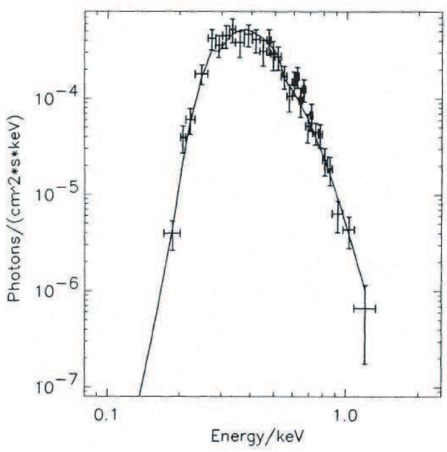

(b) BD +30° 3639

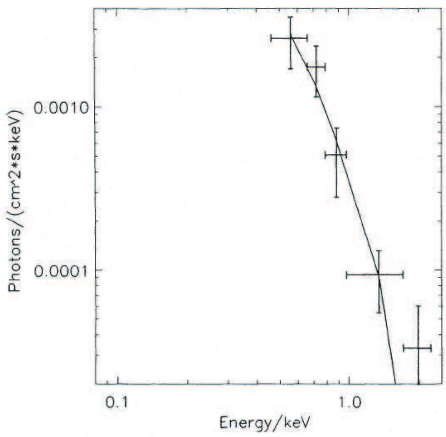

(c) NGC 6853

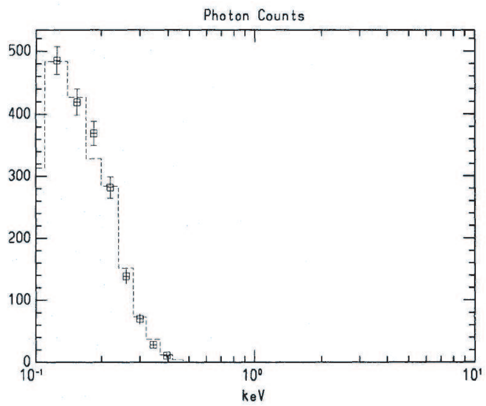

(d) Abell 30

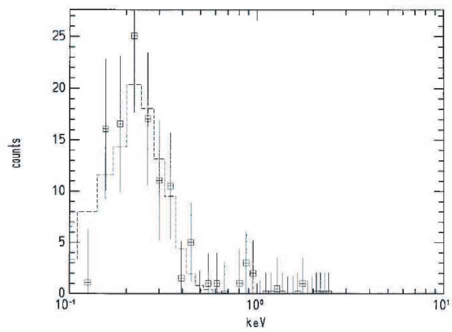

Figure 2.14: X-ray spectra of PNe obtained with the *ROSAT* PSPC. (a) NGC 6543 and (b) BD +30° 3639 are by Kreysing et al. 1992, (c) NGC 6583 from Chu et al. 1993, and (d) Abell 30 from Chu and Ho 1995.

2001). *XMM-Newton*, which has a good angular resolution of $\sim 4''$ also detected diffuse X-ray emission from NGC 2392 and NGC 7009 (Guerrero et al. 2005; Guerrero et al. 2002). Now 7 PNe are confirmed to emit diffuse X-rays, presumably emitted by hot plasma as optically-thin thermal emission.

NGC 7293 has been known as an X-ray emitting PN from the *Einstein* and *EXOSAT* era. Its X-ray emission has not been spatially resolved even with the superb angular resolution of *Chandra*.

2.5.4 X-ray spectroscopy of PNe

Through the X-ray imagery conducted for these 5 years, the presence of diffuse X-ray emission from hot plasmas in PNe have become a consensus of astrophysicists. The next step is their X-ray spectroscopy. Our objective in the present thesis is to determine abundance ratios of X-ray emitting matter in PNe, and to probe into the nucleosynthesis inside intermediate-mass stars.

Until 2000, we had only a single example of X-ray spectrum usable for abundance measurements, namely that of BD +30° 3639 obtained with *ASCA* (Arnaud et al. 1996; §2.5.2). The strong emission line of He-like Ne in the spectrum indicates that X-rays from PNe may reflect heavy elements produced inside stars. With a comparable energy resolution to that of *ASCA*, and a much improved efficiency in lower energies below 0.7 keV, *Chandra* and *XMM-Newton* have enabled us to take K-lines from C, N, and O at 0.3–0.7 keV into account (e.g. Chu et al. 2001; Maness et al. 2003). However, the energy resolutions of these new missions are not yet sufficient to resolve individual lines, thus leaving large uncertainties in the X-ray determination of abundances. Finally, the X-ray Imaging Spectrometer (XIS; §3.3.4) onboard *Suzaku*, the new-borne Japanese X-ray mission, has realized the capability to resolve these C, N, and O lines.

Chandra and *XMM-Newton* have enlarged our sample of X-ray emitting PNe. Utilizing these available data and the newest X-ray observatory *Suzaku*, we carry out determinations of abundance ratios in PNe by means of X-ray spectroscopy.

Chapter 3

INSTRUMENTATION

3.1 Chandra X-ray Observatory

3.1.1 Overview of the satellite

Launch on July 23, 1999, the *Chandra X-ray Observatory* is the NASA's flagship mission for X-ray astronomy. The most outstanding characteristic of *Chandra* is its unprecedented angular resolution of $0.''5$, which is superior by one order of magnitude than those of previous X-ray astrophysics missions.

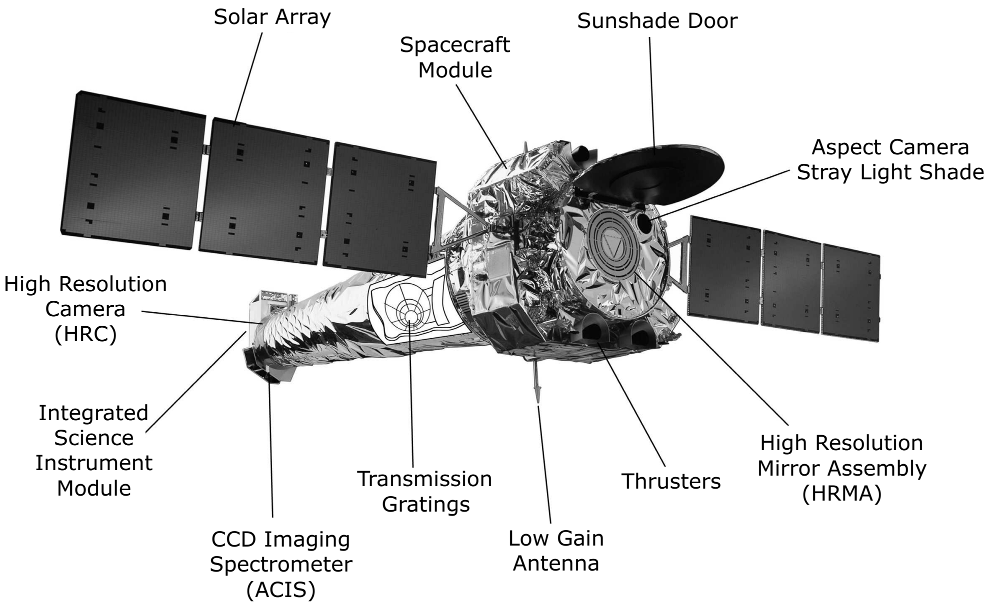

Figure 3.1: A schematic drawing of the *Chandra* satellite.

The observatory was successfully launched by the NASA's Space Shuttle Columbia into a highly elliptical orbit, with the apogee height of $\sim 120,000$ km and the perigee height of $\sim 29,000$ km. The orbit enables the satellite to spend its observational time mostly outside the radiation belt of the earth, and provides high observing efficiency without hampered by Earth occultations of the targets. A long continuous observations with a duration of ~ 160 ks is possible by virtue of the orbital period of 63.5 h.

A schematic drawing of the *Chandra* observatory is shown in figure 3.1. It consists of the spacecraft, the High Resolution Mirror Assembly (HRMA, §3.1.2), and the focal plane science instruments which is composed of the Advanced CCD Imaging Spectrometer (ACIS, §3.1.3) and the High Resolution Camera (HRC). Two kinds of objective transmission gratings, the Low and High Energy Transmission Grating (LETG and HETG), are optionally inserted to the optical path on the HRMA, and produce wavelength-dispersed images of point sources on the ACIS or HRC.

3.1.2 High Resolution Mirror Assembly (HRMA)

The splendid angular resolution characterizing *Chandra* is achieved by its telescope system, namely the HRMA. As schematically shown in figure 3.2, it consists of 4 pairs of concentric thin-walled, grazing-incidence Wolter Type-I mirrors. The front section of each pair is a paraboloid mirror and the rear section a hyperboloid mirror. Unlike ordinary optical mirrors, X-rays comes in with a very shallow angle to the mirror surface, reflected twice, and are focused. The substrate of the HRMA is Zerodur glass, which is polished and coated with iridium on a binding layer of chromium. Design parameters and performance of the HRMA are summarized in table 3.1.

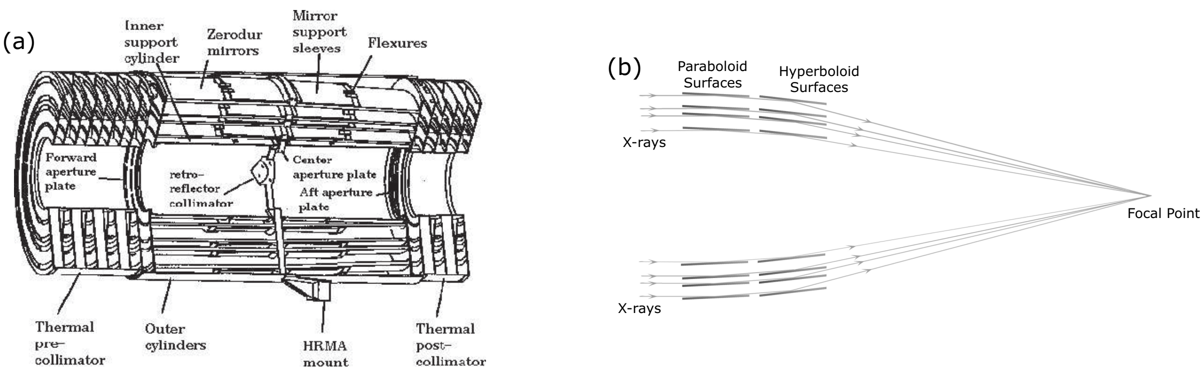

Figure 3.2: (a) The 4 nested HRMA mirror pairs and associated structure. (b) Schematic X-ray grazing path in the HRMA.

Table 3.1: Design parameters and performance of the *Chandra* HRMA.

Optics	Wolter Type I
Mirror coating (nominal thickness)	Iridium (330 Å)
Mirror length (paraboloid or hyperboloid)	84 cm
Total length (pre-collimator to post-collimator)	276 cm
Mirror outer diameter (1, 3, 4, 6)	1.23, 0.99, 0.87, 0.65 m
Focal length	10.070 ± 0.003 m
Plate scale	48.82 ± 0.02 μm arcsec^{-1}
Total weight	1484 kg
Unobscured clear aperture	1145 cm^2
PSF (with detector)	0.5 arcsec
Effective area (@ 0.25, 5.0, 8.0 keV)	800, 400, 100 cm^2
Ghost-free field of view	30 arcmin dir

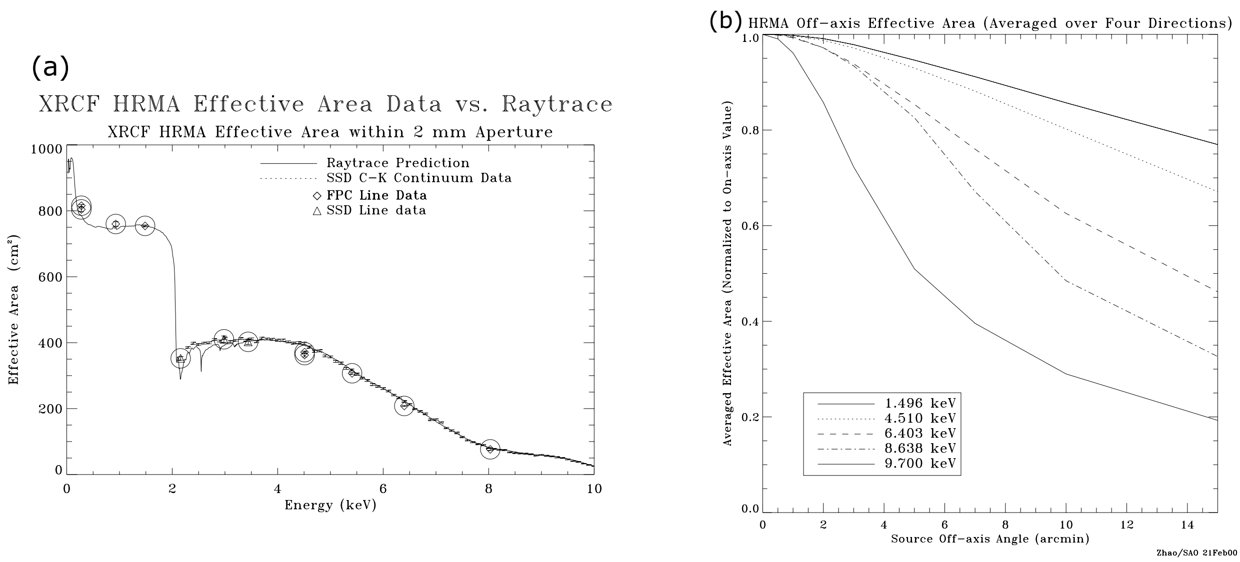

Figure 3.3: The HRMA effective area, shown as a function of energy (panel a), and of the off-axis angle (panel b). In panel (a), the solid line is the ray-trace simulation of the effective area within a 2 mm diameter aperture at the focus. Dashed line shows data for C-K continuum source taken by a solid state detector (SSD), and the diamonds and triangles are those for atomic lines taken by a flow proportional counter (FPC) and SSD. In panel (b), The HRMA effective area versus off-axis angle averaged over azimuth is shown for selected energies. Each curve is normalized to the on-axis area for that energy.

Since the X-ray reflectivity depends on the energy as well as the grazing angle, the effective area of X-ray telescopes generally varies depending on these two quantities. Figure 3.3 shows the HRMA effective area as a function of the incident X-ray energy. The sharp drop at $\sim$ 2 keV is due to M-edge of iridium. The mirror becomes no longer reflective above an X-ray energy of $\sim$ 10 keV. As shown in figure 3.3 (b), the effective area also decreases with increasing off-axis angle of the source. X-ray telescopes generally show this characteristic, so-called vignetting, which is caused by an increase in the grazing angle over the azimuthal sector opposite to the target shift, and a decrease in the projected geometrical area over the other sector.

Another important HRMA property is stray light, which originates from strong sources outside the field of view. Baffle plates prevent non-reflected or singly reflected X-ray photons from coming into the focal plane within central 30 arcmin diameter of the field of view. Outside this region, however, singly reflected rays from luminous off-axis source may produce ghost images.

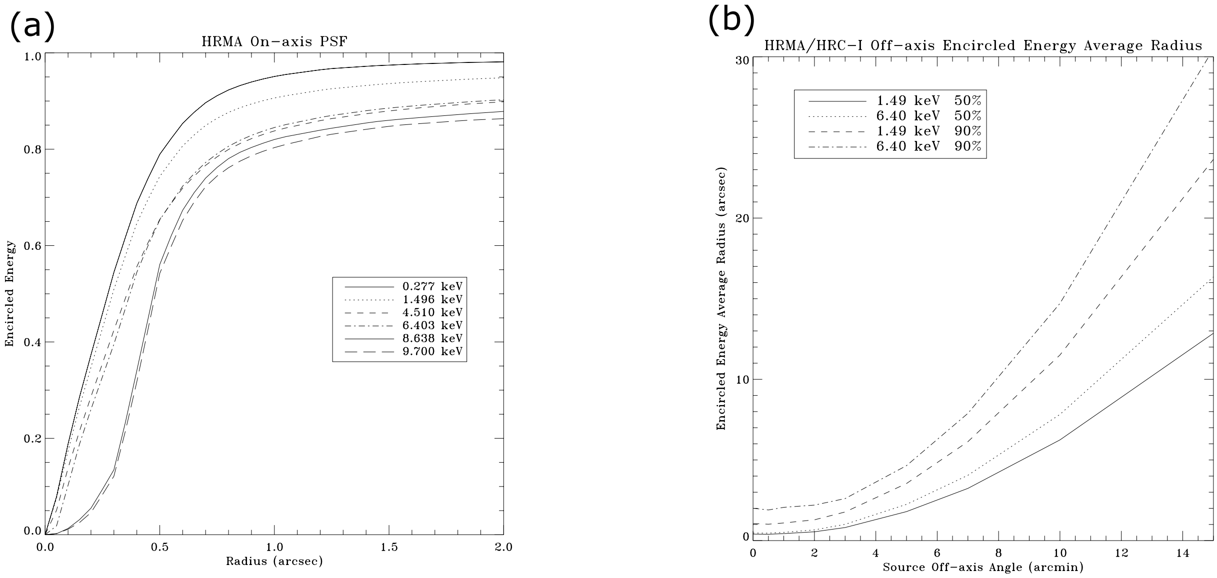

Figure 3.4: (a) The fractional encircled energy as a function of angular distance from the optical axis, calculated for an on-axis point source at selected X-ray energies. (b) Average angular radii for the HRMA to enclose 50 % and 90 % of the in-coming X-rays, presented as a function of off-axis angle. The calculation is performed at energies of 1.49 and 6.40 keV.

The two-dimensional brightness distribution, created on the focal plane by a mono-energetic point source placed at a certain location in the field of view, is called point-spread function (PSF) of a telescope. A useful parameter characterizing the PSF is encircled energy fraction, which is two-dimensional integral of the PSF calculated as a function of radius from the image center. The PSF, and here the encircled energy fraction for a given radius, again depends on the X-ray energy and the off-axis angle. The optical axis of the HRMA is defined, and calibrated in flight, as the direction where the PSF becomes sharpest. The PSF broadens, and here the encircled energy fraction decreases, when the off-axis angle increases because of mirror aberration, and also when the X-ray energy increases because of more enhanced X-ray scattering. These properties are shown in figure 3.4 (a) and (b).

3.1.3 Advanced CCD Imaging Spectrometer (ACIS)

The Japanese *ASCA* satellite for the first time carried on-board X-ray CCDs operated in the single-photon mode. Since then CCDs have been used as the most standard focal-plane detector of imaging X-ray telescopes. In combination with an X-ray telescope, CCDs enable us to measure the position and pulse-height of each detected X-ray photon, and hence obtain images and spectra at once in a typical energy range of $\sim$0.5 – 10 keV.

The ACIS has been designed to simultaneously acquire high angular-resolution images and moderate energy-resolution spectra of celestial X-ray sources. The ACIS is also utilized as the 1-dimensional detector to register dispersed images when the LETG or HETG is employed. A photograph and a schematic layout of the ACIS are shown in figure 3.5 and 3.6, respectively. The ACIS is composed of mainly two parts; one is ACIS-I, which consists of 4 chips arranged in a 2×2 configuration, and the other is ACIS-S, which consists of 6 chips lined up. The former is used mainly in imaging-oriented observations, whereas the latter mainly used in spectroscopy-oriented ones. The grating readout is performed with ACIS-S.

The ACIS employs two kinds of chips with different irradiation method; front-illuminated (FI) and back-illuminated (BI). As shown in figure 3.6, two chips of ACIS-S are BI devices, and the other 8 chips are FI. The response of BI devices extends to energies lower than that accessible with the FI devices. The characteristics of the ACIS are summarized in table 3.2. The ACIS can be physically moved on the focal plane, so that the HRMA optical axis fall on the desired CCD chip.

3.1.4 Performance of the ACIS

Figure 3.7 shows the effective area (i.e., the HRMA effective area of figure 3.3a multiplied by the CCD quantum efficiency) of the ACIS plus HRMA. ACIS-S, which incorporates 2 BI chips, has the advantage of a larger effective area below 1.0 keV than that of the ACIS-

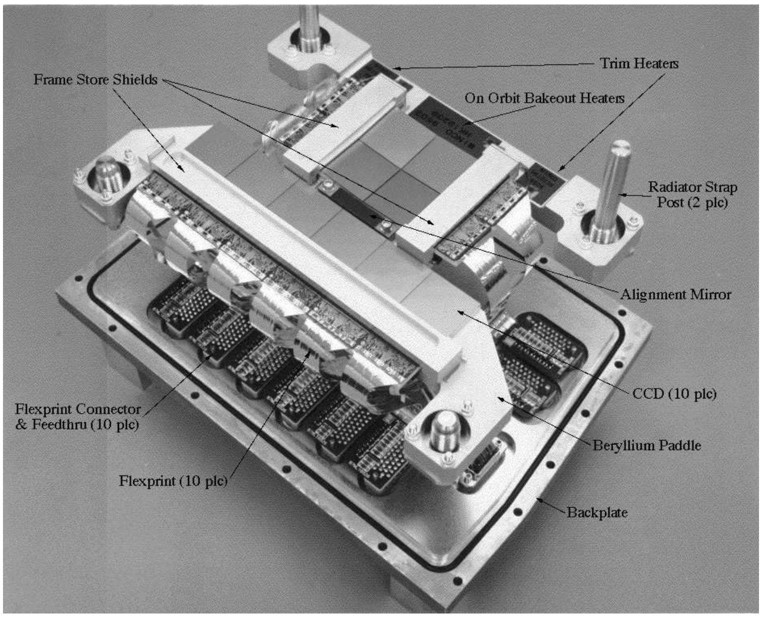

Figure 3.5: A photograph of the ACIS.

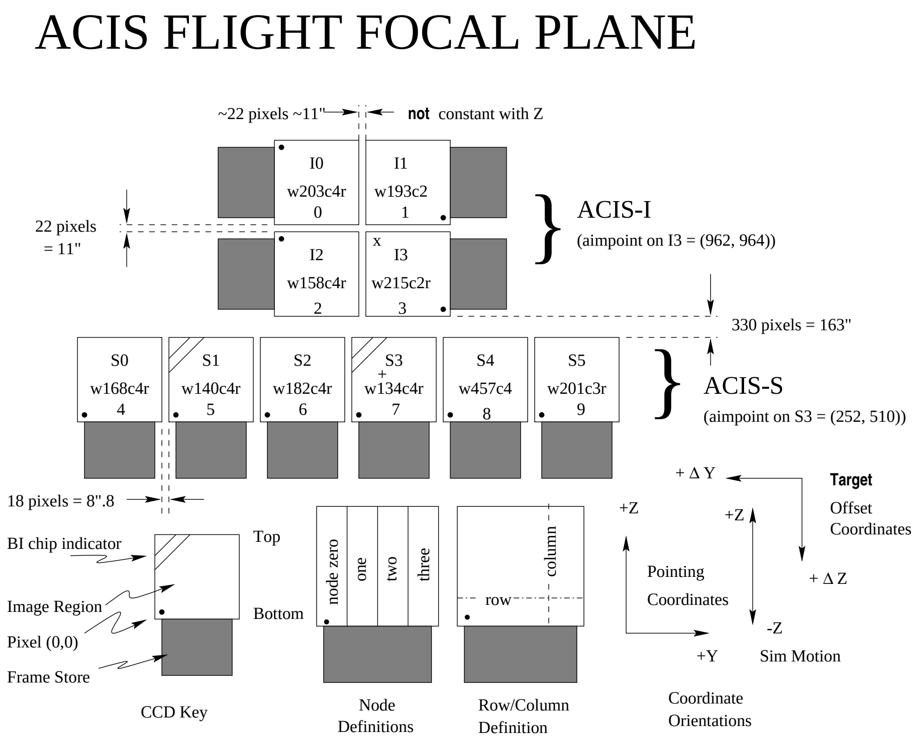

Figure 3.6: The focal-plane layout of the ACIS CCD chips.

Table 3.2: The characteristics of the *Chandra* ACIS.

CCD format	1024×1024 pixels
Pixel size	24.0 μm (0.4920$\pm$0.0001 arcsec)
Array size (ACIS-I/S)	16.9×16.9 arcmin / 8.3×50.6 arcmin
On-axis effective area	110, 600, 40 cm^2 @ 0.5, 1.5, 8 keV for FI
Quantum efficiency (for FI)	$> 80\%$ (3.0–5.0 keV), $> 30\%$ (0.8–8.0 keV)
Quantum efficiency (for BI)	$> 80\%$ (0.8–6.5 keV), $> 30\%$ (0.3–8.0 keV)
Charge transfer inefficiency (parallel)	$\sim 2 \times 10^{-4}$ (FI), $\sim 2 \times 10^{-5}$ (BI)
Charge transfer inefficiency (serial)	$< 2 \times 10^{-5}$ (FI), $\sim 7 \times 10^{-5}$ (S3, BI)
System noise	< 2 electrons per pixel
Minimum row readout time	2.8 ms
Nominal frame time (allowable frame times)	3.2 s (0.2–10 s)
Point-source sensitivity	4×10^{-15} erg cm^{-2} s^{-1} in 10^4 s
Detector operating temperature	$-90 \sim -120$ °C

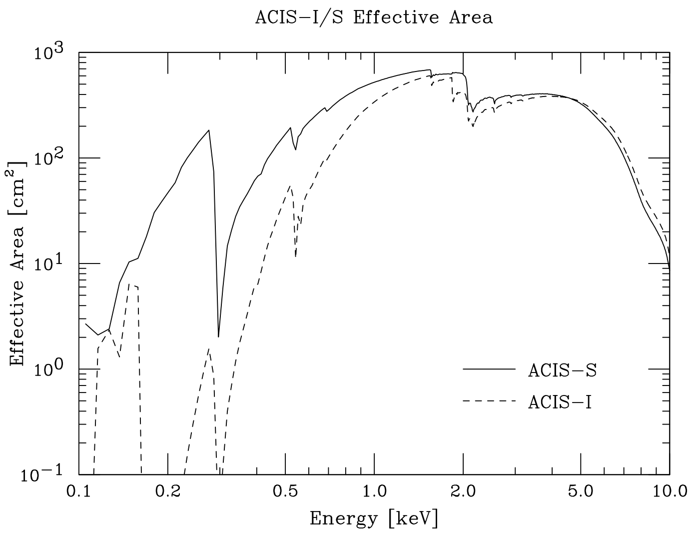

Figure 3.7: The Effective area of the ACIS when used in combination with the HRMA, drawn separately for ACIS-I and ACIS-S.

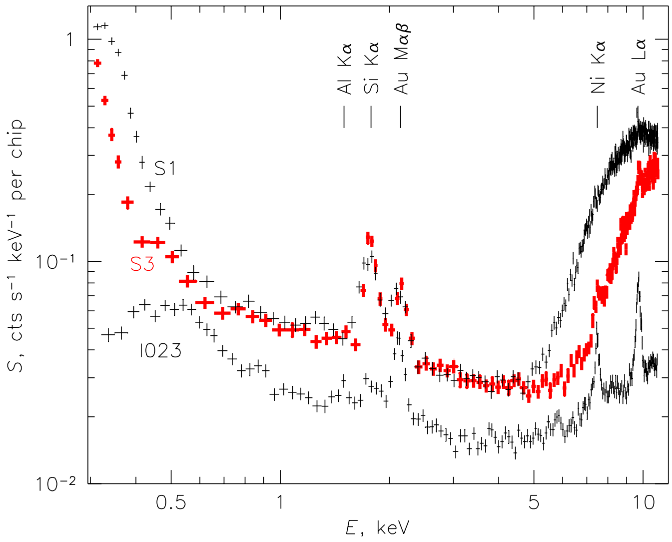

Figure 3.8: The background spectra of the ACIS, obtained in the stowed position. The chip designations refer to figure 3.6.

I. Above ~ 5 keV, the effective area decreases because of the reduced quantum efficiency of the CCD chips and the decreasing reflectivity of the HRMA. The reduction toward lower energies is due to photoelectric absorption by electrodes and protective layers of the CCD. We observe a sharp feature at ~ 2 keV due to Ir-M edge.

The background spectra shown in figure 3.8 were obtained with the ACIS in its stowed position, shielded from the sky and the on-board calibration source illumination. Charged-particle events, which produce hits over multiple CCD pixels, have been removed using charge-split patterns. The BI devices which correspond to S1 and S3 chips have higher background than the FI devices which is denoted "I0123" in figure 3.8. Differences between the BI and FI chips are described later (§3.3.4). There are line features due to fluorescence of materials in the telescope and the focal plane. These spectra serve as templates of quiescent non X-ray background, which includes gamma-rays, residual charged particles, secondary X-rays, and so on. We expect these contributions essentially the same between the stowed position and the normal focal position.

In actual observations, two more background components are added to the non-celestial contribution represented by figure 3.8. One is cosmic X-ray background (CXB), which is resolved ultimately into faint discrete sources in a sufficiently long exposure,

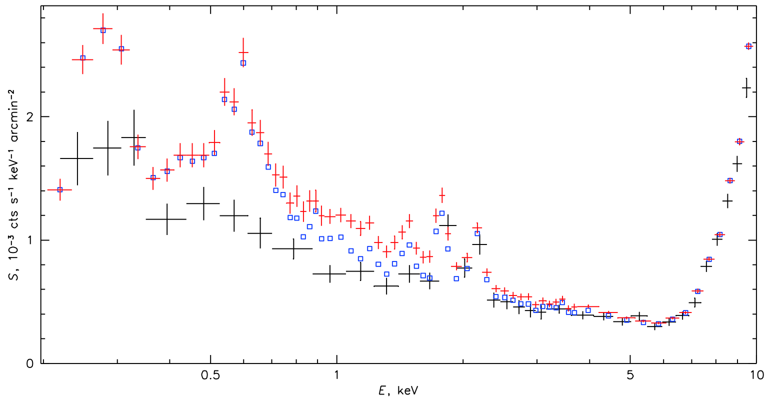

Figure 3.9: The total background spectra of the ACIS-S3. Small red crosses show blank sky spectrum, while blue squares are diffuse component, left after exclusion of resolved point sources which are detectable in a 90 ks observation. Large black crosses represent the non-X-ray (the dark Moon) background spectrum.

except for Galactic diffuse component below 1 keV. Figure 3.9 shows total background spectrum in quiescent blank-sky observations, compared with dark-Moon spectrum which is essentially the same as those shown in figure 3.8. The residuals between them are due to the CXB; thus, the CXB is significant in the 0.4–2 keV range, but otherwise overwhelmed by the non celestial contribution. The other is a time-variable component, called "flares", caused by soft protons reflected from the telescope. This component is described later (§3.2.4)

3.2 XMM-Newton

3.2.1 Overview of the satellite

XMM-Newton, or the X-ray Multi-Mirror Mission, is the second cornerstone of the Horizon 2000 program of the the European Space Agency (ESA). It was launched on 1999 December 10, by an Ariane 5 launcher, into a highly elliptical orbit with the apogee height of $\sim$ 115,000 km and the perigee height of $\sim$ 6,000 km. The most remarkable characteristic of *XMM-Newton* is the large effective area available for X-ray collection.

Figure 3.10 shows a schematic view of *XMM-Newton*. As represented by the name of X-ray Multi-Mirror Mission, the satellite has three X-ray mirror assemblies.

The telescopes are coupled to two X-ray instruments, the European Photon Imaging Camera (EPIC) and the Reflection Grating Spectrometer (RGS). In addition, there is a

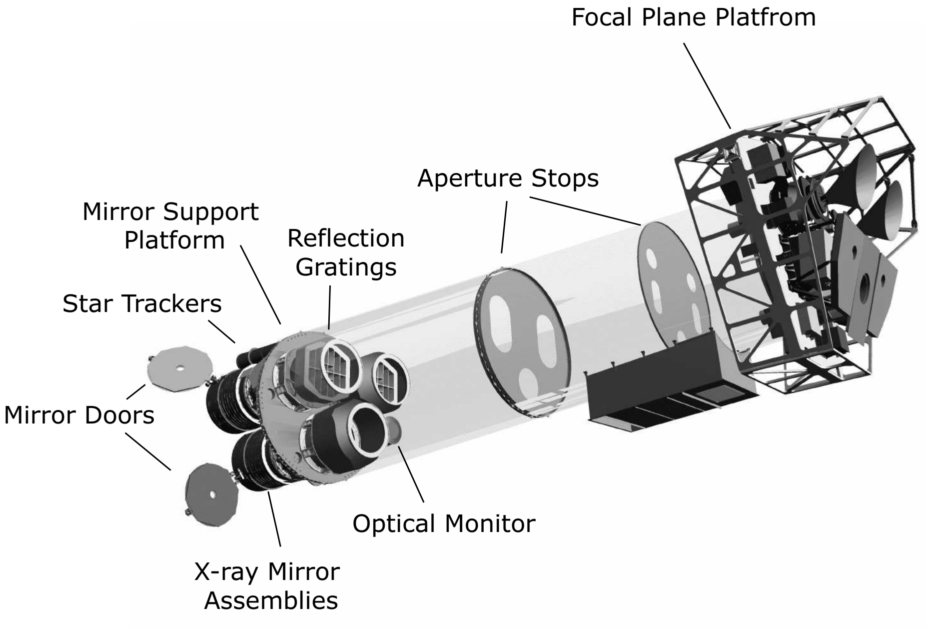

Figure 3.10: A schematic illustration of the *XMM-Newton* satellite.

co-aligned optical/UV telescope called the Optical Monitor (OM). The EPIC, the RGS, and the OM can simultaneous observe the same target, thus providing the mission with another important feature.

The EPIC is composed of three CCD cameras, one for each telescope; two of them are called MOS cameras, and the other pn camera. The RGS consists of two identical units, sharing the same telescopes as the two MOS cameras. Each of them is mainly composed of a reflection grating array and a focal plane camera unit; as shown in figure 3.11, the former is directly attached to the corresponding mirror assembly, while the latter is a strip of CCD detectors and is set at the secondary focal plane platform. About 40% of X-rays which come into the telescope are dispersed and focused on the RGS detector, while 50% of them directly reach the EPIC MOS camera.

3.2.2 Telescope system

The three telescopes of *XMM-Newton*, which are basically identical, were designed to obtain the highest effective area, particularly in the range of around 7 keV, ever achieved with X-ray reflective optics in orbit. In order to provide sufficient reflectivity in the high energy range, the mirror has been required to utilize a very shallow grazing angle. Basic parameters of the telescopes are summarized in table 3.3

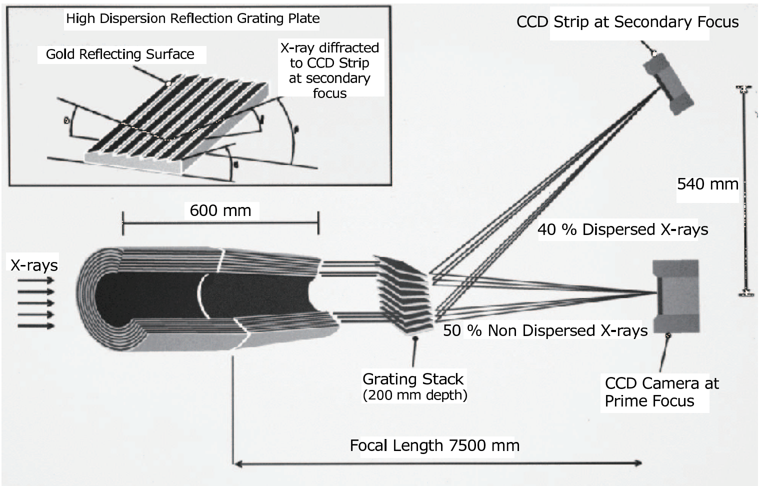

Figure 3.11: An illustration of an *XMM-Newton* telescope, together with the EPIC MOS camera and the RGS instrument attached to it.

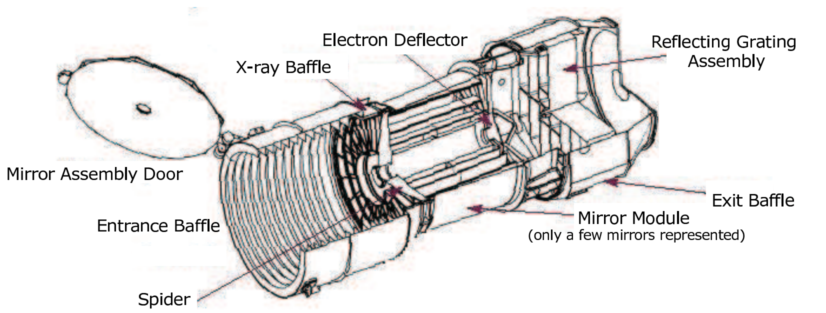

Figure 3.12: The nested mirrors and associated structure of the telescopes.

Each of the X-ray telescopes consists of 58 thin mirror shells nested in a coaxial and co-focal configuration. Similar to the *Chandra* HRMA, each mirror shell is composed of a paraboloid and an associated hyperboloid. In the case of *XMM-Newton*, the effective area is increased by nesting a number of mirrors and thus filling the front aperture with high efficiency. The nesting efficiency is determined by the mirror thickness and the minimum radial separation required for integration and alignment. Such highly nested design requires manufacturing a large number of X-ray-quality mirror shells. They are thin monolithic gold-coated nickel shells, replicated from super-polished gold coated mandrels using a nickel electro-forming technique. The achieved effective area is shown in figure 3.13; compared to the *Chandra* HRMA in figure 3.3, the *XMM-newton* X-ray telescopes have a significantly larger effective area. The sharp drop of the area at ~ 2 keV is due to M-edge of gold.

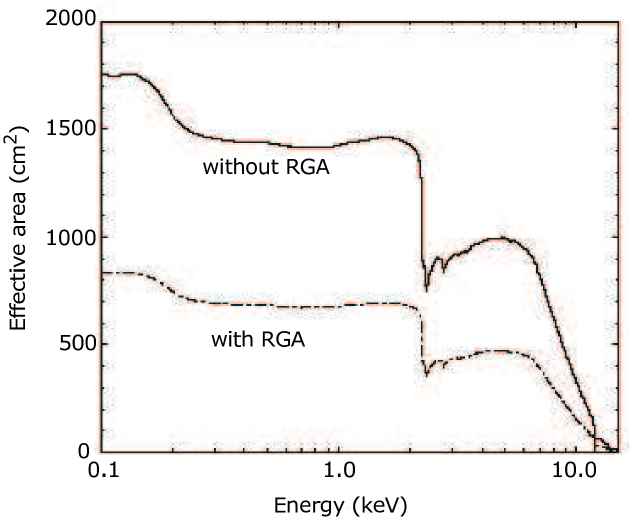

Figure 3.13: The effective area of each telescope of *XMM-Newton*.

Although the three telescopes on-board *XMM-Newton* are basically identical, their PSFs (§3.1.2) practically vary to some extent. Full width at half maximum (FWHM) and half energy width (HEW) of their PSFs are listed in table 3.4. In the case of the pn camera, FWHM cannot be measured on orbit because of the large pixel size. Figure 3.14 displays the azimuthally averaged PSF of a telescope. Thus, we may consider the angular resolution of *XMM-Newton* to be $\sim 10''$.

Figure 3.15(a) shows fractional encircled energy of MOS1 as a function of the radius from the image center. For on-axis sources, high energy photons are reflected and focused predominantly by inner shells of the telescope. Since the inner shells apparently give

Table 3.3: Basic parameters and performance of the *XMM-Newton* Telescope

Optics	Wolter Type I
Mirror substrate	Nickel
Mirror coating (thickness)	Gold (250 nm)
Mirror length (paraboloid or hyperboloid)	60 cm
Mirror diameter (outer / inner)	70.0 / 30.6 cm
Mirror thickness (outer / inner)	1.07 / 0.47 mm
Focal length	7.500 m
Mirror module mass	420 kg
Effective area (@ 1.5, 8.0, 12 keV)	1475, 580, 130 cm^2
Field of view	30 arcmin dir

Table 3.4: Point Spread Function of the *XMM-Newton* Telescope.

Mirror module number	2	3	4
Instruments	pn	MOS1 + RGS1	MOS2 + RGS2
	on-orbit / ground	on-orbit / ground	on-orbit / ground
FWHM [arcsec]	<12.5 / 6.6	4.3 / 6.0	4.4 / 4.5
HEW [arcsec]	15.2 / 15.1	13.8 / 13.6	13.0 / 12.8

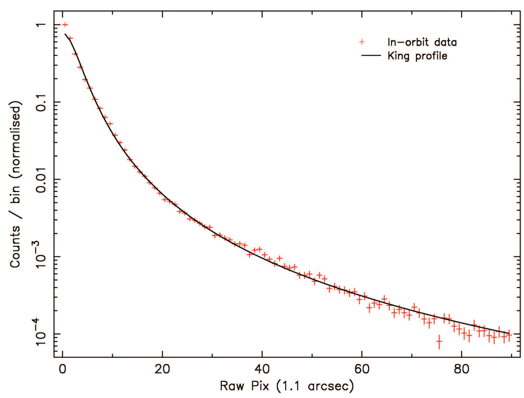

Figure 3.14: A radial count distribution of an X-ray point source placed at the optical axis of the MOS1 telescopes (mirror module number 3). This represents the on-axis PSF. Crosses show the in-orbit measurement in the energy range from 0.75 to 2.25 keV. A best-fit King profile is overlaid with the black solid line.

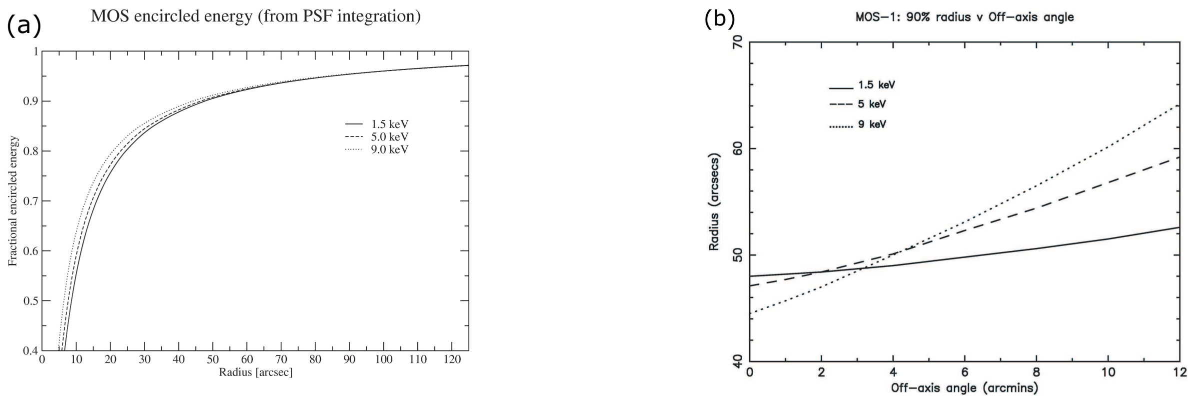

Figure 3.15: (a) The MOS1 fractional encircled energy, presented of an on-axis source as a function of the angular distance from the image center. (b) The radius which contains 90 % of the total photons from a point source, shown as a function of off-axis angle at different energies.

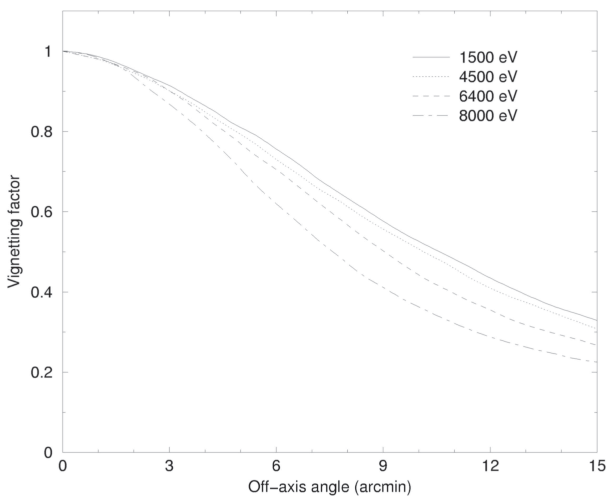

Figure 3.16: Vignetting function of the pn X-ray telescope (mirror module number: 2), based on a simulation, shown as a function of the off-axis angle.

better focus than the average of all shells, the fractional encircled energy increases as the photon energy becomes higher.

As already mentioned in reference to the *Chandra* HRMA, the PSF of *XMM-Newton* is expected to depend on the off-axis angle, and also slightly on the source azimuth within the field of view. In figure 3.15(b), we actually observe that the radius which encircle 90 % of the total photons from a point source varies with the off-axis angle. In particular, the energy dependence of the PSF increases toward larger off-axis angles. This is because the reflection of off-axis high energy photons is no longer confined to inner shells of the telescope.

Not only the PSF but also the effective area of the telescope depends on the off-axis angle. As the off-axis angle gets larger, a smaller fraction of incident photons actually reach the focal plane, causing the "vignetting" effect as already mentioned in §3.1.2. Figure 3.16 displays the vignetting of the *XMM-Newton* telescope. Thus, the effect is qualitatively similar to the case of the *Chandra* HRMA (figure 3.3(b)), but the energy dependence is weaker.

The X-ray baffles illustrated in figure 3.12 prevent stray light from entering and reaching the focal plane. The collecting area of stray light is ~ 3 cm^2 for a source located at between 20 arcmin and 1.4 degree from the optical axis. At higher off-axis angles, it is completely negligible.

3.2.3 European Photon Imaging Camera (EPIC)

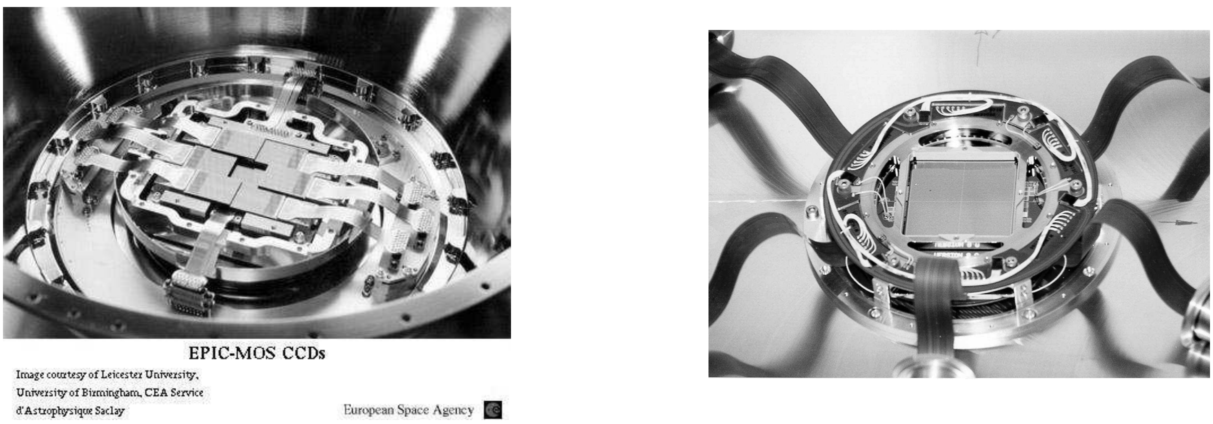

Figure 3.17: The photograph of the EPIC MOS (left) and pn (right) cameras.

As described in §3.2.1, *XMM-Newton* has three X-ray CCD cameras, namely European Photon Imaging Camera (EPIC). Two of the cameras, namely MOS cameras, utilize MOS (Metal Oxide Semi-conductor) CCD arrays, each consisting of 7 chips as illustrated in figure 3.17 (left) and 3.18 (left). They are installed behind those mirror assemblies which are equipped with the reflection gratings. Therefore, about a half of the incoming flux reaches the MOS cameras. As can be seen on the photograph in figure 3.17(left), the seven chips are arranged to have slightly different heights, in order to suppress the inter-chip gaps and to better trace the slightly curving focal plane.

At the focal plane of the third telescope, the pn camera using pn CCDs is installed. As shown in figure 3.17 (right) and 3.18 (right), the pn camera utilizes 12 chips configured on a common plane. The characteristics of the EPIC MOS and pn cameras are listed in table 3.5. The MOS camera has a better angular resolution because of its smaller pixel size, while the pn camera possesses higher efficiency in the lower energy range because of adopting the back-illuminated method like ACIS-S (§3.1.4).

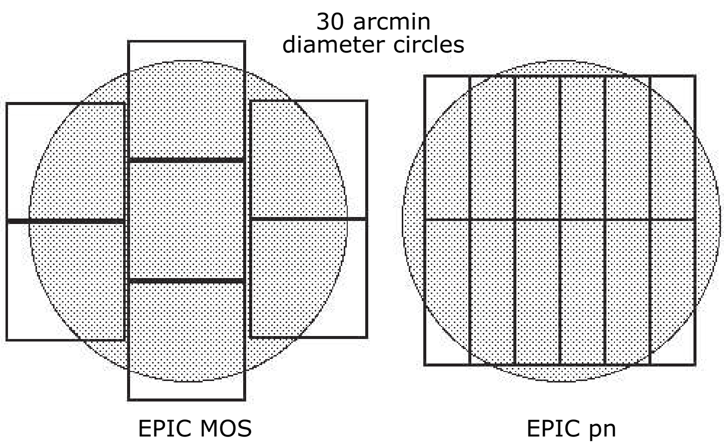

Figure 3.18: A schematic CCD layout of the EPIC MOS (left) and pn (right), overlaid with the field of view.

3.2.4 Performance of the EPIC

An important factor affecting the effective area of a telescope+detector system is the quantum efficiency of the detector. The quantum efficiency of the EPIC MOS and pn is displayed in figure 3.19 left and right, respectively. In both ends of the energy band, the EPIC pn has a larger effective area than the EPIC MOS.

Figure 3.20 shows the overall (telescope times detector) effective area of individual instruments of *XMM-Newton*. In virtue of the higher quantum efficiency and the larger fraction of X-rays reaching the primary focus, the EPIC pn has a larger effective area than even the two MOS cameras summed together. The effective area of the pn camera is near

Table 3.5: The characteristics of the *XMM-Newton* EPIC.

	MOS	pn
Illumination method	Front illuminated	Back illuminated
CCD format (1 chips)	600×600 pixels	199×64 pixels
Pixel size	40 μm (1.1 arcsec)	150 μm (4.1 arcsec)
Chip size	2.4×2.4 cm^2	3×1 cm^2
Time resolution	2.6 s	73.4 ms
Detector operating temperature	$-100, -120$°C	-90°C

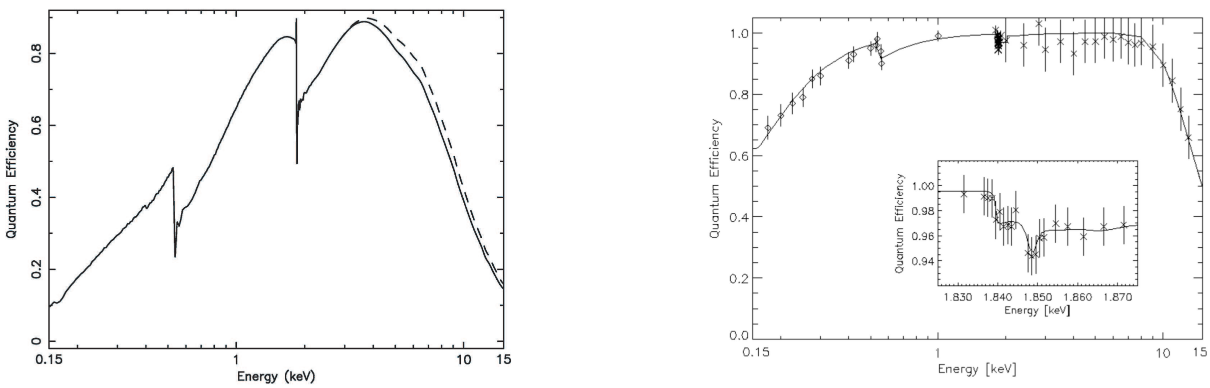

Figure 3.19: The quantum efficiency of the EPIC MOS (left) and pn (right).

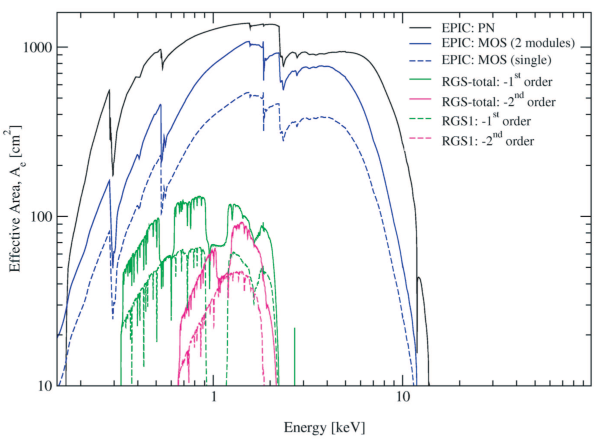

Figure 3.20: The effective area of the EPIC and the RGS, including both the telescope and detector characteristics.

1000 cm^2 at 0.5 keV, while that of *Chandra* ACIS-S is 100–200 cm^2. The pn has a great advantage especially in the lower energy range, compared with ACIS-S which utilizes also back-illuminated devices.

As shown in figure 3.21, the EPIC background count rate often exhibits sudden increases by a factor of several, or even more than an order of magnitude. Similar strong variations in the background count rate are known in the case of *Chandra*, while the *ASCA* SIS, which is the first satellite-borne X-ray CCD camera operated in the single-photon detection mode, did not experience such effects. This difference is attributed to the difference in their orbits: *XMM-Newton* and *Chandra* have high eccentric orbits, and consequently spend most of time outside the Earth's magnetosphere, while *ASCA* had a near-Earth orbit which is inside the magnetosphere. Now it is thought that the EPIC background flare is due to soft protons below 1 MeV, which are reflected and focused by the X-ray telescopes. Because such soft protons cannot penetrate the Earth's magnetosphere, *ASCA* was free from their bombardments.

Figure 3.22 shows the background spectra of the EPIC acquired under different conditions. The highest in each spectrum is measured during a background flare. It is dominated by continuum component, and known to be variable. The lowest is obtained with the closed filter; therefore it includes only non-X-ray background (NXB). The NXB spectra exhibit several fluorescence lines of instrumental origin. The blank-sky spectrum shows excess above the NXB spectrum, particularly in the lower energies. This excess represents the cosmic X-ray background component.

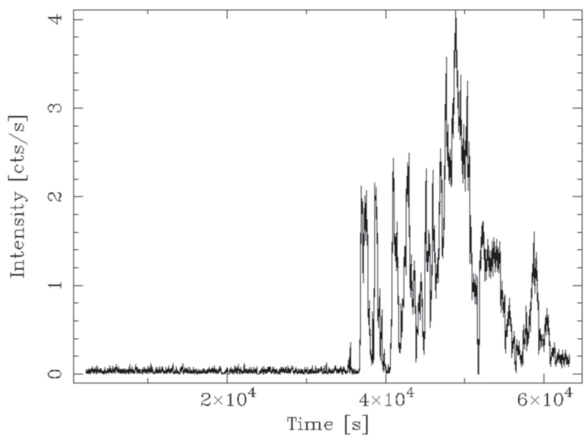

Figure 3.21: Episodes of sporadic increase of the EPIC background count rate, called "background flares".

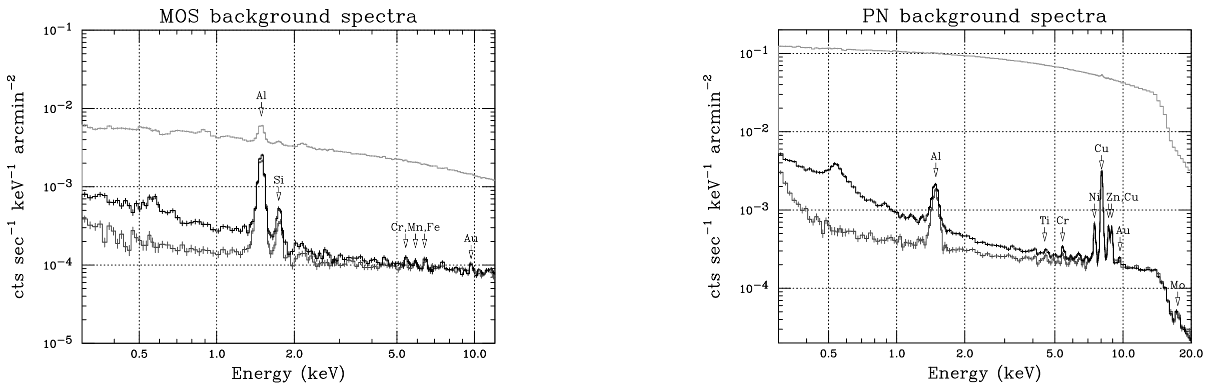

Figure 3.22: Background spectra of the EPIC MOS (left) and pn (right). (light gray) Those extracted during a proton flare. (black) Spectra extracted from blank sky region, excluding resolved point-like sources. (dark gray) Those observed with the closed filter.

3.3 Suzaku

3.3.1 Overview of the satellite

Suzaku (*Astro-E2*) is the newest X-ray observatory, which is the fifth Japanese X-ray mission after *ASCA*, successfully launched by a M-V (mu-five) launcher from Uchinoura on 2005 July 10. It is the recovery mission to *Astro-E*, which was lost on 2000 February 10 due to malfunctioning in the first stage of the launch vehicle. *Suzaku* has a near-Earth circular orbit with the altitude of $\sim$ 570 km and the inclination of 31 degree. The most notable characteristic of *Suzaku* is the high throughput over the broad-band energy range from 0.3 to 600 keV.

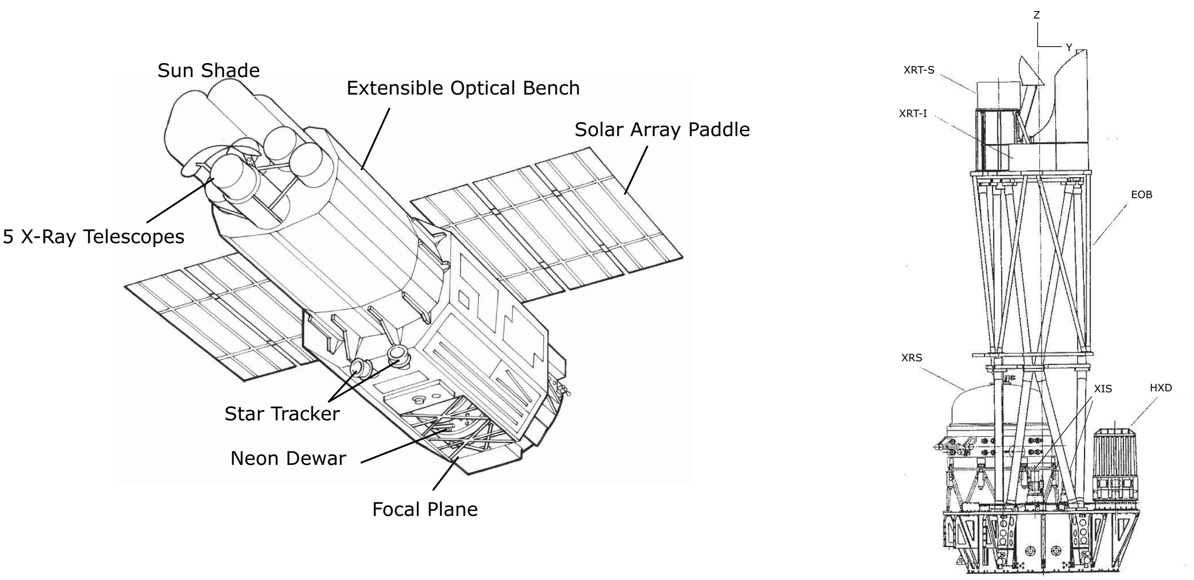

Figure 3.23: A schematic drawing of the *Suzaku* satellite (left), and its side-view (right).

Figure 3.23 shows a schematic drawing of *Suzaku*. It has five X-Ray Telescopes (XRTs) and two kinds of focal-plane detectors; the X-ray Imaging Spectrometer (XIS) and the X-Ray Spectrometer (XRS). The XRS are installed on the focal plane of one of the XRTs, and four XISs are coupled to the remaining four. They cover the energy range below $\sim$ 10 keV. *Suzaku* also carries onboard the Hard X-ray Detector (HXD) which shoulders observations in the higher energies of 10–600 keV. Although the XRS, to our deep regret, has stopped its function on 2005 August 8 before the start of its observation, *Suzaku* is now providing us with a series of novel broad-band data by utilizing the XIS and the HXD simultaneously.

As described in detail in §3.3.5, the XIS possesses superior effective area and energy resolution especially below 1 keV than *Chandra* ACIS-S and *XMM-Newton* EPIC-pn. This is greatly advantageous to observe soft X-ray sources. Since the HXD has achieved the highest sensitivity among previous hard X-ray and soft γ-ray missions, *Suzaku* is also favorable to obtain a spectrum in the higher energies up to several hundreds keV.

3.3.2 X-Ray Telescope (XRT)

Suzaku has five light-weight thin-foil X-Ray Telescopes. Four of them, basically identical, are called "XRT-I", and used to focus on the XIS. The other is called "XRT-S" for the XRS, and has slightly different parameters. The XRTs are arranged on the Extensible Optical Bench (EOB) as shown in figure 3.24. Basic parameters of these two kinds of telescopes are summarized in table 3.6

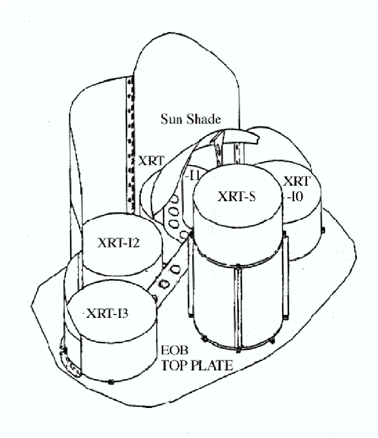

Figure 3.24: A schematic drawing of the X-Ray Telescope (XRT).

The *Suzaku* XRT utilizes the same Wolter Type-I configuration as the *Chandra* HRMA and the *XMM-Newton* telescopes, but employs conical approximation to the exact paraboloid

Table 3.6: Basic parameters and performance of the *Suzaku* Telescopes.

	XRT-I	XRT-S
Number of Telescopes	4	1
Substrate (thickness)	Aluminum (155 μm)	
Mirror coating	Gold	
Total height	279 mm	
Weight	19.5 kg	18.5 kg
Number of nested shells	175	168
Mirror diameter (outer/inner)	39.9 / 11.8 cm	40.0 / 11.9 cm
Focal length	4.75 m	4.5 m
Plate scale	0.724 mm arcmin^{-1}	0.764 mm arcmin^{-1}
Geometrical area	873 cm^2	887 cm^2
Effective area (@ 1.5, 8 keV)	440, 250 cm^2	
Field of view (@ 1.5, 8 keV)	17, 13 arcmin	
Angular resolution (HPD)	2 arcmin	

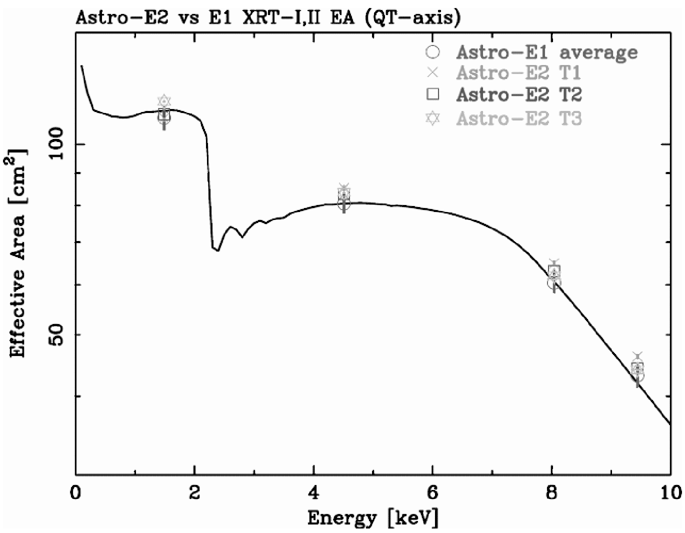

Figure 3.25: The effective area of the *Suzaku* XRT-I. The predicted response is compared to pre-launch measurements performed at particular energies for three different XRTs.

or hyperboloid surfaces. Tightly nested mirror shells employ thin Aluminum foils as substrates, which are glued by epoxy to gold-coated glass mandrels, heat treated to achieve a stable shape, and then lifted off the mandrel to become a self-supported gold-coated mirror surface. This replication method allows a mirror shell to be thin, and hence to realize a high aperture efficiency can be achieved, providing a light-weight telescope with a large effective area. Although the use of thin foils with conical approximation makes the angular resolution of the *Suzaku* XRT significantly worse than those of *Chandra* and *XMM-Newton*, it is actually considerably better than those of the *ASCA* telescopes which utilized similar thin foils without replication process.

Figure 3.25 shows the effective area of a single XRT-I. Although the XRT has smaller effective area than the *Chandra* HRMA (figure 3.3a) and the *XMM-Newton* telescope (figure 3.13), the XRT keeps a high reflectivity up to 10 keV. As shown in figure 3.26, the angular resolution of the XRT is about 1.′9 (half-power diameter), and is nearly independent of X-ray energy.

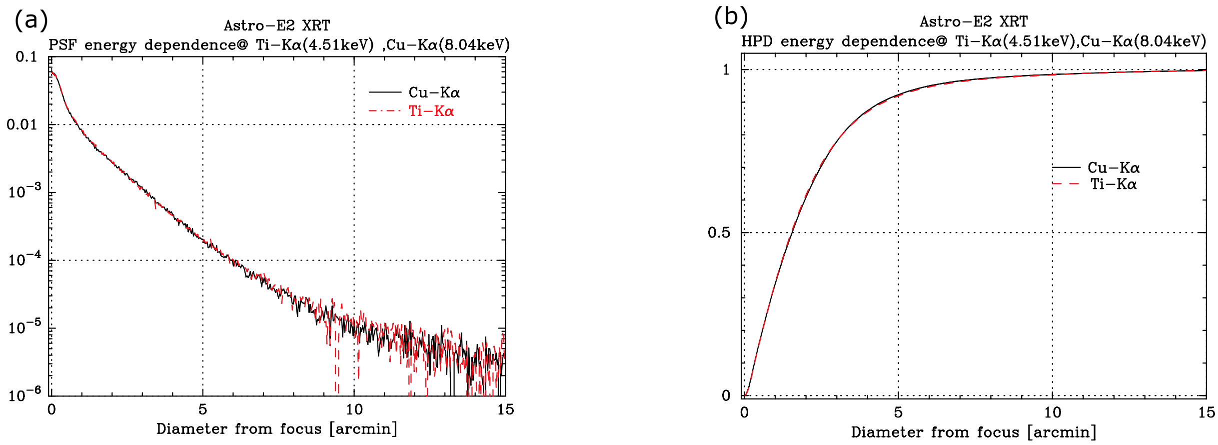

Figure 3.26: The PSF (panel a) and the fractional encircled energy (panel b) of XRT-I measured at Ti-K (4.5 keV) and Cu-K (8.0 keV) energies, presented as functions of angular distance from the optical axis.

3.3.3 X-Ray Spectrometer (XRS)

Developed by a collaboration mainly among Goddard Space Flight Center of NASA, the Institute of Space and Astronautical Science (ISAS), and Tokyo Metropolitan University, the XRS has an unprecedented energy resolution of 5–7 eV (FWHM) over a broad energy range of 0.3–12 keV. This is better by one to two orders of magnitude than those of other previous X-ray detectors, including X-ray CCD cameras in particular. The XRS works by measuring an increase of temperature caused by the absorption of an X-ray photon,

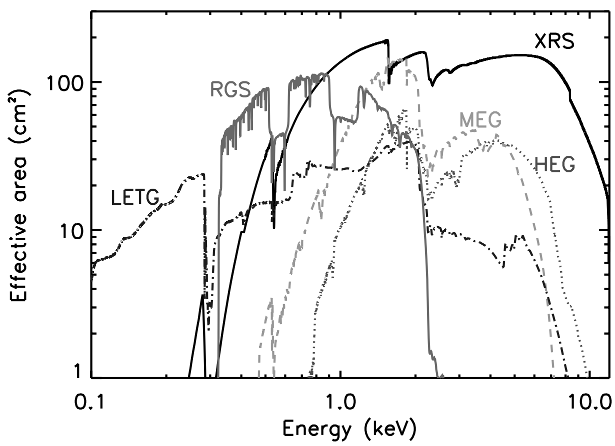

Figure 3.27: The effective area of the *Suzaku* XRS, compared with those of the *Chandra* gratings and the *XMM-Newton* RGS. Mirror responses are all inclusive.

and thus it is a "micro-calorimeter". This non-dispersive method enables us to achieve a superior energy resolution and a high efficiency even in the higher energy range, while gratings such as the *Chandra* HETG and LETG, or the *XMM* -Newton RGS, dose not have sufficient efficiency above 5 keV where Fe-K lines exist. The effective area of these instruments, all including respective mirror responses, are shown in figure 3.27.

In order to measure the extremely small temperature increases ($\sim$ 1.6 milli–Kelvin per 1 keV photon), the XRS sensors must be operated at a precisely regulated cryogenic temperature, typically 60 mK. The cryogenic dewar includes a solid neon tank (at $\sim$ 15 K) surrounding a helium tank ($\sim$ 4 K), and a mechanical cooler. Inside the helium tank, an adiabatic demagnetization refrigerator was placed, to cool the sensor head down to $\sim$ 60 mK. Unfortunately, the XRS stopped its function one month after the launch, due to loss of helium, which in turn is due probably to an unexpected increase in heat inflow into the dewar interior. However, it is the first X-ray micro-calorimeter carried onboard an orbiting observatory, and achieved in orbit an excellent energy resolution of 7 eV at $\sim$ 5.9 keV using a built-in calibration source. With this energy resolution, Kα_1 and Kα_2 lines (5.899 and 5.88 keV, respectively) were resolved clearly.

3.3.4 X-ray Imaging Spectrometer (XIS)

As described in §3.3.2, *Suzaku* has four XIS instruments (XIS-0, 1, 2, and 3), each fixed on the focal plane of the corresponding XRT-I. As shown schematically in figure 3.28, each XIS sensor consists of a single CCD chip which has an exposure area of 1024 $\times$ 1024 pixels, divided into four segments and a frame store area. In the same way as *Chandra* ACIS-S and *XMM-Newton* EPIC pn, the XIS employs two kinds of chips; front-illuminated (FI) and back illuminated (BI) ones: XIS-1 is a BI device, and the others are FI devices. The XIS is based on a collaboration among Osaka University, Kyoto University, ISAS, Massachusetts Institute of Technology (MIT), and several Japanese groups. The CCD chips have been fabricated by the Lincoln Laboratory of MIT. Basic parameters of the XIS-BI and XIS-FI detectors are summarized in table 3.7. Although the mirror focal length of *Suzaku* is about half that of *XMM-Newton*, the *Suzaku* XIS has a rather limited field of view because it is a single-chip detector unlike the EPIC cameras.

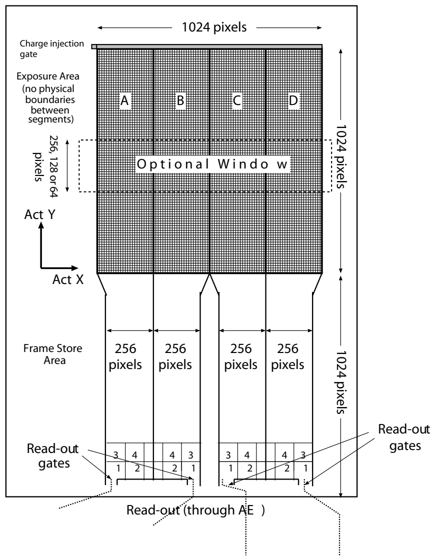

Figure 3.28: The structure of each CCD chip employed by the *Suzaku* XIS.

3.3.5 Performance of the XIS

As already described in §3.1.4 and §3.2.4, the XIS-BI CCD has a larger effective area than the FI CCDs especially in lower energies. Left panel of figure 3.29 shows effective areas of a single BI or FI chip. The effective area at 0.4 keV of the BI is larger by nearly an order of magnitude than that of the FI CCD. The effective area of a single XIS-FI camera, in contrast, becomes larger than that of BI above 4 keV. The XIS-FI cameras have an effective area of 147 cm^2 each at 8 keV. Since *Suzaku* has three identical XIS-FI cameras, XIS-0, XIS-2, and XIS-3, the total effective area obtained at 8 keV is $\sim$ 440 cm^2, which is comparable to that of the *XMM-Newton* EPIC-pn (figure 3.20).

One of the most remarkable features of the *Suzaku* XIS is its improved energy resolution, for example $\sim$ 60 eV at 1 keV and $\sim$ 130 eV at 6 keV. The XIS-BI achieves

Table 3.7: The characteristics of the *Suzaku* XIS.

Pixel grid	1024×1024 pixels
Pixel size	$24\ \mu m \times 24\ \mu m$
Field of view	18×18 arcmin
Effective area (@ 1.5 keV)	344 cm^2 (FI), 393 cm^2 (BI)
Effective area (@ 8 keV)	147 cm^2 (FI), 103 cm^2 (BI)
System noise	$<$ 2 electrons per pixel
Time resolution (Normal/ P-sum mode)	8 s / 7.8 ms
Depletion layer	50–70 μm
Dark current	$<$ 0.1 electrons s^{-1} pixel^{-1}
Readout noise	$<$ 3–4 electrons rms, typical

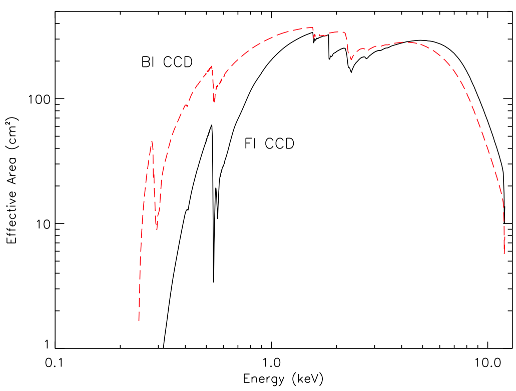

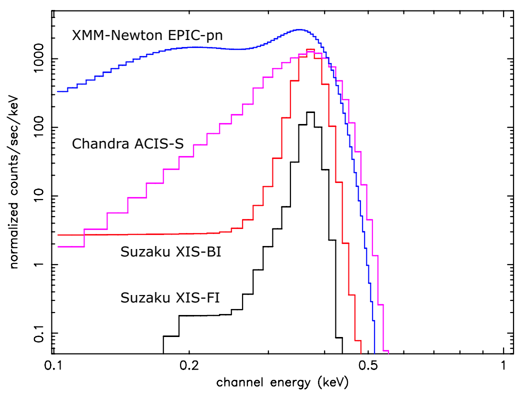

Figure 3.29: (left) The effective areas of the *Suzaku* XIS-BI (red dashed line) and FI (black solid line), including the mirror (XRT-I) response. (right) Line profiles at 0.37 keV of XIS-BI and FI responses predictions, compared with those of EPIC-pn and ACIS-S.

simultaneously the good energy resolution and the large effective area in lower energies. In the fabrication process, the backside of XIS-BI is first oxidized, then coated with a very thin (~ 1 nm) layer of silver, and the silver layer is capped with a 5 nm layer of hafnium oxide. According to Burke et al. (2004), the silver catalyzes dissociation of molecular oxygen, leaving negative charged oxygen atoms on the surface. These ions improve the collection of photo-electrons induced near the back surface. Thus, the XIS-BI has an improved charge collection efficiency for soft X-ray photons, which ensures its superior energy resolution to those of other CCD cameras employing BI devices, such as the *Chandra* ACIS-S and the *XMM-Newton* EPIC-pn. Right panel of figure 3.29 demonstrates this effect, by comparing predicted line profiles at 0.37 keV among various CCDs. The XIS has thus a reduced tail component and a clear line profiles, while EPIC-pn has a significant low-energy tail which makes line detections rather difficult.

Another advantage of the *Suzaku* XIS is low and stable background relative to other present missions, *Chandra* and *XMM-Newton*. Due to the low earth orbit, *Suzaku* does not suffer from background flares, which are bother to observations with *Chandra* and *XMM-Newton* (§3.1.4 and §3.2.4). Figure 3.30 gives the spectra of North Ecliptic Pole and night earth with XIS-1 and XIS-2, which employ BI and FI devices, respectively. The night earth spectrum represents the non-X-ray background (NXB), while that of North Ecliptic Pole consists of cosmic X-ray background and Galactic soft X-ray background, in addition to the NXB. The NXB spectra show instrumental lines from O, Al, Si, Ni, and Au. Mn-K lines are also seen, which comes from built-in calibration sources. In the North Ecliptic Pole spectra, emission lines from C VI (0.37 keV), O VII (0.56 keV), and O VIII (0.65 keV) are clearly detected. These are thought to comes from local hot bubbles surrounding the solar system, and this component is called "soft X-ray background".

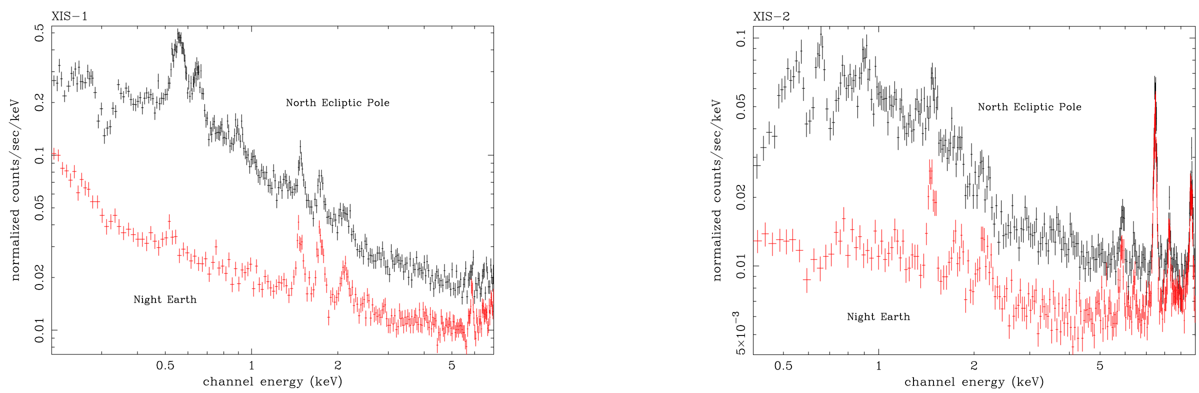

Figure 3.30: The spectra of North Ecliptic Pole (black) and night earth (red), obtained with XIS-1 (left) and XIS-2 (right).

3.3.6 Hard X-ray Detector (HXD)

The Hard X-ray Detector (HXD) is a non-imaging, collimated hard X-ray instrument sensitive in a higher energies of 10–600 keV. It has been developed by a collaboration among the University of Tokyo, ISAS, RIKEN, Hiroshima University, Saitama University, Aoyama Gakuin University, Kanazawa University, Osaka University, and Stanford University. As shown in figure 3.31, the HXD has 16 main detectors called "Well" units arranged in a 4×4 array, surrounded by 20 thick crystal scintillators for active shielding. As illustrated in the bottom panel of figure 3.31, each main unit consists of two types of detectors; a GSO (Gd_2SiO_5:Ce 0.5 % mol) / BGO ($Bi_4Ge_3O_{12}$) phoswich scintillation counter, and four 2 mm-thick silicon PIN diodes located inside the BGO shield. Softer photons (typically below $\sim$ 40 keV) are detected mainly by the PIN diodes, while harder photons penetrating the diodes are detected by the GSO. Figure 3.32 shows the effective area of the HXD.

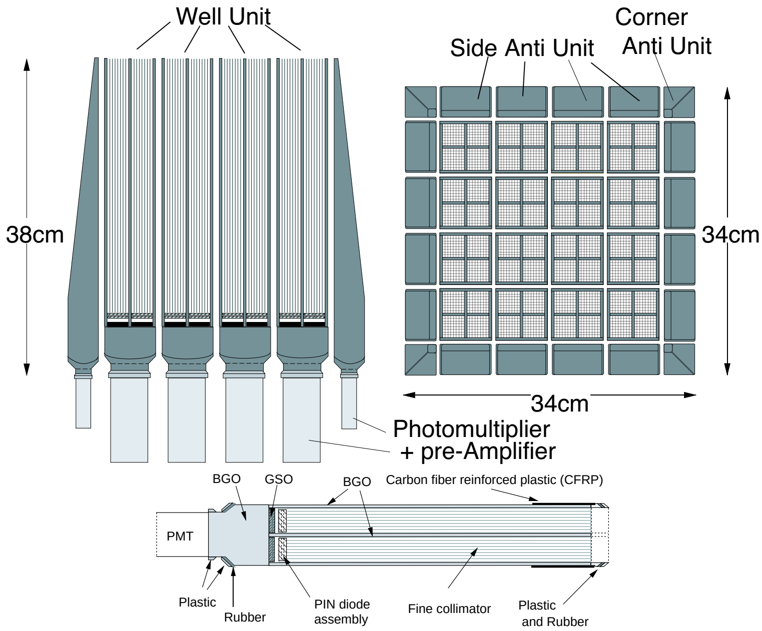

Figure 3.31: A schematic view of the *Suzaku* HXD. Top panel shows side view (left) and top view (right) of the HXD layout. Bottom panel shows a cross-sectional view of a single Well unit.

The most remarkable characteristic of the *Suzaku* HXD is its low background. In the hard X-ray and soft γ-ray band, observations suffer from high backgrounds due to charged particles, cosmic diffuse γ-rays, secondary γ-rays produced in the environment, activation caused by cosmic protons, and so on. In order to reduce the background, the HXD has

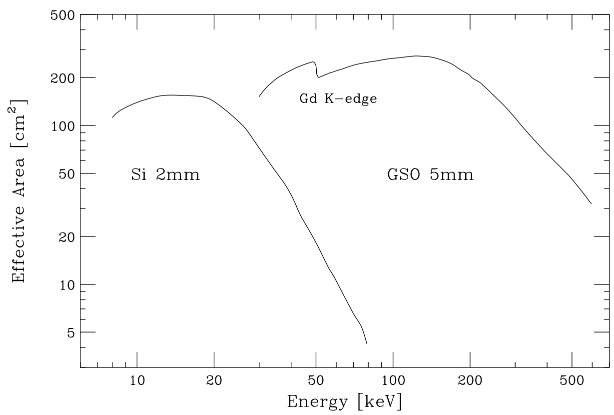

Figure 3.32: The effective area (for the silicon PIN and the GSO) of the *Suzaku* HXD.

employed the following eight techniques.

- A phoswich device using GSO and BGO scintillators, the latter having a high γ-ray stopping power while the former having a fast scintillation time constant.
- A tight collimation by "Well"-shaped active BGO shield, providing a $4° \times 4°$ field of view.
- Active shield of 20 thick BGO counters surrounding the Well units.
- Anti-coincidence among units configured in the form of 6×6 matrix.
- Fine collimator ($0°.5 \times 0°.5$), made of phosphorous bronze, suppressing cosmic diffuse γ-rays and source confusion in the PIN range.
- Analog signal processing of $\sim$ 100 channels in parallel, utilizing high-speed electronics with low-power consumption ($\sim$ 30 W).
- Flexible onboard event selection utilizing a Central Processing Unit (80C386).
- Detector materials thoroughly selected by emphasis on low radioactive contamination and expected low activation background.

Figure 3.33 shows the spectra of the Crab nebula obtained with the HXD-PIN and GSO, shown together with in-flight background spectra. The source signals are clearly detected up to 400 keV. In addition to intrinsic background components that were already present in laboratory environments, the in-flight backgrounds include additional of components due to activation by intense cosmic-ray protons, and possibly due to secondary

γ-rays produced in the spacecraft environment. The latter is strongly anti-correlated with geomagnetic cut-off rigidity.

Twenty thick BGO counters, surrounding the Well units as the active shield, is a large area array for γ-rays up to ~ 2 MeV. We call it as an array, "Wide-band All-sky Monitor (WAM)". WAM has already detected several gamma-ray bursts and solar flares during 5 months after the launch.

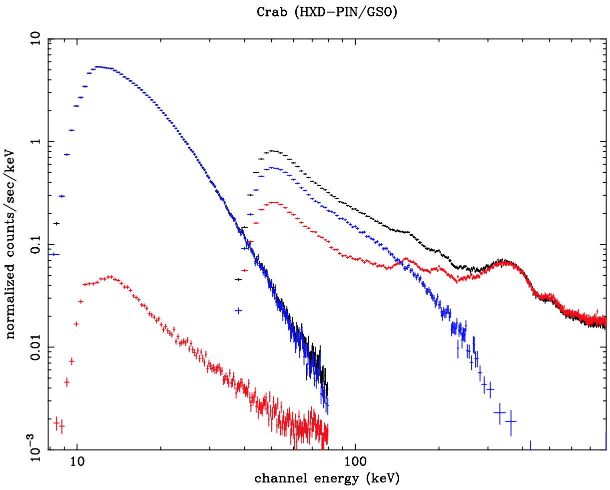

Figure 3.33: The hard X-ray and soft γ-ray spectra of the Crab nebula, obtained with the *Suzaku* HXD-PIN (< 90 keV) and GSO (> 40 keV). The observed spectra (black) are shown together with a background template obtained in orbit (red). The background subtracted spectra are represented by blue crosses.

Chapter 4

OBSERVATION

4.1 Chandra and XMM-Newton Observations

4.1.1 Sample definition

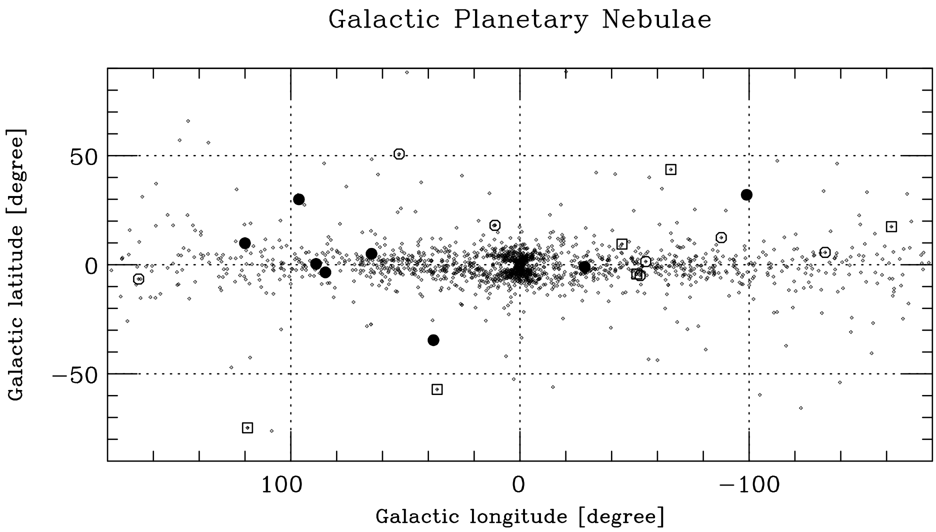

Figure 4.1: Galactic distribution of all the known planetary nebulae. Circles and squares show PNe observed by *Chandra* or *XMM-Newton*. Filled circles, open circles, and squares mean those with diffuse X-ray emission, only with point-like emission, and without detectable X-ray emission, respectively.

In order to analyze spectra of diffuse X-ray emission from planetary nebulae (PNe) for heavy element abundances, we need high-quality spectra. However, PNe compose a relatively new category of X-ray sources, and hence there have been rather few X-ray observations. Accordingly, we searched the entire *Chandra* and *XMM-Newton* data base

Table 4.1: X-ray observation log of planetary nebulae with *Chandra* and/or *XMM-Newton*.

Target name		Instrument	Date	Exposure* [ks]
AFGL 618	166.4-06.5	ACIS-S	2003/12/31	45.6
BD +30° 3639	064.7+05.0	ACIS-S	2000/03/21	19.0
BD +33° 2642	052.7+50.7	EPIC	2002/08/11	4.3
Hen 2-90	305.1+01.4	ACIS-S	2002/06/19	9.3
Hen 2-99	309.0-04.2	ACIS-S	2003/11/12	28.7
Hen 2-104	315.4+09.4	ACIS-S	2002/04/08	19.7
M 1-16	226.7+05.6	ACIS-S	2002/02/11	49.5
M 2-9	010.8+18.0	ACIS-S	2003/01/24	19.6
MyCn 18	307.5-04.9	ACIS-S	2002/12/31	39.5
Mz 3	331.7-01.0	ACIS-S	2002/10/23	40.8
NGC 40	120.0+09.8	ACIS-S	2004/06/13	19.9
NGC 246	118.8-74.7	ACIS-S	2002/10/22	40.4
NGC 2392	197.8+17.3	EPIC	2004/04/02	12.5
NGC 3132	272.1+12.3	ACIS-S	2004/08/08	24.0
NGC 3242	261.0+32.0	EPIC	2003/12/04	13.9
NGC 4361	294.1+43.6	ACIS-S	2003/02/17	29.4
NGC 6543	096.4+29.9	ACIS-S	2000/05/10	46.1
NGC 7009	037.7-34.5	EPIC	2001/04/30	31.6
NGC 7026	089.0+00.3	EPIC	2004/06/10	14.1
NGC 7027	084.9-03.4	ACIS-S	2000/06/01	18.2
NGC 7293	036.1-57.1	ACIS-S	1999/11/17	36.7
		ACIS-S	1999/11/18	11.0
		EPIC	2002/11/26	13.0

* The value of pn camera in the case of EPIC.

for PN observations, and found 21 objects which were observed with either satellite and already archived as of 2005 August. These 21 PNe thus constitute our basic sample. In the case of *Chandra* observations, we have not included the HRC or grating data, which cannot provide us with X-ray images and spectra simultaneously.

Table 4.1 gives observational log of our sample; among the 21 PNe, 15 were thus observed by only *Chandra*, and other 5 by only *XMM-Newton*. The remaining one, NGC 7293 was observed twice by *Chandra* and once by *XMM-Newton*. In figure 4.1, we show these 21 PNe on the Galactic coordinates, together with all the other known Galactic PNe (1700 in total).

4.1.2 Data reduction

An archival data file in X-ray astronomy is generally available in "FITS" format, which assembles all the usable photons (but including backgrounds) from that observation. Each photon is tagged with such pieces of information as the energy, position, arrival time, event grades, and so on. An X-ray image can be created by arranging these photons (usually those in a specified energy interval) over the sky plane. Similarly, an X-ray spectrum can be produced by sorting them (usually those in a specified spatial region) along the energy axis.

Before extracting images or spectra, however, we have to "screen" the events in each file. In the case of *Chandra*, we retrieved archival "Level 1" event files from *Chandra* X-ray Center. Filtering the events against "good time intervals (GTI)", excluding hot pixels and cosmic-ray afterglows, applying newest gain maps, and correcting pulse heights for charge transfer inefficiency, we created "Level 2" event files. Here, GTI means these time intervals when the observation is thought to have conducted normally, without hampered by predicted high background regions, earth occultation of the target, data gaps due to various operational reasons, and so on. The processing utilized the software package *Chandra* Interactive Analysis of Observations version 3.2.1, and the calibration data base CALDB 3.0.0, both released on 2005 February by *Chandra* X-ray Center.

In the case of *XMM-Newton*, we retrieved publicly available Observation Data Files from the Science Operation Centre. In these files, individual events are already re-formatted from telemetry format into the standard FITS format, but some quantities are yet to be calibrated. Utilizing the Science Analysis Software package of version 6.5.0 released on 2005 August by the operation center, we applied newest calibration files, screened the data in a similar way to *Chandra*, and created screened event files of each

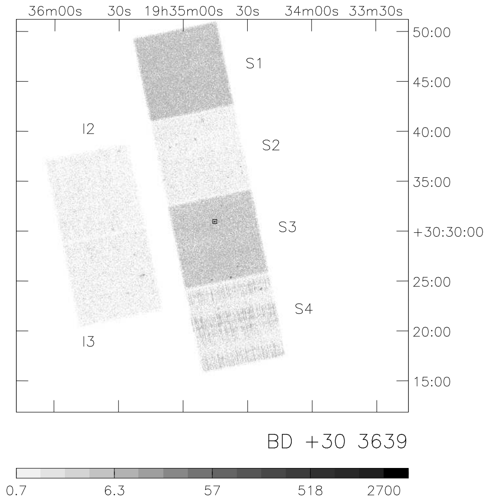

Figure 4.2: An unscreened X-ray image of BD +30° 3639 obtained with the *Chandra* ACIS-S. The target position is indicated by a very small box with the size of 25″ × 25″ superposed on S3 chip.

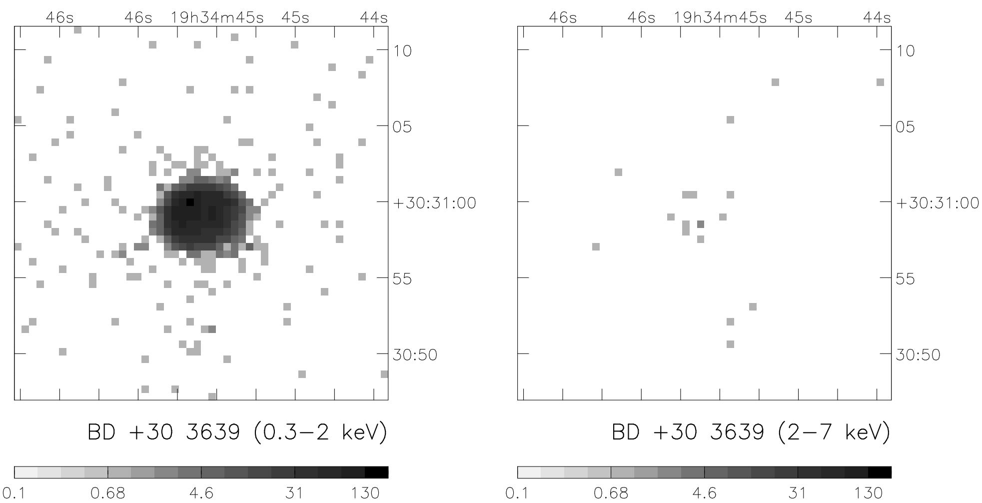

Figure 4.3: Enlarged and screened X-ray images of BD +30° 3639 in the soft band (left; 0.3–2 keV) and hard band (right; 2–7 keV). The image size corresponds to the box in figure 4.2.

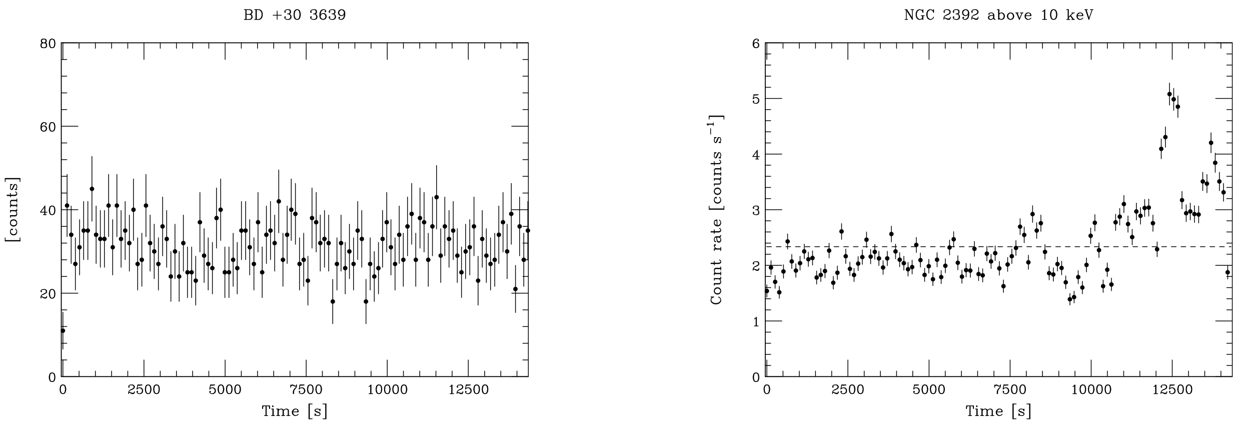

Figure 4.4: Light curves binned into 128 sec. (left) That of the *Chandra* observation of BD +30° 3639. It includes all events in the 25″ × 25″ region indicated in figure 4.2. (right) That of the *XMM-Newton* observation of NGC 2392. It consists of events above 10 keV, accumulated over the entire region of the EPIC-pn. The dashed line represents 3 σ deviations from the mean value.

instrument.

Figure 4.2 shows a raw image of BD +30° 3639 obtained with the *Chandra* ACIS-S. The target is placed nearly on the on-axis point. Enlarged images of the target region are presented in figure 4.3 with a pixel size of 0.″5, which corresponds to the physical 1-pixel size of the CCD chip (table 3.2). Hereafter in the present thesis, we present *Chandra* images with a pixel size of 0.″5.

In the case of *XMM-Newton*, the two EPIC-MOS cameras have a better angular resolution and a smaller pixel size (∼ 4″ FWHM and 1.″1, respectively) than those of EPIC-pn (§3.2.3). Therefore, we mainly utilize the EPIC-MOS data to analyze X-ray images, and present the images with a pixel size of 1.″1 However, the lower energy boundary of EPIC-MOS, ∼ 0.5 keV, is not low enough to efficiently collect soft X-rays from PNe which are concentrated in energies below ∼ 1 keV. Therefore we principally utilize EPIC-pn data for spectroscopy, even though those of EPIC-MOS1 and MOS2 are also available. Thus, the MOS and pn cameras are complementary to each other.

As shown in figure 4.4, a light curve can be also extracted from the screened event files. The light curves are necessary to eliminate bad data portion, because the background count rate of the *Chandra* ACIS and the *XMM-Newton* EPIC are both known to exhibit sudden increases caused by soft protons (§3.1.4 and §3.2.4), but these time periods are not yet excluded from the original GTI information provided by the spacecraft operation centers. As exemplified by figure 4.4, the *Chandra* observation of BD +30° 3639 was free from such flares, whereas the *XMM-Newton* data of NGC 2392 suffer from them. We excluded such flares from our analysis, by discarding time period when the count rates above 10 keV in a light curve deviate by more than 3 σ from the time average over no-flare period: in such higher energies, background events are dominant. We thus examined 128-sec bin light curves of all observations, and excluded the detected background flares from the analysis. Hereafter, we utilize the GTI information which has been revised in this way.

4.1.3 Target selection

As the first step of our scientific analysis, we examined each data set for signal detection in the following way. A 0.3–7 keV image of each observation was extracted from the screened event file prepared in the way as described in §4.1.2, and a "source region" centered on the target position was defined as a circle with the radius which is 50 % larger than that determined by optical or radio observations. In the cases of NGC 7293, NGC 246, and NGC 4361, the source-region radius was set to $5''$, since they have relatively large optical radii of $980''$, $245''$, and $63''$, respectively, and probably contain point-like sources. X-ray images of NGC 6543 and Mz 3 indicate that they have not only diffuse emission but also possibly point-like sources. In these two cases, we therefore employed a software known as "wavedetect", and determined the position, significance, and the angular extent of the point-like sources. These objects have an point source associated with the central star, while Mz 3 also has a point-like source distant from the center. The results were utilized to separately define two kinds of source regions for each object, one covering the point source and the other representing the diffuse emission.

Background regions were defined as circles or annuli near the source region, of which the total area is more than 2 times larger than that of the source region. Figure 4.5 gives an example of the region definition in a *Chandra* image of NGC 7027.

We counted the number of photons in the source and background regions, $N_{\rm src}$ and $N_{\rm bgd}$, respectively. The number of background counts was normalized as $N^*_{\rm bgd} = N_{\rm bgd}(A_{\rm src}/A_{\rm bgd})$, where $A_{\rm src}$ and $A_{\rm bgd}$ are areas of the source and background regions, respectively. The number of net count was then derived as $N_{\rm net} = N_{\rm src} - N^*_{\rm bgd}$. Statistical errors associated with each $N_{\rm net}$ was calculated as $[N_{\rm src} + (A_{\rm src}/A_{\rm bgd})^2 N_{\rm bgd}]^{1/2}$.

Table 4.2 summarizes these net counts, together with the statistical errors and consequent signal-to-noise ratios. There, three out of the 21 PNe, AFGL 618, M 1-16, and M 2-9, have no photons from the source region at all. Four PNe, BD +33° 2642, Hen 2-90,

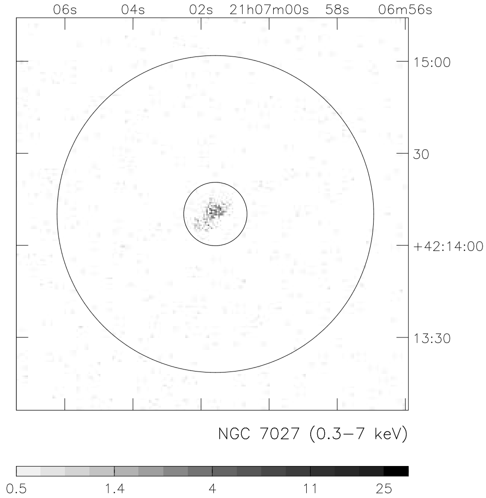

Figure 4.5: An X-ray image of NGC 7027 in 0.3–7 keV obtained with the *Chandra* ACIS-S. The source region is inside the inner circle with the radius of 10″.5, and the background region is defined as the annulus between the inner and outer (52″.5 radius) circles.

MyCn 18, and NGC 3132, have signal-to-noise ratios of less than 3 σ, so that we regard their X-ray emission as insignificant. In contrast, the remaining 14 PNe are concluded to exhibit significant X-ray emission. Figure 4.6 gives X-ray images of three representative objects; M 2-9 without detectable emission, NGC 7293 with a possibly point-like source, and NGC 6543 with diffuse X-ray emission and a possibly point-like source. The X-ray emission center in most cases coincides with the central stars, except two, Hen 2-99 and a point-like source in Mz 3, which are offset from the central star by $\sim 7.''5$ and $\sim 17.''5$, respectively.

Count rates of the 14 PNe are listed in the sixth column of table 4.2 with statistical errors. Most of them are weak X-ray sources with count rates less than 0.1 counts s^{-1} except for BD +30° 3639. For example, although NGC 4361 has a relatively long exposure of 28.9 ks, its count rate is less than 0.002 counts sec^{-1} and hence total net count is only $\sim$ 50. Since statistically high-quality spectra are needed for spectroscopy, we exclude from subsequent analysis 6 PNe (Hen 2-99, Hen 2-104, Mz 3, NGC 40, NGC 4361, and NGC 7026) of which the net counts are less than 100. We are thus left with 8 PNe, which we call our "final sample". These objects are summarized in table 4.3. In particular, BD +30° 3639 is the brightest target among them, and plays the most important role in the present thesis.

The next step is to examine whether the X-ray emission from the 8 objects is extended or not. The emission from such objects as BD +30° 3639 and NGC 7027, shown in figure

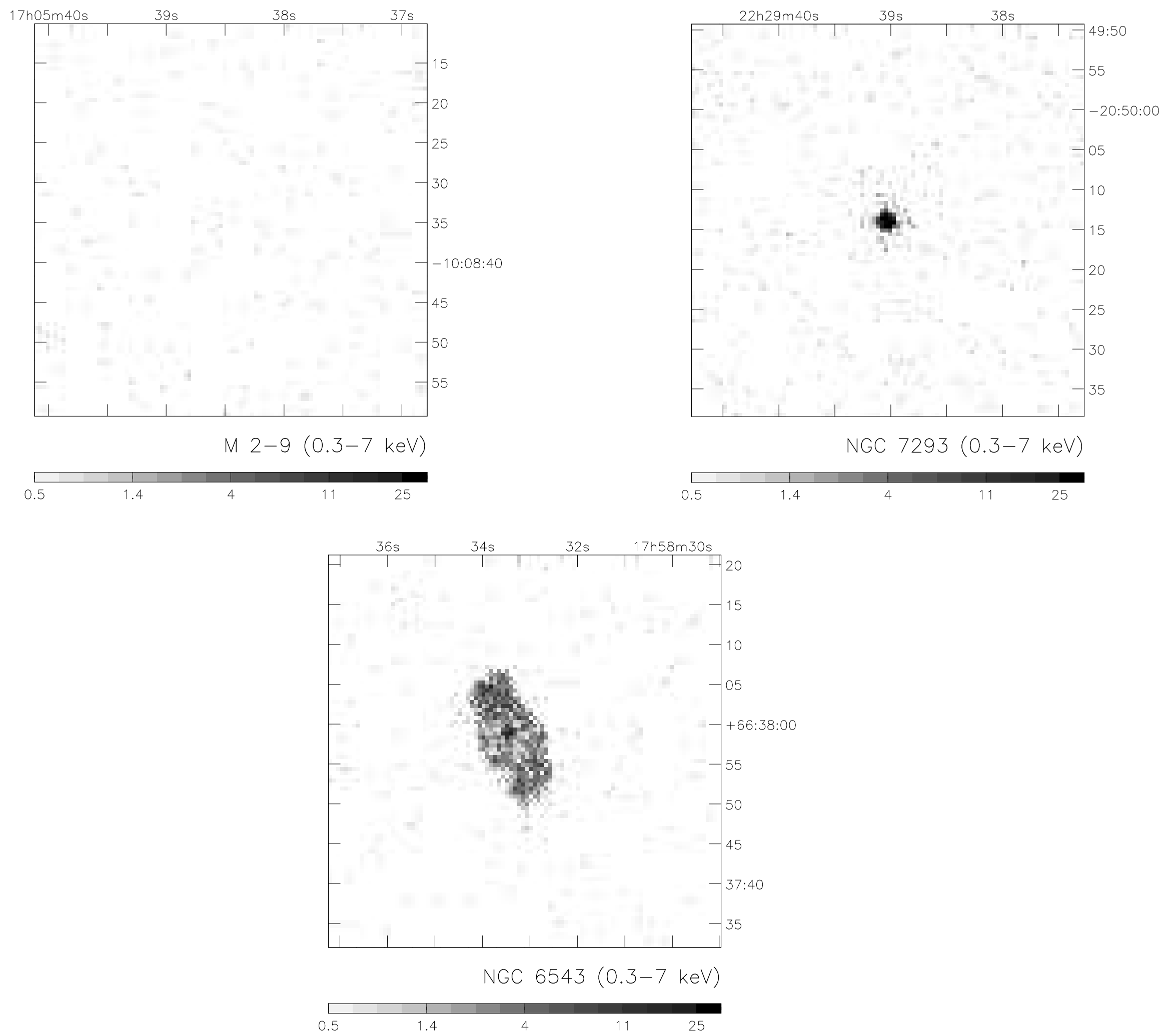

Figure 4.6: 0.3–7 keV X-ray images of M 2-9, NGC 7293, and NGC 6543, obtained with the *Chandra* ACIS-S.

Table 4.2: X-ray counts from the planetary nebulae in the sample defined in Table 4.1

Target name	Inst.	Exposure[a,b] [ks]	S/N[a,c] [σ]	Net counts[a,c,d]	Count rate[a,c,d] [counts s^{-1}]	Note [e]
AFGL 618	ACIS-S	35.9 (45.6)	–	0±3.6		
BD +30° 3639	ACIS-S	19.0	67	4490±67	0.24±0.035	d
BD +33° 2642	EPIC	4.3	2.1	12 ± 5.8	$< 2.8 \times 10^{-3}$	
Hen 2-90	ACIS-S	9.3	0.75	1.5 ± 2.0	$< 0.16 \times 10^{-3}$	
Hen 2-99	ACIS-S	26.5 (28.7)	4.8	40±8.5	$(1.5 \pm 0.3) \times 10^{-3}$	p[f]
Hen 2-104	ACIS-S	19.2 (19.7)	6.5	45±6.9	$(2.3 \pm 0.36) \times 10^{-3}$	p
M 1-16	ACIS-S	49.3 (49.5)	–	0 ± 0.2		
M 2-9	ACIS-S	18.3 (19.6)	–	0 ± 5.4		
MyCn 18	ACIS-S	39.5	2.0	5.6 ± 2.8	$< 0.14 \times 10^{-3}$	
Mz 3	ACIS-S	40.5 (40.8)	5.4	74±14	$(1.8 \pm 0.35) \times 10^{-3}$	d
			3.9	17±4.4	$(0.42 \pm 0.11) \times 10^{-3}$	p
			6.8	47±6.9	$(1.2 \pm 0.17) \times 10^{-3}$	p[f]
NGC 40	ACIS-S	19.9	4.5	65 ± 15	$(3.3 \pm 0.75) \times 10^{-3}$	d
NGC 246	ACIS-S	22.4 (40.4)	21	457±21	$(2.0 \pm 0.096) \times 10^{-2}$	p
NGC 2392	EPIC	8.1 (12.5)	17	423±25	$(5.2 \pm 0.31) \times 10^{-2}$	
NGC 3132	ACIS-S	22.1 (24.0)	0.94	8 ± 8.8	$< 0.36 \times 10^{-3}$	
NGC 3242	EPIC	13.6 (13.9)	21	547±28	$(4.0 \pm 0.20) \times 10^{-2}$	
NGC 4361	ACIS-S	28.9 (29.4)	6.8	49±7.3	$(1.7 \pm 0.25) \times 10^{-3}$	p
NGC 6543	ACIS-S	46.1	37	1383±38	$(3.0 \pm 0.082) \times 10^{-2}$	d
			12	145±12	$(3.2 \pm 0.26) \times 10^{-3}$	p
NGC 7009	EPIC	24.2 (31.6)	34	1493±44	$(6.2 \pm 0.18) \times 10^{-2}$	d
NGC 7026	EPIC	13.2 (14.1)	5.0	80±17	$(6.1 \pm 1.3) \times 10^{-3}$	d
NGC 7027	ACIS-S	18.2	16	280±17	$(1.5 \pm 0.094) \times 10^{-2}$	d
NGC 7293	ACIS-S	34.7 (36.7)	38	1471 ± 38	$(4.2 \pm 0.11) \times 10^{-2}$	p
	ACIS-S	9.8 (11.0)	19	351±19	$(3.6 \pm 0.19) \times 10^{-2}$	p
	EPIC	11.2 (13.0)	24	638±27	$(5.7 \pm 0.24) \times 10^{-2}$	p

[a] The value of pn camera in the case of EPIC.

[b] After eliminating “flares” with the primary value in parenthesis.

[c] Errors refer to statistical 1σ limits.

[d] In the energy ranges from 0.3 to 7 keV.

[e] Morphology suggested by X-ray images. (d) Diffuse emission, (p) A point-like source.

[f] Not associated with a central star.

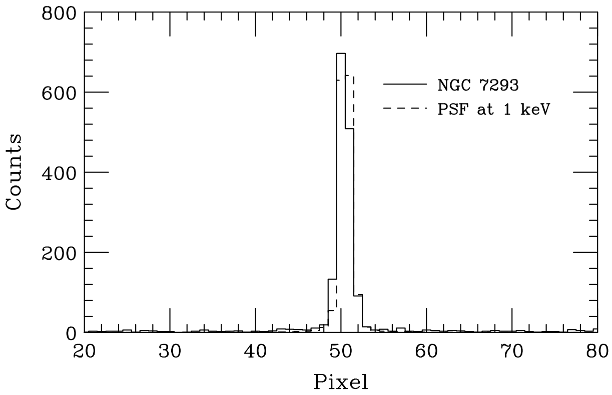

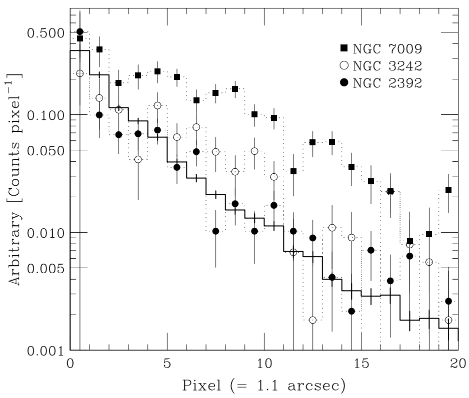

Figure 4.7: (left) The background-inclusive 0.3–7 keV profile of NGC 7293 projected on the vertical axis in figure 4.6. Simulated PSF at 1 keV is superposed with a dashed line. (right) The radial count-rate profiles of 3 PNe obtained with the EPIC-MOS1, in the 0.3–7 keV range after background subtraction. Filled squares, filled circles, and open circles indicate NGC 7009, NGC 2392, and NGC 3242, respectively. A solid line gives a radial profile of PHL 1092 as an example of a point source.

4.2, 4.5 respectively, are obviously extended. As described above, NGC 6543 has the extended emission shown in its raw X-ray image 4.6, and has a possibly point-like source in the central. However, there are less obvious cases, including NGC 7293 shown in figure 4.6. Accordingly, we produced in figure 4.7 (left) its projected brightness profile, and compared it with the calculated PSF explained in §3.1.2 and §3.2.2. In this particular case, the two profiles agree within errors, indicating that the emission is point-like even within the superb angular resolution of *Chandra*. The emission from NGC 246 was also confirmed to be point-like in the same way as NGC 7293.

The EPIC data have to be examined more carefully for the source angular extent, because of its moderate angular resolution, $\sim 4''$ and $\sim 12.''5$ for the EPIC-MOS and EPIC-pn, respectively. Accordingly, we produced the radial profiles of NGC 2392, NGC 3242, and NGC 7009 in figure 4.7 (right) and compared them with that of an active galactic nucleus PHL 1092 representing a point source. The emission from NGC 7009 is obviously extended, while the radial profile of NGC 2392 agrees with that of the point source within errors. Although NGC 3242 is a marginal case, its emission is concluded to be extended, because its radial profile deviates outward significantly from that of PHL 1092.

In this way, we have confirmed that the X-ray emission from three out of the 8 PNe is consistent with being point-like. The other five emit diffuse X-rays, among only NGC 6543 has mixed morphology consisting of a point-like source and the diffuse component.

These results on the X-ray morphology is summarized in table 4.3.

Table 4.3: X-ray morphology of our final sample.

Target name	Inst.	Exposure* [ks]	Count rate [counts s^{-1}]	X-ray morphology
BD +30° 3639	ACIS-S	35.9	0.24 ± 0.035	Diffuse
NGC 246	ACIS-S	22.4	$(2.0 \pm 0.096) \times 10^{-2}$	Point-like
NGC 2392	EPIC	8.1	$(5.2 \pm 0.31) \times 10^{-2}$	Point-like
NGC 3242	EPIC	13.6	$(4.0 \pm 0.20) \times 10^{-2}$	Diffuse
NGC 6543	ACIS-S	46.1	$(3.0 \pm 0.082) \times 10^{-2}$	Diffuse
			$(3.2 \pm 0.026) \times 10^{-3}$	Point-like†
NGC 7009	EPIC	24.2	$(6.2 \pm 0.18) \times 10^{-2}$	Diffuse
NGC 7027	EPIC	18.2	$(1.5 \pm 0.094) \times 10^{-2}$	Diffuse
NGC 7293	ACIS-S	34.7	$(4.2 \pm 0.11) \times 10^{-2}$	Point-like
	ACIS-S	9.8	$(3.6 \pm 0.19) \times 10^{-2}$	
	EPIC	11.2	$(5.7 \pm 0.24) \times 10^{-2}$	

* After eliminating "flares"

† Detailed in §6.1

4.2 Suzaku Observation of BD +30° 3639

4.2.1 Performance verification observations

In an early phase after the launch of a satellite, calibration observations using well understood objects are of the most urgent importance. Subsequent series of observations are usually devoted to the verification and demonstration of the anticipated performance of the satellite, and are called "performance verification" observations. In the case of *Suzaku*, the performance verification observations were initially scheduled focusing particularly on the XRS, because its superb capability is one of the most outstanding features of *Suzaku*, and because it has a finite cryogenic lifetime. However, the XRS has been lost unfortunately (§3.3.3). As a result, the performance verification targets were re-selected by the Science Working Group of *Suzaku* in 2005 early September.

As described in §3.3.5, the *Suzaku* XIS-BI has a superior energy resolution (though not as good as the XRS) and a high quantum efficiency in soft energies below 0.5 keV. Of course, the gratings onboard *Chandra* and *XMM-Newton* are also capable of resolving lines below 0.5 keV, but they require a long exposure due to their dispersive function. For the same reason, the gratings cannot retain their high performance on an extended source. It means that the XIS-BI is much more advantageous in emission-line spectroscopy of faint and/or extended soft-X-ray sources than any previous X-ray missions.

A planetary nebula is very faint and soft in X-rays. As described later in §4.3, previous X-ray observations of PNe suggest enhanced abundances of particular elements, such as C, N, and Ne. However, the suggestion is not conclusive, since it has been very difficult to resolve K-lines from ionized C, N, and O which appear in the energy range of 0.3–0.7 keV. The XIS-BI onboard *Suzaku* for the first time enables us to resolve such CNO lines, especially He-like C-K line at 0.37 keV which plays a vital role in the determination of abundances. A *Suzaku* observation of a planetary nebula is expected to serve as a nice demonstration of the XIS-BI performance in these low energies. At the same time, it will provide us with scientifically very important results. We have therefore proposed a 40 ks observation of BD +30° 3639, the brightest X-ray emitting PN (§4.1.3), and the proposal has been accepted by the *Suzaku* Science Working Group.

4.2.2 The observation

As a part of the PV-observation program, *Suzaku* observed BD +30° 3639 for about 40 ks on 2005 September 21, about 70 days after the launch. Figure 4.8 (left) shows the XIS field of view actually employed in this pointing observation. As presented in figure 4.8 (right), this PN happens to lie on the sky plane inside a large supernova remnant, G65.2+5.7, which is nearly 4° diameter.

Figure 4.9 shows a kind of diagram, called “DP10”, utilized as a support to the *Suzaku* operation. First devised during the *Hakucho* mission (1979–1985) and then improved continually, it summarizes daily operational conditions of a near-earth satellite. Each row of the diagram represents a single 100 minutes orbit of *Suzaku* with the time running from left to right. Various pieces of information indicated on the diagram can be classified into three categories; those determined by the spacecraft orbit (e.g., satellite day/night, visible contacts from the tracking station, the South Atlantic Anomaly, etc.), those depending also on the target position (e.g., the periods of earth occultation), and those representing satellite operations such as the timing programmed commands (not shown in this case).

With the DP10 diagram, we roughly know where to take the data, and how much exposure can be achieved. For example, major parts of the instruments are turned off

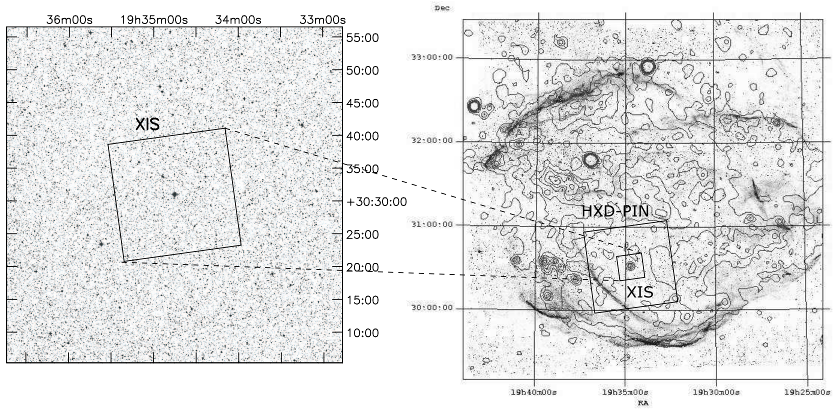

Figure 4.8: The fields of view (FOV) of the *Suzaku* XIS and HXD in the BD+30° 3639 observation. (left) The XIS FOV is shown as a box superposed on a gray scale optical image taken by Digitized Sky Survey. BD +30° 3639 is at the center of this image. (right) A gray-scale [OIII] map of SNR G65.2+5.7 is shown, together with X-ray emission contours obtained with *ROSAT* (Mavromatakis et al. 2002). The smaller square indicates the XIS FOV, while the larger one that of the HXD-PIN.

Table 4.4: *Suzaku* observation of BD +30° 3639.

Data rate	Start time (UT)		Stop time (UT)		XIS mode
Medium	2005/09/21	08:48		10:43	3×3
High		10:43		17:42	5×5
Medium		17:42	09/22	05:55	3×3

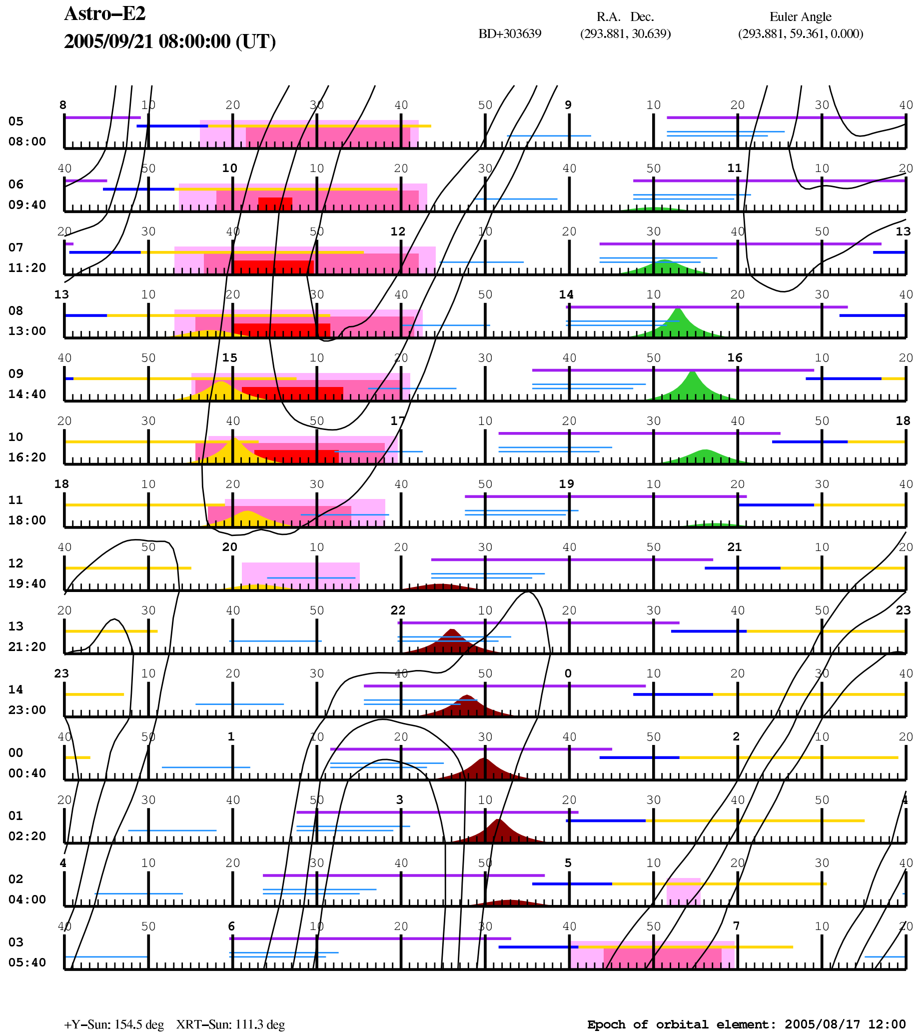

Figure 4.9: A DP10 diagram of the *Suzaku* observation of BD $+30°$ 3639. Fourteen out of the daily 15 orbits are shown in this diagram. Black contours mean geomagnetic cutoff rigidity in levels of 4, 6, and 8 GeV/c. Red and pink regions indicate the South Atlantic Anomaly. Five green hills represent the duration and elevation angle of the satellite view from the downlink station, Uchinoura Space Center. Horizontal purple lines, each lasting for $\sim$ 32 min, show spacecraft nights. Over the thick blue and yellow lines, the target is occulted (and hence unobservable) by dark and sunlit earth, respectively.

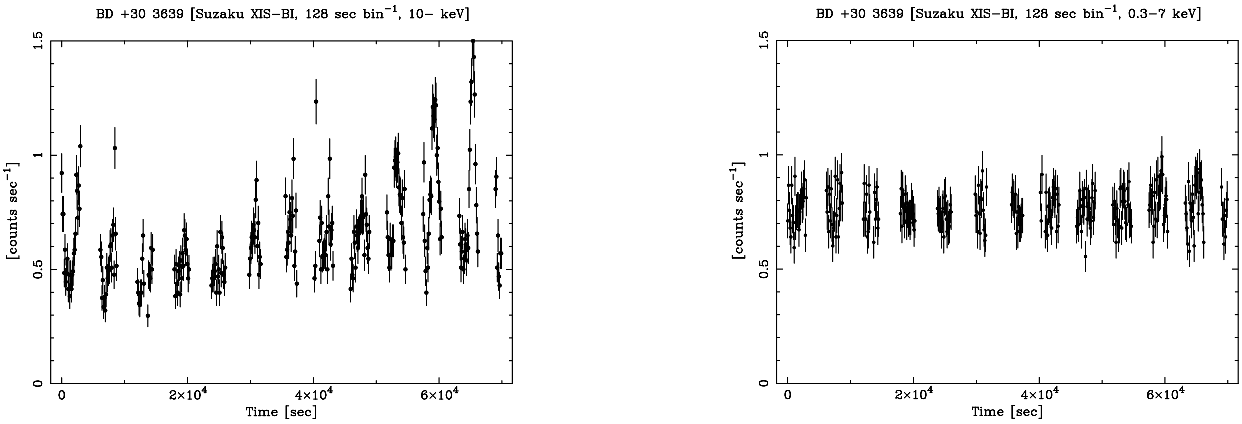

Figure 4.10: The light curves of BD +30° 3639 with the *Suzaku* XIS-1. These are binned into 128 sec. Left panel shows count rates in the range above 10 keV, while right in 0.3–7 keV.

during passages through the South Atlantic Anomaly where proton flux is higher than in other regions by $\sim$ 3 orders of magnitude. Periods of low cutoff rigidity are also unfavorable due to high background caused by enhanced flux of charged particles, and hence the data acquisition in such regions is not recommended. In the particular case of BD +30° 3639, earth occultations partially overlapped with the regions of low cutoff rigidity, and therefore the observation was moderately time-efficient.

The actual data acquisition started at 08:48 UT on 2005 September 21 (table 4.4), after *Suzaku* completed a $\sim$ 50° attitude maneuvering from the preceding target. This start corresponding to about the middle of the top row of DP10 in figure 4.9. Then, the observation ended at 05:55 UT of the next day (on the bottom row of DP10). Although the total elapsed time is thus 21.12 hours or 76 ks, the actually achieved GTI (good time interval) is $\sim$ 40 ks as initially planned, due to earth occultations and the South Atlantic Anomalies. This exemplifies a typical efficiency of *Suzaku* observations.

Table 4.4 summarizes the operation of the XIS and HXD, actually employed in the observation of BD +30° 3639. The XIS operation mode was selected considering the signal count rate, as well as the date recording rates to maximize the exposure in GTIs (§4.1.2)

4.2.3 XIS data

We retrieved a set of screened event files which are exclusive to members of the *Suzaku* Science Working Group. The XIS events are already clear of earth occultations and passages through the South Atlantic Anomaly, but not yet screened against other high background regions. Accordingly, we produced XIS-1 light curves in two energy bands. As shown in figure 4.10 (left), the count rate in the range above 10 keV. was observed to vary significantly. However, the 0.3–7 keV count rate (figure 4.10 right), which is relevant to our study, is quite constant within Poisson statistics. Therefore, we have decided to utilize most of the data without further screening. The obtained net exposure is 34.3 ks. For reference, the count-rate variation in the higher energy band is anti-correlated with geomagnetic cutoff rigidity, and can be easily predicted unlike "flares" of *Chandra* and *XMM-Newton* which suddenly occur.

Figure 4.11 shows a raw X-ray image of BD +30° 3639 obtained with XIS-1 which employs the BI chip (§3.3.4). Thus, the signal X-rays from the PN have been successfully detected. As shown there, we defined the source region to be a $2.'5$ radius circle centered on the source position, which includes 90% of the signal events. The background region was defined as an annulus with an outer radius of $5'$ around the source region. The 0.3–7 keV net counts, calculated in the same way as in §4.1.3, is 1116 ± 46, 3039 ± 74, 1174 ± 47, and 1012 ± 44, for XIS-0, 1, 2, and 3, respectively. The count of XIS-1 is higher nearly by a factor of three than those of the others, because it uses the BI chip, and hence has a much higher low-energy efficiency than the other three cameras that use FI chips.

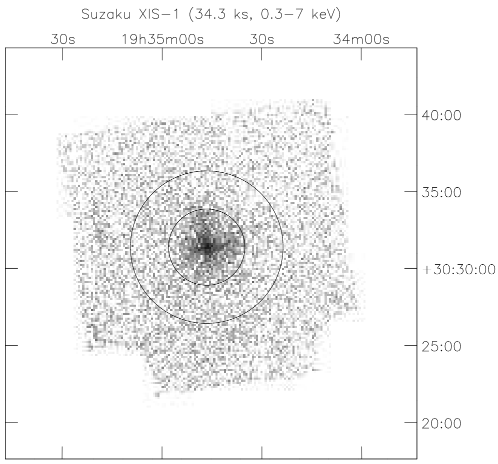

Figure 4.11: An X-ray image of BD +30° 3639 obtained in the 0.3–7 keV range with the *Suzaku* XIS-1. Two bottom corner regions are masked to eliminate Mn-Kα photons from the built-in ^{55}Fe calibration source. The employed source region is indicated with the inner circle with the radius of $2.'5$, and the background region is defined as the annulus between inner and outer ($5'$) circles.

4.2.4 HXD data

The *Suzaku* HXD simultaneously observed BD +30° 3639. It has not been expected to detect signals from the PN, since its observable energy range is above 10 keV where the PN emission is insignificant. Figure 4.12 shows screened spectra obtained with the HXD-PIN, in comparison with a background template obtained in orbit. To our surprise, the on-source spectrum exhibit a slight but apparently significant excess above the background. By fitting the background-subtracted HXD-PIN spectrum with a power-law, we obtained a photon index of ~ 1. This hard X-ray signal is most likely from the SNR, G65.3+5.7, surrounding the PN (figure 4.8), although its significance must be carefully examined against the HXD background reproducibility. This is beyond the scope of the present thesis.

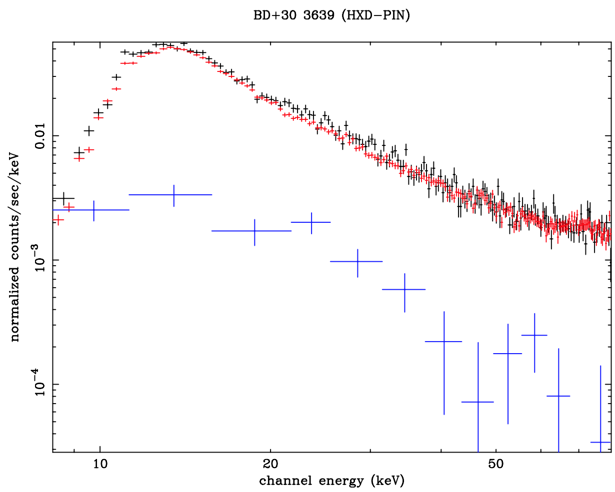

Figure 4.12: The *Suzaku* HXD-PIN spectrum of the BD +30° 3639 observation (black), shown together with a background template obtained in orbit (red). The background-subtracted spectrum is represented by blue crosses.

4.3 Notes on Individual Targets

In §4.1.3, we have selected 8 PNe for our final sample (table 4.3) to be studied in the present thesis. We summarize their basic parameters in table 4.5, their optical images in figure 4.13 and 4.14, and describe below their properties.

Table 4.5: Summary of basic parameters of the PNe in our final sample.

Target name	$v_{\rm exp}$ [km s^{-1}]	v_∞ [km s^{-1}]*	Distance [kpc]	Spectral type †	Ref.
BD +30° 3639	22 ± 4	790 ± 50	1.3 ± 0.2	WC9	a
NGC 246	85	–	$0.495^{+0.145}_{-0.100}$	O VII	i, j
NGC 2392	30 ± 10	~ 400	1.25	O7f	b, c, d
NGC 3242	26 ± 4	2200	0.55 ± 0.23	sdO	a, e, m
NGC 6543	16.4 ± 0.16	1600 ± 100	1.55 ± 0.44	Of/WR	a, f
NGC 7009	114 ± 32	2800	0.86 ± 0.34	O	g, h
NGC 7027	17.5 ± 1.5	–	0.68 ± 0.17		a
NGC 7293	40	–	0.213	hgO(H)	k, l, n

(a) Mellema (2004), (b) Hajian et al. (1995), (c) Pauldrach et al. (2003)
(d) Pottasch (1978), (e)Hamann et al. (1984), (f) de Koter et al. (1996)
(g) Cerruti-Sola and Perinotto (1989), (h) Fernández et al. (2004)
(i) Bond and Ciardullo (1999), (j) Szentgyorgyi et al. (2003), (k) O'Dell et al. (2004)
(l) Harris et al. (1997), (m) Balick et al. (1998), (n) Mendez (1991)

* Terminal velocity of stellar wind from a central star.

† Spectral type of a central star.

(a) BD +30 ° 3639

(b) NGC 246

(c) NGC 2392

(d) NGC 3242

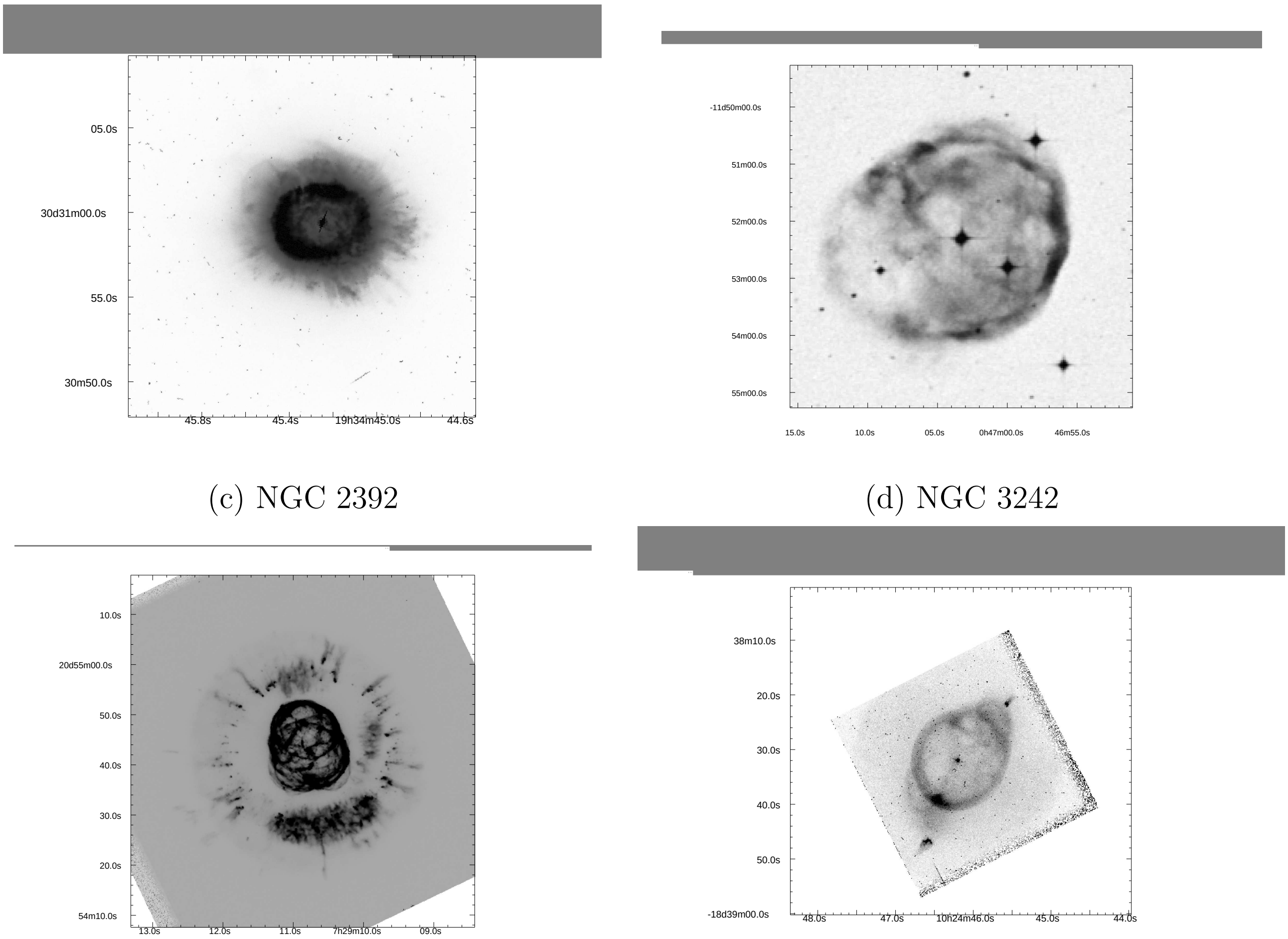

Figure 4.13: Optical images of the 4 PNe in our final sample. (b) is taken by Digitized Sky Survey, while the others are obtained with the *HST* WFPC2.

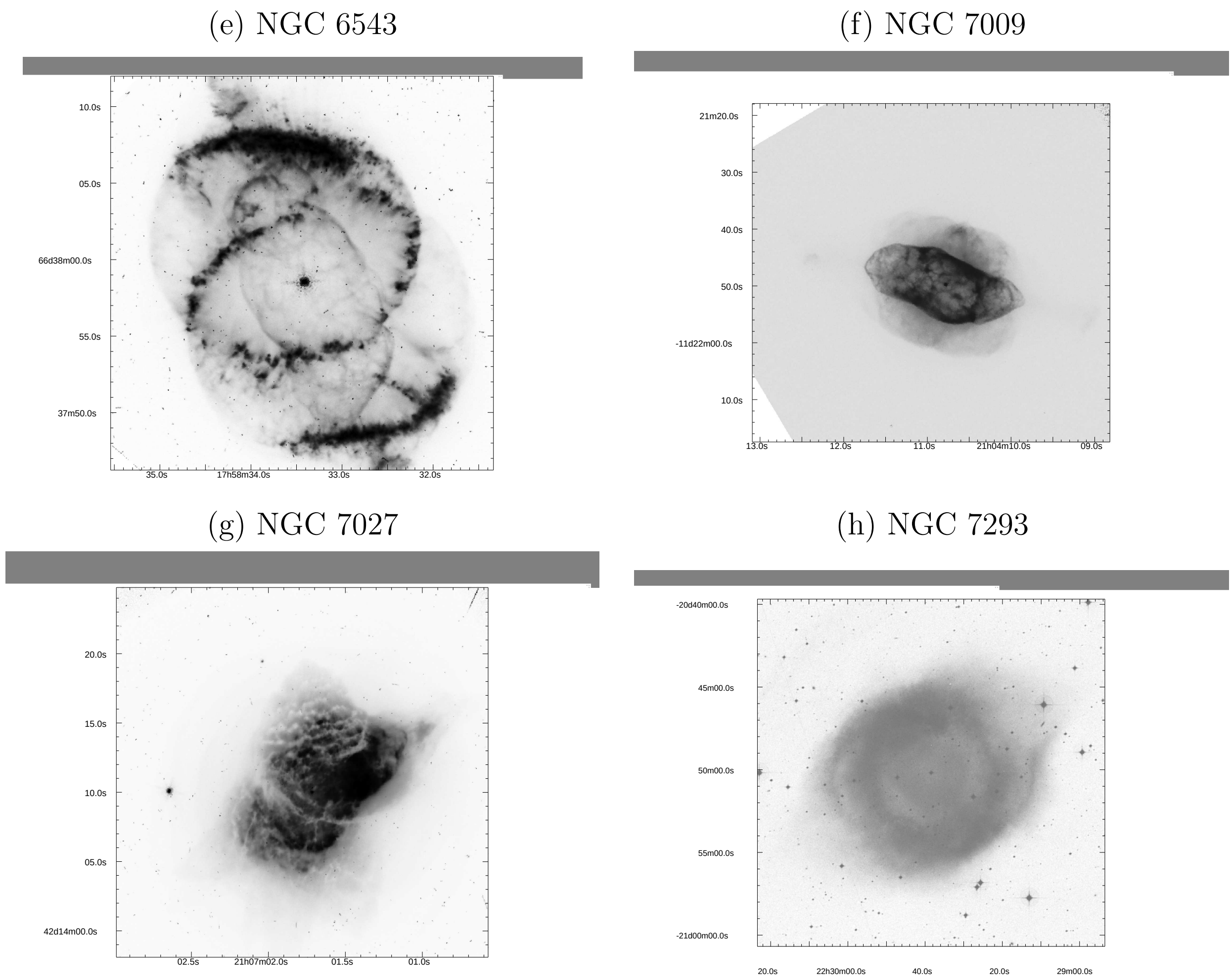

Figure 4.14: Optical images of the 4 PNe in our final sample. (h) is taken by Digitized Sky Survey, while the others are obtained with the *HST* WFPC2.

4.3.1 BD +30° 3639

BD +30° 3639 is a well-studied planetary nebula, and its central star is of spectral type [WC9], meaning that it is carbon-rich and hydrogen-deficient. A P-Cygni profile of the C III 2297 Å line, observed with the *International Ultraviolet Explorer* (*IUE*), yields a terminal velocity of 790 ± 50 km s^{-1} for the mass outflow from the central star (Pwa et al. 1986). UV and Optical spectra indicate that the nebular shell is in low ionization stages, and abundances of C, N, O, and other elements roughly follows the solar ratios (Pwa et al. 1986; Aller and Hyung 1995). In contrast, a recent analysis of the infrared spectra, obtained with the *Infrared Space Observatory* (*ISO*), indicates that abundances of C and Ne are about twice solar in relative number to H (Bernard-Salas et al. 2003).

As shown in figure 4.15, its nebular shell appears in radio continuum as a clear ring-like HII region (Masson 1989). A high resolution CO line mapping revealed a pair of high-velocity molecular knots, which are located symmetrically about the central star and have velocities of $\sim$ 50 km s^{-1} (Bachiller et al. 2000). Near-infrared mapping of fluorescence from H_2 revealed a pair of shell-like morphology (Shupe et al. 1998), and 21 cm line observations detected also neutral hydrogen in absorption and emission (Taylor et al. 1990).

The infrared spectrum of BD +30° 3639 obtained with *ISO* exhibits a remarkable emission feature at 3.3 μm, and images in this band show a ring around the central star which correlates closely with the spatially resolved HII region (Bernard et al. 1994). This feature is attributed to infrared fluorescence from Polycyclic Aromatic Hydrocarbon (PAH) molecules excited by UV photons from the central star, although alternative explanations are not completely excluded. The 3.3 μm feature, therefore, is thought to indicate the C-rich nature. Although the formation process of PAH is not well understood, these molecules could be produced generally in the dense material around C-rich red giant mass-losing stars. In the same infrared spectra obtained by *ISO*, there are also solid state features indicating O-rich nature (Waters et al. 1998). Waters et al. (1998) concluded that the central star experienced strong mass loss as an O-rich star at the end of its AGB stage, immediately followed by a change to C-rich chemistry.

X-rays from BD +30° 3639 were detected by *ROSAT* for the first time (Kreysing et al. 1992), and the emission was suggested to be extended (Leahy et al. 2000). The most remarkable feature was found in the *ASCA* spectrum as shown in figure 4.16 (left), that is, a strongly enhanced He-like Ne emission at 0.9 keV (Arnaud et al. 1996). They reported a temperature of 3×10^6 K and the Ne abundance of several times solar, although

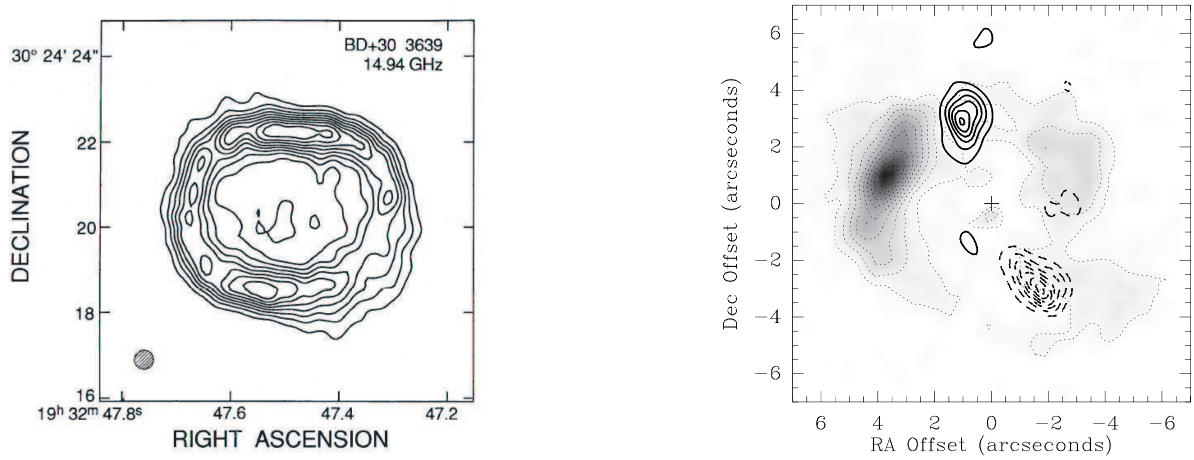

Figure 4.15: Radio maps of BD +30° 3639. (left) A VLA map at 14.94 GHz (Masson 1989). (right) Surface brightness of CO 2–1 line emission in thick lines, overlaid on that of H_2 1–0 S(1) emission in gray scale (Bachiller et al. 2000).

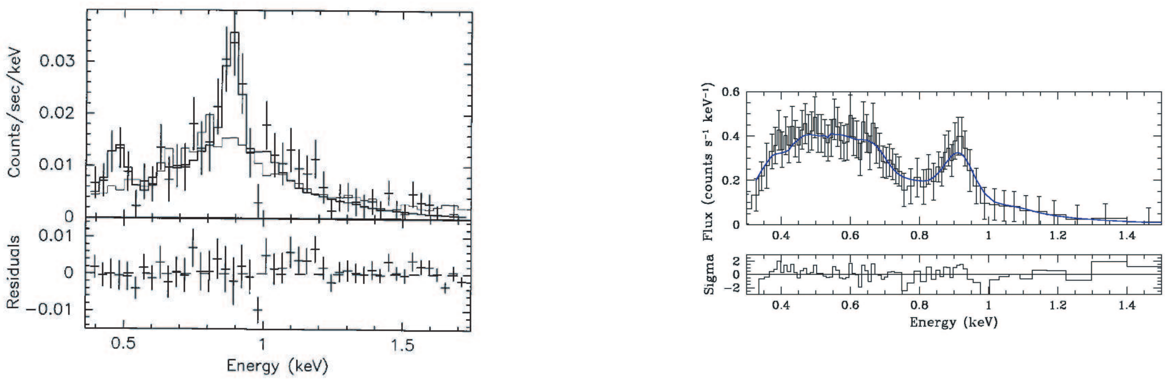

Figure 4.16: The spectra of BD +30° 3639. (left) Obtained with the *ASCA* SIS (Arnaud et al. 1996). (right) Obtained with the *Chandra* ACIS-S (Maness et al. 2003).

Table 4.6: Published results on the X-ray spectra of BD +30° 3639 obtained with *ASCA* and *Chandra*.

	$N_{\rm H}$ [cm^{-2}]	kT [keV]	C	N	O	Ne	Fe
ASCA*	$1.2 \times 10^{21\ddagger}$	$0.258^{+0.030}_{-0.027}$	$354^{\ddagger}$	9.11 (<34.5)	1.26(<2.69)	$10.5^{+7.66}_{-4.48}$	0
	$1.2 \times 10^{21\ddagger}$	0.227 ± 0.026	$1^{\ddagger}$	0.5	0.04 (<0.09)	$0.22^{+0.14}_{-0.09}$	< 0.05
Chandra†	2.5×10^{21}	0.181	$354^{\ddagger}$	$9.1^{\ddagger}$	4.2 ± 0.3	19.3 ± 1.4	0

* Arnaud et al. 1996

† Maness et al. 2003

‡ Assumed.

large uncertainties have remained because of the lack of *ASCA* efficiency toward lower energies where O-K, N-K, and C-K lines are expected. As summarized in table 4.6, the abundances determined by a model fitting to the *ASCA* spectrum is strongly affected by the assumption of C abundance.

The superior angular resolution of *Chandra* confirmed the X-rays from BD $+30^\circ$ 3639 to be extended (Kastner et al. 2000; Kastner et al. 2002). At the same time, the spectrum in the range down to 0.3 keV was obtained with the ACIS, which led Maness et al. (2003) into an attempt to determine the abundances. Since a broad 0.3-0.7 keV feature, which is thought to be a blend of lines from C, N, and O, is not resolved into individual lines, they assumed an unrealistically high C abundance, 354 times solar, like Arnaud et al. (1996). The *Chandra* results are also summarized in figure 4.16 (right) and table 4.6. In §5, we ourselves reanalyze the X-ray image and spectrum obtained with the *Chandra* ACIS-S

4.3.2 Other planetary nebulae

NGC 246

This object is an oval-shaped, high-excited PN with the diameter of $\sim 4'$. The spatial kinematics is well studied by optical, UV, and infrared observations, and the interaction with the interstellar medium is suggested (Muthu et al. 2000; Szentgyorgyi et al. 2003). The central star of this planetary nebula is a hot ($\sim 1.5 \times 10^5$K) O VI star and has a G8-K0 V companion at a separation of $3''.8$ (Bond and Ciardullo 1999). Bond and Ciardullo (1999) estimated the distance to the PN as 495^{+145}_{-100} pc by fitting the companion to the zero-age main sequence.

The X-ray emission from NGC 246 was discovered by *Einstein* for the first time (Tarafdar and Apparao 1988). Although an *Chandra* X-ray observation was conducted, the results have not published as of October 2005.

NGC 2392

NGC 2392 is composed of a bright inner disk of about $18'' \times 15''$ in full width, and an outer disk with a lower surface brightness and a diameter of $24''$. This nebula shows wide variety of ionization stages (O'Dell et al. 2002). Detailed optical spectroscopic observations revealed that this PN has a high velocity component, interpreted as a collimated jet-like bipolar mass outflow with a velocity of nearly 200 km s^{-1} (Gieseking et al. 1985).

Guerrero et al. (2005) conducted an *XMM-Newton* observation of NGC 2392 and detected diffuse X-ray emission. They reported the temperature to be 0.175 keV, and higher abundances of N and Ne by a factor of 3.5 and 3.0, respectively, than nebular values estimated by optical and UV observations. Although Guerrero et al. (2005) suggested that this PN has diffuse X-ray emission, we concluded that spatial distribution of the X-ray emission cannot be resolved with the angular resolution of *XMM-Newton* (§4.1.3).

NGC 3242

This is a high-excitation planetary nebula which has a very bright elliptical shell with a diameter of $\sim 21''$, a bright line-emitting inner shell ($50.''5$ diameter), and two fainter outer shells ($109''$ and $192''$ diameters), as reported by Meaburn et al. (2000). Analyzing its optical and UV spectra, Henry et al. (2000) reported enhanced C/O and Ne/O ratios, 2.5 and 1.5 times the solar values, respectively, as well as a depleted O/H ratio nearly by a factor of two. This object is also known as the planetary nebula with a firm detection of ^{3}He (Rood et al. 1992).

Although an X-ray observation of NGC 3242 was conducted for the first time with *XMM-Newton* by the same investigators as for NGC 2392, the results have not yet been published as of October 2005.

NGC 6543

Known as the "Cat's Eye Nebula", NGC 6543 is one of the most well-studied PNe. It consists of a hydrogen-deficient nucleus, a bright elliptical inner shell with the major axis of $\sim 16''$, and a surrounding envelope with multiple semicircular features. In the [N II] line image, a pair of linear jet-like features are also observed along the major axis (Reed et al. 1999). From optical and UV spectra, Hyung et al. (2000) reported enhanced He together with depleted C and N, compared to the solar abundances. Combining infrared spectra obtained by *ISO* with UV and optical spectra, Bernard-Salas et al. (2003) reported enhanced abundances of N, O, and Ne compared to the solar values by a factor of 2.5, 1.1, and 1.6, respectively.

X-ray emission from NGC 6543 was discovered and marginally resolved to be diffuse by *ROSAT* (Kreysing et al. 1992). The *Chandra* observation revealed that this PN consists of a point-like source associated with the central star, and diffuse emission consistent in shape with the optical inner shell (Chu et al. 2001; Guerrero et al. 2001). Analyzing the spectra of the diffuse X-ray emission, Chu et al. (2001) measured a temperature of $\sim 1.7 \times 10^{6}$ K, and reported that the X-ray spectra cannot be reproduced if adopting the nebular abundances determined by its optical spectra (de Koter et al. 1996). Therefore, the

X-ray and optical sources are inferred to have different elemental abundances. Guerrero et al. (2001) reported a temperature of $\sim 10^6$ K and a greatly enhanced Ne abundance of the X-ray associated with the central star.

NGC 7009

In an Hα image (Guerrero et al. 2002) taken with the *HST* WFPC2, NGC 7009 shows a bright elliptical inner shell with a size of $25'' \times 10''$, surrounded by an envelope of $25'' \times 20''$. This PN is excited by an O-type central star (Mendez et al. 1988).

Examining all pointed and serendipitous observations of PNe in the *ROSAT* archives, Guerrero et al. (2002) found that NGC 7009 hosts an X-ray source, and carried out a follow-up observation with *XMM-Newton*. They successfully detected diffuse X-ray emission associated with the optical inner shell, and reported a temperature of 1.8×10^6 K adopting nebular abundances with slightly enhanced He and N relative to solar, which had been derived from optical and UV spectra (Kwitter and Henry 1998). However, these X-ray abundances are no more than a consistency argument, since the *XMM-Newton* spectra, with its relatively poor energy resolution on lower energies, is not very sensitive to nitrogen lines, and of course, not at all to helium lines.

NGC 7027

This is a young dense planetary nebula, highly ionized by a hot central star. The *HST* image revealed a bright, compact core region with a radius of $\sim 5''$, encircled by concentric rings extended to $15''$ in radius (Kastner et al. 2001). This PN, like BD +30° 3639, exhibits the H_2, HII and 3.3 μm features in emission (Woodward et al. 1989; Woodward et al. 1992; Graham et al. 1993). Optical spectra indicate enhanced C/O and N/O ratios by several times solar (Zhang et al. 2005); similarly, C-rich and O-depleted abundances are reported from *ISO* observations (Bernard Salas et al. 2001).

A *Chandra* observations discovered extended X-ray emission from NGC 7027 (Kastner et al. 2001). The X-ray emission exhibits a butterfly-like morphology, which appears to differ from an elliptical shape of the optical nebula. Maness et al. (2003) reported a temperature of 8.4×10^6 K, and enhanced O and Mg abundances compared to the values estimated from UV, optical, and infrared spectra (Bernard Salas et al. 2001).

NGC 7293

Known as the "Helix Nebula", NGC 7293 is one of the closest and brightest planetary nebulae. The images taken by *HST* revealed that the main ring of this PN is composed of an inner disk of $\sim 499''$ diameter, surrounded by an outer ring of $742''$ diameter (O'Dell et al. 2004). Optical and UV observations suggest that the N/O and Ne/O ratios are several times higher than the solar values, while the O/H and C/O ratios are roughly solar (Henry et al. 1999).

The X-ray emission from NGC 7293 has been known from *Einstein* and *EXOSAT* era (Tarafdar and Apparao 1988; Apparao and Tarafdar 1989). Leahy et al. (1996) reported that the X-ray spectrum of this PN is reproduced by two components; one is a blackbody with a temperature of 0.27×10^6 K, and the other is an optically thin plasma emission with a temperature of 1.08×10^7 K. This X-ray source cannot be resolved even with the high angular resolution of *Chandra* (Guerrero et al. 2001). Analyzing the X-ray spectrum obtained with the *Chandra* ACIS-S, Guerrero et al. (2001) reported a temperature of $\sim 7.4 \times 10^6$ K with the solar abundance. They also detected $\sim 20\%$ X-ray intensity changes between 36.7 and 11.0 ks observations separated by a 22.6 ks intervals.

Chapter 5

ANALYSIS AND RESULTS ON BD $+30^\circ$ 3639

5.1 X-ray Morphology

5.1.1 The Chandra ACIS-S image

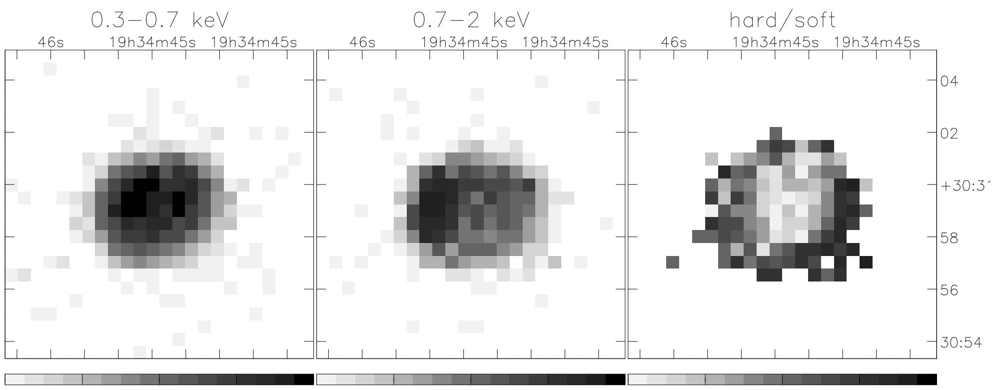

Figure 5.1: Raw X-ray images of BD $+30^\circ$ 3639 obtained with the *Chandra* ACIS-S in 0.3–0.7 keV (left) and 0.7–2 keV (middle). The ratio of the 0.7–2 keV brightness to that in 0.3–0.7 keV is shown in the right panel.

Figure 5.1 gives energy-resolved X-ray images of BD $+30^\circ$ 3639 obtained with the *Chandra* ACIS-S. The soft band (0.3–0.7 keV) corresponds to a blend of K-lines from C, N, and O, while the hard band (0.7–2 keV) includes the enhanced Ne-K line (figure 4.16). Although the two images both show an enhancement on the eastern side, soft photons distribute more uniformly compared with hard photons. This result is consistent with Kastner et al. (2002). Right panel of figure 5.1 shows a hardness-ratio map, obtained

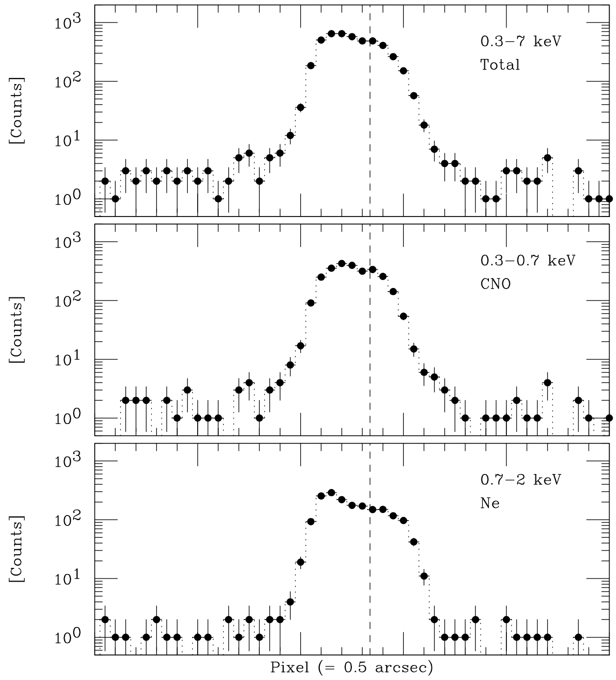

Figure 5.2: The background-inclusive surface brightness profiles of BD +30° 3639 projected on the horizontal axis in figure 5.1. Top panel shows the 0.3–7 keV profile, while middle and bottom ones show those in 0.3–0.7 and 0.7–2 keV, respectively. The dashed line indicates the position of the central star.

by dividing the hard-band image by the soft-band one. The hardness is enhanced at the nebular rim, suggesting that Ne is more enhanced toward the rim relative to CNO.

The projected surface brightness profiles in the total, soft, and hard bands are shown in figure 5.2. The X-ray distribution is thus clearly enhanced toward the left side of the central star. Although this X-ray enhancement is more prominent in the 0.7–2 keV profile, the 0.3–0.7 keV intensity also exhibits the same trend. Apart from the left-to-right asymmetry, the hard-band profile is more rim brightened, and this causes the enhancement of the hardness ratio map in the nebular rim (figure 5.1). In other words, the X-ray emitting ionized Ne ions are distributed to larger radii than the C, N, and O ions.

5.1.2 Comparison with optical image

Left panel of figure 5.3 gives a smoothed 0.3–7 keV X-ray image of BD +30° 3639 obtained with the ACIS-S, and right panel compares it with an optical image. Thus, the X-ray emission is concentrated within the optical nebula. The region of the highest X-ray surface brightness is associated with a filament-like feature in the Hα image. We do not observe particular X-ray features associated with the central star.

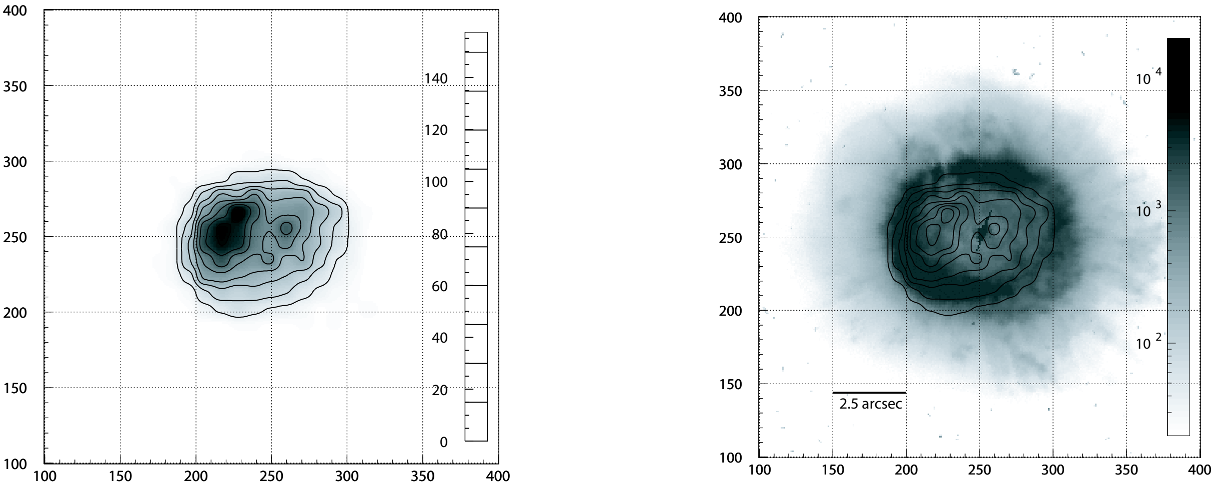

Figure 5.3: (left) Smoothed X-ray brightness contours of BD +30° 3639, superposed on its gray-scale image. (right) An Hα image of BD +30° 3639 obtained by the *HST* WFPC2, on which the X-ray contours of left panel are superposed. In both panels, 10 angular bins correspond to $0.''5$.

5.1.3 The Suzaku XIS images

Since BD +30° 3639 has a diameter of $\sim 5''$, it is essentially a point source for the *Suzaku* XIS which has an angular resolution of $2'$ in HPD (§3.3.2). Figure 5.4 gives four background-inclusive images of BD +30° 3639, obtained with the four XIS cameras. Only XIS-1 employs the BI chip (§3.3.4), and hence its higher sensitivity results in larger photon counts compared with the other cameras, namely XIS-0, XIS-2, and XIS-3, which employ FI CCDs. The cross-like feature is an artifact caused by the quadrant structure of the X-Ray Telescope. The FI-camera images reveal several weaker X-ray sources, although it it not obvious (at this stage) whether they are point sources or some diffuse structure.

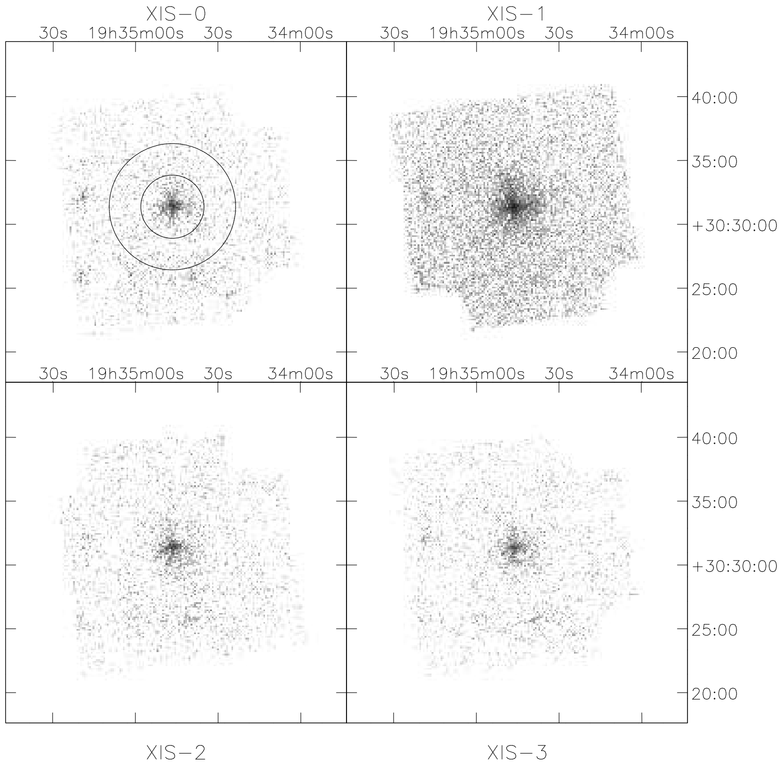

Figure 5.4: The raw 0.3–7 keV X-ray images of BD +30° 3639 obtained with the *Suzaku* XIS-0, 1, 2, and 3. Two corner regions of each image are masked to eliminate photons from the built-in calibration sources. The definition of source and background region is superposed on the XIS-0 image.

5.2 The Suzaku XIS Spectra

5.2.1 The XIS spectra

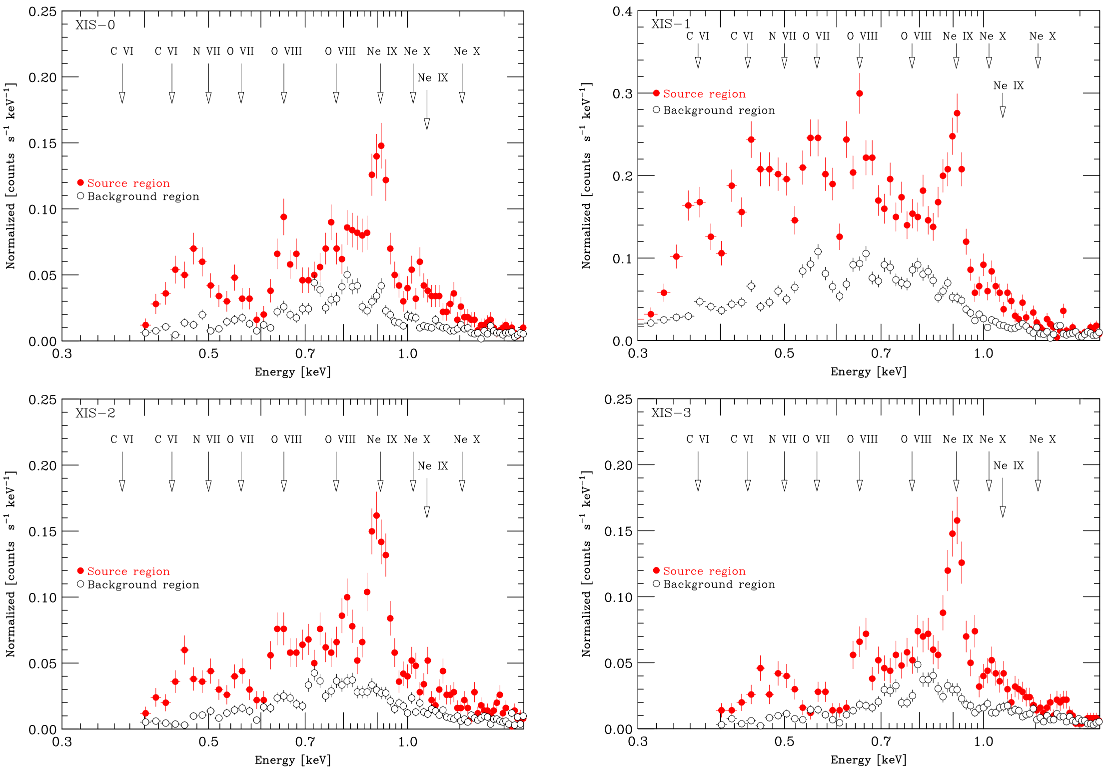

Figure 5.5: The 0.3–1.5 keV spectra of BD +30° 3639 obtained with XIS-0 (top-left), XIS-1 (top-right), XIS-2 (bottom-left), and XIS-3 (bottom-right). Filled red circles and open black circles indicate the spectra extracted from the source and background regions, respectively. The definition of regions is same as figure 4.11.

An X-ray photon observed with the XIS has pulse-hight information, like in the case of many other X-ray detectors. By accumulating photons over a certain region, and sorting them with respect to the pulse heights, we obtain an X-ray spectrum. Figure 5.5 shows the 0.3–1.5 keV X-ray spectra of the source and background regions obtained with each XIS camera, presented without removing the detector response. The employed on-source and background regions are indicated in figure 5.4 with a small circle and an annulus, respectively. Each background spectrum is scaled to the geometrical area and the vignetting factor of the background region, so as to match those of the on-source region. XIS-0, XIS-2, and XIS-3, which employs FI chips, have the observable lower limit of 0.4 keV, while that of XIS-1 is 0.3 keV. We discard the energy region above 1.5 keV, where the signal photons are absent in agreement with the previous observations (figure

4.3, figure 4.16).

These *Suzaku* spectra reconfirms the enhanced He-like Ne (Ne IX) K-line at 0.9 keV, which was reported by *ASCA* and *Chandra*. Furthermore, the superior energy resolution of the XIS has successfully resolved the blend of CNO lines, as we expected. K-lines from H-like and He-like O (O VII, VIII) are resolved by both the BI and FI chips. The apparent absence of Fe-L complex in 0.7–1 keV indicates a low plasma temperature, and/or a depleted iron abundance.

The most remarkable feature revealed by these spectra is a H-like C (C VI) K-line at 0.37 keV, seen in the XIS-1 spectrum. Since the effective area of the XIS-BI sharply falls below 0.5 keV (figure 3.29), the clear detection of C-K line indicates an actually enhanced C abundance of the X-ray emitting material in the PN.

When quantitatively analyzing an X-ray spectrum such as those in figure 5.5, we usually start with a theoretical model (e.g. blackbody or bremsstrahlung) with several free parameters. Then we convolve the model through the XIS response, compare the obtained prediction with the observed spectrum, and optimize the model parameters so as to minimize chi-squared of the fit between the data and the model predictions. We do not removed the detector response from the observational data, since such "deconvolution" is known to amplify statistical errors, and make it difficult to quantify the spectrum and associated uncertainties. Hereafter, we analyze the background-subtracted XIS spectra. Since XIS-0, XIS-2, and XIS-3, which employ FI chips, are essentially identical devices, we have combined their spectra into a single spectrum, and call it "XIS-023".

5.2.2 Emission lines

Since many emission lines are clearly visible in the XIS spectra of BD +30° 3639, we tried reproducing the background-subtracted spectra with a continuum and several emission lines, employing a bremsstrahlung and Gaussian models, respectively. Such a semi-empirical modeling gives a simple approximation to the X-ray spectrum emerging from an optically thin thermal plasma; the bremsstrahlung represents continuum, while the Gaussians represent lines from bound-bound transitions. Because the expected X-ray lines are intrinsically narrow, the widths of the Gaussian models are fixed to a value, 3.65 eV, which is much smaller than the energy resolution of the XIS ($\sim$ 60 eV in these energies). Furthermore, we have fixed the center energies of the lines at theoretical values of expected ions, namely, helium-like and hydrogen-like C, N, O, and Ne. Table 5.1 gives the theoretical center energies of these lines which are employed in the model fit.

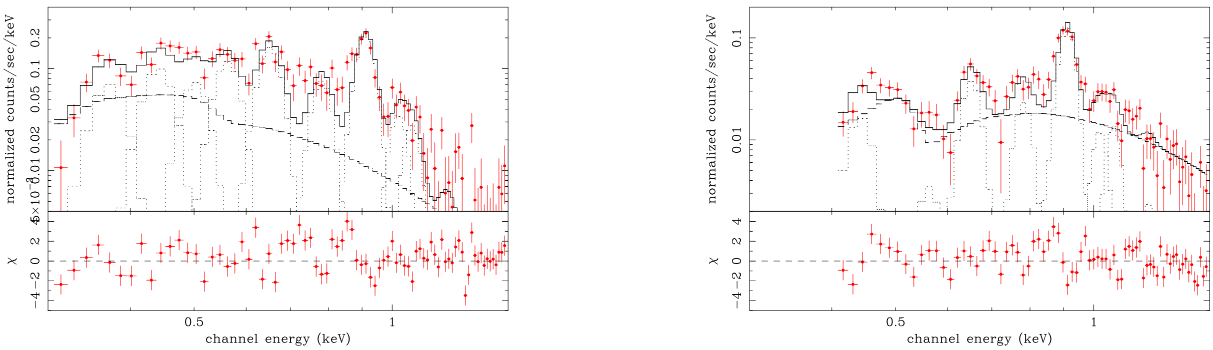

Figure 5.6: The XIS-1 (left) and XIS-023 (right) spectra of BD +30° 3639, fitted with bremsstrahlung (a dashed line) and Gaussians (dotted lines). The total model is superposed with a solid line. Bottom panels show residuals between the data and the model.

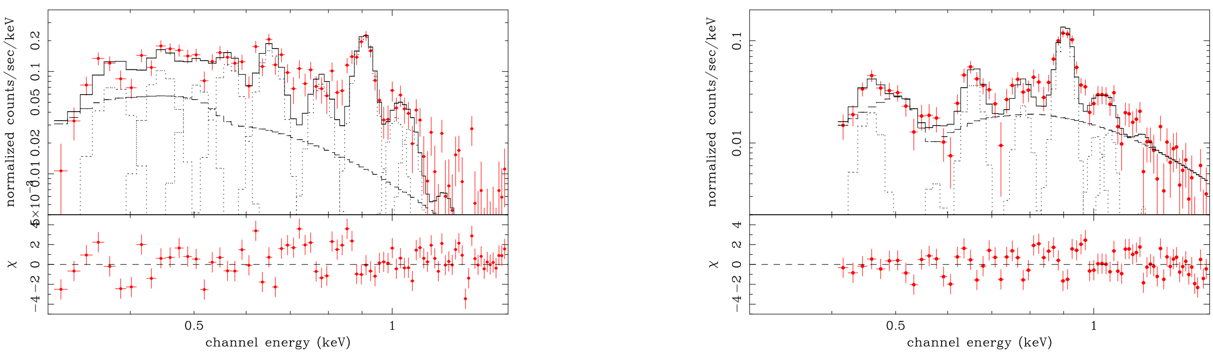

Figure 5.7: The same as figure 5.6, but the energy gain is adjusted.

Table 5.1: Emission lines identified in the XIS spectra of BD +30° 3639

Energy*	Ion		Flux [10^{-5} photons cm^{-2} s^{-1}]	
[keV]			XIS-1	XIS-023
0.37	C VI	Hα	$5.1^{+0.6}_{-3.2}$	–
0.44	C VI	Hβ	$4.4^{+1.5}_{-0.7}$	$3.0^{+1.0}_{-1.2}$
0.50	N VII	Hα	$2.5^{+0.6}_{-0.9}$	$0(< 0.08)$
0.56	O VII	Heα	5.3 ± 1	$0.95(< 2.5)$
0.65	O VIII	Hα	$5.3^{+0.8}_{-0.7}$	$3.5^{+0.83}_{-0.65}$
0.78	O VIII	Hβ	$2.0^{+0.6}_{-0.4}$	$1.1^{+0.39}_{-0.38}$
0.91	Ne IX	Heα	$5.1^{+0.4}_{-0.7}$	$4.0^{+0.37}_{-0.34}$
1.02	Ne X	Hα	$0.8^{+0.04}_{-0.02}$	$0.33^{+0.18}_{-0.17}$
1.07	Ne IX	Heβ	$0.6^{+0.2}_{-0.3}$	$0.35^{+0.15}_{-0.23}$
1.21	Ne IX	Heβ	$0.007(< 0.3)$	$0.05(< 0.15)$
Bremsstrahlung	kT [keV]		$0.30^{+0.32}_{-0.009}$	$0.43^{+0.04}_{-0.05}$
	Normalization		3.7×10^{-4}	4.2×10^{-4}
Gain†	a		0.98	0.95
	b		0.016	0.042
χ^2/d.o.f			189/67	102/61

* Theoretical values, to which the Gaussian center energies are fixed.

† Reforming to equation (5.1)

The results of this empirical model fit are shown in figure 5.6. Thus, the general spectral shapes are reproduced to a fair extent. However, we find that the line components in the actual data are systematically shifted toward lower energies, in both spectra, compared to the model predictions (dotted black lines). This is probably because the pulse-height to energy calibration of the XIS still has some uncertainties, at this early stage of the mission. Accordingly, we tried re-adjusting the energy of individual XIS events as

$$E' = (E/a) - b, \tag{5.1}$$

where E is the originally assigned energy, E' is the adjusted value, while a and b are free parameters. We have repeated the same fitting to the XIS-1 and XIS-023 spectra (separately), now including a and b as two additional free parameters. This has yielded the results as shown in figure 5.7 and table 5.1. Thus, the XIS-1 and XIS-023 spectra both reveals hydrogen-like and helium-like K-lines from O and Ne. Furthermore, we reconfirm the detection of the hydrogen-like C lines with XIS-1 below 0.4 keV. Nitrogens lines are rather weak, or insignificant. The inferred gain error ($= 1 - a$), 2–3%, is wel within the current calibration accuracy.

The line ratio of an ion gives an ionization temperature, because the ionic fractions strongly depend on the temperature (figure 2.10). The observed flux ratio between O VIII and O VII, about 1–3.5, suggests an ionization temperature of ~ 0.2 keV, while the ratio between Ne IX and Ne X, 0.08–0.16, suggests that of ~ 0.1 keV. Although the XIS spectra can be roughly reproduced in this way by 0.3–0.4 keV bremsstrahlung and 10 lines, the fits are not yet acceptable (table 5.1), and the bremsstrahlung temperature is not consistent with the estimated ionization temperatures of the oxygen or neon lines. Clearly, we should analyze the spectra using more appropriate plasma emission models (§2.4.3), which simultaneously account for the continuum and lines.

5.2.3 Low-energy response of the XIS

Although we can now fit the XIS spectra with the plasma models, responses of the *Suzaku* instruments are still subject to various residual uncertainties, which we must take into account. There are two major issues in the XRT+XIS calibration uncertainty; one is the energy gain already considered in a preliminary manner in §5.2.2; while the other is effective area, including quantum efficiency, and absorption by such materials as optical blocking filters of the XIS and thermal shield of the XRT.

Since the spectra of BD +30° 3539 contain many lines, they are suitable for self-calibrating the XIS gain, namely the first uncertainty. As a start point of this self calibration, we re-fitted the ACIS-S spectrum of BD +30° 3639 in the same way as Maness et al. (2003), where the plasma model VMEKAL is adopted, and kT, O and Ne abundances are treated as free parameters (table 4.6), while the C abundance is fixed at a very high (almost unphysical) value. Hereafter, we represent abundances in the unit of solar abundances by Anders and Grevesse (1989) (Appendix A), unless noted otherwise. The column density for the photoelectric absorption was fixed at $N_{\rm H} = 2.5 \times 10^{21}$ cm^{-2}, which is reported by Maness et al. (2003). The parameters are summarized in table 5.2, these are consistent with those of Maness et al. (2003) within $\sim 50\%$. We hereafter call this model "tentative plasma model", because it is used only for the purpose of XIS gain adjustment.

As a next step, we applied the tentative plasma model to the XIS-1 and XIS-023 spectra, fixing the model parameters but allowing the XIS gains to be adjusted again according to equation (5.1). As a result, The gain correction factors have been determined as summarized in table 5.3. The obtained values of a are close to those estimated in §5.7, using the Gaussian approximations, although this is not the case with the offset b. The spectra after the gain correction are shown in figure 5.8, together with predictions of the tentative plasma model.

Table 5.2: The "tentative" plasma model indicated by the ACIS-S spectrum.

	kT [keV]	C*	N*	O	Ne	Fe*	Others*	χ^2/d.o.f
ACIS	$0.17^{+0.004}_{-0.007}$	354	9.1	$3.4^{+0.55}_{-0.52}$	29^{+3}_{-10}	0	1	116/81

$N_{\rm H} = 2.5 \times 10^{20}$ cm^{-2} (Maness et al. 2003).

* Fixed to the same values as Maness et al. (2003).

Although the XIS energy gains have thus been calibrated, the XIS data, in 5.8, fall

Table 5.3: The gain correction parameters to the XIS-1 and XIS-023 spectra, determined with the tentative plasma emission model of table 5.2.

	a^*	b^* [keV]
XIS-1	0.98	−0.0015
XIS-023	0.97	0.012

*Referring to equation (5.1)

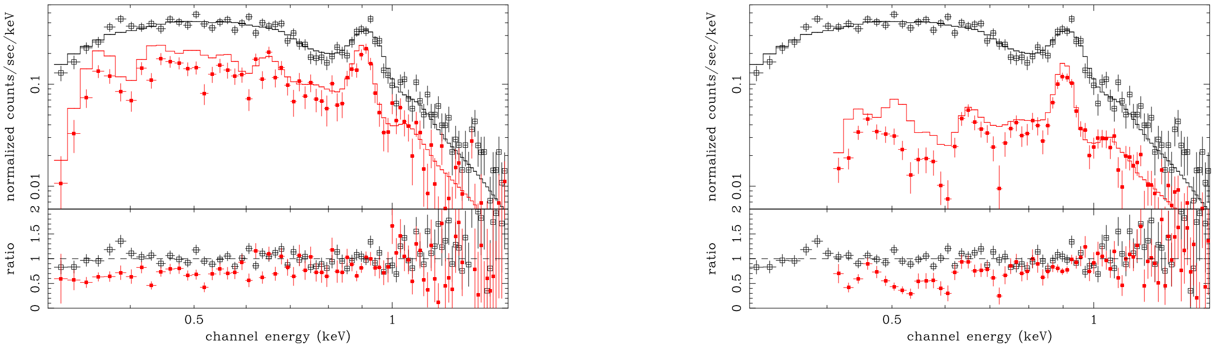

Figure 5.8: The ACIS-S (black open squares) and the XIS (red filled squares) spectra of BD +30° 3639. Predictions of the tentative plasma model, determined with the ACIS-S spectrum, are superposed with solid lines of the corresponding colors. Left panel shows the XIS-1 spectrum, while right panel shows combined spectrum of XIS-0, XIS-2, and XIS-3. Bottom panels represent the data to model ratio. The XIS gain have been optimized according to equation (5.1).

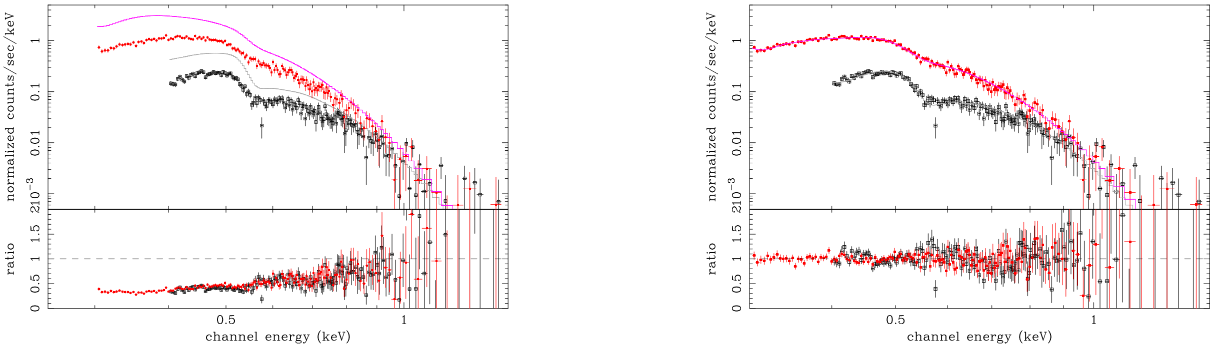

Figure 5.9: The XIS-1 (red filled squares) and XIS-023 (black open squares) spectra of RX J1856.5-3754. In left panel, predictions of the blackbody model determined with the *Chandra* LETG (Burwitz et al. 2003) are superposed with solid lines. In right panel, the correction factors involving multiple absorption edges are applied to the model, before convolving through the respective responses. Bottom panels show the data to model ratio.

systematically below the model predictions, in energies below 1 keV. This is not due to a simple uncertainty in the relative normalizations of the two instruments (ACIS and XIS), since the data-to-model discrepancy disappears in higher energies. Therefore, we suspect, that the low-energy effective areas (including quantum efficiency) of the XIS are still subject to significant uncertainties (the second calibration issue). Actually, such a concern is reported by the XIS hardware team; the flux below 1 keV of several soft X-ray sources measured with the XIS is lower by $\sim 50\%$ than those determined by previous X-ray observatories, such as *Chandra* and *XMM-Newton*.

Soft X-ray photons below 1 keV suffer strongly from absorption by the materials intercepting the X-ray paths (thermal shield of the XRT, optical blocking filter of the XIS, and so on). In addition, there are instrumental absorption edges of C-K (0.28 keV) and Au-N (0.35–0.7 keV) below 1 keV. Therefore, a slight excess in the amount of these materials would cause excess absorption, which in turn would produce the flux deficit toward lower energies. Therefore, the XRT and XIS teams have been making every effort to estimate the exact amount of these absorbers, and to identify the cause of the apparent excess absorption. However, their effort has not been successful yet, since the flux deficit is too large to be explained by these known factors even considering the associated uncertainties. One remaining possibility is that the excess absorption is due to contamination by materials involving C, N, and O, either on the XRT surface, ore on the XIS entrance windows, or both. Actually, build-up of such contamination is reported on the *Chandra* ACIS. Hereafter, we employ this possibility as a working hypothesis.

In order to temporarily take into account the suspected excess absorption, we resort to applying an empirical absorption factor to the XIS spectra. In order to determine the excess absorption factor as a function of energy, we need a "calibration" which has a smooth featureless spectrum of a known form. As an ideal calibration, here we employ RX J1856.5-3754, an isolated neutron star, which is known to have a simple black body spectrum with a temperature of ~ 63 eV; its blackbody temperature and radiation region size (which represents the normalization) have been accurately determined by both *Chandra* and *XMM-Newton* (Burwitz et al. 2003). This compact X-ray source was observed with *Suzaku* on 2005 October 24 as a calibration target in lower energies. After the standard screening the same as of BD +30° 3639, we obtained an exposure of 73 ks.

Left panel of figure 5.9 shows the XIS spectra of RX J1856.5-3754, in comparison with predictions of the best-fit model to the *Chandra* LETG data (Burwitz et al. 2003). We see again that the XIS data fall below the *Chandra* model toward lower energies, even through the data and model agree reasonably above ~ 1 keV. A simple way of simulating such an effect is to multiply the model spectrum with an empirical edge absorption factor, expressed as

$$M(E) = \begin{cases} 1 & (E < E_{\rm edge}) \\ \exp\left\{-\tau\left(\frac{E}{E_{\rm edge}}\right)^{-3}\right\} & (E > E_{\rm edge}) \end{cases} \tag{5.2}$$

where $E_{\rm edge}$ and τ are threshold energy and optical depth, respectively. However, the flux decrement seen in figure 5.9 depends on the energy more weakly than is implied by equation (5.2). Accordingly, we introduced multiple edges with different energies, based on a purely empirical consideration. The threshold energies were fixed in the step of 0.05 keV from 0.25 to 0.50 keV, while the optical depths were free parameters. The *Chandra* LETG model multiplied by this multiple-edge absorption model were compared with the observational XIS data, and the optical depths of the 5 (or 3) edges were adjusted to obtain best fits. As shown in figure 5.9 (right), the *Chandra* blackbody model has nearly successfully reproduced the XIS spectra of RX J1856.5-3754, when the optimum flux correction factor is multiplied to it. The obtained parameters of the flux correction factor are summarized in table 5.4.

Table 5.4: The flux correction factor of the XIS-1 and XIS-023 spectra.

Threshold energy	Optical depth τ	
$E_{\rm edge}$ [keV]	XIS-0	XIS-023
0.25	0.51	–
0.30	1.24	–
0.35	0.44	1.29
0.40	0.18	0.49
0.50	0.30	0.45
χ^2/d.o.f*	181/151	123/158
Scaling factor†‡	0.51	0.86
χ^2/d.o.f†	128/80	252/161

* As determined by the RX J1856.5-3754 spectra.

† As indicated by the BD +30° 3639 spectra.

‡ Scaling factor for the optical depths.

Now we have come to the stage of applying the flux correction factor to the tentative plasma model of table 5.2, in the hope of reducing the model-to-data discrepancy observed

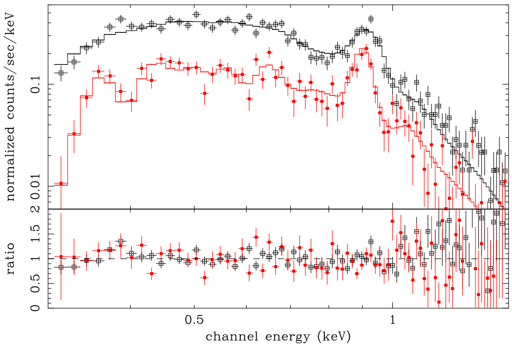

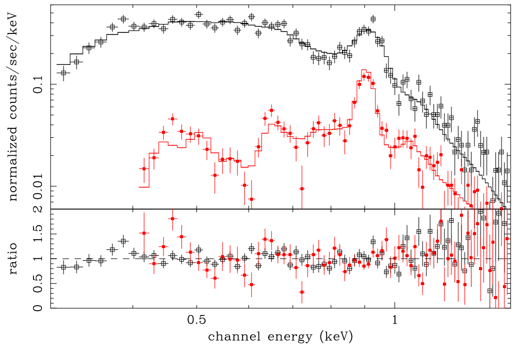

Figure 5.10: The same as figure 5.8, but the model applied to the XIS spectra are subjected by the flux correction factor.

in figure 5.8. However, by carefully looking at figure 5.8 and left panel of figure 5.9, we notice that the deviation is not exactly same between these two objects, with RX J1856.5-3754 showing a larger discrepancy. We have therefore decided to introduce another free parameter, which scales the optical depths of the flux correction model with their ratios kept unchanged. This may apply to such a case as the contamination developing with time, with its chemical composition kept the same. We re-fitted the XIS spectra with the tentative plasma model (table 5.2) multiplied by the correction model (table 5.4), as we let the optical depths vary freely but keeping the ratios among them. As shown in figure 5.10 (left), the XIS-1 spectrum of BD +30° 3639 has been reproduced rather well when the optical depths of the flux correction factor are set approximately half those determined with RX J1856.5-3754. Similarly, the XIS-023 spectrum favors 0.76 times smaller optical depths. These scaling factors of the optical depths are added to table 5.4. Since there is nearly a month interval between the *Suzaku* observations of BD +30° 3639 and RX J1856.5-3754, on September 21 and October 24, respectively, the present results indeed suggest the increase of contamination.

In this way, we have calibrated the XIS gain, and obtained the flux correction factor, of which the energy dependence is expressed by multiplication of 5 (or 3) photo-absorption edges with small ($\lesssim 1$) optical depths. Hereafter, we utilize this flux correction factor and the gain correction, fixing their parameters. It must be emphasized that the tentative plasma model (figure 5.8 and figure 5.10) is not our final goal, since it has been adjusted to reproduce only the ACIS spectrum, and utilized to improve the XIS responses. The plasma model parameters are yet to be adjusted so as to give the best fit to the *Suzaku* XIS spectra, which must be significantly more informative than the *Chandra* ACIS-S data.

5.3 Estimation of Metal Abundances

5.3.1 Solar abundance modelings

With the XIS data calibrated in the way described in §5.2.3, we begin to analyze the XIS spectra of BD +30° 3639 for metal abundances, in an attempt to much improve the knowledge over what was obtained with *ASCA* and *Chandra*. Hereafter, we utilize the plasma model vAPEC (§2.4.3), which includes He, C, N, O, Ne, Na, Mg, Al, Si, S, Ar, Ca, Fe, and Ni, and assumes collisional ionization equilibria. Parameters of the model are the plasma temperature kT, abundances of individual elements, and normalization. The last quantity is defined as $\frac{10^{-4}}{4\pi D^2}\int n_e n_i dV$, where D (cm) and V are the distance to the source and the volume of the source, respectively, while n_e and n_i are the electron and ion densities (cm^{-3}), respectively. In other words, the flux of a vAPEC fit gives the emission measure (§2.4.3). The abundance of each element is given as a relative number to hydrogen in the unit of 1 solar abundance. In addition to the plasma modeling, the interstellar absorption should be considered, referring to the equivalent hydrogen column density, $N_{\rm H} = 1.0 \times 10^{21}$ cm^{-2}, derived from the ratio of radio and Hβ fluxes (Appendix B).

As the simplest start point, figure 5.11 gives the XIS spectra compared with the prediction of 1 solar plasma model. Fixing the abundances of all elements to 1 solar values, we fitted the spectra, and obtained parameters in table 5.5. Thus, the helium-like and hydrogen-like oxygen K-lines (0.56 keV and 0.65 keV) are well reproduced by a temperature of $\sim$ 0.2 keV, which is consistent with the results of the modeling by bremsstrahlung and emission lines (§5.2.2). However, the fit is totally unacceptable, because the 1 solar model severely underpredicts C, N, and Ne lines at 0.37, 0.50, and 0.91 keV, respectively, while it overpredicts the oxygen lines as well as Fe-L lines around 0.8 keV. Thus, the hot plasma in this PN is inferred to have very low O/C and Fe/C ratios.

Then, we let the overall abundance vary freely, but constraining the abundance ratios to obey the solar values. As summarized in table 5.5, a very low metallicities were obtained. As shown in figure 5.12, it cannot yet reproduce the strong C and Ne emission lines, and the Fe-L excess of the model prediction still remains. The very low metallicity obtained in this fit is a simple consequence of the model trying to make weaker the oxygen lines, while to enhance the flux below 0.5 keV using an increased continuum.

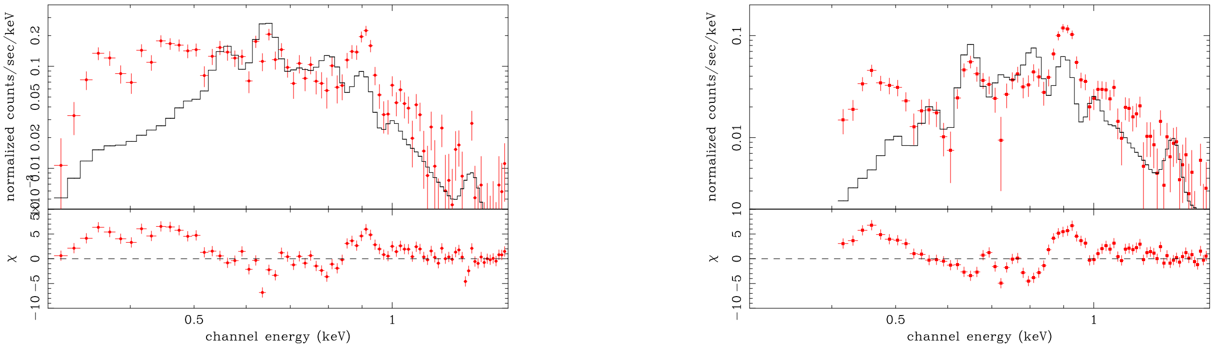

Figure 5.11: The XIS-1 (left) and XIS-023 (right) spectra of BD +30° 3639 fitted with vAPEC model with all metal abundances fixed to 1 solar values.

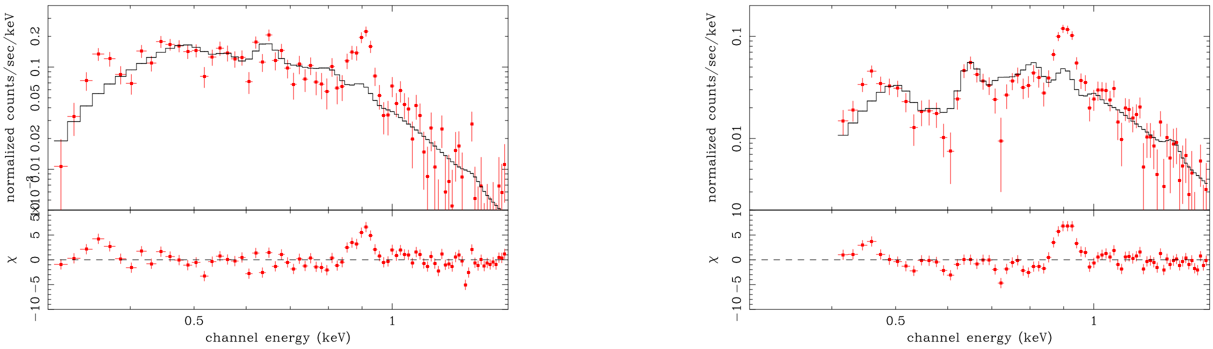

Figure 5.12: The XIS-1 (left) and XIS-023 (right) spectra of BD +30° 3639 fitted with the model assuming relative solar abundances.

Table 5.5: The best fit vAPEC parameters of the X-ray emission from BD +30° 3639 assuming solar abundance ratios.

Parameter	1 Solar		Relative to solar abundances	
	XIS-1	XIS-023	XIS-1	XIS-023
N_H* [cm^{-2}]	1.0×10^{21}	1.0×10^{21}	1.0×10^{21}	1.0×10^{21}
kT [keV]†	0.24 ± 0.007	$0.25^{+0.009}_{-0.008}$	$0.23^{+0.008}_{-0.007}$	$0.24^{+0.009}_{-0.008}$
Abundance	1*	1*	0.0098	0.018
Norm.	4.8×10^{-4}	4.9×10^{-4}	1.5×10^{-2}	1.3×10^{-2}
χ^2/d.o.f	648/79	550/72	296/78	339/71

* Fixed.

† Errors have little meanings, because the fit is highly unacceptable.

5.3.2 Non-solar abundance modelings

Now we have confirmed that the chemical composition of the hot plasma in BD +30° 3639 is significantly deviated from solar abundance ratios, we take the abundances of C, N, O, Ne, and Fe as free parameters; the former four elements have already been identified by the analysis using bremsstrahlung and lines (§5.2.2), and iron represents heavier elements. The He abundance is fixed to the solar value, and other heavy elements are neglected. We first fitted the XIS-1 and XIS-023 spectra separately, with the C abundance fixed to the solar value for the XIS-023 spectrum, since the energy of C-K line (0.37 keV) is out of its energy range. As shown in table 5.6 top panels of figure 5.13, the non-solar abundance model has successfully reproduced the observed data, yielding reduced chi-squared which are greatly improved compared with those for the solar abundance modeling (table 5.5). As we suspected in §5.3.1, the C to O ratio is extremely high, and iron is depleted so that the Fe to O ratio becomes rather low.

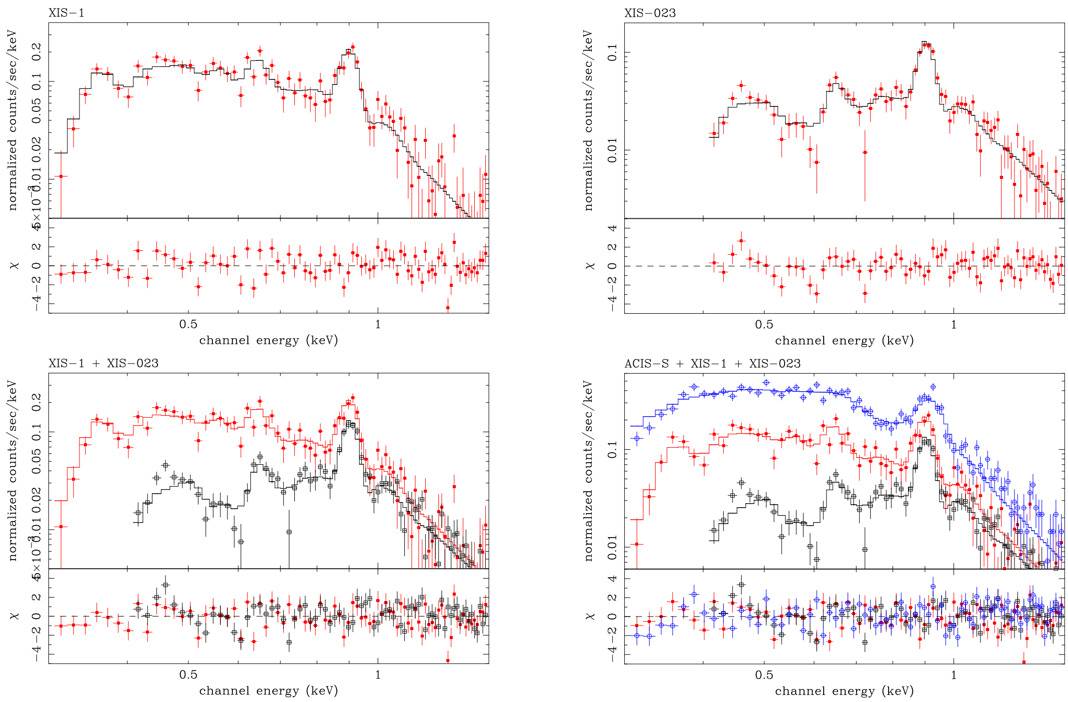

Figure 5.13: The 0.3-1.5 keV spectra of BD +30° 3639 fitted with vAPEC models with non-solar abundances. Top panels show the XIS-1 (left) and XIS-023 (right) spectra. Bottom-left panel shows the combined fit to the XIS-1 and XIS-023 spectra, and bottom-right shows that to the XIS-1, XIS-023, and ACIS spectra.

The best-fit parameters (table 5.6), obtained by the separate fits to the XIS-1 and XIS-023 spectra, are consistent with each other within statistical errors. Therefore, we

Table 5.6: The best fit vAPEC parameters of the X-ray emission from BD +30° 3639, allowing non-solar abundance ratios.

Parameter	XIS-1	XIS-023	XIS-1+XIS-023*	XIS-1+XIS-023+ACIS*
$N_H^\dagger$ [cm^{-2}]	1.0×10^{21}	1.0×10^{21}	1.0×10^{21}	1.0×10^{21}
kT [keV]	$0.22^{+0.012}_{-0.019}$	$0.22^{+0.008}_{-0.007}$	$0.22^{+0.008}_{-0.006}$	$0.23^{+0.006}_{-0.005}$
He†	1	1	1	1
C	$0.94^{+1.5}_{-0.60}$	$1^\dagger$	$0.89^{+0.74}_{-0.37}$	$0.55^{+0.39}_{-0.18}$
N	$0.081(< 0.37)$	$0(< 0.059)$	$0.035(< 0.15)$	$0.016(< 0.094)$
O	$0.022^{+0.030}_{-0.011}$	$0.017^{+0.008}_{-0.005}$	$0.019^{+0.014}_{-0,007}$	$0.016^{+0.008}_{-0.004}$
Ne	$0.17^{+0.16}_{-0.062}$	$0.13^{+0.024}_{-0.015}$	$0.14^{+0.062}_{-0.033}$	$0.12^{+0.037}_{-0.019}$
Fe	$0.018(< 0.054)$	$0(< 0.0082)$	$0.0051(< 0.018)$	$0.0013(< 0.0092)$
Others†	0	0	0	0
Norm.	8.6×10^{-3}	1.1×10^{-2}	9.6×10^{-3}	1.1×10^{-2}
χ^2/d.o.f	117/74	89/68	215/148	336/229
C/O	43^{+90}_{-35}	59^{+28}_{-17}	47^{+52}_{-26}	34^{+30}_{-14}
N/O	$3.7(< 18)$	$0(< 3.5)$	$1.8(< 8.0)$	$1.0(< 5.9)$
Ne/O	$7.7^{+13}_{-4.8}$	$7.6^{+3.9}_{-2.4}$	$7.4^{+6.3}_{-3.2}$	$7.5^{+4.4}_{-2.2}$
Fe/O	$0.082(< 2.8)$	$0(< 0.48)$	$0.27(< 1.0)$	$0.081(< 0.58)$

* A combined fit to the spectra.

† Fixed.

performed a combined fit to these two spectra. As shown in the bottom-left panel of figure 5.13, a common single model successfully explained both the XIS-1 and XIS-023 spectra. The obtained parameters, summarized in table 5.6, agree with the results of the separate fits.

Finally, we performed a combined fitting to the XIS-1, XIS-023, and ACIS-S spectra, since the ACIS, though with a poorer energy resolution, is better calibrated because of its mission maturity. The fitting results are shown in the bottom-left panel of figure 5.13, which reveals that a single plasma model consistently reproduce the three spectra. Although most of the obtained parameters, listed in table 5.6, are consistent with those of the XIS spectral fittings, the best-fit C and N abundances are smaller by 40–50% than those derived with the XIS. The C and N abundances seem to be most sensitive to the uncertainty of the flux correction factor (§5.2.3). In order to minimize such uncertainty, and to reduce statistical errors, hereafter we employ the combined fit to all of available data, namely the XIS-1, XIS-023, and ACIS-S spectra.

In table 5.6, we also show the C/O, N/O, Ne/O, and Fe/O ratios in the unit of solar abundance ratio (NOT the number ratios). Thus, these ratios do not depend much on the data utilized, even though the abundances themselves do. The results indicate enhanced C and Ne abundances, and depleted iron. The C to O ratio of BD $+30^{\circ}$ 3639 is 30 times higher than the solar ratio. The Ne to O ratio is also by seven times higher than the solar ratio, while that of N to O is nearly consistent with the solar value. Although the abundances of the tentative model (table 5.2) which we employed for the XIS calibration (§5.2.3) are systematically much higher than the results obtained here, the relative abundance patterns it implies are rather similar to those obtained here; extremely enhanced C and Ne, and near the solar value of N.

Although figure 5.13 visualizes a rough agreement between the observed data and the model predictions, reduced chi-squares show that the fitting is not yet completely acceptable. Significant deviations between the observed data and the model are seen in the 0.4–0.5 keV region, especially in the XIS-023 data. One possible reason is residual errors in the XIS calibration. Another candidate is resonant scatterings, which affect the $K\alpha/K\beta$ line ratios. We should also consider the interstellar absorption later (§5.3.3).

Figure 5.14 shows contributions of individual elements to the best-fit plasma emission model, obtained by the combined fit to the XIS-1, XIS-023, and ACIS spectra (table 5.6). In the lowest energy ranges, the enhanced C-lines appear, while Ne-lines dominate the highest energy ranges. Oxygen emission lines are present between them, while N and Fe lines contribute little. Although X-ray emission lines of each ion in the theoretical

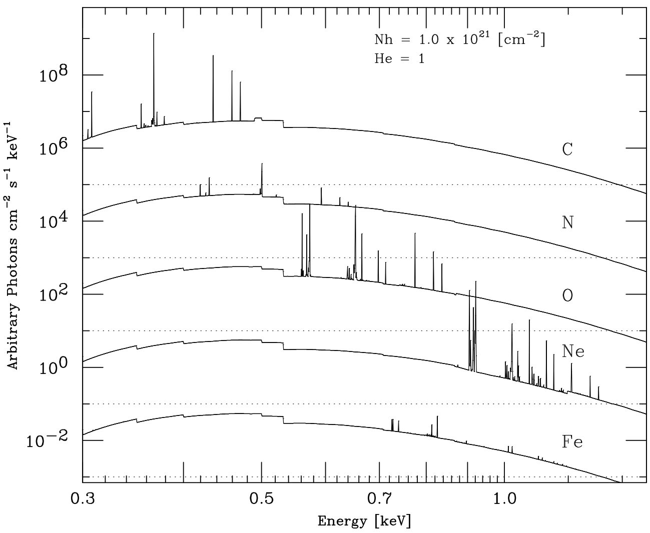

Figure 5.14: The plasma model specified by the combined fit to the XIS-1, XIS-023, and ACIS spectra. The detector responses are removed. Contributions from individual elements are drawn separately, with appropriate vertical offsets. The continuum includes contributions from hydrogen and the element itself, but not helium. The absolute level refers to the dotted lines.

model is complicated due to atomic fine structures, each line in actually observed data is broadened by the detector energy resolution.

5.3.3 Absorption

Soft X-ray photons strongly suffer from the interstellar absorption. In previous subsections (§5.3.1 and §5.3.2), we have fixed the absorption $N_{\rm H}$ to the line-of-sight column density to the PN, 1.0×10^{21} cm^{-2}, which is determined by the radio-to-optical flux ratio of BD +30° 3639 and the generally employed dust-to-gas ratio (Appendix B). However, the assumed absorption has uncertainty at least by $\sim 25\%$, and local absorption associated with the PN itself may be present. Accordingly, we let $N_{\rm H}$ vary freely and repeated the simultaneous fitting to the three spectra, assuming the absorber to have the solar abundances.

As shown in table 5.7 and figure 5.15, the fit has actually been improved by $\Delta\chi^2 \sim 20$. The obtained best-fit column density is twice higher than the fixed value. The carbon abundance has become as much as ~ 30 times higher, while those of O and Ne increased by an order of magnitude. Furthermore, the continuum normalization became $\sim 1/3$ of the previous level.

The simultaneous increases of C, O, and Ne abundances, and the decrease of the model normalization, are interpreted as follows. The excess absorption factor suppresses the model prediction toward lower energies, since the absorption optical depth is proportional to E^{-3} as described by equation (5.2). When $N_{\rm H}$ increases by 1×10^{21} cm^{-2}, for example, the flux at C-K lines (0.37 keV) become $\sim 1/5$. If, however, the normalization were raised, the flux in the whole energies would increase and that in the higher energies would exceed the actual data. Therefore, the model normalization tend to be reduced. To compensate for the low-energy suppression, the emission lines become enhanced, by certain factors which increase toward lower energies. When the C abundance becomes five times higher, the continuum, due to bremsstrahlung from carbon itself, also increases by several times above 0.6 keV. Therefore, in order to reproduce the observational data with higher $N_{\rm H}$, the C abundance has to further increase, and the consequent increase in the continuum emissivity makes its normalization decrease. At the same time, O and Ne abundances are also increased in order to keep the observed line equivalent width.

The above interpretation of the parameter changes suggests that the C abundance and the absorption are strongly correlated. In order to investigate this correlation more quantitatively, we calculated confidence contours for these two quantities, and present the results in figure 5.16. The C abundance has a large uncertainty, and only its lower limit can be determined reliably. In contrast, $N_{\rm H}$ has relative small uncertainties within $\sim 20\%$. With these in mind, we hereafter employ the case of free $N_{\rm H}$ and free C abundance as the standard fitting condition.

Before we proceed to a further analysis along our standard fitting condition, let us briefly examine what happens if we adopt other conditions. For example, we may fix the C and Fe abundances at 1 and zero solar, respectively, and constrain $N_{\rm H}$ to 1.0×10^{21} cm^{-2} (the first assumption we employed) or 2.1×10^{21} cm^{-2} (the best fit obtained above). The obtained parameters are summarized in table 5.7. By comparing these two cases, the case of higher $N_{\rm H}$, again yields systematically higher abundances, through a mechanism similar to what was considered above. However, the order of abundant elements, C>Ne>O, is unchanged, and the abundance ratios, C/O and Ne/O, dose not differ by more than a factor of 2 from that obtained with the standard condition.

5.3.4 Abundance ratios

The abundances of the relevant four elements have large uncertainties, depending on fitting conditions such as the treatment of $N_{\rm H}$. Therefore, it is difficult to constrain

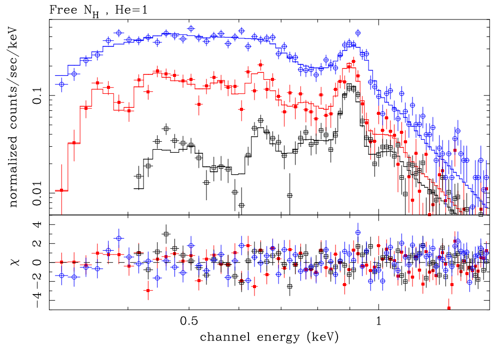

Figure 5.15: The same as bottom-right panel in figure 5.13, but the fitting is performed with $N_{\rm H}$ left free.

Table 5.7: The combined fit to the XIS-1, XIS-023, and ACIS spectra of BD +30° 3639 with a vAPEC model, with and without $N_{\rm H}$ left free.

Parameter	Free C abundance		Fixed to C=1 and Fe=0	
	Fixed $N_{\rm H}$*	Free $N_{\rm H}$	Fixed $N_{\rm H}$	Best-fit $N_{\rm H}$
$N_{\rm H}$ [cm^{-2}]	$1.0 \times 10^{21\dagger}$	$(2.1^{+0.2}_{-0.4}) \times 10^{21}$	$1.0 \times 10^{21\dagger}$	$2.1 \times 10^{21\dagger}$
kT [keV]	$0.23^{+0.006}_{-0.005}$	$0.19^{+0.008}_{-0.010}$	$0.23^{+0.004}_{-0.004}$	$0.18^{+0.003}_{-0.002}$
He†	1	1	1	1
C	$0.55^{+0.39}_{-0.18}$	19^{+43}_{-11}	$1^\dagger$	$1^\dagger$
N	$0.016(< 0.094)$	$0.67^{+0.25}_{-0.20}$	$0.079^{+0.05}_{-0.04}$	$\sim 0(< 0.013)$
O	$0.016^{+0.008}_{-0.004}$	$0.20^{+0.032}_{-0.021}$	$0.025^{+0.003}_{-0.003}$	$0.013^{+0.002}_{-0.002}$
Ne	$0.12^{+0.037}_{-0.019}$	$1.1^{+0.19}_{-0.12}$	$0.16^{+0.016}_{-0.015}$	$0.13^{+0.01}_{-0.01}$
Fe	$0.0013(< 0.0092)$	$\sim 0(< 0.073)$	$0^\dagger$	$0^\dagger$
Others†	0	0	0	0
Norm.	1.1×10^{-2}	2.8×10^{-3}	8.2×10^{-3}	3.2×10^{-2}
χ^2/d.o.f	336/229	316/228	343/231	348/231
C/O	34^{+30}_{-14}	95^{+216}_{-56}	$40^{+4.8}_{-4.8}$	77^{+12}_{-12}
N/O	$1.0(< 5.9)$	$3.3^{+1.4}_{-1.1}$	$3.2^{+2.0}_{-1.6}$	$0(< 0.9)$
Ne/O	$7.5^{+4.4}_{-2.2}$	$5.5^{+1.3}_{-0.8}$	$6.4^{+0.8}_{-0.8}$	$10^{+1.7}_{-1.7}$
Fe/O	$0.081(< 0.58)$	$0(< 0.37)$	0	0

* The same as in table 5.6

† Fixed.

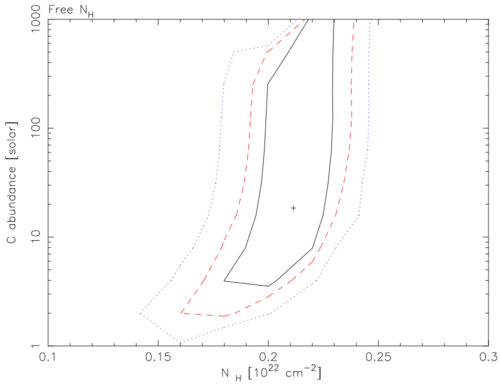

Figure 5.16: Confidence contours (68%, 90%, and 99%) for C abundance vs. column density $N_{\rm H}$. The temperature, abundances of the other elements (C, N, O, Ne, and Fe), and the spectral normalization are allowed to vary freely.

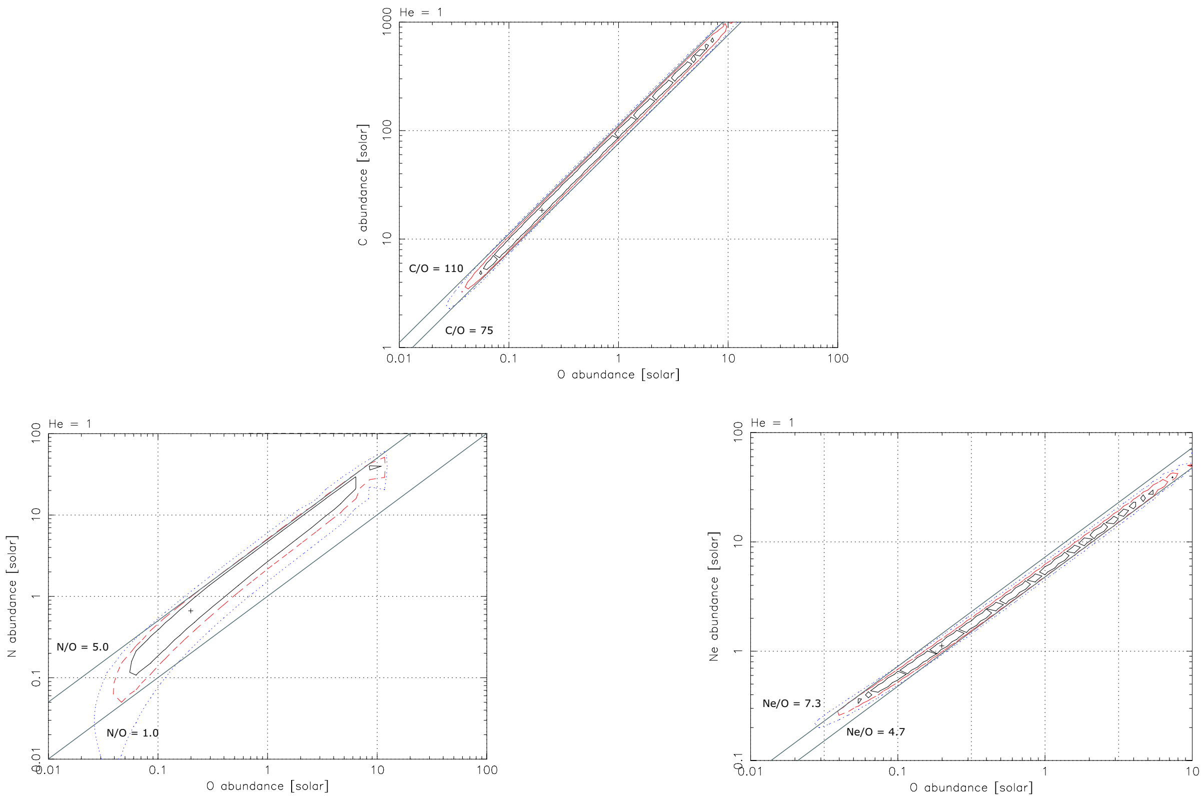

Figure 5.17: Confidence contours (68%, 90%, and 99%) of the C, N, and Ne abundances against the O abundance. $N_{\rm H}$ is fixed at 2.1×10^{21} cm^{-2}, while the temperature, the normalization, and abundances of the other elements (C, N, O, and Ne) are left free. The Fe abundance is fixed at zero.

their absolute abundances, namely the values relative to hydrogen. However, as we have already shown in previous sections, the abundance ratios are much better determined. In order to constrain the abundance ratios, we have calculated confidence contours between several parameters.

Figure 5.17 presents confidence contours calculated under the condition detailed in caption. Indeed, the contours are highly elongated, but the elongation is almost exactly along to direct the proportionality between the relevant two quantities. In short, the abundance ratios are well constrained. In the 90% confidential ranges, they are; $75 < \mathrm{C/O} < 110$, $1 < \mathrm{N/O} < 5$, and $4 < \mathrm{Ne/O} < 7$. These error regions are thought to be more accurate than the values indicated in table 5.7 which are based on simple error propagations, except that N_{H} is fixed at 2.1×10^{21} cm^{-2}. By allowing N_{H} to vary, the error ranges of these abundance ratios are essentially unchanged because of clearly resolved emission lines of C, O, and Ne.

5.3.5 He to H ratio

Although helium is the second abundant element in the universe, it has no emission line in X-ray band, and is responsible for only continuum. Therefore, it is almost impossible to determine absolute He abundance (in reference to hydrogen) with X-ray observations alone. We have therefore assumed the helium-to-hydrogen ratio to be the solar value (9.77×10^{-2}, Anders and Grevesse 1989), which reflects the big bang nucleosynthesis. However, the evolutionary scenario suggests an over-abundance of helium in such materials as are localized to PNe, and the spectral type of the central star indeed suggests hydrogen deficient. Therefore, the He/H ratio in BD +30° 3639 should be considered carefully. Accordingly, we slightly modified the standard fitting condition, and repeated the combined fitting assuming the He abundance to be 5, 10, or 20 times the solar value, and examined its impact on the other parameters; kT, C, N, O, and Ne abundances. The 10 solar helium corresponds to a case where the numbers of He and H are comparable.

The spectral fitting was carried out under the same condition as §5.3.3; N_{H}, kT, C, N, O, Ne, and Fe abundances are taken as free parameters, but the He abundance was assumed. The obtained parameters are summarized in table 5.8. As the assumed He abundance increases, the abundances of C, N, O, and Ne also increase. On the other hand, normalization, which is proportional to the emission measure (§2.4.3), decreases, because the continuum becomes more and more contributed by helium which has 4 times higher emissivity per ion [equation (2.33) in §2.4.3] than hydrogen. Since the number of hydrogen reduces, and the number of heavy elements, including C, N, O, and Ne, increase relative to hydrogen, the abundances show large value such as ~ 30.

Although the absolute values of metal abundances are thus affected by the assumed He abundance, their ratios were unchanged even the He abundance is assumed to be 20 times solar. This is because individual emission lines have been resolved by the XIS thanks to its superior energy resolution. Figure 5.18 gives the same confidence-contour plots as figure 5.17, but assuming He/H=10 instead of 1. The results are very similar to those with the solar He abundance (figure 5.17). Thus, we have confirmed that the abundance ratios among C, N, O, and Ne are independent of the He/H ratio. The results are summarized in table 5.9

Table 5.8: The same as table 5.7, but the He abundance relative to hydrogen is changed.

Parameter	He=1*	He=5	He=10	He=20
$N_{\rm H}$ [cm^{-2}]	$(2.1^{+0.2}_{-0.4}) \times 10^{21}$	$(2.1^{+0.2}_{-0.4}) \times 10^{21}$	$(2.1^{+0.2}_{-0.3}) \times 10^{21}$	$(2.0^{+0.2}_{-0.3}) \times 10^{21}$
kT [keV]	$0.19^{+0.008}_{-0.010}$	$0.19^{+0.011}_{-0.005}$	$0.19^{+0.011}_{-0.009}$	$0.19^{+0.005}_{-0.012}$
C	19^{+43}_{-11}	29^{+114}_{-15}	$31(>10)$	$47(>16)$
N	$0.67^{+0.25}_{-0.20}$	$1.0^{+0.39}_{-0.35}$	$1.1^{+0.41}_{-0.37}$	$1.6^{+0.67}_{-0.56}$
O	$0.20^{+0.032}_{-0.021}$	$0.32^{+0.044}_{-0.039}$	$0.34^{+0.059}_{-0.036}$	$0.53^{+0.09}_{-0.06}$
Ne	$1.1^{+0.19}_{-0.12}$	$1.9^{+0.24}_{-0.24}$	$2.0^{+0.33}_{-0.21}$	$3.1^{+0.50}_{-0.34}$
Fe	$\sim 0(<0.073)$	$0(<0.12)$	$0(<0.12)$	$0(<0.18)$
Others†	0	0	0	0
Norm.	3.2×10^{-3}	1.7×10^{-3}	1.5×10^{-3}	9.5×10^{-4}
χ^2/d.o.f	317/229	316/228	317/228	317/228
C/O	95^{+216}_{-56}	91^{+360}_{-48}	$91(>29)$	$89(>29)$
N/O	$3.3^{+1.4}_{-1.1}$	$3.1^{+1.3}_{-1.2}$	$3.2^{+1.3}_{-1.1}$	$3.0^{+1.4}_{-1.1}$
Ne/O	$5.5^{+1.3}_{-0.8}$	$5.9^{+1.1}_{-1.0}$	$5.9^{+1.4}_{-0.9}$	$5.8^{+1.4}_{-0.9}$
Fe/O	$0(<0.37)$	$0(<0.375)$	$0(<0.57)$	$0(<0.34)$

* The same as table 5.7

† Fixed.

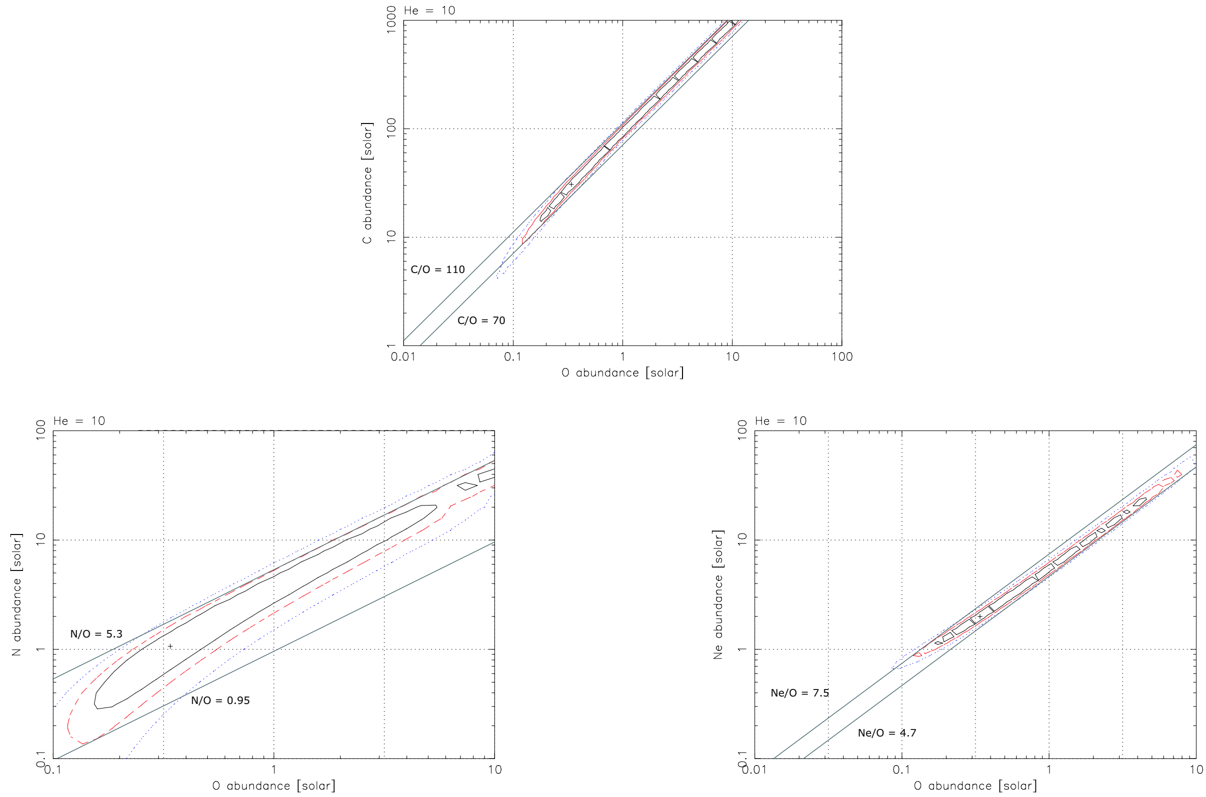

Figure 5.18: The same as figure 5.17, but He abundance is assumed to be 10 solar.

Table 5.9: The obtained abundance ratios.

Assumed He	1	10
C/O	95 (75–110)	91 (70-110)
N/O	3.3 (1.0–5.0)	3.2 (0.95–5.3)
Ne/O	5.5 (4.8–7.3)	5.9 (4.7–7.5)

The range of 90% confidence is in parentheses.

5.3.6 Systematic errors

So far, we have mainly focused on the determination of abundance ratios among C, N, O, Ne, and Fe, because their abundances themselves are subject to so large uncertainties. However, even these ratios may well be affected by various systematic effects, beyond the nominal statistical errors as given in table 5.9. Here, let us evaluate various sources of systematic errors.

As described in §5.3.3 and §5.3.5, the abundance ratios, C/O, N/O, and Ne/O, are not affected significantly by the line-of-sight absorption or the He to H ratio. There still remain two major sources of systematic errors we have to consider; uncertainties of the flux correction factor (§5.2.3), and systematic errors in the background.

In self-calibrating the XIS data, we have introduced the scaling factor to adjust the optical depths in the flux correction model (§5.2.3). In order to evaluate how possible errors in this scaling factor affect the derived parameters, we artificially changed it by $\pm 20\%$ from the nominal values employed, and carried out the same spectral fitting as §5.3.3. The obtained parameters are summarized in table 5.10, together with the nominal results. When the scaling factor is lowered by 20%, the best-fit parameters are not affected beyond their statistical errors, while the 20% larger scaling factor gives systematically lower abundances than the nominal case by 30–40%. However, the C to O ratio remains essentially unchanged. N to O and Ne to O ratios are also consistent with the nominal value within $\sim 10\%$ differences.

The other source of systematic errors is uncertainties in the background, because it amounts to 20–40% of the signal flux (figure 5.5). In order to avoid systematic effects caused by different observations, such as spacecraft condition or sky regions, we derived background spectra employing the off-source ring region surrounding the on-source region (figure 5.4) in the same observation. However, as already mentioned in §5.1.3, there are weaker X-ray sources or diffuse structures around BD $+30^\circ$ 3639. In order to examine how they affect the results, we defined four background regions, and compared their spectra. As shown in figure 5.19, the four regions are located at top, bottom, left, and right of the source region. The four background spectra of XIS-1 are compared in figure 5.20. Although they agree with one another in most energy bins within statistical errors, we notice statistically significant differences in the 0.3–0.4, 0.5–0.6, and 0.7–0.8 keV ranges. These energy ranges correspond to the C-K line (0.37 keV), O-K line (0.56 keV), and Fe-L lines complex, respectively. Therefore, the nonuniformity of background could affect our abundance measurements.

Table 5.10: The same as table 5.7, but the optical depths of the flux correction factor are changed by ±20%

	Nominal*	Nominal −20%	Nominal +20%
Scaling factor†	0.51/0.86	0.41/0.69	0.61/1.0
$N_{\rm H}$ [cm^{-2}]	$(2.1^{+0.2}_{-0.4}) \times 10^{21}$	$(2.2^{+0.1}_{-0.4}) \times 10^{21}$	$(2.1^{+0.2}_{-0.4}) \times 10^{21}$
kT [keV]	$0.19^{+0.008}_{-0.010}$	$0.19^{+0.013}_{-0.036}$	$0.19^{+0.009}_{-0.038}$
He‡	1	1	1
C	19^{+43}_{-11}	19^{+12}_{-15}	$10^{+185}_{-5.6}$
N	$0.67^{+0.25}_{-0.20}$	$0.55^{+0.23}_{-0.20}$	$0.39^{+0.14}_{-0.13}$
O	$0.20^{+0.032}_{-0.021}$	$0.21^{+0.027}_{-0.024}$	$0.11^{+0.029}_{-0.011}$
Ne	$1.1^{+0.19}_{-0.12}$	$1.2^{+0.17}_{-0.14}$	$0.66^{+0.11}_{-0.07}$
Fe	$\sim 0(< 0.073)$	$\sim 0(< 0.070)$	$0(< 0.037)$
Others‡	0	0	0
Norm.	2.8×10^{-3}	2.8×10^{-3}	4.8×10^{-3}
χ^2/d.o.f	317/229	319/228	330/228
C/O	95^{+216}_{-56}	90^{+58}_{-72}	91^{+1680}_{-52}
N/O	$3.3^{+1.4}_{-1.1}$	$2.6^{+1.1}_{-1.0}$	$3.5^{+1.6}_{-1.2}$
Ne/O	$5.5^{+1.3}_{-0.8}$	$5.7^{+1.1}_{-0.93}$	$6.0^{+1.9}_{-0.87}$
Fe/O	$0(< 0.37)$	$0(< 0.33)$	$0(< 0.34)$

* The same as table 5.7

† Scaling factor for the optical depths of XIS-1 / XIS-023.

‡ Fixed.

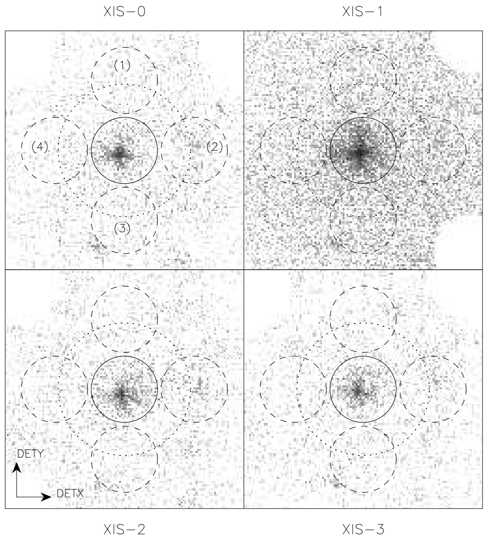

Figure 5.19: The definition of the source and background regions superposed on the 0.3–7 keV images in the detector coordinate. The source region is a circle in the center of each image. Five regions are defined as background regions; 4 circles denoted as (1) to (4), and annuli around the source region indicated by a dotted line. The last one is the nominal background region employed so far.

In order to evaluate the effect of the background, we prepared two background spectra in addition to the nominal one which we have been using so far. Background (a) is the sum of regions (1) and (3) in figure 5.19, while Background (b) is that of regions (2) and (4). In figure 5.21, these additional two background spectra of each device are compared with the nominal ones. Differences in the O-K and Fe-L ranges are noticed above statistical errors, especially in the XIS-1 and XIS-2 spectra. With these new backgrounds, we jointly re-fitted the XIS-1 and XIS-023 spectra again under the same condition as §5.3.3, with $N_{\rm H}$, kT, C, N, O, Ne, and Fe abundances taken as free parameters. The obtained parameters are summarized in table 5.11. Thus, the C abundance is not affected significantly, while those of N and O change by $\sim$ 20% and $\sim$ 15%, respectively. Although the abundance ratios are also affected, the changes are at most $\sim$ 20%.

Through a series of careful data analysis, we have successfully determined the C to O, N to O, and Ne to O abundance ratios, and evaluated systematic errors of various origins. Table 5.12 gives the final results with overall error budgets. Statistical errors are the largest error source. The abundance ratios of C to O and Ne to O have uncertainties of only several tens %, in virtue of the superior energy resolution of the *Suzaku* XIS. Even N to O ratio, which relies on very weak nitrogen emission lines in the observed spectra, has been constrained to a fair agree.

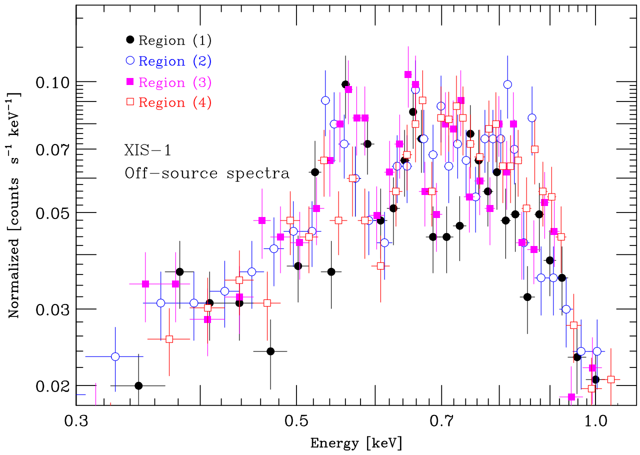

Figure 5.20: Background spectra obtained from the four regions with XIS-1. Filled black circles, open blue circles, filled magenta squares, and open red squares indicate the spectra in region (1), (2), (3), and (4) in figure 5.19, respectively.

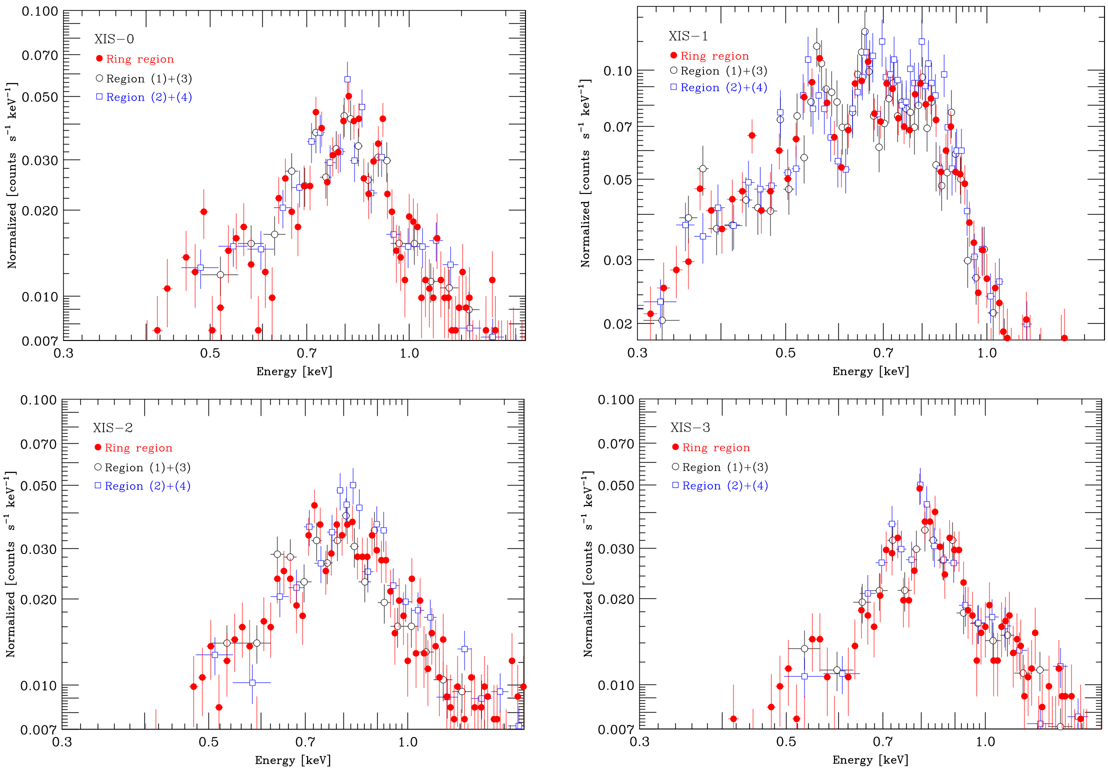

Figure 5.21: The three kinds of background spectra of XIS-0 (top-left), XIS-1 (top-right), XIS-2 (bottom-left), and XIS-3 (bottom-right). Open black circles, open blue squares, and filled red circles indicate the background (a), (b), and the nominal, respectively, defined in text §5.3.6

Table 5.11: The same as table 5.7, but the background spectra are changed.

Parameter	Nominal*	Background(a)	Background(b)
N_{H} [cm^{-2}]	$(2.1^{+0.2}_{-0.4}) \times 10^{21}$	$(2.3^{+0.1}_{-0.3}) \times 10^{21}$	$(2.1^{+0.1}_{-0.3}) \times 10^{21}$
kT [keV]	$0.19^{+0.008}_{-0.010}$	$0.19^{+0.011}_{-0.006}$	$0.19^{+0.011}_{-0.006}$
He†	1	1	1
C	19^{+43}_{-11}	20^{+18}_{-12}	19^{+18}_{-12}
N	$0.67^{+0.25}_{-0.20}$	$0.54^{+0.28}_{-0.19}$	$0.82^{+0.28}_{-0.19}$
O	$0.20^{+0.032}_{-0.021}$	$0.19^{+0.027}_{-0.055}$	$0.23^{+0.027}_{-0.055}$
Ne	$1.1^{+0.19}_{-0.12}$	$1.3^{+0.17}_{-0.16}$	$1.3^{+0.17}_{-0.16}$
Fe	$\sim 0(< 0.073)$	$\sim 0(< 0.095)$	$0(< 0.095)$
Others†	0	0	0
Norm.	2.8×10^{-3}	3.1×10^{-3}	2.4×10^{-3}
χ^2/d.o.f	317/229	307/228	301/228
C/O	95^{+216}_{-56}	105^{+95}_{-70}	83^{+79}_{-56}
N/O	$3.3^{+1.4}_{-1.1}$	$2.8^{+1.5}_{-1.3}$	$3.6^{+1.3}_{-1.2}$
Ne/O	$5.5^{+1.3}_{-0.8}$	$6.8^{+1.3}_{-2.1}$	$5.7^{+1.0}_{-1.5}$
Fe/O	$0(< 0.37)$	$0(< 0.5)$	$0(< 0.5)$

* The same as table 5.7

† Fixed.

Table 5.12: The obtained abundance ratios together with the overall error budget.

	Nominal	Statistical*	He/H†	Flux correction	Background
C/O	95	75–110	1	$\lesssim 5\%$	$\lesssim 10\%$
N/O	3.3	1.0–5.0	1	$\lesssim 10\%$	$\lesssim 15\%$
Ne/O	5.5	4.8–7.3	1	$\lesssim 10\%$	$\lesssim 24\%$

* The range of 90% confidence.

† Assumed.

Chapter 6

ANALYSIS AND RESULTS ON OTHER PLANETARY NEBULAE

6.1 Diffuse X-ray Emission in NGC 6543

6.1.1 X-ray morphology

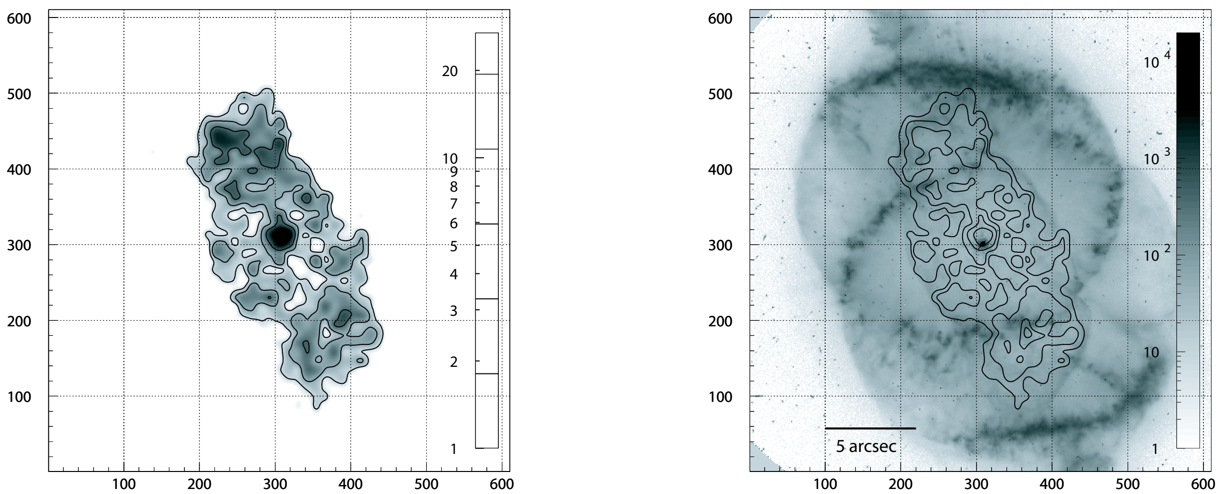

Figure 6.1: (left) Smoothed 0.3–7 keV surface brightness contours of NGC 6543, superposed on its gray-scale image. (right) An Hα image of NGC 6543 obtained by the *HST* WFPC2, overlaid on the X-ray contours of the left panel. Axes are arbitrary, but 12 bins corresponds to $0.''5$.

NGC 6543, known as "Cat's Eye nebula", has an axisymmetrical morphology in optical band. As shown in figure 6.1, *Chandra* revealed that diffuse X-ray emission is closely trace the complicated optical inner shell, and that a point-like X-ray source is associated with the central star within an error of $1''$ (§4.1.3; figure 4.6).

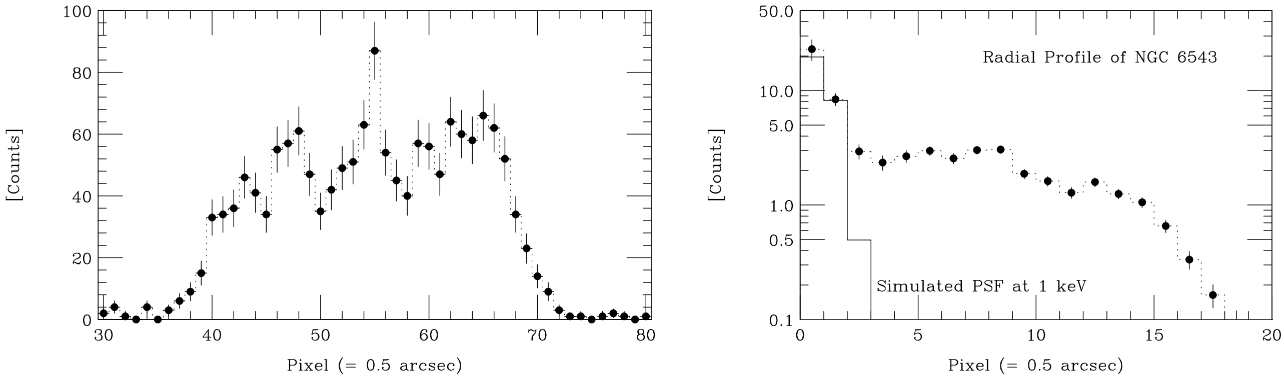

Figure 6.2: Background-inclusive 0.3–7 keV X-ray profiles of NGC 6543. (left) A linear profile projected on the vertical axis in figure 6.1. (right)A radial profile around the central star, compared with a simulated PSF.

Figure 6.2 gives a projected profile of the X-ray emission, which bears a sharp structure corresponding to the central point-like source (4.1.3). Figure 6.2 (right) compares a radial profile of NGC 6543 with a calculated PSF. Although diffuse component is present, the profile of the central feature is consistent with the PSF. We hence concluded that the point-like source is not resolved even with the superior angular resolution of *Chandra*. Below, we separately analyze the spectra of the diffuse emission and the point-like source.

6.1.2 Spectral analysis on diffuse emission

The definition of source and background regions, where spectra were extracted, are the same as in §4.1.3. As shown in 6.3, we defined two kinds of source regions; the diffuse emission and the point-like source. We first analyzed the diffuse component, which is the major subject of the present thesis. Figure 6.4 shows the 0.3–1.5 keV spectra of diffuse X-ray emission from NGC 6543. The Ne IX line is relatively clear at $\sim$ 0.9 keV of the spectrum.

The spectral fittings were carried out, using vAPEC model as same as in §5, assuming the interstellar absorption estimated by the ratio of optical and Hβ fluxes (Appendix B). Since the energy resolution of the *Chandra* ACIS-S (and that of the *XMM-Newton* EPIC-pn) is not so good as that of the *Szuaku* XIS, individual lines are not resolved. Therefore, we assume the C abundance to be the solar value. We also assume the Fe abundance to be zero, because the results of BD +30° 3639 suggests the iron depletion. We hereafter call this spectral fitting condition “nominal”. This “nominal” condition applies not only to NGC 6543, but also the other 6 sources (NGC 7027, NGC 7009, NGC 3242, NGC 2392, NGC 7293, and NGC 246) in the subsequent sections.

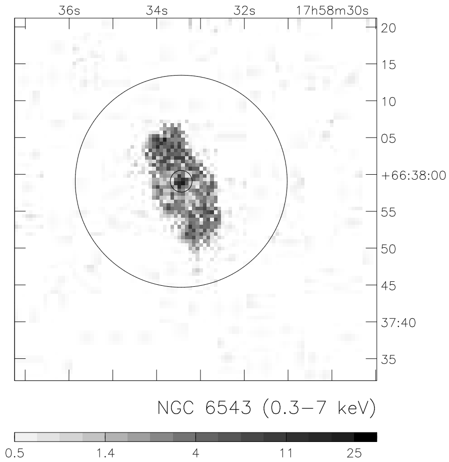

Figure 6.3: The definition of source regions, superposed on the 0.3–7 keV ACIS image of NGC 6543. The smaller circle represents the point-like source region, while the annulus indicates the diffuse emission region. The background region is defined as outside the diffuse emission region.

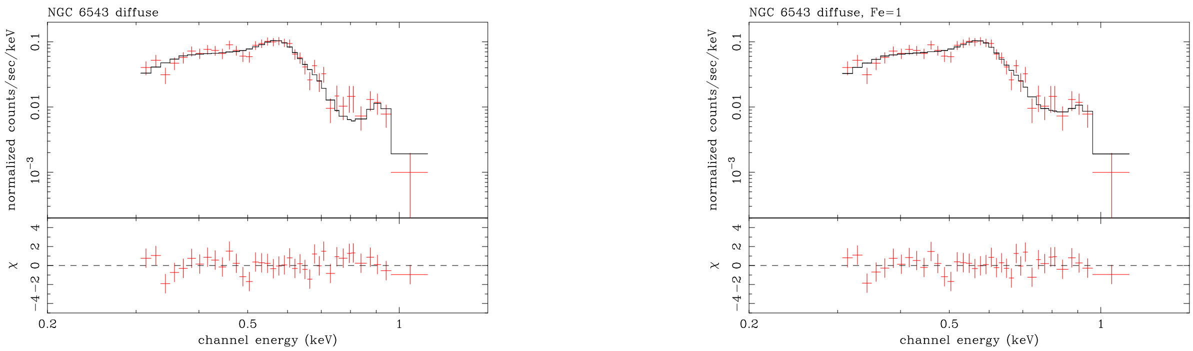

Figure 6.4: The *Chandra* ACIS spectra of the diffuse emission in NGC 6543, compared with the "nominal" vAPEC model (left) and the same model as "nominal", but assumed Fe to be the solar value (right). The bottom panel shows residuals between the data and model.

The best-fit parameters are summarized in table 6.1, and they indicate an oxygen deficit. The residuals in figure 6.4 exhibit some excess at 0.7–0.8 keV, where Fe-L lines complex is expected. We therefore tried to fit with the Fe abundance assumed to be the solar value. The residuals are eliminated (figure 6.4 right) and $\Delta\chi^2$ is slightly improved (table 6.1).

Table 6.1: Te best fit parameters of NGC 6543 with vAPEC.

Parameter	Diffuse		Point-like	
	Nominal	Fe=1	Nominal	Blackbody
$N_{\rm H}$ [cm^{-2}]*	4.4×10^{21}	4.4×10^{21}	4.4×10^{21}	4.4×10^{21}
kT [keV]	$0.15^{+0.014}_{-0.010}$	$0.14^{+0.007}_{-0.006}$	$0.17^{+0.39}_{-0.092}$	$0.11^{+0.032\dagger}_{-0.025}$
He*	1	1	1	–
C*	1	1	1	–
N	$0.88^{+0.55}_{-0.35}$	$0.94^{+0.55}_{-0.55}$	1.6	–
O	$0.27^{+0.14}_{-0.10}$	$0.30^{+0.11}_{-0.08}$	$0.22(< 238)$	–
Ne	$0.79^{+0.88}_{-0.47}$	$0.81^{+0.75}_{-0.46}$	2.5	–
Fe	0*	1*	0*	–
Norm.	3.1×10^{-4}	2.9×10^{-4}	1.9×10^{-5}	$11^{+33\dagger}_{-8}$
χ^2/d.o.f	29/33	26/33	1.5/6	5/9

* Fixed.

† The blackbody temperature and normalization.

6.1.3 Spectral analysis on a point-like source

The origin of point-like X-ray emission associated with planetary nebular nuclei is understood no better than that of the diffuse emission. One possible interpretation of the former is blackbody radiation from the surface of the central star, which has a temperature of up to $\sim 1 \times 10^5$ K. Accordingly, we first tried fitting the X-ray spectra with a blackbody model. Although the model is formally acceptable with χ^2/d.o.f =5/9 (table 6.1), the result presented in left panel of figure 6.5 suggests systematic residuals over the range of 0.4–1 keV. The obtained temperature, $\sim 1.3 \times 10^6$ K (table 6.1), is higher than the typical surface temperature of planetary nebular nuclei. In addition, the radiation region size given by the flux is too small, $\sim 0.5(D/1.55$ kpc) km, where D (kpc) is the

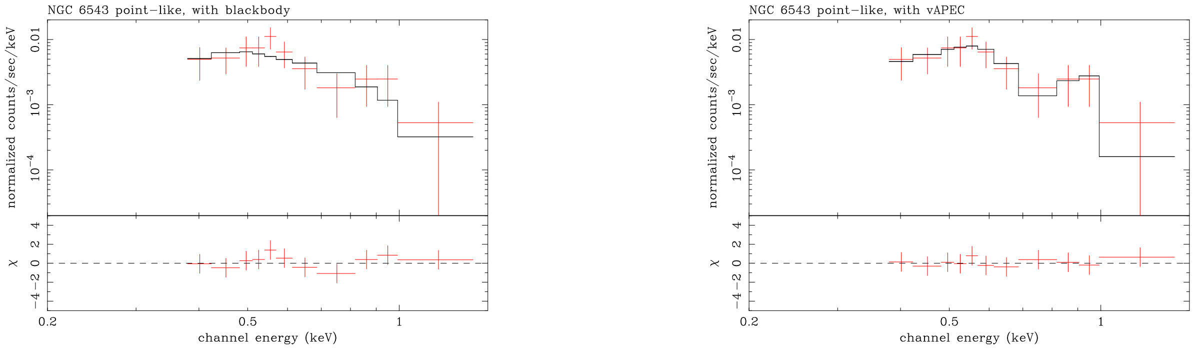

Figure 6.5: The *Chandra* ACIS spectrum of the point-like source associated with the central star of NGC 6543, compared with a blackbody model (left) and vAPEC model (right).

distance to the source. Thus the blackbody model fails to give a physically consistent view.

The residuals in the blackbody fit suggest that they are due to line emissions from an optically thin plasma. Therefore, we performed the nominal vAPEC fitting to the point-like source spectrum. As shown in right panel of figure 6.5, the plasma model better reproduce the observed data, and eliminated the residuals. Although the obtained parameters (table 6.1) are not constrained due to poor statistics, enhanced Ne and N abundances and oxygen deficit are suggested. The enhancement of N and Ne is higher than that of the diffuse emission. The plasma temperature is consistent with that of the diffuse component within errors.

The model normalization provide the emission measure $EM = n_e n_i V$ (§2.4.3 and §5.3.1), where n_e and n_i are again the densities of electron and ion, respectively, while V is the volume of the plasma. The *Chandra* angular resolution of $0.''5$ corresponds to $\sim$ 800 AU, assuming the distance of 1.55 kpc. Assuming the size of the X-ray emitting plasma associated with the central star to be $\lesssim$ 800 AU, and $n_e = n_i$, we obtain the electron density as $n_e \sim 300$ cm^{-3}. The volume and normalization of the diffuse emission are larger at least by 2 orders of magnitude, and smaller by an order of magnitude than those of point-like source, respectively. Hence the electron density of the diffuse X-ray component is inferred to be lower at least by an order of magnitude than that of the point-like source. These results suggests that a dense plasma concentrated in the center region is responsible for the point-like emission, while a much more tenuous and more extended plasma produce the diffuse X-ray component.

6.2 Diffuse X-ray Emission in NGC 7027

6.2.1 X-ray morphology

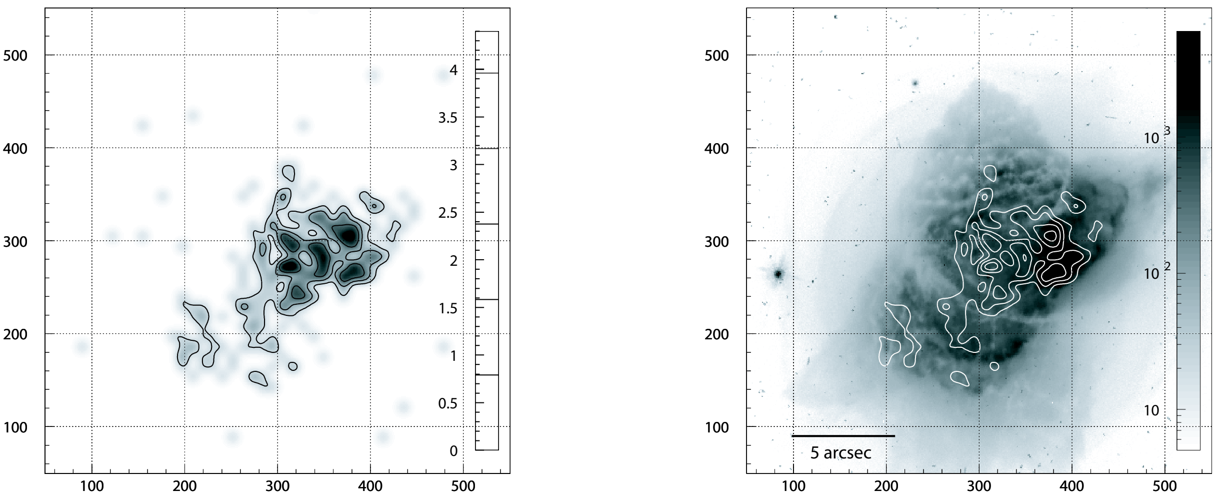

Figure 6.6: (left) Smoothed X-ray contours of NGC 7027 superposed on its gray-scale image. (right) A V-band image of NGC 7027 obtained with the *HST* WFPC2, on which the X-ray contours of the left panel are superposed. Axes are arbitrary, but 11 bins corresponds to $0.''5$.

Figure 6.6 gives the X-ray and optical images of NGC 7027. The X-ray emission has an asymmetrical and complicated morphology (left panel). However, the X-ray emission is confined within the optical dense shell, and coincides spatially with the brightest region in the optical band.

6.2.2 Spectral analysis

As shown in figure 6.7, the X-ray spectrum of NGC 7027 is remarkably hard in comparison with other X-ray emitting PNe. However, the X-ray flux sharply falls below 0.5 keV and above 1.5 keV.

We performed the nominal fitting to the X-ray spectrum. The results are shown in table 6.2 and left panel of figure 6.7. Although the nominal vAPEC model is formally acceptable, there is residuals above 1 keV. Then, we tried fitting with the Mg abundance varying freely. As shown in figure 6.7, the fit is a little improved statistically, but the parameters are unconstrained due to poor statistics. Although obtained parameters (table 6.2) suggests extremely enhanced nitrogen, its reality is questionable because N-K lines appear in energies of $\lesssim 0.5$ keV. Accordingly, we performed a fitting with the N abundance assumed to be the solar value.

Thus, it is rather difficult to quantify the spectrum of NGC 7027. One robust inference is that its plasma temperature must be relatively high ($\gtrsim$ 0.3 keV), in order for the spectrum to extend to $\sim$ 1.5 keV. In such high temperature, however, almost all carbon is fully ionized, and about half of nitrogen is also fully ionized (figure 2.10). It is likely that only Ne and Mg ions contribute the X-ray emission lines.

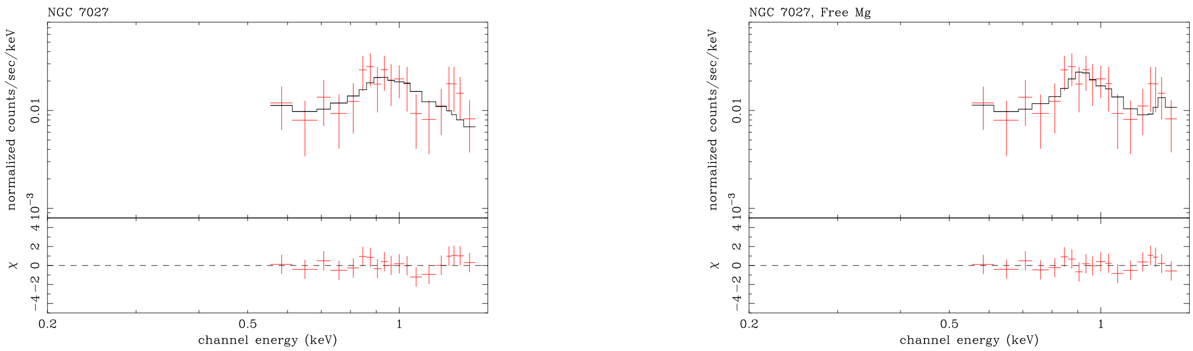

Figure 6.7: The *Chandra* ACIS spectrum of NGC 7027, compared with vAPEC models with the standard conditions (left) and Mg allowed to vary freely (right);

Table 6.2: The best-fit parameters with vAPEC of NGC 7027.

Parameter	Nominal	Free Mg	
		Free N	N=1
$N_{\rm H}$ [cm^{-2}]*	4.9×10^{21}	4.9×10^{21}	4.9×10^{21}
kT [keV]	$0.36^{+0.20}_{-0.10}$	$0.30^{+0.16}_{-0.07}$	$0.28^{+0.16}_{-0.07}$
He*	1	1	1
C*	1	1	1
N	$6.5(< 63)$	$3.6(< 51)$	1*
O	$\sim 0(< 0.45)$	$\sim 0(< 0.35)$	$\sim 0(< 0.77)$
Ne	$0.067(< 0.40)$	$0.079^{+0.80}_{-0.067}$	$0.062^{+0.84}_{-0.06}$
Mg	0*	$0.16(< 1.1)$	$0.17(< 0.63)$
Fe*	0	0	0
Norm.	1.6×10^{-3}	2.1×10^{-3}	2.7×10^{-3}
χ^2/d.o.f	8.3/14	6.1/13	6.7/14

* Fixed.

6.3 Other Diffuse X-ray Sources

6.3.1 NGC 3242

NGC 3242 was observed with *XMM-Newton* (§4.1.1), yielding an exposure of 13.6 ks after the screening. The *XMM-Newton* has moderately good angular resolution, even though not as good as that of *Chandra*. The X-ray images obtained with three cameras of the *XMM-Newton* EPIC are shown in figure 6.8, together with an optical image obtained with the *HST* in the same sky coordinate. Since the X-rays from this PN is very faint, the MOS-1 and MOS-2 images have patchy distributions. In §4.1.3, we already concluded that this X-ray source is extended by comparing their radial profiles with the simulated PSF (figure 4.7).

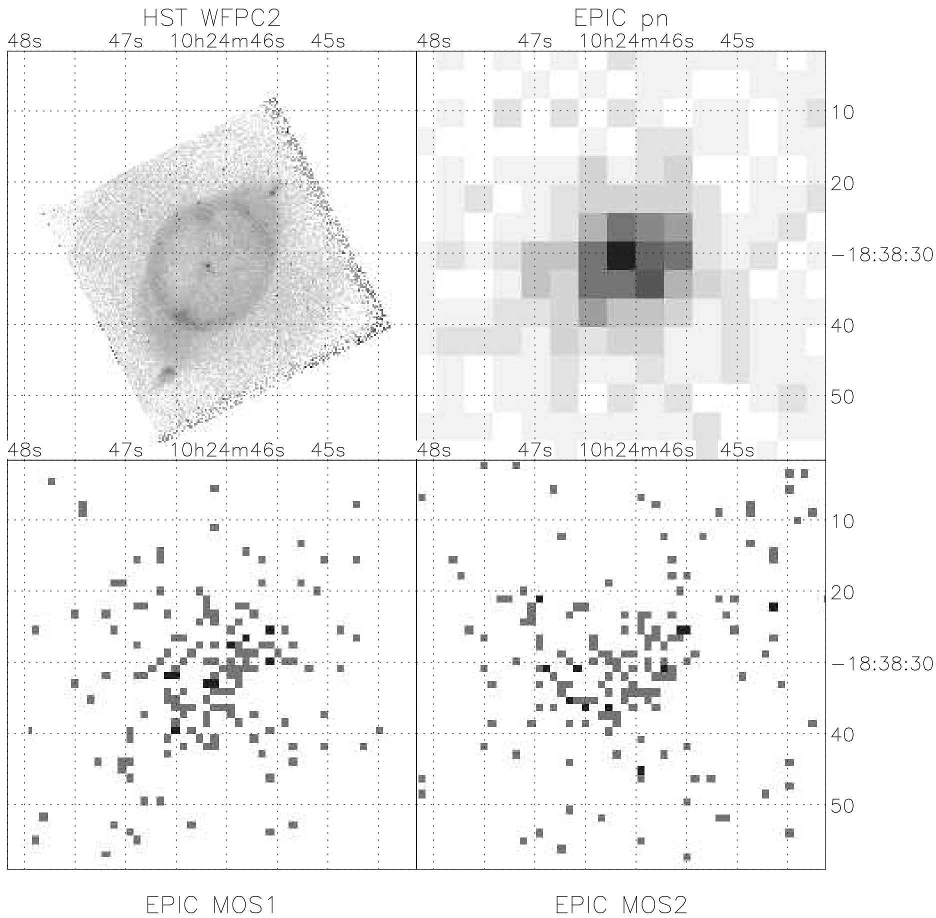

Figure 6.8: (top-left) The Hα image of NGC 3242 obtained with the *HST* WFPC2. The other three panels show raw X-ray images of NGC 3242 obtained with the *XMM-Newton* EPIC-pn, EPIC-MOS1, and EPIC-MOS2. The pixel sizes of EPIC-pn and EPIC-MOS images are 4″ and 1.″1, respectively.

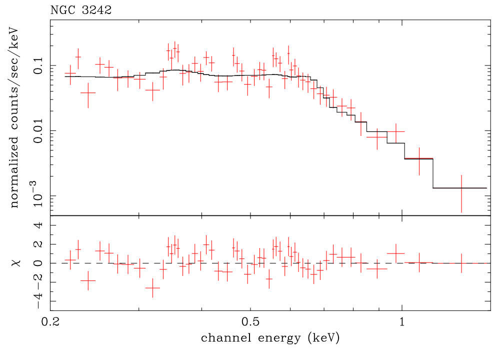

Figure 6.9: The *XMM-Newton* EPIC-pn spectrum of the diffuse emission in NGC 3242, fitted with a nominal vAPEC model.

As shown in figure 6.9, the X-ray spectrum of NGC 3242 is very soft; it retains a high flux level down to the lower energy limit of the EPIC-pn, while the flux gradually decreases toward higher energies above 0.5 keV. The nominal vAPEC model reproduce the spectrum to a fair degree (χ^2/d.o.f.$\simeq$1.35), with the fitting results summarized in table 6.3. As expected by the soft spectrum, the C and N abundances are enhanced relative to that of oxygen. One difference from other PNe is that the Ne abundance is lower than that of oxygen. Actually, the spectrum has no excess around the He-like Ne line to be expected at 0.91 keV.

Table 6.3: The vAPEC parameters obtained by the nominal fit to the spectra of NGC 3242 and NGC 7009.

Parameter	NGC 3242	NGC 7009
$N_{\rm H}$ [cm^{-2}]*	4.4×10^{20}	5.2×10^{20}
kT [keV]	$0.24^{+0.030}_{-0.030}$	$0.22^{+0.017}_{-0.015}$
He*	1	1
C*	1	1
N	$0.35^{+0.45}_{-0.30}$	$0.51^{+0.32}_{-0.23}$
O	$0.064^{+0.028}_{-0.022}$	$0.099^{+0.034}_{-0.019}$
Ne	$0.013 (< 0.051)$	$0.13^{+0.11}_{-0.069}$
Fe*	0	
Norm.	3.4×10^{-4}	4.3×10^{-4}
χ^2/d.o.f	62/46	86/103

* Fixed.

6.3.2 NGC 7009

Another diffuse X-ray emitting PN, which is observed by *XMM-Newton*, is NGC 7009 (§4.1.1). The obtained X-ray images are shown in figure 6.10, together with the optical image obtained by the *HST*. In the optical band, this PN has an elongated shape and a bipolar-like structure. X-ray morphology faithfully traces the inner bright shell in the optical image.

Figure 6.11 gives the EPIC-pn spectrum of NGC 7009, together with a successful fit with the vAPEC model. The NGC 7009 spectrum resembles that of NGC 3242 (figure 6.9) in the overall spectral shape. The best-fit parameters, summarized in table 6.3, indicate the enhanced C and N abundances relative to the O abundance, like in the case of NGC 3242. A remarkable difference between these two PNe is the Ne abundance. NGC 7009 has a relatively enhanced Ne abundance, while that of NGC 3242 is very low. Actually, the NGC 7009 spectrum exhibits a clear excess against the continuum at ∼0.91 keV, which is interpreted as the He-like Ne line.

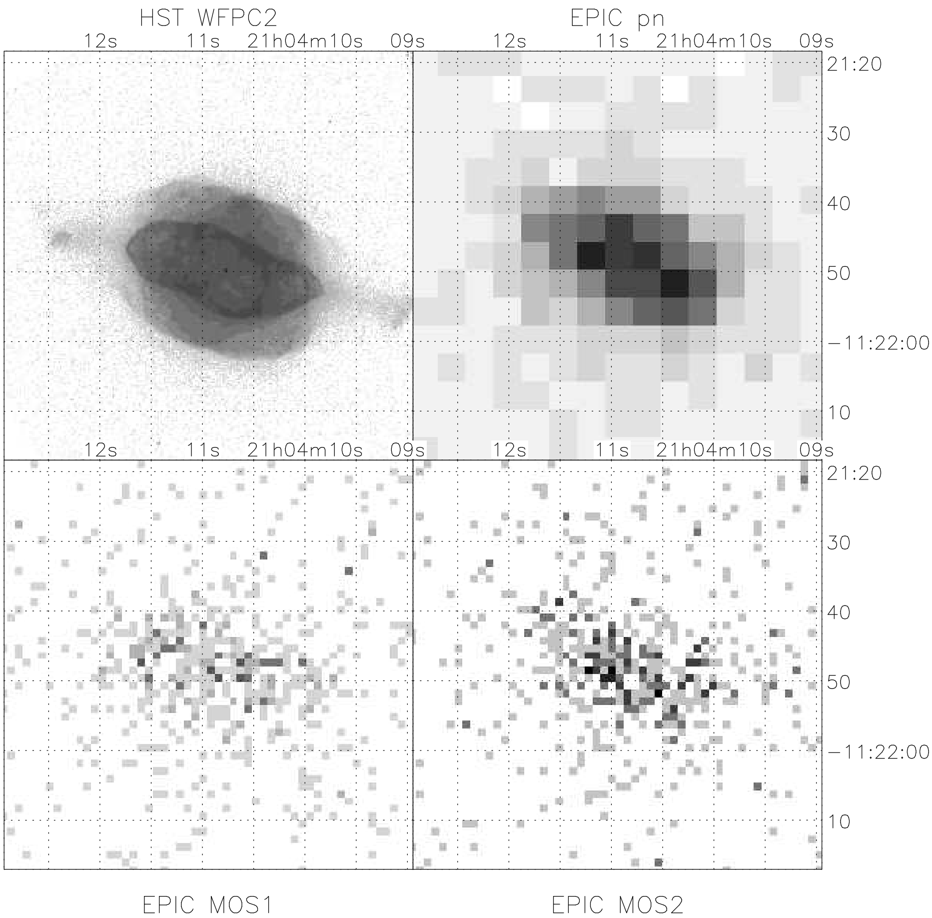

Figure 6.10: The same as figure 6.8, but for NGC 7009.

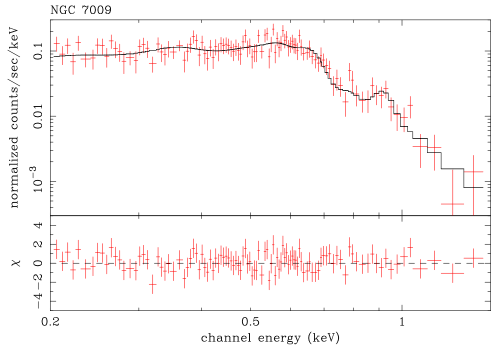

Figure 6.11: The same as figure 6.9, but for NGC 7009.

6.4 Point-Like Sources

6.4.1 NGC 2392

In the optical band, NGC 2392 has a spherical inner shell ($r \sim 15''$) with complicated filament-like features, and an impressive halo. As shown in figure 6.12, its X-ray emission (§4.1.1) concentrates into the optical bright inner shell. We did not obtained statistically enough photons to analyze the X-ray images due to a short exposure (8.1 ks) and its X-ray faintness. We compared the radial profile and the simulated PSF (figure 4.7), and then concluded that the X-ray source is not resolved spatially by the moderate angular resolution of *XMM-Newton*. However, there still remains a possibility that the X-ray emission from NGC 2392 is diffuse, since the angular resolution of *XMM-Newton*, $\sim 4''$, corresponds to 0.03 pc which is consistent with the physical size of BD $+30°$ 3639 resolved by *Chandra*.

Assuming that the X-ray emission is point-like, we first tried fitting the spectrum with a blackbody like in the case of the central source in NGC 6543 (§6.1.3). As shown in left panel of figure 6.13, a blackbody model cannot reproduce (χ^2/d.o.f.=41/29) the observed spectrum. In addition, the obtained temperature of 0.10 keV ($\sim 1.2 \times 10^6$ K) is too high for the surface temperature of the central star. Then, we fitted the X-ray spectrum with the nominal vAPEC model. The results are shown in figure 6.13 and table 6.4. Although some residuals remain between the model and the observed data, the nominal model gives an acceptable (χ^2/d.o.f=29/28) fit to the spectrum. The best-fit parameters again indicate C and N enhancements relative to oxygen. Neon significantly contributes to the X-ray spectrum, although the abundance is not so enhanced.

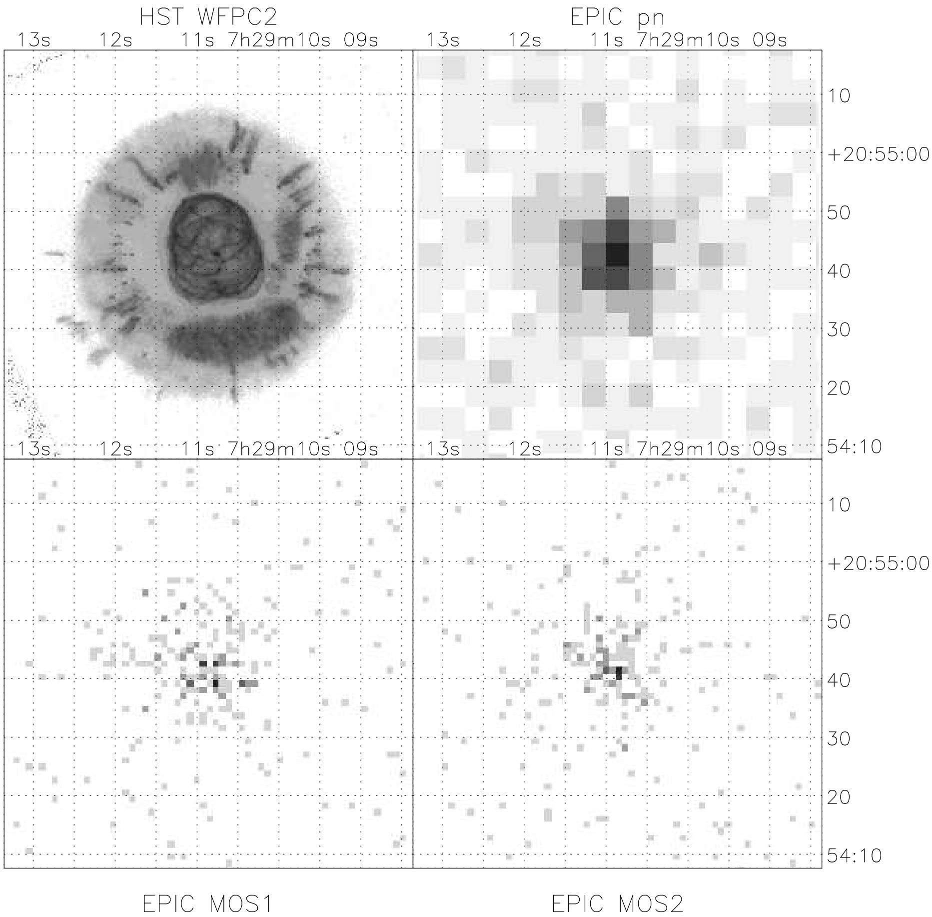

Figure 6.12: The same as figure 6.8, but for NGC 2392.

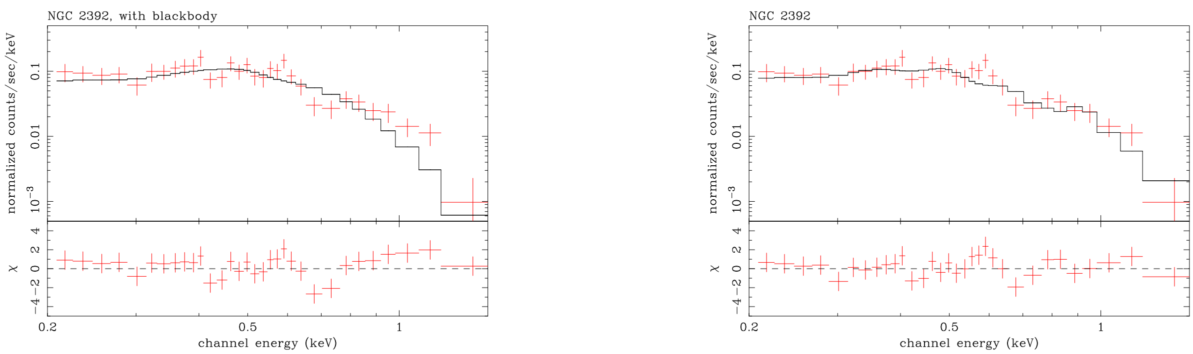

Figure 6.13: The *Chandra* ACIS spectrum of NGC 2392, fitted by a blackbody with a temperature of 0.10 keV (left), and a vAPEC model with the standard conditions (right).

Table 6.4: The best fit vAPEC parameters of NGC 2392.

Parameter	Nominal
$N_{\rm H}$ [cm^{-2}]*	7.0×10^{20}
kT [keV]	$0.26^{+0.051}_{-0.053}$
He*	1
C*	1
N	$0.49^{+0.66}_{-0.36}$
O	$0.014(< 0.031)$
Ne	$0.060^{+0.13}_{-0.06}$
Fe*	0
Norm.	6.7×10^{-4}
χ^2/d.o.f	29/28

* Fixed.

6.4.2 NGC 246

Figure 6.14 shows the optical and X-ray images of NGC 246 on the same scale. In optical bands, this PN has a large radius of $\sim 4'$. The ACIS-S image (right panel of figure 6.14) reveals a point-like source associated with the central star was detected, while no detectable X-ray diffuse emission.

The X-ray spectrum NGC 246, shown in figure 6.15, is very soft with the flux steeply falling down toward higher energies. Neither a blackbody model (top left panel) or the nominal vAPEC model (top right panel) reproduce the observed spectrum, with large values of reduced chi-squared as summarized in table 6.5. In these two fits, residuals between the model and data suggests an absorption edge at 0.4–0.5 keV. Therefore, we multiplied a photo-absorption edge to the nominal vAPEC model. As shown in bottom left panel of figure 6.15, the plasma model, multiplied by a photo-absorption edge, successfully reproduced the spectrum. The derived edge energy, 0.40 keV, is consistent with K-edge of neutral nitrogen. This fit implies a condition (table 6.5) wherein an optically thin emission, with extremely intense nitrogen lines (at 0.5 keV and several others), is absorbed by a material which is also highly nitrogen enhanced. While this case is interesting in relation to CNO-cycle products, the reality of this fit is not necessarily be clear.

Instead of a single absorption edge, we adopted alternatively an absorption model which can treat non-solar abundance. This model turned out to be also successful (table

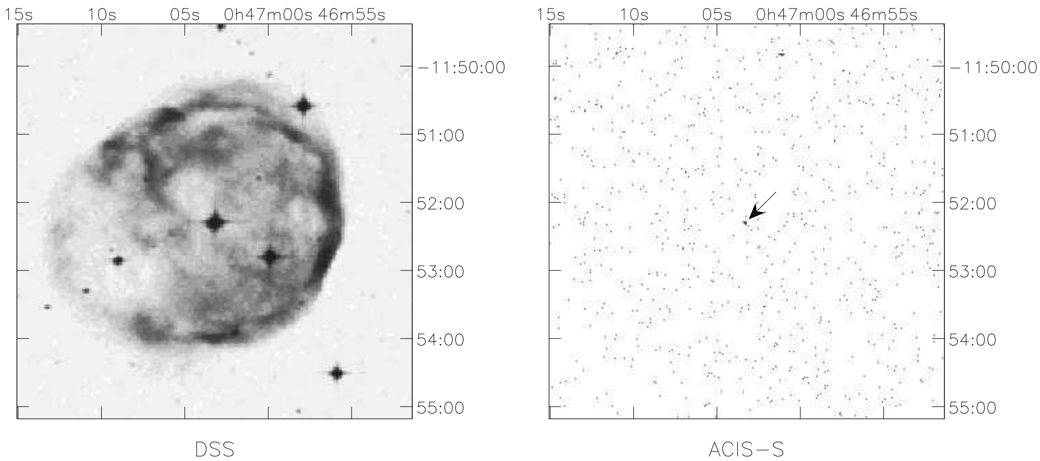

Figure 6.14: (left) An optical image of NGC 246 taken by the Digitized Sky Survey. (right) A raw 0.3–7 keV X-ray images of NGC 246 obtained with the *Chandra* ACIS-S. An arrow indicates the point-like source.

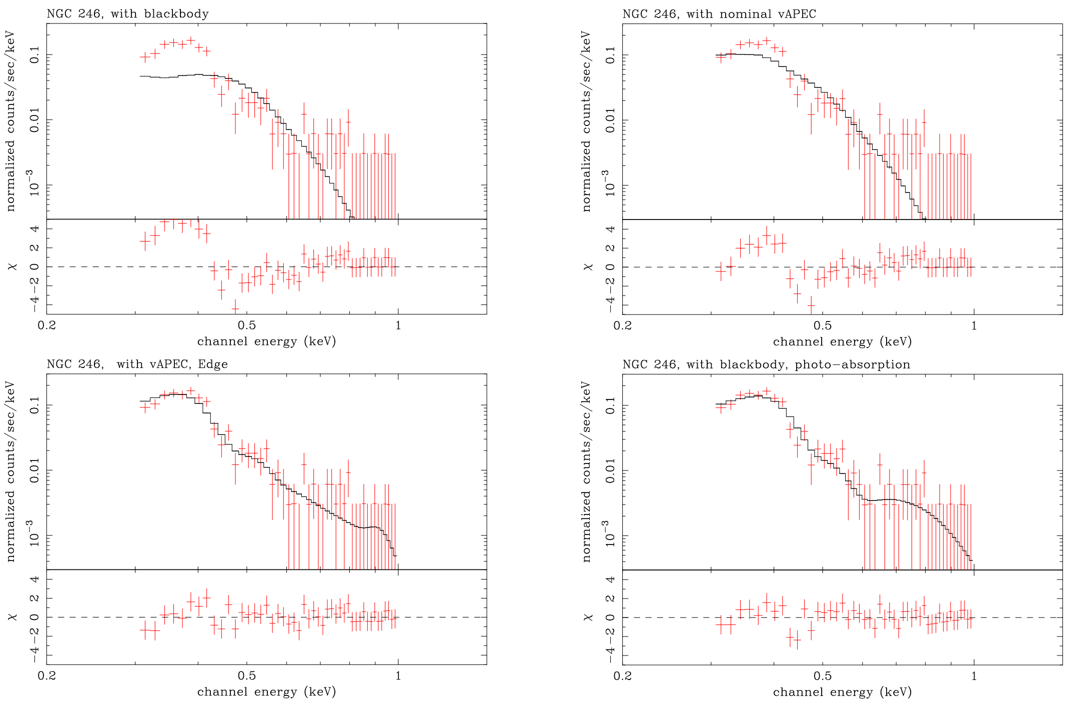

Figure 6.15: The 0.3–0.8 keV spectra of NGC 246 obtained with the *Chandra* ACIS-S, fitted with a blackbody model (top-left), the nominal vAPEC model (top-right), the vAPEC model multiplied by a photo-absorption edge (bottom-left) and a blackbody photo-absorbed by a material with variable abundances (bottom-right).

Table 6.5: The best fit vAPEC parameters of NGC 246 under various conditions.

	vAPEC			Blackbody	
Parameter	Nominal	Edge	Absorber	Fixed $N_{\rm H}$	Absorber
$N_{\rm H}$ [cm^{-2}]*	8.1×10^{20}	8.1×10^{20}	8.1×10^{20}	8.1×10^{20}	8.1×10^{20}
kT [keV]	$0.054^{+0.051}_{-0.053}$	$0.087^{+0.011}_{-0.016}$	$0.055^{+0.036}_{-0.012}$	0.045	$0.052^{+0.008}_{-0.009}$
He*	1	1	1	–	–
C*	1	1	1	–	–
N	0	$4.5^{+9.9}_{-4.0}$	$0(< 34)$	–	–
O	0	$0(< 0.087)$	$0.14(< 16)$	–	–
Ne	0	$0.18(< 1.0)$	$0(< 1.2)$	–	–
Fe*	0	0	0	–	–
Norm.	6.9×10^{-2}	6.8×10^{-3}	13	9.8×10^{4}	7.2×10^{5}
$E_{\rm edge}$	–	$0.41^{+0.006}_{-0.04}$	–	–	–
Optical depth	–	$5.0^{+2.5}_{-2.1}$	–	–	–
$N_{\rm H}$ [cm^{-2}]†	–	–	$(2.8^{+1.4}_{-2.5}) \times 10^{21}$	–	$(6.0^{+11}_{-2.5}) \times 10^{20}$
C‡	–	–	$0.3(< 31)$	–	$0.002(< 13)$
N‡	–	–	$28^{+123}_{-4.4}$	–	121^{+153}_{-15}
O‡	–	–	$3.5(< 19)$	–	$9.8^{+18}_{-3.1}$
χ^2/d.o.f	87/42	29/38	33/39	199/45	36/41

* Fixed.

† Equivalent hydrogen column density, for an additional absorber, which is allowed to have non-solar abundances.

‡ Abundances (in solar unit) of the additional absorber.

6.5), yielding again a nitrogen-enriched absorbing material. However, the implied metallicity of the emission region is very low, at least when He and C abundances are fixed at 1 solar.

The freedom introduced by non-solar-abundance absorber allows us to re-examine the blackbody scenario. Therefore, we tried fitting the spectrum with a blackbody multiplied by non-solar photo-absorption. This model successfully reproduce the spectrum as shown in bottom-right panel of figure 6.15. The best-fit parameters indicates a blackbody with a temperature of 53 eV ($\sim 6.1 \times 10^5$ K), obscured by nitrogen-rich matter. The radiation region given by the model normalization is $\sim 40(D/0.495)$ km, where D (kpc) is the distance to the source.

In this way, the spectrum of the point-like source in NGC 246 allows a variety of emission models with very different astrophysical meanings. At present, we cannot distinguish them; we cannot even tell at this stage whether the emission is optically thick or thin.

6.4.3 NGC 7293

NGC 7293, known as "Helix nebula", has a large size of $> 10'$, so that the *Chandra* ACIS-S covered a part of the nebula. The field of view and obtained images are shown in figure 6.16. *Chandra* detected the X-ray source, but was not able to resolve it even with its superb angular resolution.

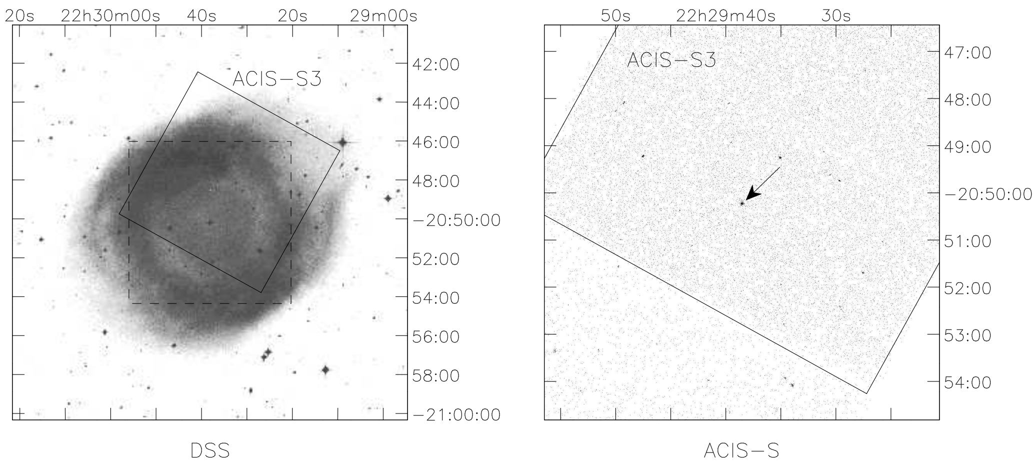

Figure 6.16: (left) An optical image of NGC 7293 taken by Digitized Sky Survey. (right) Raw X-ray image in 0.3–7 keV of NGC 7293 obtained with the *Chandra* ACIS-S. A field of view of ACIS-S3 chip is superposed on the images. An arrow in the right panel indicates a point-like X-ray source.

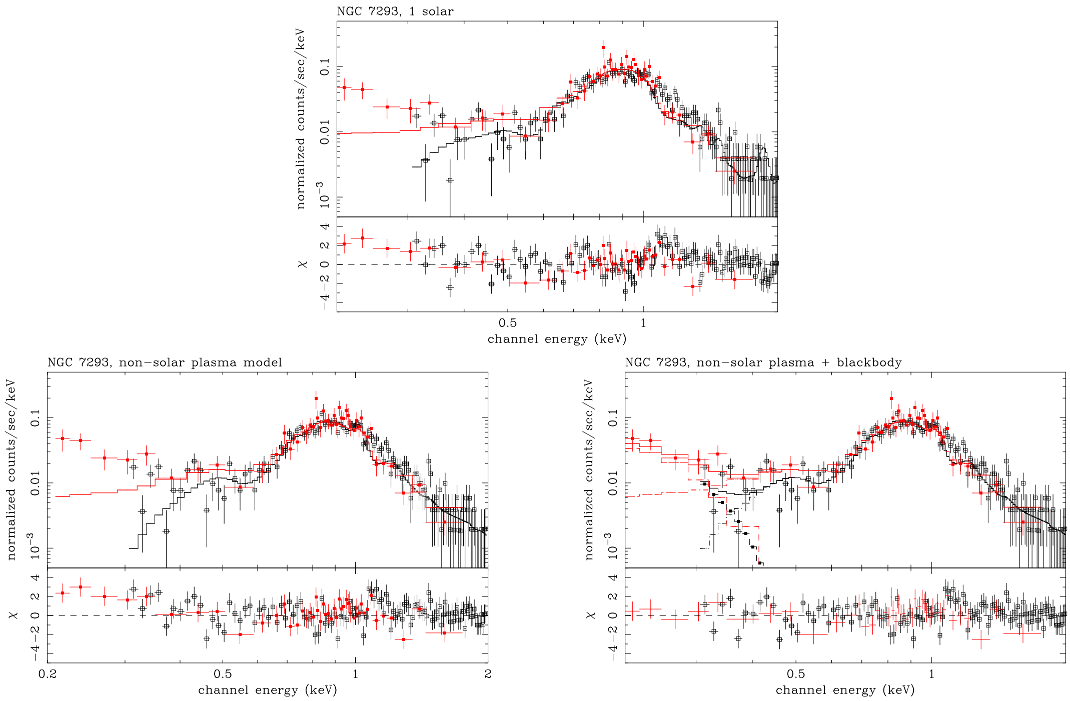

Figure 6.17: The 0.2–2 keV spectra of NGC 7293 obtained with the *Chandra* ACIS-S (black open squares) and the *XMM-Newton* EPIC-pn (red filled squares). The two spectra are fitted jointly with three models; a solar abundance plasma model (top), a non-solar plasma model (bottom-left), and a non-solar plasma model to which a blackbody is added (bottom-right).

Table 6.6: The best fit parameters with vAPEC of NGC 7293.

Parameter	1 solar	Non-solar	Non-solar plasma + blackbody
$N_{\rm H}$ [cm^{-2}]	$(5.9^{+2.2}_{-1.9}) \times 10^{20}$	$(1.5^{+0.3}_{-0.4}) \times 10^{21}$	$1.5 \times 10^{21*}$
kT [keV]	$0.77^{+0.019}_{-0.020}$	$0.67^{+0.048}_{-0.025}$	0.67^{*}
He*	1	1	
C*	1	1	
N	1^{*}	$0(< 0.54)$	0^{*}
O	1^{*}	$0.10^{+0.11}_{-0.10}$	0.10^{*}
Ne	1^{*}	$1.2^{+0.31}_{-0.26}$	1.2^{*}
Mg	1^{*}	$0.041(< 0.18)$	0.041^{*}
Fe	1^{*}	$0.29^{+0.046}_{-0.042}$	0.29^{*}
Others	1^{*}	0^{*}	0^{*}
Norm.(ACIS-S/EPIC-pn)	$4.9/3.8 \times 10^{-5}$	$1.8/1.3 \times 10^{-4}$	$1.8/1.3 \times 10^{-4*}$
χ^2/d.o.f	255/157	220/152	191/159
kT [keV]	–	–	$0.015^{\dagger}$
Norm.	–	–	6.7×10^{10}

* Fixed.

† Unconstrained.

This PN was observed by both *Chandra* and *XMM-Newton* (table 4.1). The X-ray spectra shown in figure 6.17 do not resemble X-ray spectra of any other X-ray emitting PNe. There is an excess at 0.4–1 keV, like a broad line emission, against the soft continuum. From such spectral feature, it is easy to infer that a simple blackbody cannot reproduce the spectrum.

We first tried a 1 solar plasma model to jointly fit the X-ray spectra from the *Chandra* ACIS and the *XMM-Newton* EPIC-pn. As shown in figure 6.17, the solar abundance model roughly reproduced the spectrum. However, there are residuals at 0.5–0.6 keV and above 1 keV, which make the fit unacceptable (table 6.6). These residuals suggest that Mg and Fe lines contribute significantly to the X-ray emission. Accordingly, we modified the nominal fitting conditions a little, and to let the Mg and Fe abundances vary freely. With this modified nominal conditions, we simultaneously fitted the ACIS-S and EPIC-pn spectra. The results are shown in figure 6.17 and table 6.6. The fitting was improved by $\Delta\chi \sim 35$, and the obtained parameters suggests the enhanced Ne abundance and depletion of nitrogen.

As shown in bottom-left panel of figure 6.17, residuals still remain below 0.4 keV. One possible interpretation is the presence of another soft component, such as a low-temperature blackbody which has been suggested by the *ROSAT* observation (Leahy et al. 1996). Therefore, we fixed the best-fit value of the plasma model, and added a blackbody component. The best-fit parameters indicates the blackbody temperature of 15 eV ($\sim 1.7 \times 10^5$) K, and the size of radiation region as $5500(D/0.243)$ km. Thus, the additional blackbody component is reasonably explained by optically thick radiation from the central star. Consequently, the X-ray emission of NGC 7293 may be explained as consisting of a blackbody from the central star, and an optically-thin emission from a plasma present around the central star.

Chapter 7

DISCUSSION

7.1 Summary of Results

7.1.1 X-ray luminosities

We analyzed X-ray spectra of the 8 PNe listed in table 7.1, together with their individual X-ray morphology; 4 objects emitting diffuse X-rays, 3 hosting point-like X-ray sources associated with the central stars, and the other consisting of both diffuse and point-like sources. Their absorption-corrected 0.2–2 keV flux is typically $\sim 1 \times 10^{-13}$ erg s^{-1} cm^{-2}, except BD +30° 3639 which has a higher X-ray flux than the others by more than an order of magnitude. The 0.2–2 keV X-ray luminosities of these PNe are in the range of $(0.1\text{–}5)\times 10^{31}$ erg s^{-1} cm^{-2}, while BD +30° 3639 has a much higher luminosity of 1.4×10^{33} erg s^{-1} cm^{-2}.

As described in §6.4.2, the spectrum of NGC 246 has characteristics different from those of the others, with a hint of heavy intrinsic absorption. In table 7.1, we show absorption-uncorrected flux and luminosity for NGC 246, in contrast to those of the other PNe which are corrected for the absorption. Its flux and luminosity are similar to those of typical PNe. However, if the strong absorption features are true, the intrinsic X-ray luminosity, after correction for the absorption, increases by nearly 4 orders of magnitude in 0.2–2 keV. Furthermore, we were not able to tell whether the X-ray emission from NGC 246 is due to optically thin or thick processes. Because of these uncertainties, we hereafter exclude NGC 246 from our discussion.

In order to calculate such quantities as the X-ray luminosity, we assume distances to the sources as given in table 7.1. These distances contain uncertainties at the worst case by several factors.

Table 7.1: The X-ray properties of individual PNe.

Target name	$F_x{}^*$ [erg s^{-1} cm^{-2}]	$L_x{}^*$ [erg s^{-1}]	Distance † [kpc]*	Morphology
BD +30° 3639	$6.8 \times 10^{-12\ddagger}$	$1.4 \times 10^{33\ddagger}$	1.3	diffuse
NGC 6543	1.6×10^{-13}	4.6×10^{31}	1.55	diffuse
	1.2×10^{-14}	3.5×10^{30}		point-like
NGC 7027	6.4×10^{-13}	3.5×10^{31}	0.68	diffuse
NGC 3242	1.1×10^{-13}	4.0×10^{30}	0.55	diffuse
NGC 7009	1.7×10^{-13}	1.5×10^{31}	0.86	diffuse
NGC 2392	2.0×10^{-13}	3.7×10^{31}	1.25	point-like
NGC 246	$2.2 \times 10^{-13\S}$	6.5×10^{30}	0.495	point-like
NGC 7293	$2.0 \times 10^{-13\ddagger}$	$1.1 \times 10^{30\ddagger}$	0.213	point-like
	$1.5 \times 10^{-13\|}$	$8.2 \times 10^{29\|}$	0.213	point-like

* In 0.2–2 keV, corrected for the interstellar absorption, except NGC 246.

† The same as table 4.5.

‡ The flux of the ACIS-S spectrum.

§ Absorption uncorrected fluxes.

$^\|$ The flux of the EPIC-pn spectrum.

7.1.2 Plasma densities and masses

The densities and masses of the X-ray emitting plasmas in our sample PNe can be derived from the spectral parameters, through the following steps. Generally, the X-ray luminosity L_x from an optically thin hot plasma is written as

$$L_\mathrm{x} = \Lambda(T, Z)EM = \Lambda(T, Z)n_e n_i V\eta, \tag{7.1}$$

where V is the volume of X-ray emitting region, η is a filling factor ($\eta < 1$), while $\Lambda(T, Z)$ and EM are cooling function and emission measure, respectively (§2.4.3). The measured X-ray flux of a PN yields EM of the X-ray emitting plasma associated with it. Dividing EM by V, and assuming $\eta = 1$ and $n_e = n_i$, the electron density can be derived. Three PNe, BD +30° 3639, NGC 6543, and NGC 7027, have been spatially resolved by *Chandra*, and their images provide the size of the X-ray emitting region. Two PNe, NGC 3242 and NGC 7009, have not been resolved spatially, because of the limited angular resolution of *XMM-Newton*, but their X-ray images suggests that the diffuse X-ray emission comes from optical inner shells of individual PNe (§6). Therefore, we adopt the radii of optical bright cores of these two PNe as those of the X-ray region. To simplify the calculation, we assume spherical morphology and uniform density in the X-ray emitting region. With the electron density and the assumed volume, we can finally obtain the total mass of the X-ray emitting matter.

The densities and masses of the X-ray emitting plasmas, derived in this way, are summarized in table 7.2. Assuming $n_e = n_i$, we have thus obtained electron densities of 10–130 cm^{-3}. These are lower limits, since heavy elements possibly dominate the plasma. Even in the case of NGC 7027 with the highest density, the Thomson optical depth is 5×10^{-6}, which is small enough to ensure an optically thin condition. The X-ray emitting hot plasmas in these PNe are thus inferred to have masses of $(1\text{–}4) \times 10^{-4} M_\odot$, which is a negligible fraction of the masses of these systems.

In the case of point-like X-ray sources associated with the central stars, the X-ray emitting region are not resolved, and only upper limits are set on their sizes by the angular resolution of the X-ray telescopes. By the same procedure as for the diffuse X-ray emission, we have constrained the electron densities and masses of their plasmas. As shown in table 7.3, the electron densities do not differ from those of diffuse X-ray emitting PNe. Among the 3 objects in this table, NGC 6543 and NGC 7293 were observed by *Chandra*, so that the upper limits on their X-ray sizes are tight, 100–800 AU. This means that the X-rays come from very near the central star. The total X-ray emitting masses of these two PNe are at least by 1 to 2 orders of magnitude lower than those of the diffuse X-ray emitting

Table 7.2: The plasma parameters of the diffuse X-ray emitting PNe.

Target name	Angular diameter [$''$]	Diameter [pc]	EM [cm^{-3}]	n_e [cm^{-3}]	Mass [$M_\odot$]	Distance * [kpc]*
BD +30° 3639	~ 5 (5×6)	0.03	5.7×10^{55}	120	3.9×10^{-4}	1.3
NGC 6543	~ 7 (7×16)	0.05	8.4×10^{54}	22	3.3×10^{-4}	1.55
NGC 7027	$\sim 6(6 \times 11)$	0.02	1.5×10^{55}	130	1.0×10^{-4}	0.68
NGC 3242	15†	0.04	1.2×10^{54}	12	8.3×10^{-5}	0.55
NGC 7009	10 (10×25)‡	0.04	3.8×10^{54}	21	1.6×10^{-4}	0.86

* The same as table 4.5.

† Palla et al. (2002).

‡Guerrero et al. (2002).

Table 7.3: The plasma parameters of the point-like X-ray sources associated with the central stars of PNe.

Target name	Upper limit size		EM	n_e	Mass	Distance †
	Angular	Physical	[cm^{-3}]	[cm^{-3}]	[$M_\odot$]	[kpc]
NGC 6543	$0''.5$	780 AU	5.5×10^{53}	>290	$< 1.6 \times 10^{-6}$	1.55
NGC 2392	$4''.3$	0.03 pc	1.3×10^{55}	>76	$< 1.4 \times 10^{-4}$	1.25
NGC 7293	$0''.5$	110 AU	8.4×10^{52}	>2200	$< 3.2 \times 10^{-8}$	0.213

* Angular resolution of X-ray telescopes in FWHM.

† The same as table 4.5.

Table 7.4: The plasma temperatures of the PNe.

Target name	kT [keV]	v_∞ [km s^{-1}]*	p [erg cm^{-3}]	U [erg]
BD +30° 3639	0.19±0.01	790±50	7.3×10^{-8}	4.6×10^{43}
NGC 6543	0.14±0.01	1600±100	9.9×10^{-9}	2.9×10^{43}
	$0.17^{+0.39}_{-0.09}$	–†	1.6×10^{-7}	1.6×10^{42}
NGC 7027	$0.28^{+0.16}_{-0.07}$	–	1.2×10^{-7}	2.2×10^{43}
NGC 3242	0.24±0.03	2200	9.2×10^{-9}	1.4×10^{43}
NGC 7009	0.22±0.02	2800	1.5×10^{-8}	2.2×10^{43}
NGC 2392	0.26±0.05	∼400	6.3×10^{-8}	4.0×10^{43}
NGC 7293	$0.67^{+0.05}_{-0.03}$	–†	2.4×10^{-7}	6.5×10^{39}

* The same as table 4.5.

† Point-like sources resolved by *Chandra*.

PNe. In contrast, NGC 2392 was observed with *XMM-Newton*, and hence the size is not tightly constrained. The upper limit size of 0.03 pc and the upper limit mass of 1.4×10^{-4} are rather similar to those of the diffuse X-ray emitting PNe. This object could therefore be a diffuse X-ray emitter, like those listed in table 7.2. It is worth while observing this PN with the superior angular resolution of *Chandra*.

The spectra of point-like sources in NGC 6543 and NGC 7293 are well reproduced by optically thin thermal plasma emission, which is the same model as applied to the spectra of the diffuse X-ray emission from our sample PNe. However, the sizes of their emission regions, 100–800 AU at most, is at last two orders of magnitude smaller than those of the diffuse X-ray objects. The origin of these point-like sources is still unclear.

7.1.3 Plasma temperatures

The X-ray spectra contain information on the plasma temperature, which is another important plasma parameter beside the density. The spectrally determined temperatures of our sample PNe are summarized in table 7.4, together with terminal velocities of the fast stellar wind determined by P-Cygni profiles of UV spectra, for a later comparison. The measured plasma temperatures of our sample PNe are distributed in the range of 0.14–0.28 keV, with a concentration around 0.2 keV, except NGC 7293 which has a significantly higher plasma temperature.

In §7.1.2, we have already obtained electron density n_e and volume V of the plasma associated with each PN. With these parameters and the plasma temperature, we can calculate the total plasma energy U and plasma pressure p, which are written as

$$U = 3n_e kTV, \tag{7.2}$$

$$p = 2n_e kT. \tag{7.3}$$

The obtained parameters of individual PNe are shown in table 7.4.

7.1.4 Abundances

As the most important outcome of our X-ray spectral analysis, we have estimated metal abundances of the X-ray emitting hot plasmas associated with the 7 PNe. The obtained eight abundance patterns are shown in figure 7.1, where NGC 6543 are divided into the diffuse emission and the point-like source, since we have separately analyzed them. Except BD +30° 3639, the C abundance is fixed to the solar value.

BD +30° 3639 is the only case where the observation was performed with *Suzaku*, and the CNO lines were resolved with the XIS (§5). Therefore, we have succeeded in firmly constraining the abundance ratios of C to O, N to O, and Ne to O. Table 7.5 summarizes the abundance ratios of BD +30° 3639 in solar units (§5.3), and converts them into direct number ratios among C, N, O, and Ne. Thus, this PN shows a strongly enhanced C abundance and relatively depleted oxygen. Abundances of N and Ne are several times higher than that of O.

Among the other 7 spectra, NGC 7009, NGC 2392, and NGC 6543 (diffuse) have similar abundance patterns; relatively enhanced C abundances, relatively low O, and Ne abundances higher than O. These trends are also the same as those of BD +30° 3639. Although NGC 3242 has the same pattern, C>N>O, as the 3 PNe mentioned above, this PN has a significantly lower Ne abundance. The remaining 3 spectra, including NGC 6543 (point-like), NGC 7293, NGC 7027, have large uncertainties in their abundance determinations due to poor statistics.

In figure 7.2, we plot the Ne/O ratios of the 7 spectra against the C/O ratios, together with that of BD +30° 3639. Only in the case of BD +30° 3639, 90% errors are determined by confidence contours (§5.3.4) by virtue of the Suzaku spectra. Other PNe have large uncertainties which are based on a simple error propagation. The two point-like sources has larger Ne/O than other diffuse X-ray emission, although the sample is limited. The most important inference from figure 7.2 is that the diffuse X-ray emission exhibits systematically high abundance of carbon, compared to other metals.

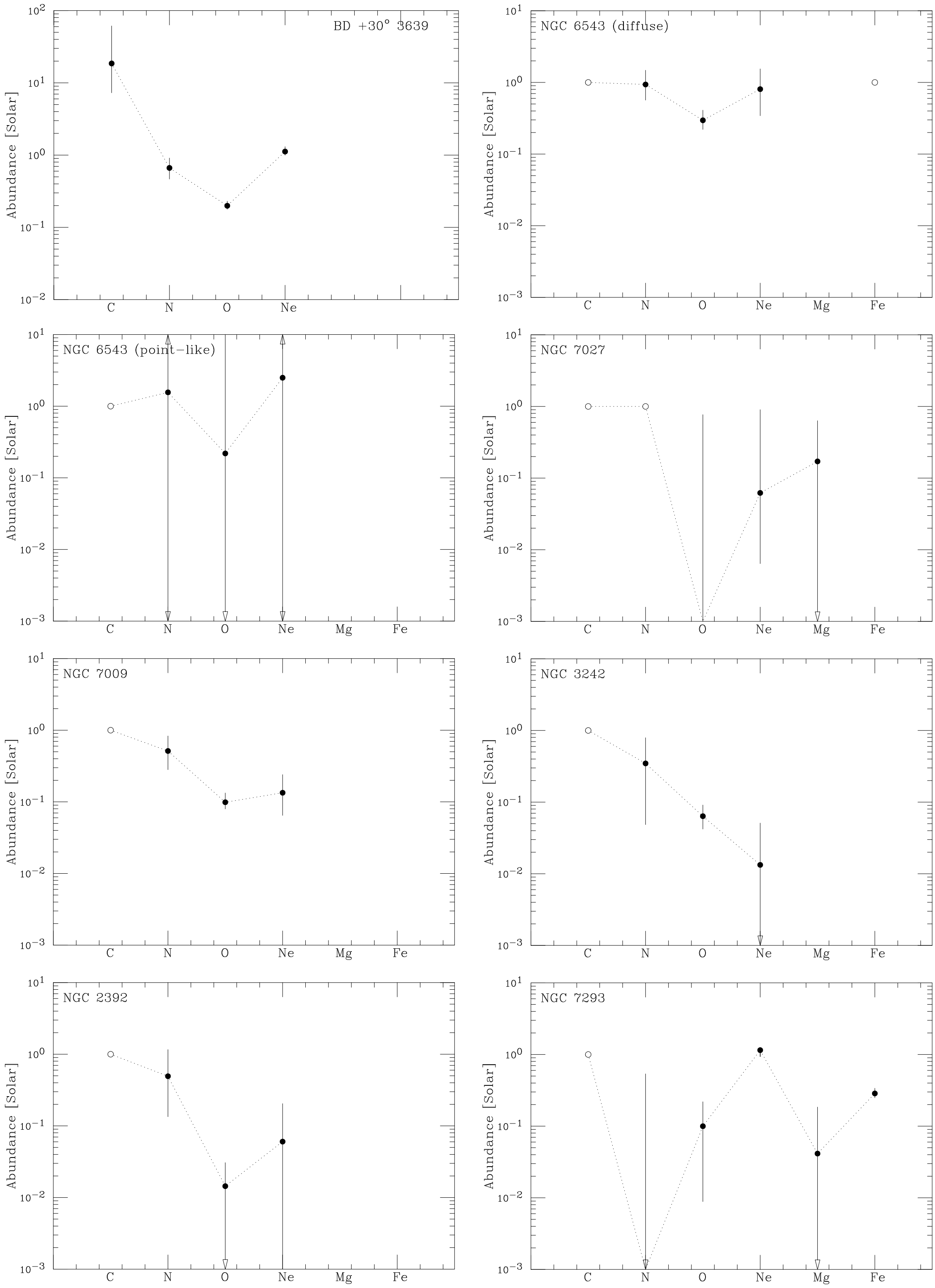

Figure 7.1: The X-ray abundance patterns of individual PNe. Open circles indicate the fixed values.

Table 7.5: The derived abundance ratios of X-ray emission from BD +30° 3639.

	Ratio [solar]	The number ratio
C/O	95	41
N/O	3.3	0.43
Ne/O	5.5	0.77

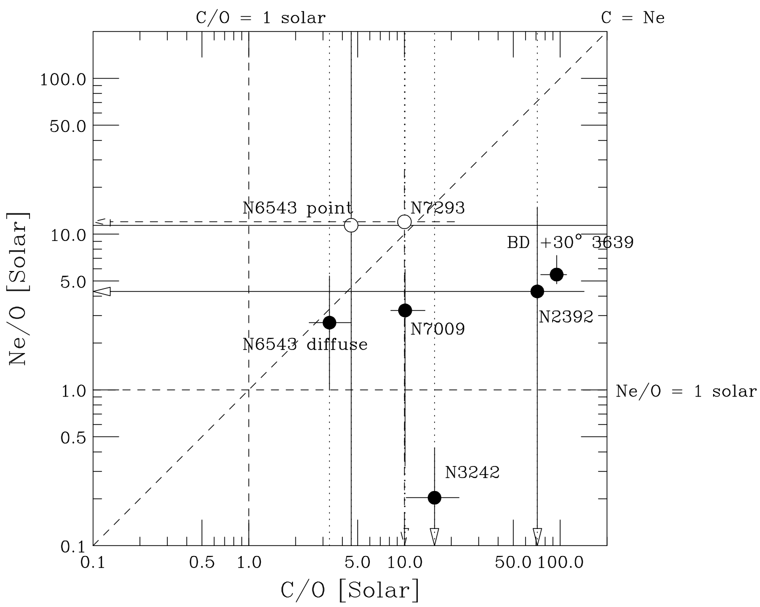

Figure 7.2: A scatter plot between the C/O vs. Ne/O ratios. Filled circles represent the diffuse X-ray emitting PNe, while open circles indicate the point-like X-ray sources. NGC 2392 is treated as a diffuse source.

7.2 Comparison with Information in Other Wavelengths

The metal abundances in PNe have been studied extensively in the infrared (IR), optical, and ultraviolet (UV) bands, long before the X-ray studies. Therefore, it is of basic importance to compare our X-ray results with IR-Optical-UV abundances. In these frequencies, abundances of individual elements are derived from line intensities of ions, which are photoionized by UV photons from the central star, or are collisionally excited by free electrons. We must however keep in mind that the X-ray and IR/optical/UV measurements do not necessarily give identical results, since these two methods sample different materials in a single PN; the former is expected to probe into the fast winds, while the latter the AGB remnant (§2.3.1).

Table 7.6 compare the abundances ratios we derived, with those obtained in other wavelengths. (We note again that the unit of abundances and abundance ratios is the solar values refereeing to Anders and Grevesse 1989.) These values in table 7.6 are visualized in figure 7.3, which compares the X-rays and IR/optical/UV results in four scatter plots corresponding to the O/H, C/O, N/O, and Ne/O ratios. Thus, in all PNe, the X-ray derived O/H ratios are lower than those from IR/optical/UV measurements. The X-ray C/O ratios are more strongly enhanced than those in the other bands, while the N/O ratios are consistent with nebular values at several times solar value. Although most of PNe have the X-ray Ne/O abundances comparable to those in the longer wavelengths, BD +30° 3639 has a significantly higher X-ray value.

Except BD +30° 3639, the 7 PNe spectra have been analyzed with the C abundance fixed to the solar value (§6). Therefore, we should be careful about them until we resolve their CNO blend lines, like in the case of BD +30° 3639, in future X-ray observations.

Figure 7.4 demonstrates how the C/O ratio of BD +30° 3639 is enhanced. Optical nebular abundances, including those of BD +30° 3639, are thus widely distributed, but not so different from those of H II regions or B stars which are expected to have nominal cosmic abundances. Compared to that, the X-ray C/O ratio of BD +30° 3639 is largely deviated from major data points. The Ne/O ratio also shows deviation from major population, while the X-ray N/O ratio is within the distribution of nebular abundance ratios.

Table 7.6: The comparison between X-ray and IR-optical-UV abundance ratios.

Target name	*	He/H	O/H	C/O	N/O	Ne/O	Ref.
BD +30° 3639	X	$1^{\dagger}$	$0.20^{+0.20}_{-0.021}$	95^{+15}_{-20}	$3.3^{+1.7}_{-2.3}$	$5.5^{+1.8}_{-0.7}$	
	O	2.2	0.54	3.7	1.8	2.8	a
	O	0.21	0.44	2.2	2.4	$> 1.8 \times 10^{-3}$	b
NGC 6543	X	$1^{\dagger}$	$0.30^{+0.11}_{-0.08}$	$3.3^{+1.2}_{-0.8}$	$3.1^{+2.2}_{-2.0}$	$2.7^{+2.7}_{-1.7}$	
	O	1.2	0.65	1.1	3.2	2.4	a
	O	1.3	0.55	1.2	2.0	1.5	c
NGC 7027	X	$1^{\dagger}$	$\sim 0(< 0.77)$	$1^{\dagger}/0$	$1^{\dagger}/0$	$0.062^{+0.84}_{-0.06}/0$	
	O	1.13 ± 0.20	0.60 ± 0.09	4.4 ± 0.9	2.4 ± 0.4	1.86 ± 0.28	d
	O	1.06	0.48	3.4	3.0	1.7	e
NGC 3242	X	$1^{\dagger}$	$0.064^{+0.028}_{-0.022}$	$16^{+6.8}_{-5.4}$	$5.5^{+7.4}_{-5.1}$	$0.20(< 0.22)$	
	O	0.82 ± 0.10	0.40 ± 0.06	2.9 ± 1.1	1.4 ± 0.5	1.66 ± 0.28	d
NGC 7009	X	$1^{\dagger}$	$0.099^{+0.034}_{-0.019}$	$10^{+3.5}_{-1.9}$	$5.2^{+3.7}_{-2.5}$	$1.3^{+1.2}_{-0.74}$	
	O	1.23 ± 0.20	0.66 ± 0.10	1.9 ± 0.7	4.3 ± 1.7	1.93 ± 0.28	d
NGC 2392	X	$1^{\dagger}$	0.014(<0.031)	$71(< 142))$	$35(< 59)$	$4.3(< 10)$	
	O	0.82 ± 0.10	0.33 ± 0.05	1.8 ± 0.7	3.0 ± 1.2	1.59 ± 0.21	d
Solar‡		9.77×10^{-2}	8.51×10^{-4}	0.43	0.13	0.14	

(a) Bernard-Salas et al. (2003), (b) Aller and Hyung (1995), (b) Hyung et al. (2000), (d) Henry et al. (2000), (e) Bernard Salas et al. (2001).

* (X) X-ray abundances, in this thesis.

(O) Abundances derived from IR, optical, and UV emission lines.

† Fixed.

‡ The number ratios of solar values.

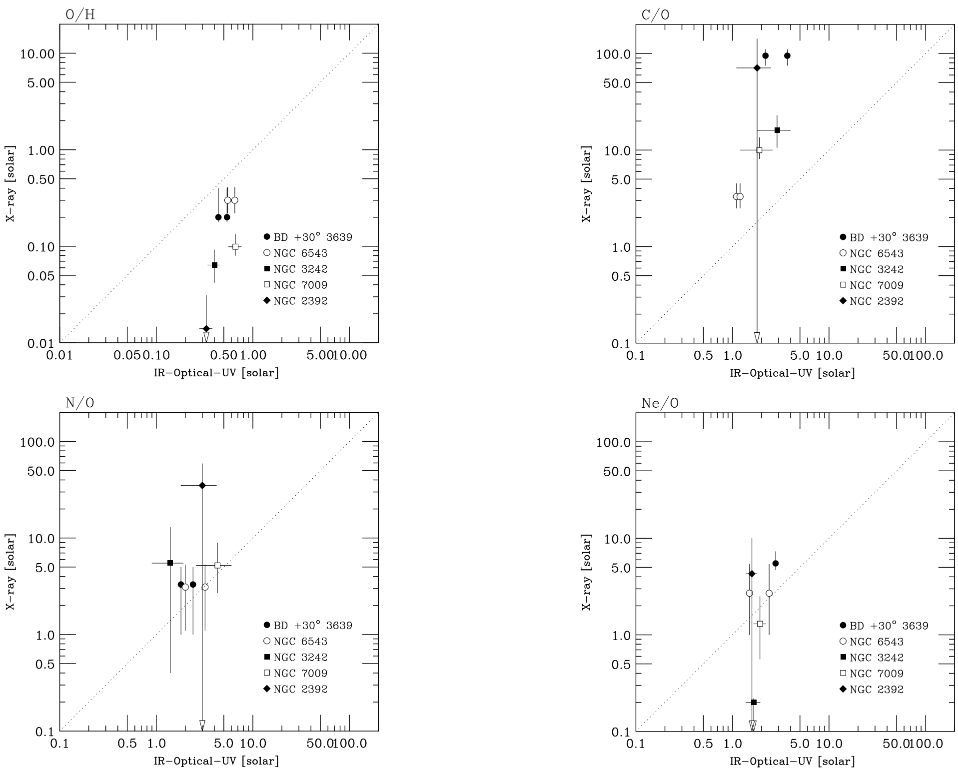

Figure 7.3: The X-ray determined abundance ratios, compared with those in IR, optical, and UV frequencies. The cases of O/H (top-left), C/O (top-right), N/O (bottom-left), and Ne/O (bottom-right) are shown.

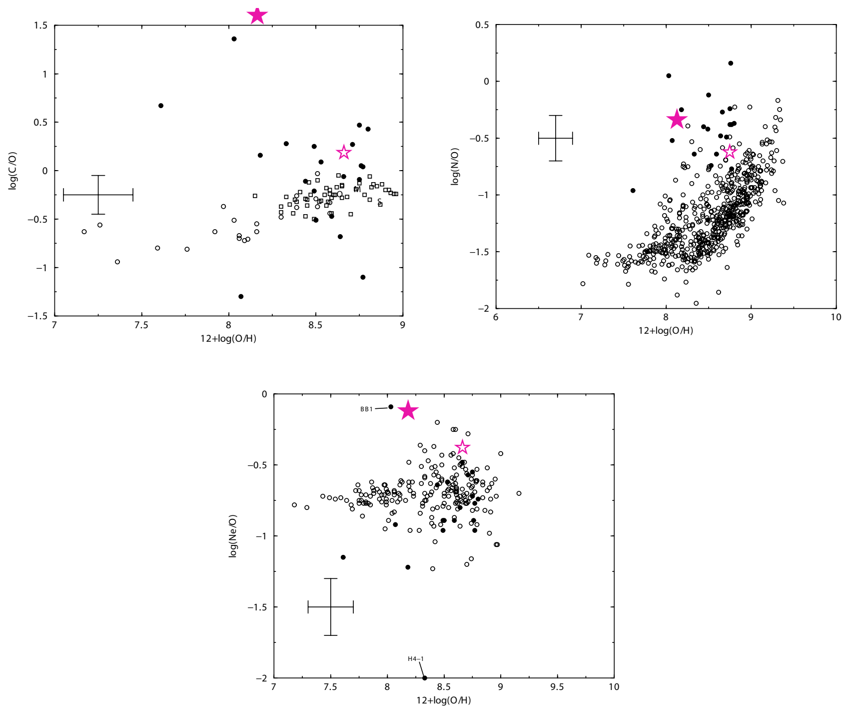

Figure 7.4: Scatter plots between abundance ratios (Henry et al. 2000). Top-left, top-right, and bottom panels show C/O vs. O/H, N/O vs. O/H, and Ne/O vs. O/H, respectively. Filled circles, open circles, and open squares indicate PNe, H II regions, and Galactic B stars, respectively. The abundance ratios of BD $+30^{\circ}$ 3639 are superposed with filled stars (X-rays) and open stars (IR-optical-UV). The values are plotted in the unit of the number ratios, rather than in solar-abundance units.

7.3 Interpretations of X-ray emission

7.3.1 Shocks in planetary nebulae

The diffuse X-ray emission from PNe is thought to originate from shock-heated gas (§2.4.1). As summarized in table 7.4, four objects in our sample (BD +30° 3639, NGC 6543, NGC 3242, and NGC 7009) meet this expectation at least qualitatively, because they have firm evidence of fast stellar winds. NGC 7293, hosting a point-like X-ray source associated with the central star, has no detectable P-Cygni profile in the UV spectra; this is consistent with its lack of diffuse X-ray component. This PN has a significantly higher plasma temperature among our sample PNe, suggesting that its X-ray emission mechanism may be slightly different from those of the other diffuse PNe. In contrast, NGC 7027, which also lacks detectable P-Cygni profiles, obviously has diffuse X-ray emission, thus posing an apparent puzzle. The marginal case is NGC 2392, which has weak P-Cygni profiles indicating relatively slow stellar winds. This support the possibility discussed in §7.1.2, that the X-ray emission from NGC 2392 is of the same diffuse origin, but not spatially resolved.

The shock velocity and the plasma temperature should be correlated through equation (2.30). Figure 7.5 plots the observed plasma temperatures against the temperature predicted by equation (2.30) and the stellar wind velocity (table 4.5). NGC 7027, which lacks detectable P-Cygni profile, is not plotted in this diagram. While the observed temperatures are concentrated around 0.2 keV, the predicted ones distribute over two orders of magnitude. In most of PNe, the observed temperature falls below the prediction, except NGC 2392 which have a low stellar wind velocity of $\sim$ 400 km s^{-1} . The lower plasma temperature than those expected from shock velocity is often observed in other astrophysical shock, such as supernova remnants, although the cause of such discrepancy is not yet explained.

One particular condition specific to PNe is that the hot bubble region (figure 2.9, region b) is located in touch with the thick cold nebular matter. Therefore, heat transport from the hot plasma to the cold nebula may be significant. Heated nebular material may flow back into the hot gas region, and mix with the hot plasma. As a result, the achieved plasma temperature may become lower than calculated by equation (2.30), which assumes energy conservation. Other possible explanations of the lower temperature include variability of the stellar wind from the central star.

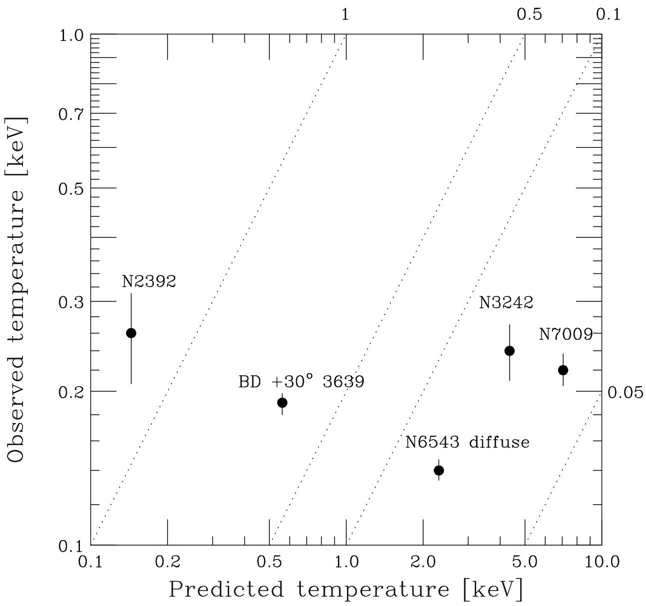

Figure 7.5: A scatter plot of the observed plasma temperatures against the temperatures predicted by the stellar wind velocity. The observed to predicted ratios, 1, 0.5, 0.1, 0.05 are indicated by dotted lines.

7.3.2 Physical quantities

In §7.1.1 and §7.1.3, we have already obtained parameters such as the X-ray luminosity, the electron density, and the total plasma energy of each PN. Combining them with the knowledge in other frequencies, we can investigate physics of the X-ray emitting region, including energetics and various characteristic time scales. Table 7.7 list the relevant physical quantities, either observed or derived, for two characteristic cases; one is an imaginary PN with typical parameters, while the other is BD +30° 3639 which has the highest X-ray luminosity among the X-ray emitting PNe. Taking the "typical" PN, below we explain how we calculated these results.

The kinetic energy input supplied from the central star is calculated as $E_{\rm input} = \frac{1}{2}\dot{M}v_{\rm wind}{}^2$. In the "typical" case, the estimated $E_{\rm input}$ exceeds the observed X-ray luminosity by more than 3 orders of magnitude, thus making the basic energetics fully self consistent. Assuming that the mass loss rate is constant, the time scale required to supply the X-ray material, $\tau_{\rm supply} = M_{\rm x}/\dot{M}$, becomes 10^3 yr. Dynamical time scale is obtained as $\tau_{\rm exp} = R/v_{\rm exp} \sim 750$ yr, simply via dividing the radius of X-ray emitting region R by the nebular expansion velocity $v_{\rm exp}$. In "typical" PNe, $\tau_{\rm exp}$ becomes comparable to $\tau_{\rm supply}$. The radiative cooling time scale of a "typical" PN is calculated as $\tau{\rm cool} = U/L_{\rm x} \sim 3\times10^5$ yr,

Table 7.7: The observed and derived physical parameters.

		Typical PNe	BD +30° 3639
R [pc]	Plasma radius	0.02	0.015
$v_{\rm exp}$ [km s^{-1}]	Nebular expansion velocity	25	23†
$v_{\rm wind}$ [km s^{-1}]	Stellar wind velocity	1000	790
$\dot{M}$ [$M_{\odot}$ yr^{-1}]	Mass loss rate	1×10^{-7}	$6.67 \times 10^{-6*}$
$L_{\rm x}$ [erg s^{-1}]	X-ray luminosity	1×10^{31}	1.4×10^{33}
kT [keV]	Plasma temperature	0.2	0.19
n_e [cm^{-3}]	Electron density	100	130
$M_{\rm x}$ [$M_{\odot}$]	X-ray emitting mass	1×10^{-4}	3.9×10^{-4}
U [erg]	Total plasma energy	1×10^{44}	4.6×10^{43}
p [dyn cm^{-2}]	Plasma pressure	6.4×10^{-8}	7.3×10^{-8}
$E_{\rm input}$ [erg s^{-1}]	Energy input	3.5×10^{34}	1.2×10^{36}
$L_{\rm x}/E_{\rm input}$		$\sim$ 0.03%	$\sim$ 0.09%
$\dot{W}$ [erg cm^{-2}]	Work done by pressure	7.7×10^{33}	4.5×10^{33}
$\dot{W}/E_{\rm input}$		$\sim$ 20%	$\sim$ 0.4%
$\tau_{\rm supply}$ [yr]	Mass supplying time scale	1000	$\sim$ 60
$\tau_{\rm exp}$ [yr]	Dynamical time scale	750	$\sim$ 700
$\tau_{\rm cool}$ [yr]	Cooling time scale	3×10^{5}	$\sim$ 1100

* de Freitas Pacheco et al. (1993).

† Acker et al. (1992).

which is much longer than the lifetime of PNe, $\sim 10^4$ yr. This indicates that the plasmas associated with PNe are not subject to significant radiative cooling.

In addition to the "typical" PNe, table 7.7 deals with the case of BD $+30°$ 3639, which is the most important target in the present thesis. By the same procedures as the typical case, we calculated the relevant quantities of this object, and list them in table 7.7, in comparison with those of the typical PN. The energy input of BD $+30°$ 3639 is by an order of magnitude higher than those of other PNe, due to its large mass loss rate, while the ratio of $L_{\rm x}/E_{\rm input}$ is similar to the typical value. The X-ray emitting matter in this PN can be supplied in only ~ 60 yr, which is shorter by an order of magnitude than the typical case. Although its cooling time scale is by two orders of magnitude shorter than that of the typical PNe, it is still considerably longer than $\tau_{\rm supply}$. The value of $\tau_{\rm exp}$ of this object is similar to those of others. These deviations in $E_{\rm input}$, $\tau_{\rm supply}$, and $\tau_{\rm cool}$ from the typical PNe may be due to the high mass loss rate, which is higher by two orders of magnitude than those of other PNe.

7.3.3 Plasma energetics

In order to interpret the present observations in terms of the ISW model (§2.4.1), it is of basic importance to examine energetics of the hot plasma in post-shock regions in PNe. The equation of energy conservation is written as a balance among the following six terms; (1) the conservation or change of internal energy carried by the flow, (2) the conservation or change of flow kinetic energy, (3) the work done by pressure, (4) the energy input from somewhere outside the system, (5) the radiative energy loss, and (6) the energy loss by heat conduction. In the present case, term (4) is just the energy input $E_{\rm input}$ at the inner boundary, i.e. reverse shock, and can be used as the boundary condition. The very long $\tau_{\rm cool}$ of PNe indicates that term (5) is negligible. The observed X-ray images indicate that the X-ray emitting plasma almost fully fills inside the optical nebula, so that the hot plasma bounds on the cold nebular matter. Therefore, the work term (3) may be represented by $\dot{W} \sim 4\pi R^2 p v_{\rm exp}$, where $p = 2n_e kT$ is the post-shock pressure, and the other nomenclature follows table 7.7. For the "typical" PNe, we have $p \sim 6 \times 10^{-8}$ dyn cm^{-2} from table 7.7, and hence $\dot{W} \sim 8 \times 10^{33}$ erg s^{-1}, corresponding to $\sim 20\%$ of $E_{\rm input}$.

In BD $+30°$ 3639, the energy input rate is very high with $\tau_{\rm supply} \sim 10^2$ yr, while dynamical changes of the system is expected to occur on a time scale of $\tau_{\rm exp} \sim 10^3$ yr. Therefore, on a time scale of $\sim 10^2$ yr, the system must be considered approximately as in a steady state, and hence terms (1) and (2) vanishes when integrated over the volume.

This means that the energy input (4) is balanced by terms (3) and (6). However, $\dot{W}$ of this PN is similar to the typical case in spite of its large $E_{\rm input}$ (table 7.7); this means that term (3) is negligible in the case of BD +30° 3639. Accordingly, the energy input is balanced by only term (6), i.e., the heat conduction. We therefore assume, as a working hypothesis, that the energy input to the emission region is transported away by efficient electron conduction in the post-shock region, and deposited on the thick cool shell. Below, this hypothesis is evaluated in somewhat more quantitative way.

With a gradient in T, the heat flux F due to conduction is written as

$$F = -\kappa \frac{dT}{dx}, \tag{7.4}$$

where κ is the coefficient of thermal conductivity. In highly ionized plasmas, this coefficient strongly depends of the temperature as $\kappa = bT^{2.5}$, where b is a constant. As an approximation, we may consider one dimensional plasma column in a steady state. The heat flows into the plasma column at $x = 0$ and runs out at $x = L$. By the heat flux conservation, we obtain

$$0 = \frac{dF}{dx} = -\frac{d}{dx}\left(bT^{2.5}\frac{dT}{dx}\right) \propto \frac{d^2}{dx^2}T^{3.5}. \tag{7.5}$$

Assuming the temperatures at the higher ($x = 0$) and lower ($x = L$) ends to be T_0 and 0, respectively, we obtain

$$T(y) = T_0(1-y)^{2/7}, \tag{7.6}$$

where $y = x/L$ is a dimensionless coordinate. Equation (7.6) indicates that the temperature sharply falls near at $x = L$, over a typical length scale of $\Delta x \sim L/5$

We may apply the one dimensional approximation to the plasma in PNe, assuming the spherical geometry and uniform density. Then, the time scale of heat conduction, $\tau_{\rm cond} = -({\rm dln}T/{\rm d}t)^{-1}$, can be written as

$$\tau_{\rm cond} \sim 18 \left(\frac{n_e}{100~{\rm cm^{-3}}}\right)\left(\frac{kT}{0.2~{\rm keV}}\right)^{-5/2}\left(\frac{\Delta x}{0.004~{\rm pc}}\right)^2~{\rm yr}. \tag{7.7}$$

The obtained $\tau_{\rm cond}$ is thus extremely short, so that the hot plasma in BD +30° 3639 is expected to lose its energy in up to $\sim$ 20 yr after reaching the contact discontinuity.

In the case of BD +30° 3639, it takes $\sim$ 10 yr for the matter ejected from the central star to arrived at the emission region. After heated up, the matter spends another several tens of years in crossing the emission region, and then loses the energy on a time scale of $\sim$ 20 yr. The sum of these time scales is consistent with the very short $\tau_{\rm supply} \sim$ 60 yr.

The rapid heat conduction may also explain the fact that the observed plasma temperature is generally lower than those predicted by the stellar wind velocity (§7.3.1). Although the quick heat conduction can explain the energetics in BD +30° 3639, it is still open whether the same scenario applies to other PNe with much lower values of E_{input}.

7.4 Interpretations of Abundance Ratios

7.4.1 X-ray abundance ratios

We have obtained X-ray spectra of 5 diffuse X-ray emitting PNe, including BD +30° 3639, NGC 6543, NGC 2392, NGC 3242, and NGC 7009, and derived the abundances of C, N, O, and Ne in the X-ray emitting plasma (figure 7.1). However, we cannot determine the absolute number of individual elements, since hydrogen and helium lack emission lines in X-rays. Therefore, we basically discuss abundance ratios. All the 5 PNe show enhanced C to O abundance ratios, and the same pattern of C>N>O. Four of them, except NGC 3242, show moderately enhanced Ne/O.

Since the rate-determining step of the CNO cycle is proton capture by ^{14}N, nitrogen would become more abundant than C and O (§2.2.2) if the hot plasma contained significant H-burning products. However, the X-ray abundances of most of the diffuse X-ray emitting PNe do not show enhanced nitrogen relative to C and O, so that the X-ray emitting materials are not H-burning products. Since carbon and neon are synthesized by He-burning, the observed X-ray abundance patterns suggests that the diffuse hot plasmas in PNe actually reflect pure He-burning products.

Major He-burning products are C and O, and then Ne and Mg follow them (§2.2.3). The final number ratio between C and O produced by He-burning is determined by reaction rates of $^{8}\mathrm{Be}(\alpha,\gamma)^{12}\mathrm{C}$ and $^{12}\mathrm{C}(\alpha,\gamma)^{16}\mathrm{O}$. Neon is synthesized via α-capture by oxygen; $^{16}\mathrm{O}(\alpha,\gamma)^{20}\mathrm{Ne}$. Subsequent α-capture produces Mg. Actually, we have successfully detected strong helium-like Ne-K lines (0.91 keV) in the X-ray spectra of 4 PNe, BD +30° 3639, NGC 6543, NGC 7027, and NGC 7009 (§5 and §6). These results reinforce our hypothesis that the diffuse X-rays from PNe reflects He-burning products. However, we of course need a more quantitative evaluation, to be presented in the next subsection.

When analyzing the X-ray spectra of PNe obtained with *Chandra* and *XMM-Newton*, we had to assumed the C abundance because of the poor energy resolution below 1 keV. In contrast, BD +30° 3639 alone was observed with the *Suzaku* XIS, and its superior energy resolution has allowed us to constrain the C/O, N/O, and Ne/O ratios without assuming the C/H ratio. Therefore, we base our discussion on the results of this particular PN. However, before doing so, it may be necessary to examine whether it can be used as a representative object.

BD +30° 3639 is by far the X-ray brightest PNe, and its X-ray luminosity is higher by nearly two orders of magnitude than those of other PNe (table 7.1). While this X-ray brightness enabled us to perform the detailed X-ray spectroscopy, this PN could be an unusual object. In particular, the high X-ray luminosity of BD +30° 3639 is due to its high mass loss rate, exceeding those of other PNe by nearly two orders of magnitude (§7.3). However, the X-ray abundance pattern of BD +30° 3639 is similar to those of other 3 PNe, NGC 6543, NGC 2392, and NGC 7009 (figure 7.1). Furthermore, the nebular abundances of BD +30° 3639, determined by IR, optical, and UV observations, indicate that this PN is not a peculiar object (figure 7.4). We therefore regard the X-ray abundance ratios of BD +30° 3639 as a typical case.

7.4.2 Quantitative evaluation

The abundance ratios of BD +30° 3639, summarized in table 7.5, are characterized by a strongly enhanced C relative to other elements, similar number of Ne and O, and the ratio of N to O which is near the solar value. The X-ray measured C/O and Ne/O ratios are considerably higher than those implied by the IR-optical-UV measured abundances of PNe, including BD +30° 3639 itself (§7.2).

The obtained number ratio of C/O seems to be too large; the number of C is by more than an order of magnitude larger than that of O. Another concern is that the number of Ne is comparable to that of O, even though Ne must be produced after the O production in He-burning (§2.2.3). Accordingly, we re-examined our spectral analysis for possible artifacts due to instrumental responses, background, or theoretical model which we have utilized. The former two issues have been studied throughly in §5 by fitting the spectra under various conditions. There, we found that the C/O and Ne/O ratios are affected by no larger than $\sim 20\%$ (table 5.12). Then, the remaining issue is whether the theoretical model, vAPEC, can be applied to such extreme abundances. The continuum would be largely affected by such high abundances of heavy ions, because the emissivity of bremsstrahlung is proportional to ${Z_i}^2$ [equation (2.31) in §2.4.3]. However, we have confirmed that contributions of heavy ions, not only free-free emission but also free-bound transition which produce “recombination continuum”, are properly included in the vAPEC model.

There could still be artifacts introduced by fixing He/H to the solar value. If the X-ray emission really reflects He-burning products, He/H should be much larger than the solar value. However, we have already analyzed the X-ray spectra by changing He/H to be 1, 5, 10, and 20, and found that the abundance ratios of C/O and Ne/O are not significantly affected beyond their 90% error ranges (§5.3.5).

Based on the discussion presented so far, we conclude that the extreme abundance ratios among C, O, and Ne, derived from the XIS spectra of BD $+30^\circ$ 3639, are not subject to major instrumental or software artifacts. In other words, the strong C-K and Ne-K lines, and the relatively weak O-K lines, are intrinsic to the X-ray spectrum of BD $+30^\circ$ 3639. It may be said that the oxygen deficit is a common cause of these two issues. We may then think of the following two interpretations.

- Oxygen is abundant in reality, but its emission lines are somehow suppressed, or they appear weak, at least compared to the Ne-K lines.
- The observed abundance ratios are actually achieved by the He-burning, at last in a certain mass range of progenitors.

These two interpretations are examined in the subsections to follow.

7.4.3 Apparent suppression of oxygen lines

The two problems encountered in §7.4.2 (the too high C/O and Ne/O ratios) could have a common origin, namely too weak oxygen lines. Therefore, we consider a scenario that a plenty of oxygen is actually present in the system, but the O-K lines (in the 0.5–0.7 keV range) are somehow weakened in the X-ray spectra. There are at least three candidates for this scenario. One is that X-ray emitting plasma consists of multi temperature components, including those temperatures where O-K lines are hardly emitted. Another is that the hot plasma is in "recombining" phase at locations near the contact discontinuity (figure 2.9), where the electron conduction (§7.3.3) may cause the electron temperature significantly lower than that of ions. The other is that a large fraction of oxygen in the hot plasma is taken into cold dusts.

Under a plasma temperature above 1 keV, most of O ions are fully ionized and has no emission lines. The oxygen emission lines will not be observed in X-rays either, if the temperature is too low ($\lesssim$ 20 eV) to excite them. Therefore, the oxygen lines would have a lower equivalent width for the abundance, if a higher or lower temperature component exists. However, the plasma temperature of BD $+30^\circ$ 3639 is firmly determined by the line intensity ratios of helium-like and hydrogen like oxygen (0.56, 0.65 keV) and Ne (0.91, 1.02 keV), which are clearly resolved by the *Suzaku* XIS (§5.2.2). Furthermore, figure 2.10 indicates that either He-like or H-like oxygen ion should be abundant as long as the temperature is in the range of 50–200 eV, where the hydrogen-like carbon line is strongly emitted. To confirm this interference, we tried to fit the XIS spectra with a two-temperature plasma model, assumed for example $kT_1 = 2kT_2$, one temperature converged to the best-fit value of the single temperature fit, and the other component became negligible in its normalization. We also tried a two temperature plasma model, fixing C/O=5 in the solar unit and allowing each temperature to vary freely. Then, $\Delta\chi^2$ became worse by ~ 60 than the single temperature fit, and Ne/O rather increased to ~ 55 solar, or ~ 7.7 in the number ratio, contrary to our expectation. Thus, the multi-temperature plasma may not apply to the XIS spectra of BD +30° 3639, and cannot explain the X-ray weakness of the oxygen lines.

As described in §7.3.3, a rapid heat conduction may occur between the hot plasma and the cold nebular matter in BD +30° 3639. When the plasma has reached the region of strong temperature gradient (§7.3.3) and the electrons begin to cool down, the conductive cooling time scale becomes considerably shorter than the ionization time scale that is estimated as $10^2/n \sim 10^{10}$ s ~ 300 yr (Masai 1994). This indicates that the cooling plasma may experience a transient over-ionized state. As a result, the electron temperature decreases, and recombination lines becomes significant relative to collisional lines. Since neon has an excitation energy of 0.9 keV which is higher than the plasma temperature of 0.2 keV, the efficiency of collisional excitation is significantly lower than in oxygen or carbon ions. In contrast, recombination lines can be produced by all free electrons, without much depending on the excitation energy. Therefore, Ne lines may become enhanced, relevant to lower-energy lines, in the recombining plasma. This possibility is apparently supported by the fact that the *Chandra* image (figure 5.1) and its projection (figure 5.2) are more rim-enhanced in the Ne-line energy band than in the CNO-line band. Furthermore, we observe an Ne-line enhancement coincident in position with the Hα filaments (§5.1.2), where the plasma is suggested to rapidly recombining. However, this mechanism may not explain the too high C/O ratio. Clearly, a more quantitative numerical analysis is needed.

The remaining explanation is that the circumstellar dust engulfs oxygen in the X-ray emitting hot plasma. The plasma temperature, lower than the predicted by the stellar wind velocity, suggests its mixing with ambient cold matter, as already pointed out based on the *ASCA* observation (Arnaud et al. 1996). In fact, the peripheral enhancement of the Ne-K line, mentioned above, may alternatively be taken as evidence that oxygen is being taken into dusts in these regions, whereas neon that is volatile remains gaseous. However, there are weak O-lines in the UV spectra of the central star of BD +30° 3639 (Leuenhagen et al. 1996). In addition, even though this hypothesis may explain the enhanced Ne/O abundance ratio, it cannot resolve the strongly enhanced C/O, since carbon would be also taken up by the dust as well as oxygen.

As a result of the discussion presented so far, the latter two hypotheses are possibly responsible for the Ne/O enhancement. In order to examine them, we need high angular resolution, superior energy resolution, and large effective area at the same time. In any case, the strongly enhanced C/O will not change.

7.4.4 He-burning products

The observed C/O ratio of BD +30° 3639 is 95 in the solar unit, or 41 in the number ratio. We may have to explain these large values as a result of He-burning, because the apparent oxygen suppression (§7.4.3) does not necessarily appear promising. The reaction rates of the processes producing ^{12}C and ^{16}O are shown in figure 7.6. Thus, over a wide range of temperature between 3×10^8 K to 1×10^9 K, the reaction rate of ^{8}Be(α,γ)^{12}C is much higher by 10 orders of magnitude than that of ^{12}C(α,γ)^{16}O. An important difference is that ^{8}Be is an extremely unstable isotope, with a very small amount being produced from two ^{4}He nuclei, whereas ^{16}O is produced from ^{12}C and is of course stable. In addition, ^{4}He, the fuel to produce ^{12}C, gets gradually exhausted with time, whereas ^{12}C itself, serving as the fuel to produce ^{16}O, should increase. In fact, according to a calculation by Imbriani et al. (2001), the mass ratio of produced C to O is 0.495/0.505 and 0.541/0.440, for initial progenitor masses of 0.8 $M_\odot$ and 6 $M_\odot$, respectively.

These theoretical C/O ratios, however, should apply to final products of He-burning, i.e. an electron degenerate CO core. The C/O number ratio ∼41 is a typical one in the middle of He-burning (Suda et al. 2004). In the post-AGB phase, He-shell burning occurs unstably at the bottom of helium layer, accompanied by convection. Therefore, the X-ray emitting matter may be interpreted as ejecta of He-burning convective layer. The X-ray observations are indeed diagnosing the He-burning products in much sensitive ways than those in longer wavelength, as predicted in §2.4.2.

The X-ray spectra gave the Ne/O ratio which is 3.3 times larger than the solar value, corresponding to 0.77 in the number ratio. The Ne/O ratio of the He-burning products is determined by the competition between ^{12}C(α,γ)^{16}O and ^{16}O(α,γ)^{20}Ne. Based on ground experiments, Kunz et al. (1997) and Buchmann and Barnes (2005) reported that the

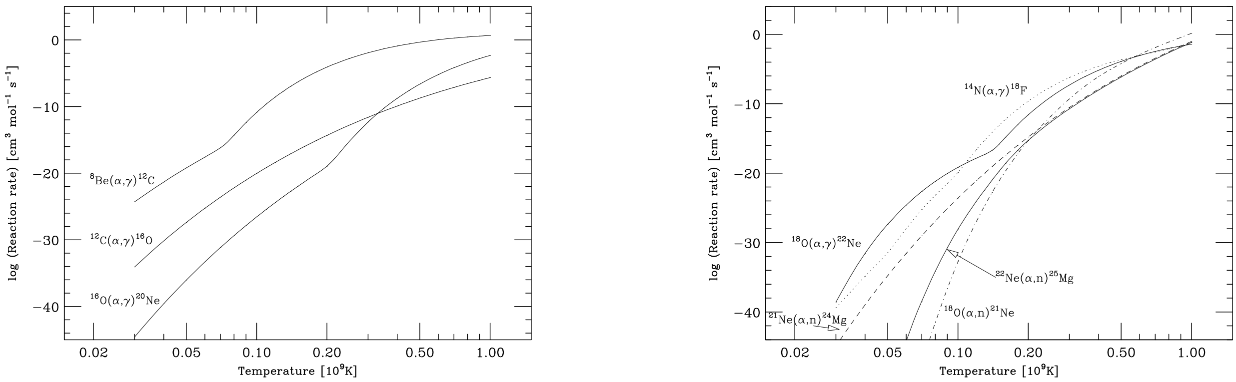

Figure 7.6: Reaction rates of the ^{12}C and ^{16}O production process (left) and those Ne isotopes (right), shown a function of temperature (Caughlan and Fowler 1998).

cross section of ^{16}O(α,γ)^{20}Ne is much smaller than that of ^{12}C(α,γ)^{16}O at the He-burning temperature. This suggests a very low Ne/O ratio, conflicting with the observed result. As the temperature increases, the reaction rate of ^{16}O(α,γ)^{20}Ne becomes higher than that of ^{12}C(α,γ)^{16}O (figure 7.6). Therefore, the observed high Ne/O ratio might be explained in a certain temperature range. However, in order to achieve such a condition, a high temperature of $\sim 3 \times 10^8$ K is required.

Another possibility to explain the observed Ne/O ratio is a neon producing path without ^{16}O. After completion of hydrogen burning, a considerable amount of ^{14}N must be contained in the helium core, as a result of ^{14}N concentration through the CNO cycle (§2.2.2). When the unstable He-shell burning occurs, this nitrogen also burns by thermonuclear reactions as ^{14}N(α,γ)^{18}F($\beta^+\nu$)^{18}O, and the synthesized ^{18}O is converted to ^{22}Ne or ^{21}Ne by α-captures. Although this nitrogen path produces heavier Ne isotopes rather than ^{20}Ne, we cannot distinguish them with X-ray emission lines. Therefore, we may be observing in X-rays Ne-K lines from ^{22}Ne and ^{21}Ne, instead of ^{20}Ne. Incidentally, these Ne isotopes, ^{22}Ne and ^{21}Ne, capture α particles and provide free neutrons which are important for the s-process (§2.1.2). If we can estimate the contribution of its ^{14}N-based process to the observed Ne, we may be able to get insight into the original CNO abundances, and hence the progenitor's metallicity.

The observed N/O ratio is 3.3 in the solar unit, or 0.43 in the number ratio. Nitrogen is synthesized in H-burning and not produced in He-burning. Therefore, this nitrogen was probably produced in the CNO cycle, and stored in the He layer, but was not caught up in the He-shell burning.

As discussed above, the X-ray emitting matter of BD +30° 3639 can be reasonably explained as a mixture between the He-shell burning products and the portions of the

He layer which were not taken in the burning. This leads to the following scenario to explain the observed C/O/Ne ratios of this PN; the hydrogen-burning envelope had already been expelled away; the outer parts of the He layer, which are composed of convective and radiative zones, were somehow ejected with a fast speed of ~ 1000 km s^{-1}; and then the wind materials were shock-heated to emit X-rays. In this way, the results on BD +30° 3639 for the first time have provided new observational facts which can be compared quantitatively with theoretical predictions.

The X-ray abundances of the other PNe (§7.1.4) suggest that the X-ray emitting PNe show some variations in their abundance patterns. This may provide a clue to the determination of the initial mass and metallicity of each progenitor. In addition, the observed X-ray abundances, may be combined with the theoretical model of stellar evolution and nucleosynthesis to constrain how and when the final fast-speed mass loss occurs.

Chapter 8

CONCLUSION

We have selected 14 X-ray emitting planetary nebulae from the archived *Chandra* and *XMM-Newton* data, and studied their X-ray spectra and images. In addition, we observed the X-ray brightest of them, BD $+30^\circ$ 3639, with *Suzaku* launched on 2005 July 10. As summarized below, the X-ray spectroscopy is opening a new window on planetary nebulae.

1. The diffuse X-ray emission, mostly confined within the optical inner shell, was detected from nearly two thirds (8 objects) of the X-ray selected sample. The obtained X-ray spectra have clear signature of optically-thin emission from hot plasmas, with a typical temperature and X-ray luminosity of ~ 0.2 keV and 1×10^{31} erg s^{-1}, respectively.

2. The derived plasma parameters and energetics of the X-ray emitting plasma are generally consistent with the prediction of the Interacting Stellar Winds model, although some unsolved issues remain. According to the ISW model, the X-ray emitting plasma is heated by a reverse shock, which is expected to stand in the fast stellar wind from the central star when the wind is strongly confined by the thick nebular shell. Therefore, the plasma is thought to represent the last products of the nucleosynthesis inside the intermediate-mass stars.

3. The newest X-ray observatory *Suzaku* revealed the extreme abundance ratios of the X-ray emitting plasma in BD $+30^\circ$ 3639; C/O$\sim$ 95, Ne/O$\sim$ 5.5, and N/O$\sim$ 3.3 in the solar unit. The *Chandra* and *XMM-Newton* spectra of other PNe show moderately enhanced C relative to the O abundance. Such enhanced C/O abundance ratios in PNe are considered to reflect the He-burning products. In particular, the X-ray emitting matter in BD $+30^\circ$ 3639 is consistently interpreted as outer parts of

the He layer, which is a mixture of a convective zone triggered by unstable He-shell burning, and a radiative zone which is unaffected by the burning.

Appendix A

DEFINITION OF SOLAR ABUNDANCES

The XSPEC package of version 11 has six sets of solar abundance tables available, as listed in table A.1. Anders and Ebihara (1982) derived abundances from chondrites of type C1, which is defined as those including more than 3.5% carbon and no chondrules, while Feldman (1992) carried out spectroscopic abundance measurements from high temperature solar plasmas. Anders and Grevesse (1989) and Grevesse and Sauval (1998) confirmed a good agreement between the abundances of chondrite and solar photosphere, and utilized them to compose abundance tables. Lodders (2003) summarized and selected the best available abundances, while Wilms et al. (2000) selected the best estimates for the "local" inter-stellar medium abundances.

Among these tables, the local intersellar determinations (wilms00) indicate systematically lower abundances than the others, by up to nearly a factor of two for Si. However, the meteoritic and solar-photospheric values show a good agreement, with the only exception of Fe for which a factor of 1.5 discrepancy remains.

Most of X-ray investigators, including us, utilize the default setting of XSPEC that is "angr" due to Anders and Grevesse (1989). However, we must be careful when we compare abundances derived by different authors, because some utilize different definitions.

Table A.1: Definitions of solar abundances by number relative to hydrogen.

	angr89	feld92	aneb92	grsa98	wilms00	lodd03
H	1.00	1.00	1.00	1.00	1.00	1.00
He	9.77×10^{-2}	9.77×10^{-2}	8.01×10^{-2}	8.51×10^{-2}	9.77×10^{-2}	7.92×10^{-2}
C	3.63×10^{-4}	3.98×10^{-4}	4.45×10^{-4}	3.31×10^{-4}	2.40×10^{-4}	2.45×10^{-4}
N	1.12×10^{-4}	1.00×10^{-4}	9.12×10^{-5}	8.32×10^{-5}	7.59×10^{-5}	6.76×10^{-5}
O	8.51×10^{-4}	8.51×10^{-4}	7.39×10^{-4}	6.76×10^{-4}	4.90×10^{-4}	4.90×10^{-4}
Ne	1.23×10^{-4}	1.29×10^{-4}	1.38×10^{-4}	1.20×10^{-4}	8.71×10^{-5}	7.41×10^{-5}
Na	2.14×10^{-6}	2.14×10^{-6}	2.10×10^{-6}	2.14×10^{-6}	1.45×10^{-6}	1.99×10^{-6}
Mg	3.80×10^{-5}	3.80×10^{-5}	3.95×10^{-5}	3.80×10^{-5}	2.51×10^{-5}	3.55×10^{-5}
Si	3.55×10^{-5}	3.55×10^{-5}	3.68×10^{-5}	3.35×10^{-5}	1.86×10^{-5}	3.47×10^{-5}
Fe	4.68×10^{-5}	3.24×10^{-5}	3.31×10^{-5}	3.16×10^{-5}	2.69×10^{-5}	2.95×10^{-5}

angr89 = Anders and Grevesse (1989); feld92 = Feldman (1992);
aneb92 = Anders and Ebihara (1982); grsa98 = Grevesse and Sauval (1998);
wilm00 = Wilms et al. (2000); lodd03 = Lodders (2003).

Appendix B

ESTIMATION OF INTERSTELLAR ABSORPTIONS

X-rays in lower energies are largely affected by photoelectric absorption due to interstellar medium. As shown in figure B.1, the absoption in the 0.3–2 keV range is predominantly due to K-shell ionization by neutral C, N, O, Ne, Mg, and Si atoms, as well as L-shell photoionization of neutral Fe. Though most abandant, hydrogen contribute no more than $\sim 25\%$ even at 0.3 keV, while helium contribution is $\sim 80\%$ at 0.3 keV and $\sim 20\%$ at 1.0 keV (assuming solar abundances). Since we emphasize spectra below 1 keV, where PNe emissions are most intense, we have to estimate equivalent hydrogen column density N_{H} for each object.

In the case of many PNe, extinction prameters, c, derived from the ratio of radio to Hβ fluxes, are available in the literature. This quantity represents the column density of interstellar dusts, which scatter UV to near-infrared radiation. X-ray photons and radio waves are both free from the dust scattering, because their wavelengths are much shorter and mauch longer than the size of dusts, respectively. Utilizing a tool based on a standard interstellar extinction curve (Scheffler 1982), we converted c into A_V, which is a more generally used parameter describing the optical extinction. It is known that N_{H} in turn strongly correlates with A_V, although the uncertainty associated with the dust-to-gass ratio along the line of sight introduces some $\sim 25\%$ errors in the A_V to N_{H} conversion. In the present thesis, we adopt a relation of $N_{\mathrm{H}}/A_V = 1.79 \times 10^{21}$ cm^{-2} derived from *ROSAT* observations of X-ray halos around persistent sources (Predehl and Schmitt 1995). The valuse of c and A_V, utilized in calculating N_{H} for our target objects, are summarized in table B.1.

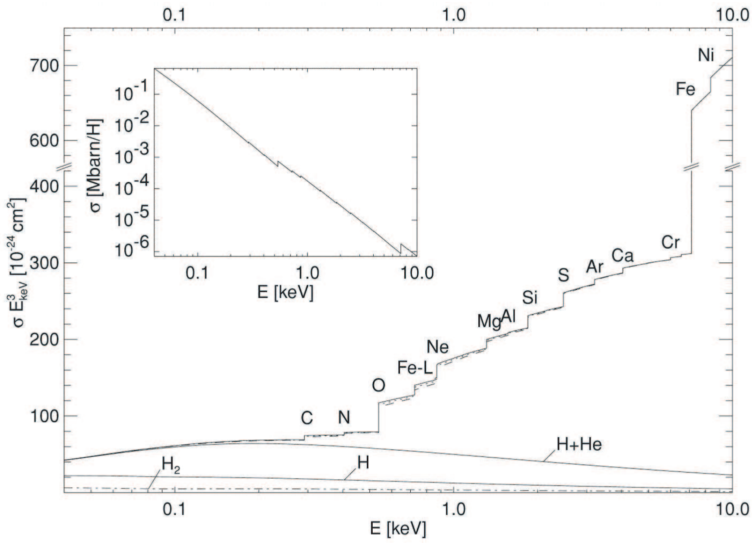

Figure B.1: Computed absorptivity per hydrogen atom of the interstellar medium (Wilms et al. 2000), shown againsts the X-ray energy E. The inset shows the cross section without the multiplication by E^3. The contributions of H, H+He, and H_2 are indicated. K absorption edge of each element and Fe-L edge are denoted in the figure.

Table B.1: Estimation of the interstellar absorption toward our sample PNe.

Target name	c	A_V	N_{H} [10^{21} cm^{-2}]	Ref.
BD +30° 3639	0.27	0.558	1.0	a
NGC 246	0.22	0.455	0.81	a
NGC 2392	0.19	0.393	0.70	b
NGC 3242	0.12	0.248	0.44	b
NGC 6543	0.12	0.248	0.44	b
NGC 7009	0.14	0.289	0.52	b
NGC 7027	1.31	2.707	4.9	b
NGC 7293				

(a) Cahn et al. (1992)

(b) Ciardullo et al. (1999),

References

Acker, A., Marcout, J., Ochsenbein, F., Stenholm, B., and Tylenda, R.: 1992, *Strasbourg - ESO catalogue of galactic planetary nebulae. Part 1; Part 2*, Garching: European Southern Observatory, 1992

Aller, L. H. and Hyung, S.: 1995, *MNRAS* **276**, 1101

Anders, E. and Ebihara, M.: 1982, *Geochimica et Cosmochimica Acta* **46**, 2363

Anders, E. and Grevesse, N.: 1989, *Geochimica et Cosmochimica Acta* **53**, 197

Apparao, K. M. V., Berthiaume, G. D., and Nousek, J. A.: 1992, *ApJ* **397**, 534

Apparao, K. M. V. and Tarafdar, S. P.: 1989, *ApJ* **344**, 826

Arnaud, K., Borkowski, K. J., and Harrington, J. P.: 1996, *ApJ* **462**, L75+

Bachiller, R., Forveille, T., Huggins, P. J., Cox, P., and Maillard, J. P.: 2000, *A&A* **353**, L5

Balick, B., Alexander, J., Hajian, A. R., Terzian, Y., Perinotto, M., and Patriarchi, P.: 1998, *AJ* **116**, 360

Bernard, J. P., Giard, M., Normand, P., and Tiphene, D.: 1994, *A&A* **289**, 524

Bernard Salas, J., Pottasch, S. R., Beintema, D. A., and Wesselius, P. R.: 2001, *A&A* **367**, 949

Bernard-Salas, J., Pottasch, S. R., Wesselius, P. R., and Feibelman, W. A.: 2003, *A&A* **406**, 165

Bond, H. E. and Ciardullo, R.: 1999, *PASP* **111**, 217

Buchmann, L., Azuma, R. E., Barnes, C. A., Humblet, J., and Langanke, K.: 1996, *Phys. Rev. C* **54**, 393

Buchmann, L. R. and Barnes, C. A.: 2005, *Nuclear Physics A* in press

Burke, B. E., Gregory, J. A., Loomis, A. H., Lesser, M., Bautz, M. W., Kissel, S. E., Rathman, D. D., Osgood, R. M., Cooper, M. J., Lind, T. A., and Ricker, G. R.: 2004, *IEEE Transaction on Nuclear Science* **51**, 2322

Burwitz, V., Haberl, F., Neuhäuser, R., Predehl, P., Trümper, J., and Zavlin, V. E.: 2003, *A&A* **399**, 1109

Cahn, J. H., Kaler, J. B., and Stanghellini, L.: 1992, *A&AS* **94**, 399

Caughlan, R. G. and Fowler, W. A.: 1988, *Atomic Data And Nuclear Data Tables* **40**, 283

Caughlan, R. G., Fowler, W. A., Harris, M. J., and Zimmerman, B. A.: 1985, *Atomic Data And Nuclear Data Tables* **32**, 197

Cerruti-Sola, M. and Perinotto, M.: 1989, *ApJ* **345**, 339

Chu, Y.-H., Guerrero, M. A., Gruendl, R. A., Williams, R. M., and Kaler, J. B.: 2001, *ApJ* **553**, L69

Chu, Y.-H. and Ho, C.-H.: 1995, *ApJ* **448**, L127+

Chu, Y.-H., Kwitter, K. B., and Kaler, J. B.: 1993, *AJ* **106**, 650

Ciardullo, R., Bond, H. E., Sipior, M. S., Fullton, L. K., Zhang, C.-Y., and Schaefer, K. G.: 1999, *AJ* **118**, 488

Davis, L. E., Seaquist, E. R., and Purton, C. R.: 1979, *ApJ* **230**, 434

de Freitas Pacheco, J. A., Costa, R. D. D., de Araujo, F. X., and Petrini, D.: 1993, *MNRAS* **260**, 401

de Korte, P. A. J., Claas, J. J., Jansen, F. A., and McKechnie, S. P.: 1985, *Advances in Space Research* **5**, 57

de Koter, A., Hubeny, I., Heap, S. R., and Lanz, T.: 1996, in *ASP Conf. Ser. 96: Hydrogen Deficient Stars*, p. 141

Feldman, U.: 1992, *Physica Scripta Volume T* **46**, 202

Fernández, R., Monteiro, H., and Schwarz, H. E.: 2004, *ApJ* **603**, 595

Gehrels, N. and Williams, E. D.: 1993, *ApJ* **418**, L25+

Gehrz, R. D. and Woolf, N. J.: 1971, *ApJ* **165**, 285

Gieseking, F., Becker, I., and Solf, J.: 1985, *ApJ* **295**, L17

Graham, J. R., Herbst, T. M., Matthews, K., Neugebauer, G., Soifer, B. T., Serabyn, E., and Beckwith, S.: 1993, *ApJ* **408**, L105

Grevesse, N. and Sauval, A. J.: 1998, *Space Science Reviews* **85**, 161

Guerrero, M. A., Chu, Y.-H., Gruendl, R. A., and Meixner, M.: 2005, *A&A* **430**, L69

Guerrero, M. A., Chu, Y.-H., Gruendl, R. A., Williams, R. M., and Kaler, J. B.: 2001, *ApJ* **553**, L55

Guerrero, M. A., Gruendl, R. A., and Chu, Y.-H.: 2002, *A&A* **387**, L1

Hajian, A. R., Terzian, Y., and Bignell, C.: 1995, *AJ* **109**, 2600

Hamann, W.-R., Kudritzki, R.-P., Mendez, R. H., and Pottasch, S. R.: 1984, *A&A* **139**, 459

Harris, H. C., Dahn, C. C., Monet, D. G., and Pier, J. R.: 1997, in *IAU Symp. 180: Planetary Nebulae*, pp 40–+

Hayakawa, S. and Sugimoto, D.: 1968, *Ap&SS* **1**, 216

Henry, R. B. C.: 2004, in *Origin and Evolution of the Elements*, pp 44–+

Henry, R. B. C., Kwitter, K. B., and Bates, J. A.: 2000, *ApJ* **531**, 928

Henry, R. B. C., Kwitter, K. B., and Dufour, R. J.: 1999, *ApJ* **517**, 782

Huggins, P. J. and Healy, A. P.: 1989, *ApJ* **346**, 201

Hyung, S., Aller, L. H., Feibelman, W. A., Lee, W. B., and de Koter, A.: 2000, *MNRAS* **318**, 77

Imbriani, G., Limongi, M., Gialanella, L., Terrasi, F., Straniero, O., and Chieffi, A.: 2001, *ApJ* **558**, 903

Kahn, F. D.: 1983, in *IAU Symp. 103: Planetary Nebulae*, pp 305–315

Kastner, J. H., Balick, B., Blackman, E. G., Frank, A., Soker, N., Vrtílek, S. D., and Li, J.: 2003, *ApJ* **591**, L37

Kastner, J. H., Li, J., Vrtilek, S. D., Gatley, I., Merrill, K. M., and Soker, N.: 2002, *ApJ* **581**, 1225

Kastner, J. H., Soker, N., Vrtilek, S. D., and Dgani, R.: 2000, *ApJ* **545**, L57

Kastner, J. H., Vrtilek, S. D., and Soker, N.: 2001, *ApJ* **550**, L189

Khromov, G. S.: 1969, *AZh* **46**, 747

Kreysing, H. C., Diesch, C., Zweigle, J., Staubert, R., Grewing, M., and Hasinger, G.: 1992, *A&A* **264**, 623

Kunz, R., Mayer, A., Joos, K.-D., Knee, H., Müller, A., Nickel, J., Plettner, C., Hammer, J. W., Baye, D., Descouvemont, P., Jaeger, M., Kölle, V., Wilmes, S., Staudt, G., Mohr, P., Chronidou, C., Harissopulos, S., Spyrou, K., and Paradellis, T.: 1997, *Nuclear Physics A* **621**, 149

Kwitter, K. B. and Henry, R. B. C.: 1998, *ApJ* **493**, 247

Kwok, S.: 1982, *ApJ* **258**, 280

Kwok, S.: 1983, in *IAU Symp. 103: Planetary Nebulae*, pp 293–302

Kwok, S.: 2000, *The Origin and Evolution of Planetary Nebulae*, The origin and evolution of planetary nebulae / Sun Kwok. Cambridge ; New York : Cambridge University Press, 2000. (Cambridge astrophysics series ; 33)

Kwok, S.: 2005, *Journal of Korean Astronomical Society* **38**, 271

Leahy, D. A., Kwok, S., and Yin, D.: 2000, *ApJ* **540**, 442

Leahy, D. A., Zhang, C. Y., Volk, K., and Kwok, S.: 1996, *ApJ* **466**, 352

Leuenhagen, U., Hamann, W.-R., and Jeffery, C. S.: 1996, *A&A* **312**, 167

Livio, M. and Shaviv, G.: 1975, *Nature* **258**, 308

Lodders, K.: 2003, *ApJ* **591**, 1220

Maness, H. L., Vrtilek, S. D., Kastner, J. H., and Soker, N.: 2003, *ApJ* **589**, 439

Masai, K.: 1984, *Ap&SS* **98**, 367

Masai, K.: 1994, *ApJ* **437**, 770

Masson, C. R.: 1989, *ApJ* **346**, 243

Matsushita, K., Ohashi, T., and Makishima, K.: 2000, *PASJ* **52**, 685

Meaburn, J., López, J. A., and Noriega-Crespo, A.: 2000, *ApJS* **128**, 321

Mellema, G.: 2004, *A&A* **416**, 623

Mendez, R. H.: 1991, in *IAU Symp. 145: Evolution of Stars: the Photospheric Abundance Connection*, pp 375–+

Mendez, R. H., Kudritzki, R. P., Herrero, A., Husfeld, D., and Groth, H. G.: 1988, *A&A* **190**, 113

Mewe, R., Gronenschild, E. H. B. M., and van den Oord, G. H. J.: 1985, *A&AS* **62**, 197

Mewe, R., Lemen, J. R., and van den Oord, G. H. J.: 1986, *A&AS* **65**, 511

Mufson, S. L., Lyon, J., and Marionni, P. A.: 1975, *ApJ* **201**, L85

Muthu, C., Anandarao, B. G., and Pottasch, S. R.: 2000, *A&A* **355**, 1098

Napiwotzki, R.: 1998, *Reviews of Modern Astronomy* **11**, 3

O'Dell, C. R., Balick, B., Hajian, A. R., Henney, W. J., and Burkert, A.: 2002, *AJ* **123**, 3329

O'Dell, C. R., McCullough, P. R., and Meixner, M.: 2004, *AJ* **128**, 2339

Palla, F., Galli, D., Marconi, A., Stanghellini, L., and Tosi, M.: 2002, *ApJ* **568**, L57

Pauldrach, A. W. A., Hoffmann, T. L., and Méndez, R. H.: 2003, in *IAU Symposium*, pp 177–+

Pettini, M.: 2004, in *Cosmochemistry. The melting pot of the elements*, pp 257–298

Pottasch, S. R.: 1978, in *IAU Symp. 76: Planetary Nebulae*, pp 93–100

Pottasch, S. R., Baud, B., Beintema, D., Emerson, J., Harris, S., Habing, H. J., Houck, J., Jennings, R., and Marsden, P.: 1984, *A&A* **138**, 10

Predehl, P. and Schmitt, J. H. M. M.: 1995, *A&A* **293**, 889

Pwa, T. H., Pottasch, S. R., and Mo, J. E.: 1986, *A&A* **164**, 184

Raymond, J. C. and Smith, B. W.: 1977, *ApJS* **35**, 419

Reed, D. S., Balick, B., Hajian, A. R., Klayton, T. L., Giovanardi, S., Casertano, S., Panagia, N., and Terzian, Y.: 1999, *AJ* **118**, 2430

Rood, R. T., Bania, T. M., and Wilson, T. L.: 1992, *Nature* **355**, 618

Scheffler, H.: 1982, in *Landolt-Bornstein: Group 6: Astronomy*, pp 45–+

Shupe, D. L., Larkin, J. E., Knop, R. A., Armus, L., Matthews, K., and Soifer, B. T.: 1998, *ApJ* **498**, 267

Smith, R. K., Brickhouse, N. S., Liedahl, D. A., and Raymond, J. C.: 2001, *ApJ* **556**, L91

Solomon, P., Jefferts, K. B., Penzias, A. A., and Wilson, R. W.: 1971, *ApJ* **163**, L53+

Suda, T., Aikawa, M., Machida, M. N., Fujimoto, M. Y., and Iben, I. J.: 2004, **611**, 476

Szentgyorgyi, A., Raymond, J., Franco, J., Villaver, E., and López-Martín, L.: 2003, *ApJ* **594**, 874

Takahara, F.: 1999, *Astrophysics*, Astrophysics / Fumio Takahara. Tokyo ; Japan : Asakura publishing,1999.

Tarafdar, S. P. and Apparao, K. M. V.: 1988, *ApJ* **327**, 342

Taylor, A. R., Gussie, G. T., and Pottasch, S. R.: 1990, *ApJ* **351**, 515

Volk, K. and Kwok, S.: 1985, *A&A* **153**, 79

Waters, L. B. F. M., Beintema, D. A., Zijlstra, A. A., de Koter, A., Molster, F. J., Bouwman, J., de Jong, T., Pottasch, S. R., and de Graauw, T.: 1998, *A&A* **331**, L61

Wilms, J., Allen, A., and McCray, R.: 2000, *ApJ* **542**, 914

Woodward, C. E., Pipher, J. L., Forrest, W. J., Moneti, A., and Shure, M. A.: 1992, *ApJ* **385**, 567

Woodward, C. E., Pipher, J. L., Shure, M., Forrest, W. J., and Sellgren, K.: 1989, *ApJ* **342**, 860

Zhang, Y., Liu, X.-W., Luo, S.-G., Péquignot, D., and Barlow, M. J.: 2005, *A&A* **442**, 249

Zweigle, J., Grewing, M., Barnstedt, J., Goelz, M., Gringel, W., Haas, C., Hopfensitz, W., Kappelmann, N., Kraemer, G., Appenzeller, I., Krautter, J., and Mandel, H.: 1997, *A&A* **321**, 891

Acknowledgments

First of all, I would like to express my deepest gratitude to Prof. K. Makishima for his continuous guidance and hearty encouragement throughout five years of my graduate course. I would also greatly appreciate Dr. M. Kokubun's warmhearted/patient encouragement and valuable discussion.

Suzaku (Astro-E2) had been developed by many people, and was successfully launched on 2005 July 10. The satellite is now in operation in low earth orbit with the great efforts of *Suzaku* team members. I greatly appreciate having the opportunity to analyze the *Suzaku* data in the present thesis. I owe a great deal to all the scientists and engineers who worked or are working on the development and operation for the *ASTRO-E/Astro-E2/Suzaku* project.

I would like to thank Prof. K. Hayashida and Dr. H. Murakami for their technical support in analyzing the XIS data. I wish to thank Prof. Y. Nakada for his valuable discussions, and Dr. K. Matsushita for her comment which encouraged me so much. I am most grateful to Prof. M. Fujimoto and Dr. T. Suda for valuable advices from the theoretical viewpoints. I am also much obliged to Dr. I. Takahashi, Dr. J. Kotoku, Dr. H. Takahashi, and all of past and present members of Makishima group in the University of Tokyo, especially, Dr. M. Kawaharada and Mr. D. Kasama, who shared my graduate course and work on the HXD-II onboard *Suzaku*.

I would like to express my gratitude to Prof. K. Hiraoka who told me how interesting science is, in my junior high school days. Finally, I would like to thank my parents and brother for their understanding and hearty supporting.